INAUGURAL-DISSERTATION

zur Erlangung der Doktorwürde (Dr. rer. nat.)
der Gesamtfakultät für Mathematik, Ingenieur- und Naturwissenschaften
der Ruprecht-Karls-Universität Heidelberg

vorgelegt von
Sebastian Steffen Lindenthal

Tag der mündlichen Prüfung
18. Juli 2025

SYNTHESIS, PURIFICATION, DOPING OF AND CHARGE TRANSPORT IN LOW-DIMENSIONAL CARBON-BASED SEMICONDUCTORS

GUTACHTER

Prof. Dr. Jana Zaumseil

Prof. Dr. Milan Kivala

ABSTRACT

Confining the electron wave functions of the semi-metal graphene by reducing its dimensionality leads to the opening of a bandgap. The resulting one-dimensional semiconductors like single-walled carbon nanotubes (SWCNTs) or graphene nanoribbons (GNRs) are promising materials for optoelectronic applications, due to their outstanding carrier mobilities and structure-dependent tunable optical and electronic properties.

The fundamental properties of SWCNTs, such as exciton dynamics, charge transport and their interaction with their environment have been studied thoroughly over the past decades and SWCNTs have been successfully integrated into a variety of optoelectronic devices. However, practical bottlenecks, associated with dispersion, purification and processing prevent scalable device integration. This thesis provides optimized and detailed protocols to obtain high-purity dispersions of long, defect-free semiconducting (6,5), (7,5) and large diameter semiconducting SWCNTs *via* polymer-wrapping in organic solvents using shear force mixing as an exfoliation method. Furthermore, a new highly soluble Lewis acid-based dopant is introduced for efficient and stable p-type doping of small-diameter, polymer-wrapped SWCNTs. In contrast to SWCNTs, many of the fundamental properties of atomically-precise GNRs are still under active investigation, as they have been first synthesized almost a decade later than SWCNTs. This work demonstrates that structural defects, which are commonly introduced during bottom-up synthesis of GNRs, significantly alter absorption and emission features in dispersions of GNRs, as well as the charge transport in GNR-based field-effect transistors. A simple method to heal defects in GNR films and thus improve their charge transport properties is presented. This work also provides first evidence of polaron formation in GNRs upon introduction of excess charge carriers *via* chemical and electrochemical doping. The findings highlight similarities between semiconducting polymers and GNRs, both in optical response to doping and charge transport in devices. Within this thesis, these findings are contextualized within the broader research landscape and implications for future studies are discussed.

KURZFASSUNG

Die Reduzierung der Dimensionalität des Halbmetalls Graphen führt zu einer räumlichen Beschränkung der Elektronenwellenfunktionen und dem Öffnen einer Bandlücke. Resultierende eindimensionale Halbleiter wie zum Beispiel einwandige Kohlenstoffnanoröhren (SWCNTs) oder Graphen-Nanostreifen (GNRs) besitzen hohe Ladungsträgermobilitäten und strukturabhängige, modulierbare elektronische und optische Eigenschaften, die sie interessant für optoelektronische Anwendungen machen.

Die grundlegenden Eigenschaften von SWCNTs – beispielsweise Exzitondynamiken, die Wechselwirkung mit ihrer Umgebung oder Ladungstransport – wurden in den letzten 30 Jahren ausführlich studiert und Nanoröhren wurden bereits erfolgreich in eine Vielzahl von optoelektonischer Bauelemente integriert. Einer skalierbaren Anwendung von Nanoröhren stehen allerdings Herausforderungen bei ihrer Dispersion, Aufreinigung und Prozessierung im Weg. Diese Arbeit bietet eine detaillierte und optimierte Anleitung, wie mithilfe konjugierter Polymere und Scherkraftmischen hochreine Dispersionen aus langen, defektfreien, halbleitenden (6,5), (7,5) und Plasma Torch SWCNTs produziert werden können. Des Weiteren wird eine Lewis-Säure als chemischer p-Dotand für polymerumwickelte Nanoröhren mit kleinen Durchmessern vorgestellt. Da GNRs fast ein Jahrzehnt später hergestellt wurden als SWCNTs, sind die grundlegenden Eigenschaften von GNRs immer noch Gegenstand aktueller Forschung. Diese Arbeit zeigt, dass strukturelle Defekte, welche bei der Synthese von GNRs auftreten, die Absorptions- und Emissionseigenschaften in Dispersion sowie den Ladungstransport in GNR-basierten Transistoren beeinflussen. Eine einfache Methode zum Ausheilen der Defekte in GNR-Filmen, zur Verbesserung der Ladungstransporteigenschaften, wird vorgestellt. Zusätzlich zeigt diese Arbeit die ersten experimentellen Hinweise zur Bildung von Polaronen in GNRs, wenn überschüssige Ladungsträger durch chemische oder elektrochemische Dotierung eingeführt werden. Die Daten zeigen ähnliches Verhalten wie bei konjugierten Polymeren bei den optischen Eigenschaften nach Dotierung als auch beim Ladungsträgertransport. Die Ergebnisse dieser Arbeit bieten Ansatzpunkte für weitere Studien, um die fundamentalen Eigenschaften von Interaktionen von Ladungsträgern und niederdimensionalen kohlenstoffbasierten Nanomaterialien besser zu verstehen.

PUBLICATION LIST

A First Author, Not Peer-Reviewed

P1 **Lindenthal, S.**; Settele, S.; Hellmann, J.; Schmitt, K.; Zaumseil, J. A Hands-On Guide to Shear Force Mixing of Single-Walled Carbon Nanotubes with Conjugated Polymers. *arXiv* **2023,** *arXiv:2311.11654v1*, https://doi.org/10.48550/arXiv.2311.11654 (accessed 2025-06-02).

B First Author, Peer-Reviewed

P2 **Lindenthal, S.**; Rippel, D.; Kistner, L.; Hawkey, A.; Zaumseil, J., Synergistic p-Doping of Polymer-Wrapped Small-Diameter Single-Walled Carbon Nanotubes by Tris(pentafluorophenyl)borane. *Journal of Physical Chemistry C* **2025,** *11*, 5520-5529, https://doi.org/10.1021/acs.jpcc.4c08584.

P3 **Lindenthal, S.**; Fazzi, D.; Zorn, N. F.; El Yumin, A. A.; Settele, S.; Weidinger, B.; Blasco, E.; Zaumseil, J., Understanding the Optical Properties of Doped and Undoped 9-Armchair Graphene Nanoribbons in Dispersion. *ACS Nano* **2023,** *17*, 18240-18252, https://doi.org/10.1021/acsnano.3c05246.

P4 **Lindenthal, S.;** Sebastian, F. L.; Herrmann, N. J.; Zorn, N. F.; Zaumseil J., Healing Defects in Armchair Graphene Nanoribbons for Improved Charge Transport. *ACS Applied Nano Materials* **2025,** *XX,* XXXXX-XXXXX, https://doi.org/10.1021/acsanm.5c01848.

C Contributing Author, Peer-Reviewed

P5 Settele, S.; Berger, F. J.; **Lindenthal, S.**; Zhao, S.; El Yumin, A. A.; Zorn, N. F.; Asyuda, A.; Zharnikov, M.; Högele, A.; Zaumseil, J. Synthetic control over the binding configuration of luminescent sp3-defects in single-walled carbon nanotubes. *Nature Communications* **2021,** *12*, 2119, https://doi.org/10.1038/s41467-021-22307-9.

P6 Balcı Leinen, M.; **Lindenthal, S.**; Heimfarth, D.; Zaumseil, J., Networks of as-dispersed, polymer-wrapped (6,5) single-walled carbon nanotubes for selective Cu2+ and glyphosate sensing. *Nanoscale* **2022,** *14*, 13542-13550, https://doi.org/10.1039/D2NR02517E.

P7 Sebastian, F. L.; Zorn, N. F.; Settele, S.; **Lindenthal, S.**; Berger, F. J.; Bendel, C.; Li, H.; Flavel, B. S.; Zaumseil, J., Absolute Quantification of sp3 Defects in Semiconducting Single-Wall Carbon Nanotubes by Raman Spectroscopy. *The Journal of Physical Chemistry Letters* **2022,** *13*, 3542-3548, https://doi.org/10.1021/acs.jpclett.2c00758.

P8 Hsu, L.-Y.; Mainik, P.; Münchinger, A.; **Lindenthal, S.**; Spratte, T.; Welle, A.; Zaumseil, J.; Selhuber-Unkel, C.; Wegener, M.; Blasco, E., A Facile Approach for 4D Microprinting of Multi-Photoresponsive Actuators. *Advanced Materials Technologies* **2023,** *8*, 2200801, https://doi.org/10.1002/admt.202200801.

P9 Frisch, S.; Neiß, C.; **Lindenthal, S.**; Zorn, N. F.; Rominger, F.; Görling, A.; Zaumseil, J.; Kivala, M., Tetra(peri-naphthylene)anthracene: A Near-IR Fluorophore with Four-Stage Amphoteric Redox Properties. *Chemistry – A European Journal* **2023,** *29*, e202203101, https://doi.org/10.1002/chem.202203101.

P10 Zorn, N. F.; Settele, S.; Zhao, S.; **Lindenthal, S.**; El Yumin, A. A.; Wedl, T.; Li, H.; Flavel, B. S.; Högele, A.; Zaumseil, J., Near-Intrinsic Photo- and Electroluminescence from Single-Walled Carbon Nanotube Thin Films on BCB-Passivated Surfaces. *Advanced Optical Materials* **2023,** *11*, 2300236, https://doi.org/10.1002/adom.202300236.

P11 Zorn, N. F.; Settele, S.; Sebastian, F. L.; **Lindenthal, S.**; Zaumseil, J., Tuning Electroluminescence from Functionalized SWCNT Networks Further into the Near-Infrared. *ACS Applied Optical Materials* **2023,** *1*, 1706-1714, https://doi.org/10.1021/acsaom.3c00261.

P12 Sebastian, F. L.; Becker, F.; Yomogida, Y.; Hosokawa, Y.; Settele, S.; **Lindenthal, S.**; Yanagi, K.; Zaumseil, J., Unified Quantification of Quantum Defects in Small-Diameter Single-Walled Carbon Nanotubes by Raman Spectroscopy. *ACS Nano* **2023,** *17*, 21771-21781, https://doi.org/10.1021/acsnano.3c07668.

P13 Jocic, A.; Wickenhäuser, T.; **Lindenthal, S.**; Zhang, W.-S.; Zaumseil, J.; Schröder, R.; Klingeler, R.; Kivala, M., Redox-active, photoluminescent porous polymers based on spirofluorene-bridged N-heterotriangulenes and their feasibility as organic cathode materials. *Chemical Science* **2024,** *15*, 19094-19103, https://doi.org/10.1039/D4SC04276J.

P14 Eberle, L.; **Lindenthal, S.**; Ballmann, J., To Split or Not to Split: [AsCCAs]-Coordinated Mo, W, and Re Complexes and Their Reactivity toward Molecular Dinitrogen. *Inorganic Chemistry* **2024,** *63*, 3682-3691, https://doi.org/10.1021/acs.inorgchem.3c03244.

P15 Settele, S.; Stammer, F.; Sebastian, F. L.; **Lindenthal, S.**; Wald, S. R.; Li, H.; Flavel, B. S.; Zaumseil, J., Easy Access to Bright Oxygen Defects in Biocompatible Single-Walled Carbon Nanotubes via a Fenton-like Reaction. *ACS Nano* **2024,** *18*, 20667-20678, https://doi.org/10.1021/acsnano.4c06448.

P16 Hawkey, A.; Dash, A.; Rodríguez-Martínez, X.; Zhao, Z.; Champ, A.; **Lindenthal, S.**; Zharnikov, M.; Kemerink, M.; Zaumseil, J., Ion-Exchange Doping of Semiconducting Single-Walled Carbon Nanotubes. *Advanced Materials* **2024,** *36*, 2404554, https://doi.org/10.1002/adma.202404554.

P17 Hawkey, A.; Rodríguez-Martínez, X.; **Lindenthal, S.**; Jansen, M. C. F.; Crispin, R.; Zaumseil, J., Bandgap-Dependent Doping of Semiconducting Carbon Nanotube Networks by Proton-Coupled Electron Transfer for Stable Thermoelectrics. *Advanced Electronic Materials* **2025**, *n/a*, 2400817, https://doi.org/10.1002/aelm.202400817.

P18 Sebastian, F. L.; Kaminski, L.; Bendel, C.; Yomogida, Y.; Hosokawa, Y.; Li, H.; **Lindenthal, S.**; Flavel, B. S.; Yanagi, K.; Zaumseil, J., Circular Dichroism of Quantum Defects in Carbon Nanotubes Created by Photocatalytic Oxygen Functionalization. *Nature Communications* **2025,** *XX*, XXXX, https://doi.org/10.1038/s41467-025-60342-y.

P19 Hermosilla-Palacios, M. A.; **Lindenthal, S.**; Earley, J. D.; Aubry, T. J.; DeLuca, D.; Al Khunaizi, H.; Spokoyny, A. M.; Zaumseil, J.; Ferguson, A. J.; Blackburn, J. L., Polaron Delocalization and Transport in Doped Graphene Nanoriubbon Thin Films. *Under Review*.

DANKSAGUNG

Zuallererst möchte ich mich hier bei meiner Doktormutter **Prof. Dr. Jana Zaumseil** bedanken: Danke für die spannenden Projekte, an denen ich zusammen mit dir arbeiten durfte. Danke für das Vertrauen, das du in mich gesetzt und die Freiheiten, die du mir gegeben hast – nur so hatte ich die Möglichkeit eigene Ideen verfolgen und entwickeln zu können. Danke für deine Hartnäckigkeit in wissenschaftlichen Diskussionen die oftmals zu mehr Arbeit für mich aber auch zu einem erfolgreichen Abschluss der Projekte geführt hat. Und natürliche danke für die vielen Möglichkeiten, die du mir gegeben hast, mich mit der wissenschaftlichen Gemeinschaft aus aller Welt zu vernetzen.

An dieser Stelle möchte ich natürlich auch **Prof. Dr. Milan Kivala** danken, der nicht nur das Zweitgutachten dieser Thesis übernommen hat, sondern mir zu Beginn der Arbeit auch einen Arbeitsplatz in einem seiner Labore überlassen hat, ohne den ein Großteil der Synthesearbeit deutlich erschwert worden wäre**. Sabine, Julian, Alex, Angi, Siegfried, Jan, Erik, Maxi, Leon, Sven, Laura, John** und **Ina** – es war eine tolle Zeit als „Gastdoktorand" bei euch und dass ich mich wohlgefühlt habe, hat man vermutlich an den zahlreichen gemeinsamen Kaffeepausen (auch nach Ende meiner Synthesearbeit) gemerkt.

Die mehr als vier Jahre im Arbeitskreis *Nanomaterials for Optoelectronics* waren eine unvergessliche Zeit und ein großer Bestandteil war die enge Zusammenarbeit mit vielen großartigen Kollegen. Besonders hervorzuheben ist hierbei das TRIFECTs Team, dessen Bestandteil ich sein durfte. Vielen Dank **Felix**, dass du mir schon im Zuge des Forschungspraktikums im Master und der Masterarbeit aber auch zu Beginn meiner Doktorarbeit stets mit Rat und Tat zur Seite standest. Danke **Nicolas**, dass du dein Wissen über Spektroskopie und Transistoren mit mir geteilt hast. Unsere gemeinsame Reise durch die wundersame Welt der Ionogel-Transistoren wird mir im Gedächtnis bleiben. Die gemeinsamen Diskussionen über erfolgreiche (und weniger erfolgreiche) Chemie an Nanomaterialien mit dir, **Simon**, waren stets extrem hilfreich, um auf neue Ideen zu kommen (und um Frust über gescheiterte Experimente abzulassen). Danke **Sonja** für deine Hilfsbereitschaft bei Fragen und Problemen jeglicher Art und auch dafür, dass du es mit uns im TRIFECTs Team ausgehalten hast. **Finn**, es war mir eine Freude mit dir den Promotionsalltag zu Meme-ifizieren, fachliche Diskussionen zu führen und gemeinsam auf Konferenzen zu reisen. An dieser Stelle auch ein riesengroßes Dankeschön für das schnelle Korrekturlesen dieser Arbeit. **Ali**, thanks for always helping me with the cryosetup when problems emerged. I really enjoyed your humor, and it is a shame that “Deutscher Donnerstag” was such a short-lived tradition, as you left shortly after.

Sebastian, Angus, Elisa, Simon W. und **Niklas** – ihr wart ideale Bürokollegen. Sowohl die produktiven als auch die nicht ganz so produktiven Gespräche mit euch haben mich gut durch den Tag gebracht. Danke ebenfalls an **Tim** und **Claudia**, die mir vor ihrem Umzug nach Kassel mit Exfoliierung, Kaskadenzentrifugation und bei AFM-Fragen geholfen haben. An dieser Stelle möchte ich auch den übrigen NMOE (**Xuqiang, Yachen, Parvathi, Xabier, Manuel, Yan, Daniel, Severin, Max, Maik, Jan, Jan G.** und **Merve**) und PC2D (**Kevin, Steffen, Farnia, Max K.** und **Beata**) Kollegen für die tolle Arbeitsatmosphäre und die große Hilfsbereitschaft in jeder Hinsicht danken.

Während meiner Dissertation konnte ich mich natürlich nicht nur auf die Unterstützung von festen Mitgliedern der NMOE und PC2D Gruppen verlassen, sondern auch auf **Joshua Hellmann, Till Schreyer, Daniel Rippel** und **Muhammed Ali Arslan**. Vielen Dank dass ihr im Zuge eurer Forschungspraktika zum Gelingen dieser Arbeit beigetragen habt. Auch nochmal einen Dank und ein Lob an dich **Niklas**, dass du trotz eines herausfordernden Themas und mir als Betreuer, der selbst erst am Beginn seiner Doktorarbeit stand, deine Masterarbeit souverän bestritten hast. Ein großer Dank geht selbstverständlich auch an die **Mitglieder der SFM Crew, die Feinmechanikwerkstatt, Frau Duchnay, Frau Jordan, Frau Ihli, Frau Haffelder, Günter, Peter, Joachim** und **Ali** ohne die die Doktorarbeit nicht so reibungslos verlaufen wäre.

Das Studium und die Promotion waren eine sowohl herausfordernde als auch wunderschöne Zeit und ich freue mich den Weg gemeinsam mit euch bestritten zu haben **Julianna, Simon, Lucas, Michael, Siegfried, Elena** und **Svenja**. Danke für die gemeinsamen Mittagspausen, die vielen lustigen (und für Elena *besonders* anstrengenden) Stunden im Labor und die gemeinsam verbrachte Zeit. Auch außerhalb der Uni konnte ich stets auf gute Freunde zählen: **Johannes** und **Joshua**, danke dass ihr mich in dieser Zeit begleitet habt, für die gemeinsamen Spieleabende, Boulder-Sessions, Urlaube und Erlebnisse, die ich mit euch machen durfte.

Schlussendlich möchte ich mich auch bei meiner Familie bedanken: Vielen Dank an euch **Mama** und **Papa, Sven, Steffi, David** und **Fiona**, und **Sina** und **Tassilo,** dass ihr mir dieses Studium durch eure vielfältige Unterstützung ermöglicht habt. Mein größter Dank gilt aber dir, **Phillip**. Wir kennen und nun schon seit meinem dritten Semester und du hast mich in all den Jahren durch die Hochs und Tiefs meiner akademischen Reise begleitet und mir geholfen, wo du auch konntest. Vielen Dank für die gemeinsame Zeit, die du bisher mit mir verbracht hast und ich freue mich auf die Zukunft, die uns beide erwartet.

CONTENTS

ABBREVIATIONS

1D	one-dimensional
2D	two-dimensional
aGNR	armchair graphene nanoribbon
ARPES	angle-resolved photo-electron spectroscopy
ATPE	aqueous two-phase extraction
BCF	tris(pentafluorophenyl)borane
CHP	N-cyclohexyl-2-pyrrolidone
CoMoCAT®	cobalt-molybdenum catalyst growth SWCNTs
CTC	charge transfer complex
CVD	chemical vapour deposition
DFT	density functional theory
DGU	density gradient ultracentrifugation
DMF	dimethyl formamide
DOS	density of states
EA	electron affinity
E_F	Fermi level
E_g	band gap
EGT	electrolyte-gated transistor
F_4TCNQ	2,3,5,6-tetrafluor-7,7,8,8-tetracyanochindimethan
FET	field-effect transistor

HiPCO®	high-pressure carbon monoxide growth SWCNTs
ICT	integer charge transfer
IE	ionization energy
LDA	local density approximation
NMP	N-methyl-2-pyrrolidone
PFO	poly[9,9-dioctylfluorenyl-2,7-diyl]
PFO-BPy	poly[(9,9-dioctylfluorenyl-2,7-diyl)-*alt*-co-(6,6'-(2,2'-bipyridine))]
PL	photoluminescence
PL-PEG	polyethylene glycol phospholipids
PLQY	photoluminescence quantum yield
SEC	Size exclusion chromatography
ssDNA	single-stranded desoxyribonucleic acid
STS	scanning tunneling spectroscopy
SWCNT	single-walled carbon nanotube
TBA	tight-binding approximation
THF	tetrahydrofuran
vHs	van-Hove singularity
zGNR	zigzag graphene nanoribbon

CHAPTER 1

INTRODUCTION

The demand for low-cost, miniaturized electronic devices keeps increasing constantly with no signs of slowing down. While components such as dielectrics, interconnects, and contact materials have seen constant innovation, the industrially-used channel materials – silicon and III-V-compounds – have remained largely unchanged.[1-3] However, these materials face limitations. Short-channel effects, increasing power dissipation and physical resolution limits of lithography prevent a further decrease of device dimensions.[4,5]

These challenges have driven the search for competitive solution-processable organic semiconductors, which offer low-cost, large-area fabrication techniques and structure-tunable optoelectronic properties.[6,7] Among these materials, especially graphene-based low-dimensional semiconductors such as single-walled carbon nanotubes (SWCNTs) and graphene nanoribbons (GNRs) have attracted interest due to their outstanding charge transport properties, mechanical strength and tunable band gaps, which arise from quantum confinement and edge effects.[8-10]

Semiconducting SWCNTs have been promising materials in a wide range of applications including field-effect transistors, neuromorphic computing, chemical and biological sensing, and thermoelectric power generators.[11-16] However, commercially available carbon nanotube raw materials, synthesized via arc-discharge, laser ablation or chemical vapor deposition contain a heterogeneous mixture of semiconducting and metallic SWCNT species, which are commonly referred to as chiralities.[17] To harness their full potential in electronic and optoelectronic applications, the semiconducting SWCNT chiralities must be isolated and the resulting dispersions must be stabilized to ensure good processability.

Over the past decade, polymer-wrapping has established itself as a powerful technique to obtain high-purity, single-chirality semiconducting SWCNT dispersions.[18,19] This process involves selective interaction of conjugated polymers with specific SWCNT chiralities, enabling their dispersion in organic solvents. When combined with the mild and scalable exfoliation method of shear force mixing resulting dispersions contain long, low-defect SWCNTs with high photoluminescence quantum yields and charge carrier mobilities.[20] At the start of this dissertation, this approach had only been employed to extract (6,5) SWCNTs (with a bandgap of ~1.24 eV) from CoMoCAT raw material. Extending this technique to large-diameter chiralities (diameter > 1 nm) with smaller bandgaps, which had thus far only been exfoliated by sonication-based methods, would greatly expand the range of purified SWCNTs for research and applications.

Regardless of their impressive intrinsic electronic properties, successful incorporation of SWCNTs in devices requires precise modulation of charge carrier concentration and type of charge carriers (*i.e.*, holes or electrons).[21] Chemical doping offers a way to achieve this, but many existing dopants suffer from poor solubility, doping efficiency and stability. Hence, establishing new, reliable molecular dopants that precisely tune the electronic properties of SWCNTs is critical for future use of SWCNTs in electronic applications.

In contrast to SWCNTs, only little is known about the fundamental properties of atomically precise GNRs primarily due to the complex synthesis routes that are associated with their creation.[22-24] As a result, fundamental questions regarding charge modulation in GNRs by chemical doping, as well as the impact of structural irregularities introduced during synthesis on optical and charge transport properties remain unanswered. Filling these knowledge gaps is essential to test theoretical models on and possible applications of GNRs.

This thesis addresses all of the outlined problems and open questions. Chapter 2 presents an overview of structure, synthesis and purification, and the electronic and optical properties of semiconducting SWCNTs and bottom-up synthesized GNRs. The concept of chemical doping to change the carrier density of low-dimensional semiconductors is introduced and the key changes in electronic properties and optical spectra of SWCNTs and GNRs upon doping are discussed. Finally, the working principle of an (electrolyte-gated) ambipolar FET is explained and current state-of-the-art GNR-based devices are reviewed.

Chapters 3-6 contain four publications that have each contributed to answering questions or solving the problems presented here :

The publication presented in **Chapter 3** provides a detailed explanation on how to expand the combined approach of shear force mixing and polymer-wrapping to isolate large quantities of semiconducting SWCNTs with chiralities other than (6,5). It also discusses potential pitfalls associated with the process and how to increase process yield and stability.

Chapter 4 explores the use of a new boron-based, highly soluble Lewis acid for doping of polymer-wrapped SWCNTs in dispersion. By combining absorption, photoluminescence and

NMR spectroscopy, a unique doping mechanism which relies on the interaction between the Lewis acidic dopant, Lewis basic functional groups in the wrapping polymer and the SWCNTs, is revealed. The dopant is then benchmarked against other commonly used p-type dopants showing superior doping efficiency and doping stability.

The study in **Chapter 5** examines the optical properties of undoped and p-doped solution-synthesized armchair graphene nanoribbons in dispersion. A method to disperse GNRs and separate two populations of GNRs is established. Absorption, (single-GNR) photoluminescence and Raman spectroscopy combined with theoretical DFT calculations reveal the nature of the two populations as GNRs with and without defects. This demonstrates the impact of defects on aggregation properties and optical properties of solution-synthesized GNRs. Finally, chemical doping of GNR dispersions leads to charge-induced absorption but no new emission features, indicating polaron formation in GNRs in contrast to trion formation observed in SWCNTs.

Finally, **Chapter 6** investigates the influence of defects in GNRs on their charge transport properties. A method to heal structural defects in films of solution-synthesized GNRs based on thermal annealing is developed. Films of GNRs with different defect densities are investigated by means of Raman and absorption spectroscopy, as well as atomic force microscopy. The electrical characterization of thin-film electrolyte-gated transistors with GNRs of different defect densities quantitatively reveals the detrimental effect that defects have on electron and hole transport.

The main results of this work are summarized in **Chapter 7**. They are contextualized within the current state of research on low-dimensional carbon- based semiconductors. Additionally, remaining questions and the potential for future studies are discussed.

CHAPTER 2

THEORETICAL BACKGROUND

Graphene is a carbon allotrope consisting of a monolayer of sp_2-hybridized carbon atoms, arranged in a honeycomb lattice. Since its first isolation by mechanical exfoliation of graphite in 2004,[25] it has been in the focus of material science due to its outstanding mechanical and electronic properties.[26-28] To harness these features for semiconductor applications, a band gap must be created in the otherwise semi-metallic graphene. This can be achieved by reducing the dimensionality of the two-dimensional (2D) material even further, which leads to quasi zero-dimensional (*e.g.,* fullerenes and graphene quantum dots) or quasi one-dimensional (1D) (*e.g.,* carbon nanotubes and graphene nanoribbons) nanomaterials. The new boundary conditions imposed on the Bloch wavefunctions of graphene lead to the opening of a bandgap with the exact electronic structure depending on the structure of the low-dimensional carbon allotrope.

This chapter explains how to derive the structures of single-walled carbon nanotubes and graphene nanoribbons starting from graphene and the implications for their electrical and optical properties. It will also cover synthesis and purification of the respective nanomaterials. Finally, it discusses doping of and charge transport in carbon nanotubes and graphene nanoribbons. which are essential for their potential applications in optoelectronic devices.

2.1 Single-Walled Carbon Nanotubes

Carbon nanotubes, first discovered in 1991,[29] are hollow cylinders of sp^2-hybridized carbon with large aspect ratios. While single- and multi-walled species exist, this work will focus on single-walled carbon nanotubes due to their defined and well-understood electronic and optical properties. In the next chapters, their structure, synthesis and purification, as well as their electronic and optical properties will be introduced.

2.1.1 Structure and Synthesis

A single-walled carbon nanotube can be conceptualized as a seamlessly rolled-up sheet of graphene, as depicted in **Figure 1**.[30]

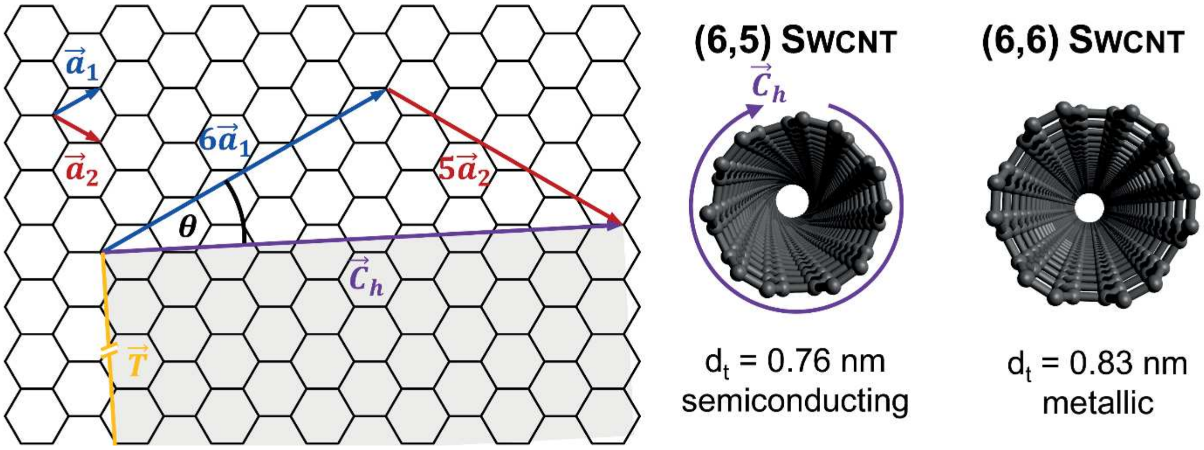

Figure 1. Schematic construction of a (6,5) SWCNT. The chiral vector $\vec{C}_h$ as well as the translational vector $\vec{T}$ for the resulting SWCNT are depicted. On the right, the front view of the constructed chiral, semiconducting (6,5) SWCNT and an achiral, metallic (6,6) SWCNT are shown.

The direction in which the graphene sheet is rolled up is defined by the chiral vector $\vec{C}_h$, which connects the two carbon atoms that overlap each other during this process. The chiral vector can be expressed via a linear combination of two lattice vectors $\vec{a}_1$ and $\vec{a}_2$

$$\vec{C}_h = n\,\vec{a}_1 + m\,\vec{a}_2, \tag{2.1}$$

with $n \geq m$ and $n, m \in \mathbb{N}_0$.[30-32] The translational vector $\vec{T}$ which is the smallest perpendicular vector to the chiral vector, can be constructed as

$$\vec{T} = \frac{2m+n}{\mathrm{gcd}}\,\vec{a}_1 - \frac{2n+m}{\mathrm{gcd}}\,\vec{a}_2, \tag{2.2}$$

where gcd is the greatest common divisor of $2m + n$ and $2n + m$.[30] Both vectors together define the unit cell of a SWCNT with a given index pair (n,m).[30-32] The schematic construction of a (6,5) SWCNT is shown in **Figure 1**.

The length $|\vec{a}|$ of the lattice vectors in **Equation (2.1)** can be calculated by $|\vec{a}| = \sqrt{3}\,a_{C-C} = 0.246$ nm, where $a_{C-C} = 0.142$ nm is the carbon-carbon bond length in graphene. The diameter d_t of a SWCNT with the index pair (n,m) is then given by

$$d_t = \frac{|\vec{C}_h|}{\pi} = \frac{|\vec{a}|}{\pi}\sqrt{n^2 + nm + m^2}. \tag{2.3}$$

The diameter of SWCNTs typically ranges from 0.7-2 nm but smaller and larger species have been reported.[32-34] SWCNTs with diameters smaller than 0.43 nm are, however, unattainable, as their structure would put immense strain on the carbon lattice, while tubes with large diameters (>2.6 nm) collapse.[35-37] The chiral angle θ between $\vec{a}_1$ and $\vec{C}_h$ can be calculated as

$$cos(\theta) = \frac{2n + m}{2\sqrt{n^2 + nm + m^2}} \tag{2.4}$$

and can only reach values between 0° and 30° due to the hexagonal symmetry of the graphene lattice.[30-32]

SWCNTs with an index pair of (n,0) (chiral angle $\theta = 0°$) are called zigzag nanotubes, while those with an index pair of (n,n) (chiral angle $\theta = 30°$) are known as armchair nanotubes.[30,31] Both of these nanotube types are achiral due their mirror symmetry.[30,31] Every other combination of indices leads to chiral nanotubes with the enantiomeric pairs (n,m) and (n+m,–m). These pairs will have the same optical and electrical properties, except for their interaction with circularly polarized light.[32,38,39] Regardless of a nanotube's actual chirality, the term is often used synonymously with helicity.

To obtain SWCNTs, a multitude of synthesis methods have been developed. In commercial SWCNT synthesis a carbon source is decomposed on catalytically active metal particles (typically transition metals) at high temperatures.[17,40] The chirality distribution within the resulting raw material strongly depends on the exact synthesis parameters, such as temperature or catalyst type and size.[17,40] Laser-ablation and arc-discharge methods create large-diameter SWCNTs (d_t~1-2 nm).[41,42] Plasma torch processes, which decompose carbon black in an argon plasma torch, yield slightly smaller SWCNTs with a diameter d_t between 0.9-1.5 nm.[43] To obtain small diameter nanotubes, chemical vapor deposition (CVD) methods have been established which also offer the advantage of comparatively mild synthesis conditions.[17,40,44] The most relevant for this thesis are the HiPco® (high-pressure carbon monoxide) and the CoMoCAT® (cobalt-molybdenum catalyst) processes. In the former, carbon monoxide is mixed with $Fe(CO)_5$ at high pressures (1-10 bar) and heated to 800-1200 °C. At these temperatures, the iron complexes decompose into catalytically active iron particles, at which the carbon monoxide reacts to form SWCNTs.[45,46] The resulting nanotubes have a diameter between 0.8-1.3 nm (*e.g.*, (10,5) SWCNTs).[45,46] The CoMoCAT® process, which uses silicon dioxide-supported cobalt-molybdenum catalysts to form SWCNTs from carbon monoxide at temperatures between 700-900 °C, produces even narrower nanotubes (d_t ~ 0.7-1.0 nm) – predominantly (6,5) and (7,5) SWCNTs.[47-50]

While significant progress has been made in the development of synthesis methods that yield either a narrow distribution of nanotubes chiralities or even monochiral SWCNTs,[40,49,50] all commercial large-scale processes still lead to raw material containing a variety of SWCNT chiralities with different electrical and optical properties (*e.g.*, metallic *vs.* semiconducting). Additionally, the resulting raw material still contains significant amounts of impurities despite post-synthetic treatment. Consequently, methods to purify and sort SWCNTs by their chirality are required for their application.

2.1.2 Purification and Chirality Sorting

Aside from the removal of non-SWCNT impurities and enrichment of a desired SWCNT chirality, the purification process must first individualize and stabilize the SWCNTs in dispersion. Exceptionally high van-der-Waals forces (~1 eV per nm of SWCNT) between nanotubes lead to bundling once they are synthesized.[51-53] These bundles need to be broken up by applying sufficient mechanical forces for successful dispersion of individual SWCNTs. This can be achieved by bath or tip sonication for minutes to hours[54,55], shear force mixing for a few days[20] or stirring for a few days to weeks.[56,57] Milder dispersion methods (*i.e.*, stirring and shear force mixing) lead to dispersions with longer SWCNTs, that contain less structural defects, which is beneficial for their optical and electrical properties.[20]

There are two options to prevent re-aggregation of the individualized, dispersed SWCNTs. SWCNTs can be dispersed in a solvent with suitable Hansen solubility parameters such as N-methyl-2-pyrrolidone (NMP), dimethyl formamide (DMF) or N-cyclohexyl-2-pyrrolidone (CHP).[58-60] These solvents are however toxic and difficult to remove after processing (*e.g.*, after film deposition) due to their high boiling points.[61,62] More commonly, surfactants or (bio)polymers are added to water or less toxic organic solvents to achieve stable, processable dispersions.[63] The general process of dispersing and sorting SWCNTs in an aqueous environment with surfactants or in an organic solvent using selective polymer-wrapping is shown in **Figure 2.**

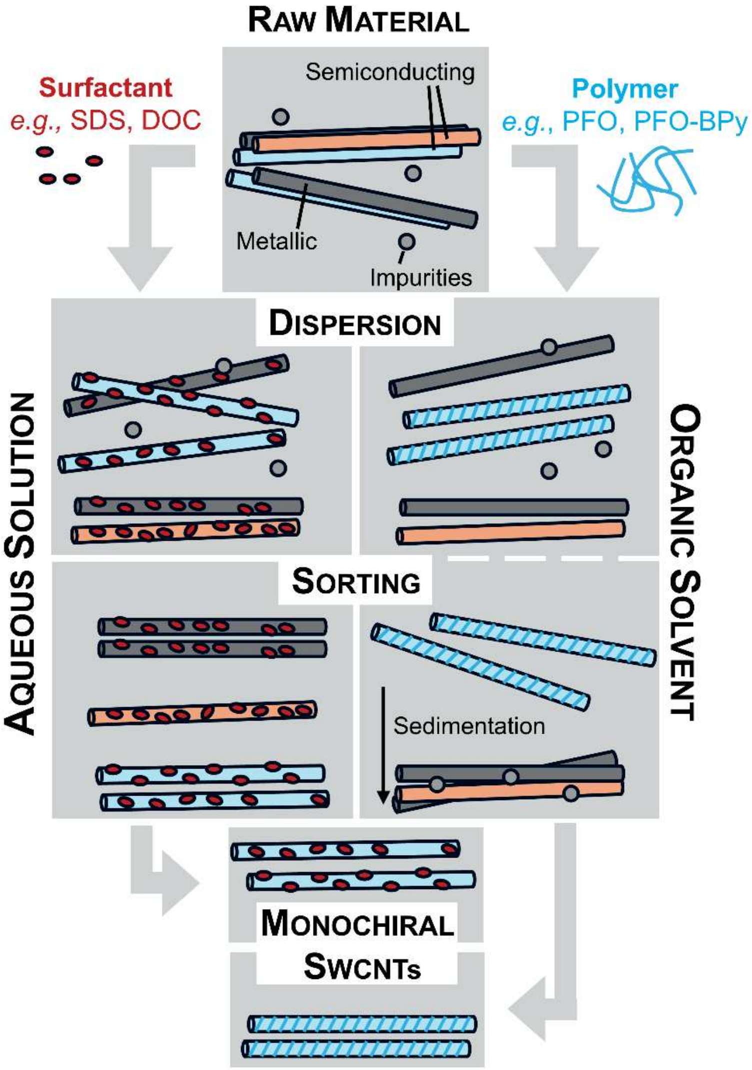

Figure 2. Schematic depiction of the purification process of SWCNTs in an aqueous and organic solventresulting in chirality-pure SWCNT dispersions. Nanotubes depicted in blue and orange represent semiconducting SWCNTs with different chiral indies (n,m).

To stabilize SWCNTs in an aqueous environment, surfactants like sodium deoxycholate (DOC) or sodium dodecyl sulfate (SDS), or biocompatible polymers like polyethylene glycole phospholipids (PL-PEG) or single-stranded DNA (ssDNA) are sonicated with SWCNT raw material in an aqueous environment.[64,65] The hydrophobic parts of surfactants interact with the SWCNT sidewalls, and the zeta-potential of their ionic head-groups leads to stable dispersions. Surfactants and biocompatible polymers are, however, mostly not selective towards a single nanotube chirality and resulting dispersions typically contain a broad mixture of semiconducting and metallic nanotubes as indicated in **Figure 2**.[64,65] Hence, a subsequent sorting step is necessary to obtain chirality-enriched SWCNT dispersions. Over the past two decades this has been achieved by numerous methods such as density gradient ultracentrifugation (DGU)[66,67], electrophoresis[68], gel-chromatography[69,70] and aqueous two-phase extraction (ATPE).[71,72] The resulting chirality-enriched dispersions are typically of high quality and nowadays many different nanotube chiralities can be isolated. The required sorting steps, however, require expensive equipment such as ultracentrifuges or special size-exclusion chromatography (SEC) columns. Additionally, the resulting aqueous dispersions are difficult to process (*i.e.*, in film deposition).

Selective polymer-wrapping of SWCNTs in organic solvents offers a way to disperse and simultaneously sort SWCNTs by type (semiconducting *vs.* metallic) or chirality (see **Figure 2**). Different types of conjugated polymers, such as polyfluorenes, polythiophenes and polycarbazoles exhibit strong electronic interactions with SWCNTs.[73-75] Upon de-bundling of SWCNTs in solutions of these polymers in organic media, polymer strands wrap individualized SWCNTs, preventing re-aggregation.[76] A simple centrifugation step can then sediment unexfoliated or re-aggregated material, which leaves behind a stable nanotube dispersion. It was also shown that certain fluorene-based polymers exhibit a high selectivity towards wrapping of certain semiconducting SWCNT chiralities.[77,78] Dispersion of CoMoCAT® raw material with polyfluorene poly[9,9-dioctylfluorenyl-2,7-diyl] (PFO) led to an enrichment in (7,5) SWCNTs[77], while dispersion with the polyfluorene co-polymer poly[(9,9-dioctylfluorenyl-2,7-diyl)-*alt*-co-(6,6’-(2,2’-bipyridine))] (PFO-BPy) resulted in dispersions of (6,5) SWCNTs (**Figure 3**).

Since then, understanding the selectivity of the polymer wrapping process towards certain chiralities and factors that influence the extracted SWCNT chiralities, dispersion selectivity, stability and yield have been a focus of research. Unfortunately, the investigated systems are complex and the interplay of polymer-related (*e.g.*, backbone structure, side chain length, molecular weight), solvent-related (*e.g.*, viscosity, dielectric constant) and process-related parameters (*e.g.*, temperature, sonication power) determines the outcome of the dispersion process.

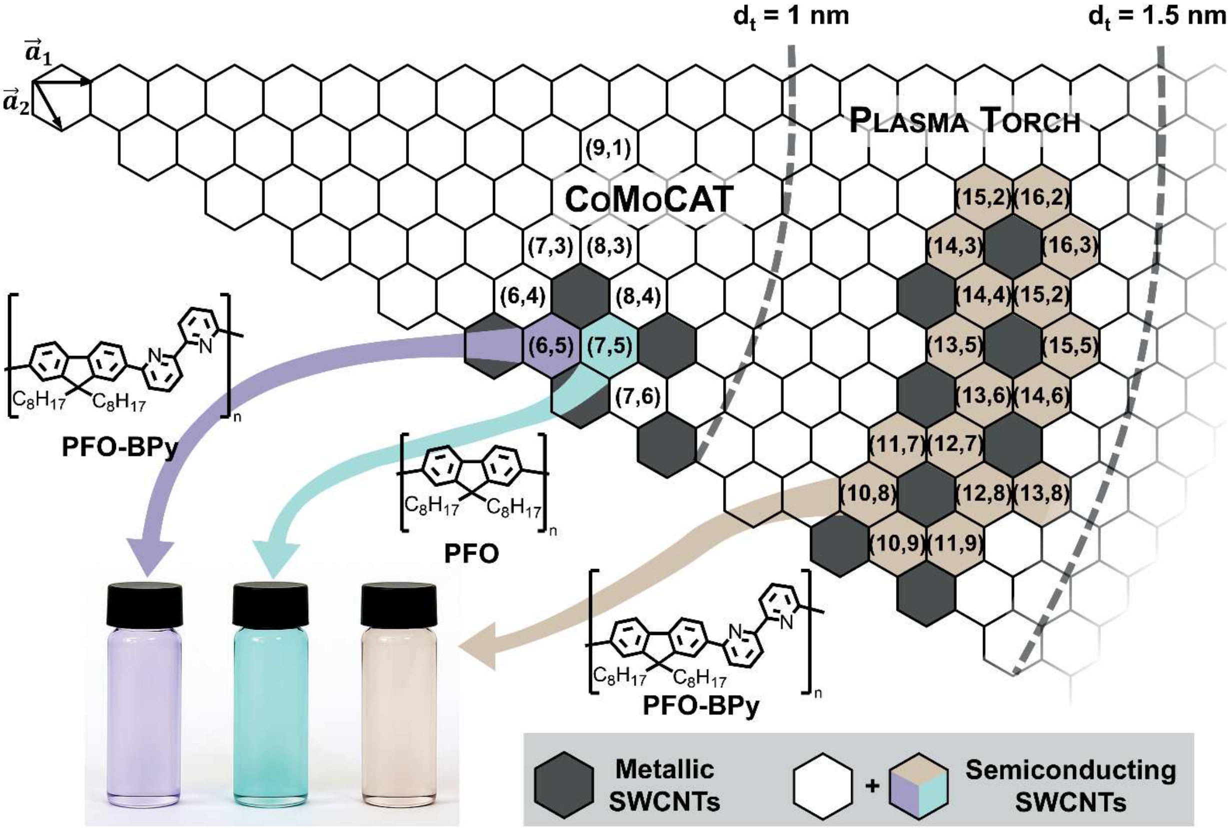

Figure 3. Schematic depiction of the SWCNT chiralities present in either CoMoCAT or Plasma Torch raw material. Metallic nanotubes that are also present in the raw material are highlighted by dark grey hexagons. The semiconducting chiralities highlighted in purple, blue and orange can be extracted from SWCNT raw material by selective polymer wrapping with either PFO or PFO-BPy. A photograph of resulting dispersions is shown in the bottom left corner.

So far, the mechanism for the selectivity of polymer wrapping has not yet been fully understood. It is suggested that the flexibility of the polymer backbone plays a crucial role in determining which chiralities are preferentially wrapped in the dispersion process.[77,79,80] Polymers with flexible backbones select smaller diameter nanotubes, as they can conform to the high surface curvature of these SWCNTs, while more rigid polymers show stronger interactions with large diameter SWCNTs.[79] Thus, changing the structure of the backbone significantly influences the selected chirality, selectivity and yield of the dispersion process. Nowadays, there are many polyfluorene derivatives, which show at least some selectivity towards a certain nanotube chirality.[77,78,81-85] The selectivity of PFO-BPy for (6,5) SWCNTs is however still unmatched and dispersion processes that enrich other chiralities (with different polymers) also disperse some unwanted semiconducting SWCNT chiralities.[74] Regardless of the exact nanotube chirality targeted by the employed polymer, the resulting dispersions contain mostly semiconducting

SWCNTs, while metallic nanotubes are removed during the centrifugation process.[74] This has been attributed to the higher polarizability of metallic SWCNTs in comparison to semiconducting SWCNTs.[86] Thus, the hybrids between metallic SWCNTs and polymers exhibit strong dipole-dipole interactions, which leads to aggregation in non-polar organic solvents and subsequent removal by centrifugation.[87,88] It has also been suggested that doping of SWCNTs by atmospheric oxygen and the electronic structure of the employed polymer play a role in stabilizing semiconducting SWCNTs (and destabilizing metallic SWCNTs) in dispersion.[74,89]

Which SWCNT chirality is extracted also depends on the combination of nanotube raw material and wrapping polymer. Dispersion of small diameter CoMoCAT® raw material in solutions of PFO results in enrichment of (7,5) SWCNTs, while dispersion of HiPCO® raw material, which contains slightly larger SWCNTs, with PFO leads to an enrichment of (8,6) SWCNTs amongst other semiconducting chiralities.[77,81] Similarly, PFO-BPy extracts (6,5) SWCNTs from CoMoCAT® raw material, while it disperses several semiconducting SWCNT chiralities when Plasma Torch raw material is used, as schematically shown in **Figure 3**.[90]

Aside from the general structure of the polymer backbone and choice of SWCNT raw material, several other polymer-related parameters have been found to influence the dispersion process. Increasing the side chain length of polyfluorenes (*e.g.* from octyl to dodecyl side chains) leads to an increased extraction efficiency (*i.e.* dispersion yield) and a higher interaction strength with SWCNTs of larger diameters but also a higher content of metallic nanotubes.[91,92] Using branched instead of n-alkyl side chains also enhances the dispersion selectivity for certain SWCNT chiralities.[93-95] Increasing the average molecular weight M_W of fluorene-based polymers leads to more stable dispersions with higher SCWNT loading.[83,85,96] While some studies find a decreased selectivity for high M_W polymers, which was attributed to an increased viscosity of the dispersion medium that allows for kinetic stabilization of otherwise unfavorable polymer-SWCNT hybrids,[83] others only report an increase in dispersion yield without any changes in selectivity.[85] For dispersion of SWCNTs with fluorene oligomers a stabilization of SWCNT-oligomer hybrids was observed for longer oligomer chains.[97] However, polymers with low M_W were shown to increase the content of dispersed metallic SWCNTs.[96] Hence, an intermediate polymer weight (*i.e.,* 10-40 kDa) appears to be optimal to achieve both high yield and selectivity toward semiconducting SWCNTs in general and to certain SWCNT chiralities in particular. Increasing the polymer concentration and the SWCNT-to-polymer ratio during the dispersion process typically increases the yield but above a certain threshold decreases selectivity.[83,92,98] While some studies attributed this to a change in viscosity of dispersion medium upon higher polymer concentrations[83], there are also indications that a change in polymer concentration influences the interaction and coverage of the SWCNTs with polymer.[99] Recently, it was shown that even the chain conformation of the solubilized polymers influences the dispersion process.[100] While PFO forms random coils in commonly used organic solvents such as toluene or xylene, more viscous solvents such as tetralin promote the formation of the more rigid β-phase of PFO. The latter can interact with large diameter nanotubes, and it was shown that (10,9) SWCNTs can be enriched from Plasma Torch raw material with PFO in tetralin.[100]

The solvent itself can also be used to systematically impact the dispersion process. Effective removal of unexfoliated or non-stabilized SWCNTs and other impurities *via* centrifugation is only possible if the employed solvent has a lower density than the impurities (*i.e.* nanotube bundles).[74] Additionally, solvents that typically stabilize SWCNTs without any surfactants (*e.g.* NMP or DMF) decrease the selectivity of the dispersion process. Hence, to improve the selectivity, solvents like toluene or xylene should be used. It was also demonstrated that the polymer wrapping process is only selective toward semiconducting SWCNTs for solvents with low dielectric constants such as toluene.[75] For high dielectric constant solvents (*e.g.* chlorinated solvents or THF), metallic SWCNTs were stabilized in dispersion and purification by centrifugation was not possible.[75] Since the viscosity of the dispersion medium has an influence on the dispersion process, the solvent viscosity can also be used to improve either selectivity (low viscosity solvents) or dispersion stability (high viscosity solvents).[83]

For process-related parameters, it is not possible to make generalized statements. The temperature during exfoliation should normally be kept between 10-20 °C, as for lower and higher temperatures formation of SWCNT bundles is observed.[101] However, certain polymers require higher dispersion temperatures. For example, an ideal dispersion temperature of 50 °C was found for the dispersion of semiconducting SWCNTs with polythiophene-based polymers.[93] To ensure sufficient dispersion of raw material, sonication power and time must be adjusted as well, although a low sonication power and time is desired to avoid the introduction of defects.[54,55,102-104] As sonication-based exfoliation relies on cavitation, which in turn depends on solvent properties, temperature and flask geometry, sonication time and power have to be optimized whenever one of these parameters is changed.[55] To achieve reproducible exfoliation and avoid unwanted defect introduction during exfoliation, stirring or shear force mixing (SFM) can be used to disperse the SWCNT raw material, which leads to long and low-defect SWCNTs.[20]

The complex interplay between the above-mentioned factors and the lack of generality for process-related parameters makes monitoring and optimization upon changes in the process (*e.g.,* use of new raw material with known polymer and dispersion method) necessary to improve dispersion yield and quality. A deeper understanding of the process could push the efficiency and utility of the polymer wrapping process to the next level and is required for the implementation of this dispersion and sorting method in potential future applications.

2.1.3 Electronic Structure

Analogous to the geometrical structure, the electronic structure of SWCNTs can be derived from graphene. In first approximation, the electronic structure of graphene can be simplified to the π- and π*-bands (*i.e.,* valence and conduction bands) that arise from the interaction of the $2p_z$-orbitals of the sp^2-hybridized carbon atoms.[27,32] Within the nearest-neighbor tight-binding formalism, which is valid for energies around the Fermi-level where electron-hole-symmetry can be assumed, the 2D-energy dispersion $E(\vec{k})$ in reciprocal space is calculated as

$$E(\vec{k}) = \pm t\sqrt{1 + 4\cos\left(\frac{\sqrt{3}k_x|\vec{a}|}{2}\right)\cos\left(\frac{k_y|\vec{a}|}{2}\right) + 4\cos^2\left(\frac{k_y|\vec{a}|}{2}\right)} \tag{2.5}$$

with $\vec{k}$ as the wave vector, t as the nearest-neighbor interaction energy, which is usually estimated with values between 2.9-3.1 eV and the Fermi level set to zero.[27,32] Plotting the resulting band structure of graphene as shown in **Figure 4A** reveals points of high symmetry – the K and K' points – located at the corners of the Brillouin zone of graphene.[27] The valence and conduction bands intersect at these points and exhibit a linear dispersion in their vicinity (see **Figure 4D**). Graphene itself can thus be described as a zero-bandgap semiconductor or a semi-metal.[27]

To calculate the electronic structure of a SWCNT, its Brillouin zone is constructed from its Bravais lattice, according to the reciprocity condition

$$e^{i(\overrightarrow{K_a}+\overrightarrow{K_C})(\overrightarrow{C_h}+\vec{T})} = 1 \tag{2.6}$$

with $\overrightarrow{K_a}$ and $\overrightarrow{K_C}$ as the reciprocal lattice vectors along the SWCNTs axis and circumference.[105]

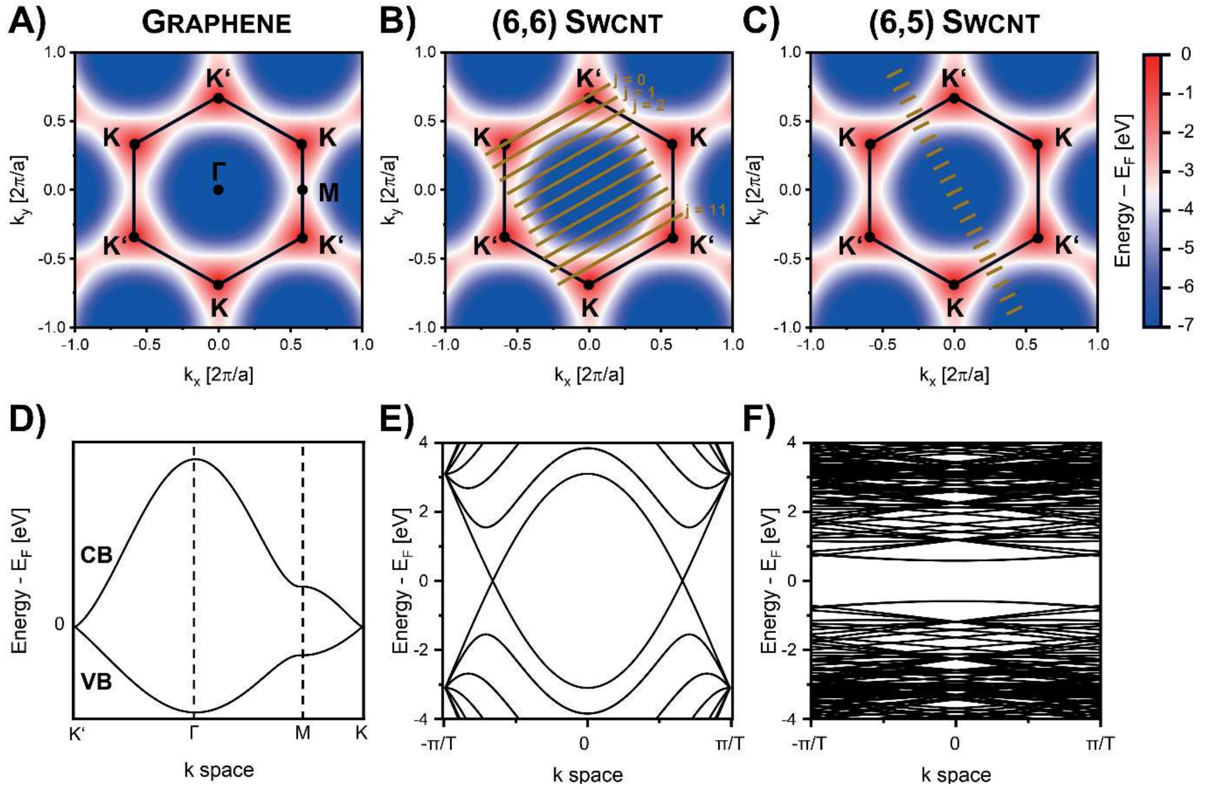

Figure 4. **A)** Brillouin zone and 2D energy dispersion of graphene. Points of high symmetry (Γ, M, K, K') are marked. **B)** Brillouin zone of a metallic (6,6) SWCNT (golden) superimposed on the Brillouin zone and 2D energy dispersion of graphene. Some of the allowed circumferential wave vectors are numbered by their respective index j. **C)** Brillouin zone of a semiconducting (6,5) SWCNT (golden) superimposed on the Brillouin zone and 2D energy dispersion of graphene. Band structures for **D)** graphene, **E)** a (6,6)-SWCNT and **F)** a (6,5)-SWCNT are shown in the bottom panel.

Rolling up a sheet of graphene into a nanotube leads to boundary conditions imposed on the resulting wave vectors. Hence, a set of quantized wave vectors in the circumferential direction is obtained.[32,105] The number of circumferential wave vectors in the Brillouin zone of SWCNTs depends on their chiral indices by

$$j = 0, 1, 2, \dots, \frac{2(n^2 + nm + m^2)}{gcd} - 2, \frac{2(n^2 + nm + m^2)}{gcd} - 1 \qquad (2.7)$$

where each wave vector is continuously numbered by the index j.[32,105] This is schematically shown in **Figure 4B** and **C** where the allowed wave vectors for a (6,6) and (6,5) SWCNT in circumferential direction are shown superimposed on the Brillouin zone and 2D energy dispersion of graphene.

Similar boundary conditions also apply to the wave vectors along the nanotube axis but the spacing between the resulting wave vectors vanishes for nanotubes, as their length is typically orders of magnitude larger than the length of $\vec{T}$. Thus, the allowed set of wave vectors in axial direction can be seen as a quasi-continuous variable l.[32,105]

To simplify calculation of the band structure of a SWCNT, a general wave vector k_g is constructed:

$$k_g = l\frac{\overrightarrow{K_a}\,|\vec{T}|}{2\pi} + j\,\overrightarrow{K_C}, \left(-\frac{\pi}{|\vec{T}|} < k_g < -\frac{\pi}{|\vec{T}|}\right), \tag{2.8}$$

which describes the location within the carbon nanotubes Brillouin zone. The band structure can then be calculated by **Equation (2.5)** where k_x and k_y are substituted by

$$k_x = \frac{2\pi\sqrt{3}|\vec{a}|j(n+m)\left|\overrightarrow{C_h}\right| + |\vec{a}|^3 k_g(n^3 - m^3)}{2\left|\overrightarrow{C_h}\right|^3} \tag{2.9}$$

and

$$k_y = \frac{\sqrt{3}|\vec{a}|k_g(n+m)\left|\overrightarrow{C_h}\right| + 2\pi|\vec{a}|j(n-m)}{2\left|\overrightarrow{C_h}\right|^2}. \tag{2.10}$$

The calculated band structures of a metallic (6,6) and a semiconducting (6,5) SWCNT are shown in **Figure 4E** and **F**. In the band structure of the metallic (6,6) SWCNT, the valence and conduction bands overlap at $k_g = 0$ for $j = 0$, while a bandgap opens for the semiconducting (6,5) SWCNT.

To visualize the origin of the SWCNT bands within the energy dispersion of graphene, the so-called zone-folding model can be applied.[32,105] Every band with a certain index j can be imagined as a cut of the corresponding wave vector $\overrightarrow{K_C}$ with the same index j through the 2D energy dispersion of graphene. For the metallic (6,6) SWCNT $\overrightarrow{K_C}$ with $j = 0$ cuts directly through a K-/K'-point in the energy dispersion of graphene (**Figure 4B**). Consequently, the corresponding SWCNT band structure exhibits an intersecting valence and conduction band (as observed for graphene in the K-/K'-point) (**Figure 4E**). For a (6,5) SWCNT, none of the wavevectors $\overrightarrow{K_C}$ cut through a K- or K'-point, which leads to the opening of bandgap in the SWCNT band structure and semiconducting behavior. Upon investigation of a large number of

SWCNT chiralities, it becomes apparent that SWCNTs are metallic if (n-m) is a multiple of 3 and semiconducting otherwise.

The total density of states (DOS) distribution of an SWCNT $g_{tot}(E)$ can be calculated by

$$g_{tot}(E) = g(E,j) = \sum_{j} \frac{1}{\pi}\left|\frac{\partial k}{\partial E(k,j)}\right|, \tag{2.11}$$

where $g(E,j)$ is the DOS of the sub-band with the index j.[32,105] For semiconducting SWCNTs, the DOS at the Fermi level is zero, while metallic SWCNTs show a non-zero DOS at the Fermi level. The resulting total DOS distributions of a (6,6) and a (6,5) SWCNT are shown in **Figure 5** and exhibit a series of sharp peaks, which are known as van-Hove singularities (vHs) and are characteristic for 1D materials.[32,105] Starting from the Fermi level, each of these vHs is continuously numbered by an index i = 0,1,2,… leading to v_i for valence band vHs and c_i for conduction band vHs.

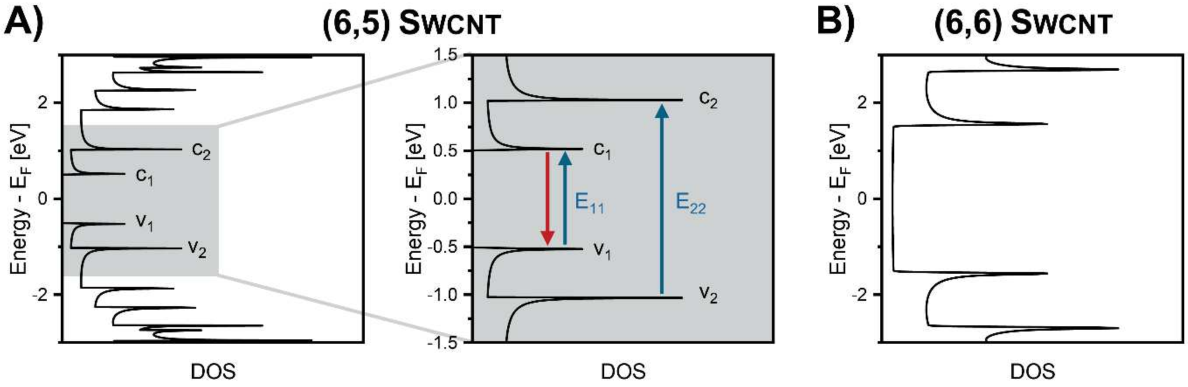

Figure 5. A) DOS distribution for a semiconducting (6,5) SWCNT. The right panel shows a zoom-in on the DOS in the region -1.5 to 1.5 eV and the possible E_{ii} optical transitions between the vHs $v_i \rightarrow c_i$ of the valence and conduction band, respectively. Black arrows indicate absorption processes while the red arrow indicates an emission process. **B)** DOS for a metallic (6,6) SWCNT.

The obtained band structures and DOS are based on several approximations and do not include any curvature effects. The calculated results are, however, in good agreement with band structures obtained from scanning tunneling spectroscopy[106] and can be used to discuss the optical properties of SWCNTs in the next chapter.

2.1.4 Optical Properties

In first approximation, the optical transitions in SWCNTs can be described within the single-particle picture as an excitation of an electron from the valence to the conduction band (**Figure 5A**). Due to Fermi's golden rule, which states that the probability of this process is directly proportional to the DOS, transitions between vHs in the valence and conduction band dominate the SWCNTs optical response.[107] While transitions between vHs with different indices i (*e.g.*, $v_2 \rightarrow c_1$) are allowed for excitation perpendicular to the SWCNTs axis, excitation parallel to the tube axis only leads to transitions between vHs with the same indices i (*i.e.*, $v_i \rightarrow c_i$) to conserve angular momentum.[108] As the absorption cross section parallel to the tube axis is significantly larger than that perpendicular to the tube axis, the optical spectra are dominated by E_{ii} transitions (between vHs with the same indices i).[109] Analysis of the optical spectra of SWCNTs, however, revealed discrepancies between observed E_{11} transition energies and the calculated bandgap E_g, indicating that the free-electron-hole model is insufficient to describe optical the processes in SWCNTs.[107,110,111] Due to the 1D-nature of SWCNTs, electrons and holes experience reduced dielectric screening, and strong electron-hole interactions lead to the formation of excitons (*i.e.*, bound electron-hole pairs), which are stable at room temperature due to their large exciton binding energies E_b (several 100 meV).[112-114] Additionally, Coulombic repulsion of the electron in the conduction band and the remaining electrons in the valence band lead to a second correction term E_{self}, so that the energy of the optical transition E_{11} is described by

$$E_{11} = E_g - E_b + E_{\text{self}}. \tag{2.12}$$

Since E_{self} is larger than E_b in SWCNTs, E_{11} is larger than E_g.[112,115]

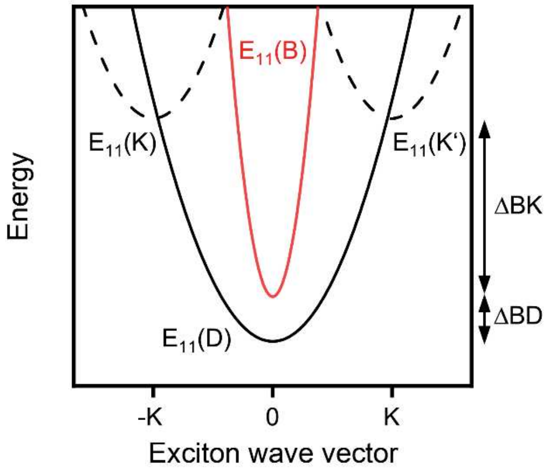

Figure 6. Schematic energy dispersion of singlet excitons in a SWCNT.

Due to the K- and K'-valley degeneracy in graphene, each excitonic state in SWCNTs exhibits a fourfold degeneracy with the possible configurations KK, K'K, KK' and K'K', which indicate the positions of electron and hole. As the electron and hole of each of these states exhibit spin degeneracy, they are further split into one singlet and three triplet states, yielding 16 possible exciton configurations..

A schematic energy dispersion of the four singlet excitons is shown in **Figure 6**. Intervalley (KK' and K'K) excitons E_{11}(K) and E_{11}(K') are optically forbidden, as direct transitions violate momentum conservation in these configurations. Triplet excitons are also optically forbidden but due to spin conservation. Short-range Coulomb interaction leads to mixing of the singlet intravalley (KK and K'K') excitons and the formation of a bonding state with even and an anti-bonding state with odd parity. Since selection rules require optical transitions to occur between states with different parities (and the ground state has even parity), the even-parity, intravalley exciton E_{11}(D) is dark and the odd-parity, intravalley exciton E_{11}(B) is bright.[116] The energy difference ΔBD between E_{11}(D) and E_{11}(B) is typically on the order of a few meV, while the energy difference ΔBK between the bright intravalley and the dark intervalley excitons is roughly 25 meV.[117,118] The latter can become optically active upon coupling to a D-phonon.[118,119] This and other processes, which are relevant for the spectroscopic investigation of SWCNTs are discussed with the help of experimentally recorded spectra of (6,5) SWCNTs.

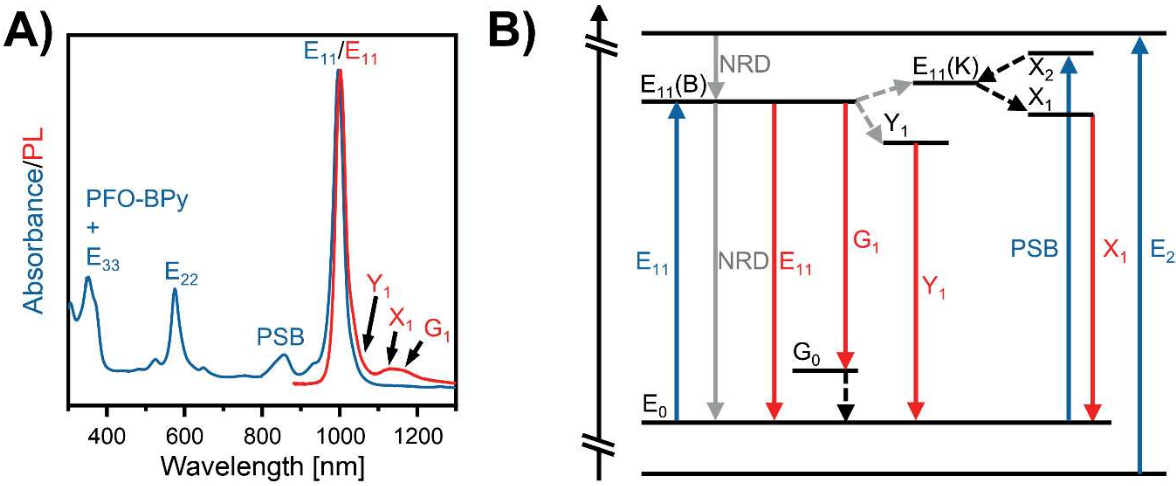

Figure 7. A) Absorption (blue line) and photoluminescence (red line) spectra of a dispersion of PFO-BPy-wrapped (6,5) SWCNTs. For photoluminescence spectra, dispersions were excited at the E_{22} transition. Bands related to (6,5) SWCNTs are labelled. **B)** Schematic energy level diagram (energy axis not to scale) showing the main absorption (blue arrows) and emission (red arrows) transitions. The black dashed arrows mark the creation or annihilation of either a D (for the PSB/X_1 transition) or a G phonon (for the G_1 transition). Grey dashed arrows indicate population of states from the E_{11}(B) valley by unknown mechanisms. Additionally, non-radiative decay (NRD) paths are indicated by dark grey, solid arrows.

The absorption and photoluminescence (PL) spectra of a dispersion of (6,5) SWCNTs, obtained by the polymer wrapping process as detailed in **Chapter 2.1.2**, are shown in **Figure 7A**. The absorption spectrum exhibits sharp peaks, which can be assigned to the E_{11} (~1000 nm), E_{22}

(~575 nm) and E_{33} (~350 nm) optical transitions. The E_{33} transition is masked by the absorption of the PFO-BPy wrapping polymer at 352 nm. Additionally, the phonon side band (PSB, ~850 nm) is visible in the absorption spectrum. This peak originates from the population of the E_{11}(K) (or E_{11}(K')) valley *via* absorption of a photon and simultaneous creation of a D-phonon.[118,119] This process is schematically depicted in **Figure 7B**.

Upon optical excitation of the SWCNTs into a higher excitonic state (e.g. *via* the E_{22} transition), fast internal conversion on the time scale of ~100 fs leads to relaxation into the emissive E_{11}(B) state (**Figure 7B**).[99,120] Radiative decay from this state into the ground state E_0 leads to a sharp E_{11} emission band at ~1004 nm (**Figure 7A**). The small Stokes shift (~4 meV) originates from the rigidity of the SWCNTs and hence a small reorganization energy.[121] The main E_{11} transition is accompanied by red-shifted lower-intensity peaks, namely the Y_1, X_1 and G_1 transitions. The origin of the Y_1 mode has previously been assigned to extrinsic effects or interaction with triplet states[122] but a recent study found a correlation between Y_1 emission and structural defects, hinting towards a defect-related origin.[123] The X_1 emission stems from brightening of the K-momentum dark excitons *via* simultaneous emission of a photon and a D-phonon.[118,119,122] Exciton scattering at defect sites is proposed to be the main mechanism for population of the involved E_{11}(K) state.[124,125] Lastly, G_1 emission originates in coupling of the E_{11}(B) state with a G phonon mode.[122] The schematic energy diagram shown in **Figure 7B** visualizes these processes.

The photoluminescence quantum yield (PLQY) of SWCNTs in dispersion is typically low (< 1%). Non-radiative decay paths are more likely to occur for nIR emitters such as SWCNTs, as the small bandgap makes interactions between the higher vibrational levels of the ground state and the lowest level of the excited state more probable ("energy-gap law").[126] Additionally, low lying dark and triplet states in SWCNTs provide additional non-radiative decay pathways for excitons and contribute to the observed low PLQYs.[127] Furthermore, external factors such as interaction with surrounding solvent or excess charge carriers (see **Chapter 2.3.2**) can influence the emissive properties of SWCNTs. [128,129] Excitons on SWCNTs are also highly mobile with diffusion constants on the order of 1-10 cm^2s^{-1}.[108,130,131] This enables fast exciton diffusion along the SWCNT toward tube ends and defects which act as non-radiative exciton quenching sites.[130,132] Thus, it is crucial to minimize unintentional defect introduction or nanotube shortening during exfoliation by employing mild exfoliation methods to obtain bright SWCNTs. The shear force mixing process was shown to yield long (average length ~1.6 µm) and defect-free (6,5) SWCNTs with an average PLQY of 1-2 %.[20,133]

2.2 Graphene Nanoribbons

In 1996, Nakada et al. first described the structure and theoretically studied the electronic properties of narrow, atomically precise graphene nanoribbons (GNRs).[134] After the discovery of graphene in 2004[25], first top-down fabrication approaches, which used graphene as a starting material, only yielded GNRs with widths of several tens to hundreds of nanometers and undefined edge structures.[135-138] The first synthesis of narrow, atomically precise GNRs was reported in 2008 by Müllen and co-workers.[139] Since then, a plethora of bottom-up synthesis methods was developed and nowadays provides access to GNRs with different edge and core structures, side chain configurations and even GNRs in which carbon atoms are substituted by heteroatoms.[22,23,140] The following chapters will discuss the possible structures of bottom-up synthesized, atomically precise GNRs and the influence of their edge structure and width on the electronic and optical properties. Additionally, a review of state-of-the-art synthesis techniques is provided.

2.2.1 Structure

Graphene nanoribbons can be conceptualized as 1D stripes directly cut from a sp^2-hybridized graphene lattice. The resulting edge geometry is defined by the cutting direction: cutting along an armchair edge leads to armchair GNRs (aGNRs), while zigzag-direction cuts yield zigzag GNRs (zGNRs).[22,140] Cuts along other directions result in GNRs with mixed edge structures. Examples of complex GNRs – namely chevron, fjord, chiral and cove GNRs - are shown in **Figure 8**, but even more sophisticated GNR edge geometries can nowadays be realized (*e.g.*, helical, janus,…).[141-143] The edges of GNRs are usually hydrogen-terminated. The second defining structural parameter is the width W of the GNR that typically ranges from 0.5 – 3 nm for bottom-up synthesized GNRs.[22,140]

While there is so far no general naming convention for GNRs – most likely due to the large number of possible GNR structures – a system to unambiguously name aGNRs and zGNRs has been established. For both types of GNRs, an index n is introduced, that defines the width of the GNR. For n-aGNRs, it denotes the number of carbon dimer lines perpendicular to the GNR axis while for n-zGNRs, the number of zigzag carbon chains perpendicular to the GNR axis is counted (see **Figure 8** for representative structures of a 9-aGNR and a 5-zGNR).

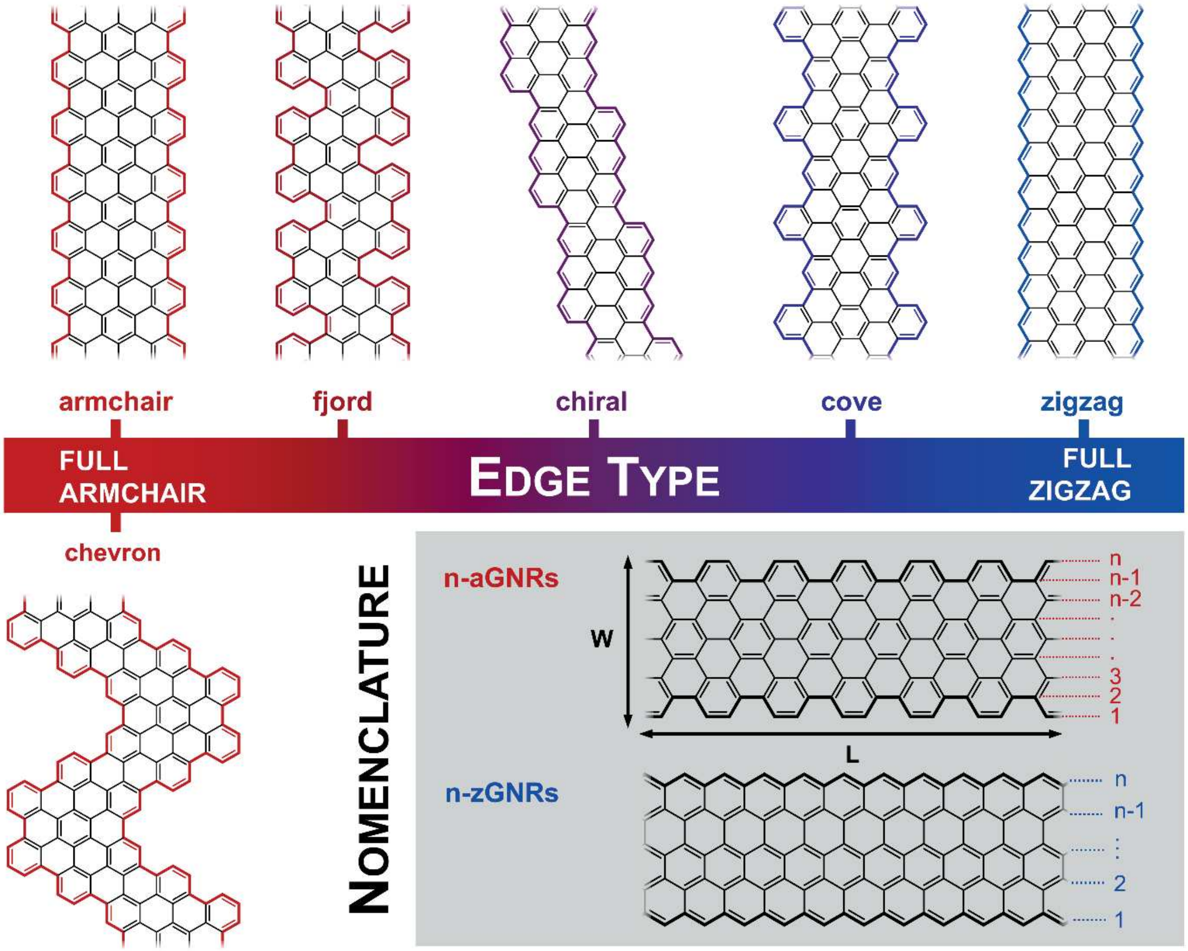

Figure 8. Schematic depiction of GNRs with different edge structures and nomenclature for aGNRs and zGNRs.

The GNR lengths L strongly depend on the synthesis methods and reported lengths typically span a range between 10-100 nm. It should be noted that an exact length determination is only possible through scanning tunneling microscopy (STM) images. Many studies estimate L based on mass spectrometry or size exclusion chromatography which either tend to over- or underestimate the real values. Hence, GNR lengths in the literature should be evaluated critically. GNRs obtained by bottom-up synthesis are usually also polydisperse in length, but efforts have been made to reduce polydispersity in these systems.[144,145]

Several other structural parameters, such as the presence of side chains, lattice distortions, heteroatoms in the core or defects can have a strong impact on the rigidity, processability and electronic properties of GNRs and will be discussed in the following chapters.

2.2.2 Synthesis

GNRs can be synthesized either *via* top-down or bottom-up strategies. Top-down methods use lithography and catalytic etching of graphene[135,137,138,146] or oxidative unzipping of carbon nanotubes[147-149] to produce stripes of graphene with widths ranging from a few to tens of nanometers. Aside from the unsatisfactory width control, resulting GNRs exhibit inconsistent edge structures, and – due to harsh reaction conditions – can even contain lattice defects (**Figure 9**). As the electronic properties of GNRs strongly depend on their structure, top-down fabricated nanoribbons are consequently not suitable for studies that investigate their fundamental properties and thus will not be discussed here.

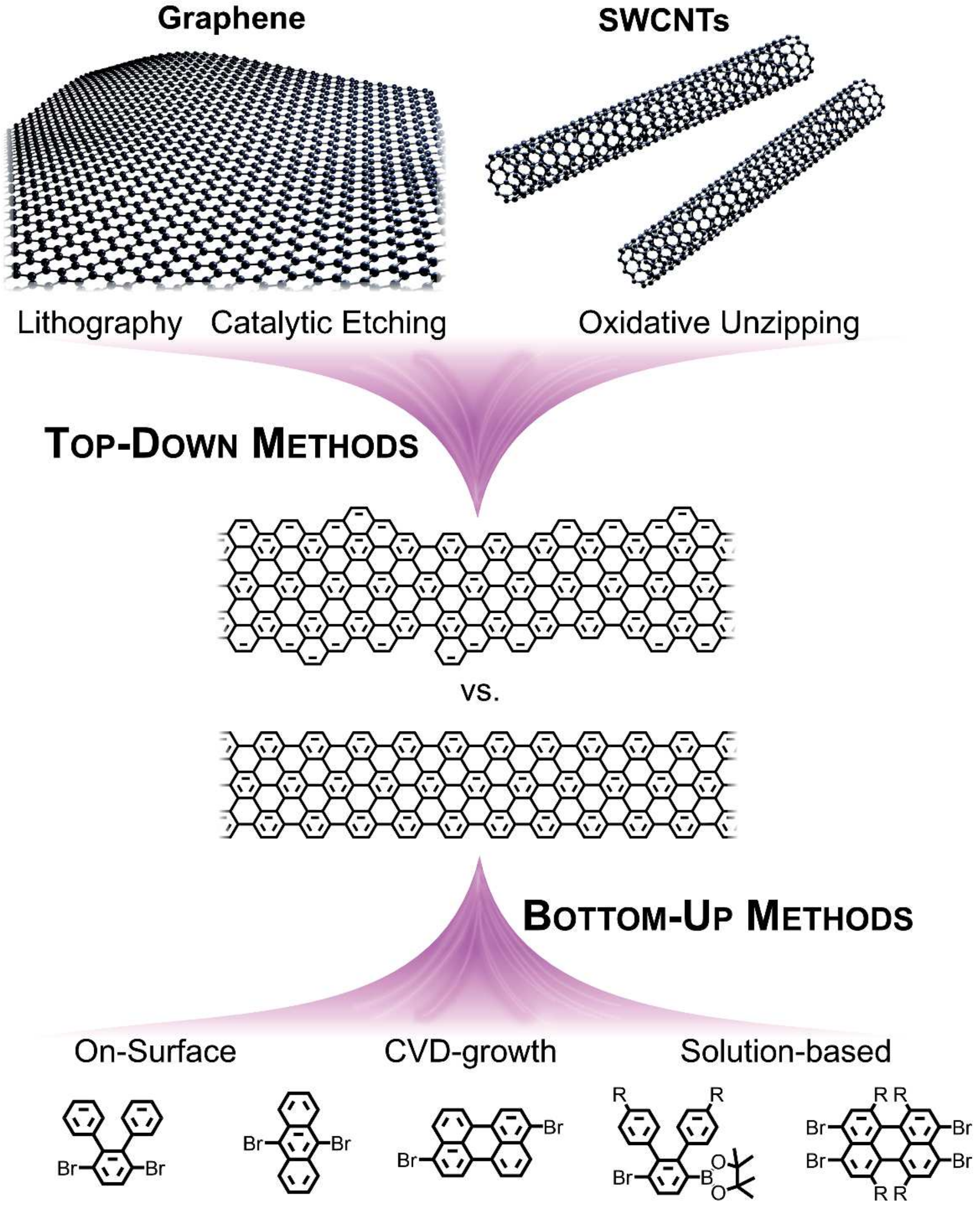

Figure 9. Schematic depiction of GNR fabrication based on top-down and bottom-up methods.

Bottom-up synthesis (*e.g.*, solution-based or on-surface synthesis) yields GNRs with smooth edges and precisely tunable widths **(Figure 9**). The first synthesis route of an atomically precise GNR was reported in 2008, when Müllen and coworkers synthesized up to 10 nm long 9-aGNRs *via* a solution-based approach.[139] Two years later, Cai et al. reported the on-surface synthesis of 7-aGNRs on an Au(111) surface.[150] For completeness, CVD-growth and solid-state synthesis of GNRs are briefly mentioned here.[151-154] However, due to the limited amount of accessible GNRs with these methods, the focus will be on solution-based and on-surface synthesis, which have been constantly refined to access a larger number of GNR edge geometries and widths, and to improve GNR length and processability.

On-surface and solution-based synthesis methods follow a common basic idea, which is depicted in **Figure 10A**: Custom synthesized monomeric precursors that contain suitable reactive moieties are polymerized, and the resulting polymer is then graphitized in a cyclodehydrogenation reaction to yield the GNR. In both synthesis processes, the structure of the polymer and thus the nanoribbon is mainly governed by the shape of the precursor monomers and the position and chemical nature of the reactive units involved in polymerization. (10,10')-dibromo-(9,9')-bianthracene monomers for example lead to synthesis of 7-aGNRs in on-surface coupling, while shifting the bromines to the (2,2')-positions yields the chiral graphene nanoribbon depicted in **Figure 8**.[150,155]

For on-surface synthesis (**Figure 10B**), halogen-containing monomer units are evaporated on top of an ultraclean coinage metal surface (*i.e.*, Au(111), Au(110), Ag(111) or Cu(111)) and polymerized.[23,140,156] This polymerization reaction is known as Ullmann-type coupling, which describes the coinage metal-catalyzed homocoupling of halogen-containing reactants (halogen = Cl, Br, I).[23,140,156] It has, however, been shown that other surfaces such as metal oxides are also capable of coupling specifically designed fluorine-containing precursors.[157,158] Surface-catalyzed thermal cyclodehydrogenation at even higher temperatures (typically >250 °C) then yields the GNRs.[23,140,156]

On-surface synthesis nowadays provides access to all n-aGNRs for n between 5 and 15 with the exception of 11-aGNRs, as well as 17-, 18- and 21-aGNRs.[23,140,156] Additionally, 6-zGNRs[159] and more complex GNR structures, such as chiral, chevron and cove-type GNRs can be produced.[23,140,150,155,160-164] The resulting GNRs are of high quality and do not suffer from structural distortions due to solubility-promoting side chains. The synthesis process, however, requires ultra-high vacuum ($<10^{-7}$ mbar) and elaborate equipment.[165] For characterization beyond scanning tunneling microscopy and spectroscopy, such as photoluminescence measurements or device characterization, GNRs need to be transferred to an insulating substrate.[165-168] This additional processing step might damage or dope the GNRs. Additionally, the scale of GNR production is limited by the surface area, as usually only a monolayer of GNRs can be produced. Furthermore, resulting GNRs are typically only 10-20 nm long and – depending on synthesis conditions – lattice defects can be introduced, which in turn might impede charge transport properties (see also **Chapter 2.4.3**).[23] Hence, in this work a solution-based synthesis protocol was employed to obtain GNRs.

Constant advances of solution-based synthesis made n-aGNRs (n = 5, 6, 8, 9, 12, 13, 18), as well as chevron, fjord, chiral and cove-type GNRs available[22] while zigzag GNRs, are currently only accessible *via* on-surface synthesis. Plenty of reactions to polymerize precursor monomers have been established. The most prominent ones are transition metal-catalyzed cross-coupling reactions (*e.g.*, Yamamoto coupling, Suzuki coupling, Stille coupling) or Diels-Alder reactions.[22] In **Figure 10C**, the solution-based Suzuki polymerization of a 2-(6'-bromo-[1,1':2',1''-terphenyl]-3'-yl)-4,4,5,5-tetramethyl-1,3,2-dioxaborolane leads to the preliminary polymer, which is then graphitized in an oxidative Scholl reaction.[144]

To achieve long and defect-free GNRs, several synthetic strategies have to be employed: An increase in polymer flexibility extends the maximum polymer length before precipitation occurs.[22,144,169] This was demonstrated in 2016 by Li et al. who prepared significantly longer 9-aGNRs compared to the first reported synthesis of 9-aGNRs in 2008. This was achieved by AB-type Suzuki polymerization of terphenyl monomers, leading to the flexible polymer shown in **Figure 10C**, in contrast to the previously employed AA-BB-type Suzuki polymerization, which resulted in rigid and short polymer chains.[139,144] Additionally, fine-tuning of polymerization reaction parameters, such as solvent system, catalyst loading, reactant concentration and temperature was necessary to improve GNR length and reduce polydispersity.[144] Bulky, solubility-promoting side groups R such as branched alkyl side chains (R = 3,7-dimethyloctane in **Figure 10C**) that prevent precipitation during the polymerization reaction, can further increase GNR length.[144,169-172] In 2023, Niu et al. reported the synthesis of GNRs with a record length of 371 nm (measured using gel-permeation chromatography) which was achieved by combining the aforementioned strategies and using especially bulky side groups consisting of the Diels-alder reaction product of an anthracene unit with maleimide.[173] If such bulky side groups are used, they can also prevent π-stacking of GNRs leading to a large improvement of GNR dispersibility and processability.[169-173] Unfortunately, these side-groups also lead to structural deformation, which changes the electronic properties[174] or promotes lattice defects as steric hindrance by bulky side groups prevents effective cyclodehydrogenation *via* Scholl oxidation.[175]

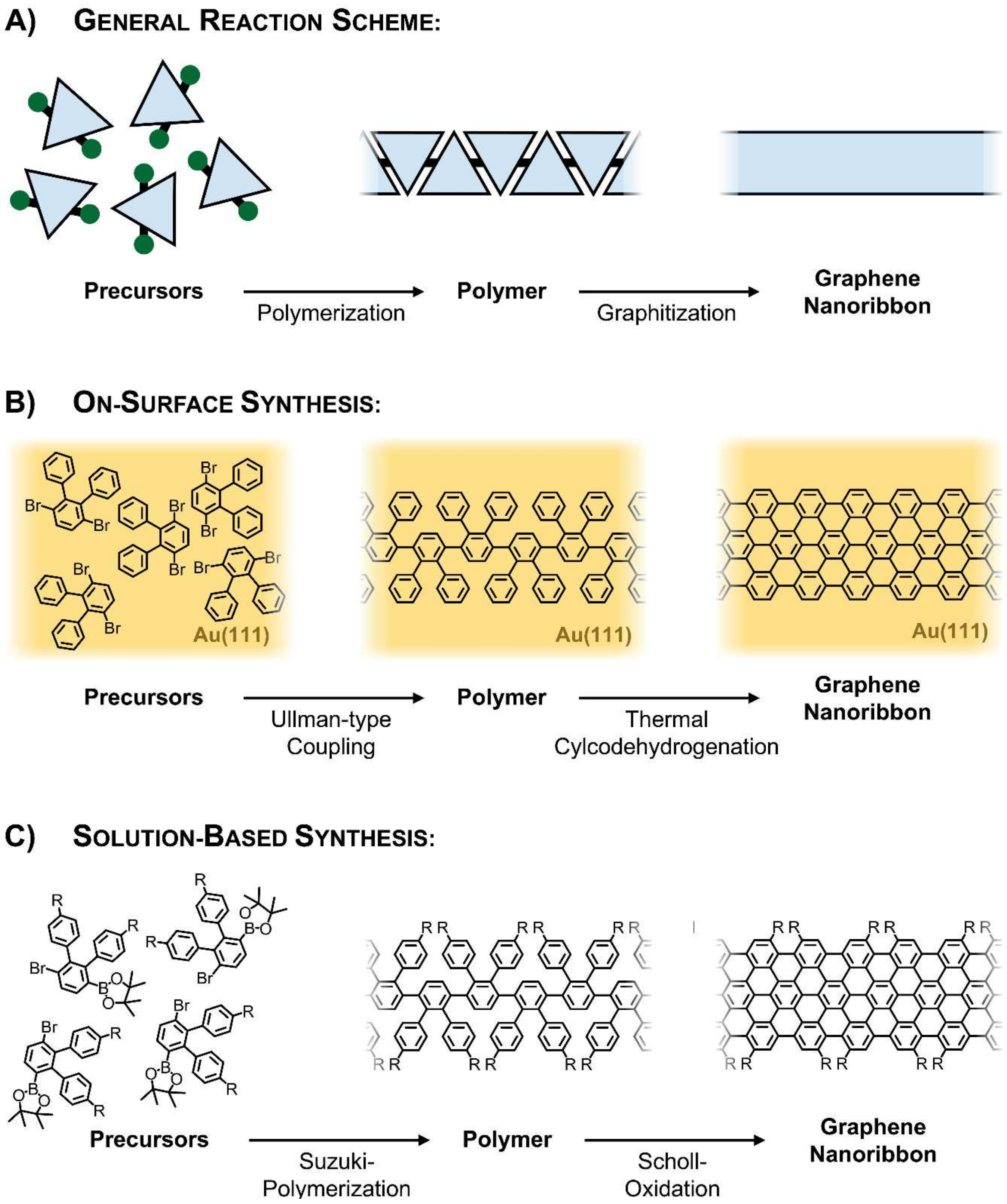

Figure 10. A) Schematic depiction of the general synthesis process to obtain GNRs. **B)** On-surface synthesis of 9-aGNRs starting from 3’,6’-dibromo-1,1’:2’,1”-terphenyl monomers. Polymerization on an Au(111) surface at 200 °C yields the depicted polymer which is then graphitized in a thermal cyclodehydrogenation at 400 °C. **C)** Solution-based synthesis of 9-aGNRs starting from 2-(6'-bromo-[1,1':2',1''-terphenyl]-3'-yl)-4,4,5,5-tetramethyl-1,3,2-dioxaborolane, which is polymerized with a Suzuki coupling and graphitized in an oxidative Scholl reaction. The side chains R in this case are 2,7-dimethyloctane chains.

Lattice defects can also arise from inefficient Scholl oxidation conditions. Hence, a thorough screening to find suitable oxidation agents and reaction conditions must be performed for each polymer. However, even under optimized conditions, the introduction of defects into the lattice cannot be entirely avoided, as typical Scholl oxidation efficiencies of 99% result in formation of a few defects when tens to hundreds of bonds must be closed. [176] A method to circumvent this problem was presented by Fischer and coworkers, who synthesized a precursor polymer *via* a solution-based approach which was then transferred onto a Au(111) surface to obtain GNRs by thermal cyclodehydrogenation.[145,177] While this approach combines the cyclodehydrogenation efficiency of on-surface synthesis with the superior GNR length of solution-based polymerization, some limitations of on-surface synthesis (*i.e.*, limited yield, need to transfer GNRs for characterization) still apply.[145,177]

The generally increased availability of GNRs with different widths and edge geometries also promoted the investigation of their electronic and optical properties. As zigzag GNRs are synthetically not accessible and thus of no further interest in this thesis, only the electronic structure of armchair GNRs will be discussed next.

2.2.3 Electronic Structure

The first theoretical studies of aGNRs derived the electronic structure from that of graphene by using the zone-folding model within the nearest-neighbor tight-binding formalism. [134,178-180] The resulting general wavefunction $\phi_J(k,\theta)$ for a n-aGNR within the tight binding model is given by

$$\phi_J(k,\theta) \; = \frac{1}{\sqrt{n}} e^{-ik|\vec{a}|(J-1)} sin\left(J\theta \begin{pmatrix} e^{-i\Theta(k,\theta)} \\ s \end{pmatrix}\right) \qquad (2.13)$$

where k is the wave vector parallel to the GNR axis, θ the phase perpendicular to the GNR axis, J the coordinate (*i.e.*, the dimer line, J = 1, 2, 3,… n) perpendicular to the GNR axis, $\Theta(k,\theta)$ the so-called polar angle in the k,θ-space and $s = \pm 1$ the superscript for valence and conduction band.[181,182] The boundary conditions, that are imposed on the Bloch wavefunctions of graphene for a n-aGNR are

$$\phi_{J=0}(k,\theta) = \; 0 \text{ and } \phi_{J=n+1}(k,\theta) = \; 0 \;, \qquad (2.14)$$

as the wavefunction needs to be contained within the n-aGNR.[181,182] These boundary conditions require a quantization of the phase θ according to

$$\theta = \frac{b\pi}{n+1}, \tag{2.15}$$

where $b = 0,1, \dots n$ is a sub-band index.[181,182] The quantization of θ effectively results in a quantization of allowed wave vectors perpendicular to the GNR axis. Within the framework of the zone-folding model, the 1D energy dispersion of n-aGNRs is then constructed by summation of the energy values along all cuts that the quantized wave vectors create within the 2D energy dispersion of graphene.[181,182] The resulting energy dispersion can be calculated *via*

$$E_b(k,\theta) = st\sqrt{1 + 4\cos(\theta)\cos\left(\frac{k}{2}\right) + 4\cos^2(\theta)}. \tag{2.16}$$

The calculated energy dispersions for a 7-, 8- and 9-aGNRs are shown in **Figure 11A-C**.

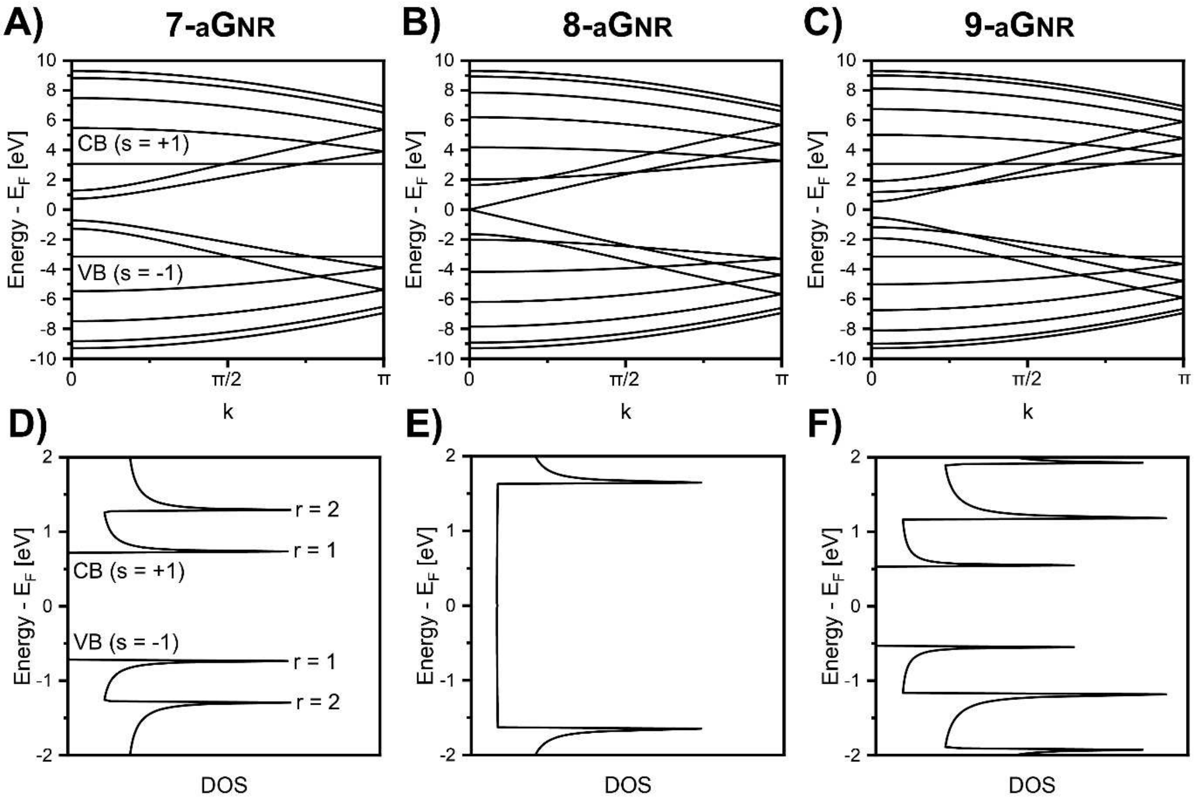

Figure 11. Band structure of a 7-aGNR **(A)**, 8-aGNR **(B)** and 9-aGNR **(C)** calculated with the zone folding model within the nearest-neighbor tight-binding formalism. Resulting total density of states distribution of a 7-aGNR **(D)**, 8-aGNR **(E)** and 9-aGNR **(F)**. Conduction and valence bands are marked in panel A and D. Additionally, the vHs are numbered by the index r as indicated in panel D.

The corresponding total DOS distribution, which can be calculated analogous to the DOS of SWCNTs *via* **Equation (2.11)** is shown in **Figure 11D-F**.

It becomes apparent that the 7- and 9-aGNRs are semiconducting according to the zone-folding model, while the 8-aGNR does not exhibit a bandgap. This can be explained by a cut directly through a K-point of the 2D energy dispersion of graphene by one of its quantized wave vectors (like in metallic SWCNTs). The DOS of the graphene nanoribbons also exhibits van-Hove singularities due to the valence (conduction) band maxima (minima) in the energy dispersion at k = 0. The electronic bandgap can be retrieved as energy difference between the highest valence and lowest conduction band vHs. **Figure 12A** shows bandgap values of n-aGNRs with n = 3-20, based on the zone-folding model. From this plot, a 'family behavior' becomes apparent. Nanoribbons with n = 3q or 3q+1 (where q is an arbitrary integer) exhibit a bandgap, while a metallic behavior is predicted for n-aGNRs with n = 3q+2. [134,178,180]

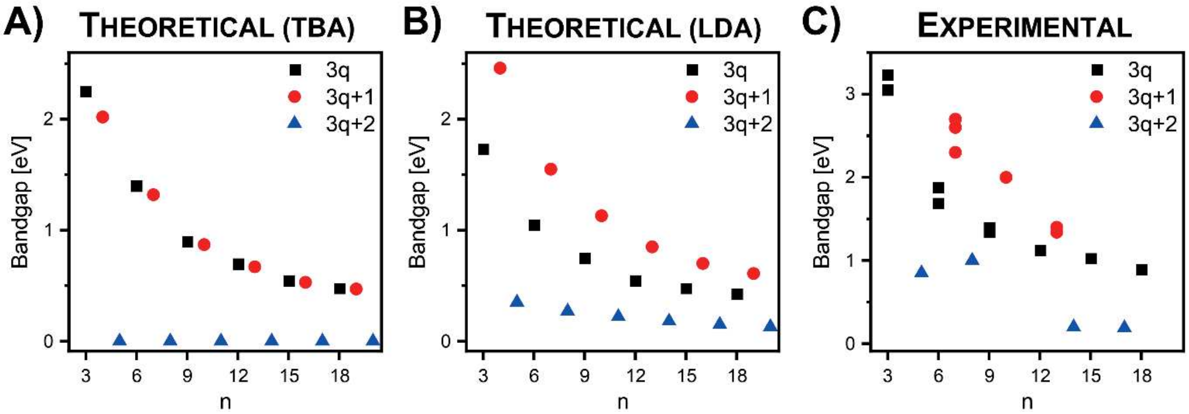

Figure 12. A) Electronic bandgaps of n-aGNRs calculated with the zone-folding model. Bandgap values were obtained from Son *et al.*[183] **B)** Electronic bandgaps of geometry-optimized n-aGNRs obtained by DFT calculations within the LDA. Bandgap values were obtained from Son *et al.* [183] **C)** Experimentally (*via* scanning tunneling spectroscopy or angle-resolved photo-electron spectroscopy) determined bandgaps for different on-surface synthesized n-aGNRs. For different n-aGNRs, bandgap values were obtained from different publications: n = 3[161,184], 5[185], 6[161,184], 7[186-188], 8[189], 9[161,186,190], 10[189], 12[161], 13[191,192], 14[186], 15[161], 17[192], 18.[186] No values are depicted for n = 4, 11 and 16, as they are not synthetically accessible so far.

However, in stark contrast to graphene and SWCNTs, the binding configuration (*e.g.*, bond length) of carbon atoms within a GNR varies drastically especially for atoms at the edges.[183] Due to these edge effects, approximations made within the zone-folding model and tight-binding formalism are inaccurate and a more sophisticated theoretical model is needed to accurately describe the electronic structure of GNRs. In 2006, Son *et al.* used density functional theory (DFT) calculations within the local density approximation (LDA) to model the electronic structure for geometry-optimized armchair and zigzag GNRs.[183] The results show a direct bandgap for all investigated aGNRs (**Figure 12B**) with the bandgap size strongly depending on the GNRs family affiliation (*i.e.*, whether n = 3q, 3q+1 or 3q+2). Nanoribbons with n = 3q+2 exhibit the smallest bandgaps but are not metallic, while GNRs with n = 3q+1 exhibit the largest bandgaps. The bandgaps within an aGNR family are inversely proportional to the GNR width.

After bottom-up synthesis methods provided access to an increasing number of n-aGNRs, their electronic bandgaps could be determined experimentally, for example *via* STS measurements. **Figure 12C** gives an overview of reported bandgaps of on-surface synthesized aGNRs depending on their width. While the experimentally determined bandgaps qualitatively fit the theoretically predicted values (decreasing bandgap for increasing ribbon width and family dependence of the bandgaps), the exact values deviate quite significantly. This was attributed to hybridization between surface states of Au(111) and the GNR.[193] Spatially resolved STS measurements also revealed a localization of electron density at the GNR edges for states associated with valence or conduction bands of the GNR.[145,161,191,193] Hence, the electronic structure of GNRs is especially sensitive towards edge modifications such as edge expansion or defects (*e.g.*, missing phenyl rings or unclosed bonds).[194-196] Additionally, spatially resolved STS revealed distinct edge states that originate from the zigzag ends of on-surface synthesized armchair GNRs. These edge states are localized for long GNRs but can mix with the valence and conduction bands of the GNR core for $L < 10$ nm.[185,191,197] Aside from end-state mixing, the GNR length only has an influence on the electronic structure if it is on the same length scale as the GNR width. For aspect ratios of roughly ten it converges towards the bandgap values for an infinitely long GNR.[187]

2.2.4 Optical Properties

Analogous to SWCNTs, optical transitions in aGNRs can be approximated as transitions between vHs of the conduction and valence band. For light polarized perpendicular to the GNR axis, only transitions between vHs with different indices r are allowed ($\Delta r = \pm 1$).[182,198] For light polarized parallel to the GNR axis, only transitions between vHs with the same indices are allowed ($\Delta r = 0$).[182,198] Due to their one-dimensional nature, graphene nanoribbons have a significantly larger absorption cross section parallel to their axis. Consequently, their optical spectra are dominated by electronic transitions between vHs with the same indices.[182,198]

Motivated by theoretical and experimental findings of large exciton-binding energies in SWCNTs, several studies investigated the role of many-body effects on the optical spectra of aGNRs with different widths.[199-201] In these studies, a three step many-body perturbation theory approach was used: First, the electronic structure of the nanoribbons was determined by LDA-DFT calculations. Then the LDA eigenvalues were corrected for the self-energy of a many-body system E_{self} (compare **Equation (2.12)**) within the G_0W_0-approximation. Finally, electron-hole interactions (*i.e.*, the exciton binding energy E_b) were included by solving the Bethe-Salpeter equation for the derived systems.[199,201] The studies found large values for E_{self} and exciton binding energies E_b between hundreds of meV up to 2 eV.[199-201] Calculated self-energy values were slightly larger than exciton binding energies, which resulted in an increase of the transition energies compared to the electronic bandgap calculated by LDA-DFT.[199,201] Based on these results, the studies predicted that optical absorption spectra of GNRs would be dominated by excitonic absorption peaks instead of transitions between the vHs of the aGNRs. It should be noted that the Brillouin zone of aGNRs only contains a single K-point, and thus no exciton splitting due to a K-valley degeneracy (like in SWCNTs) is observed, which simplifies their optical spectra. The presence of excitonic states within aGNRs was later confirmed by several experimental studies.[160,202-204]

Two theoretical studies independently found the presence of dark spin-singlet excitons in the 3q+1 n-aGNR family, which arise from a mixing of two pairs of bands close to the bandgap.[200,201] These dark excitons provide additional decay channels to excited states and were predicted to significantly alter the photoluminescence properties of aGNRs within the 3q+1 family. This was confirmed by experimental studies of on-surface synthesized 7-aGNRs that attested intrinsically low photoluminescence quantum yields to pristine 7-aGNRs.[166,205,206] Later studies, however, suggested funneling of excitons into dark states originating from 7-aGNR zigzag ends as a reason for the previously observed intrinsically low photoluminescence.[203,207]

The influence of edge and basal plane modifications on GNR absorption and emission properties was also investigated. DFT calculations predicted significant changes of band structures and thus optical properties upon defect introduction.[208] This was later confirmed by Senkovskyi *et al.*, who introduced basal-plane defects in 7-aGNRs and observed defect-related photoluminescence and a general brightening of photoluminescence by harvesting excitons from the dark excitonic states.[166] The effect of edge defects on the optical properties of GNRs, however, has not yet been explored experimentally. Additionally, there are only a few in-depth studies on the optical properties of solution-synthesized non-armchair graphene nanoribbons. These typically observed broad absorption and emission peaks, despite no discernible aggregation.[171,172,209] Even fewer studies have spectroscopically investigated solution-synthesized aGNRs. Thus, more studies should be conducted to understand the optical properties of aGNRs and the effect of defects on them.

2.3 Chemical Doping of Low-Dimensional Carbon-Based Nanomaterials

Chemical doping is crucial to tailor the electronic properties of semiconductors for (opto)electronic applications in transistors[210,211], light-emitting diodes[212], photovoltaics[213,214] and energy conversion devices.[11,215] It can reduce contact resistances, fill trap states or increase the conductivity of semiconducting layers. In this work, doping refers to the post-synthetic modification of charge carrier density in semiconductors, which can be performed electrostatically, electrochemically and chemically. This chapter will introduce models to describe chemical doping and commonly used doping methods. Additionally, resulting changes in the optical spectra of GNRs and SWCNTs are discussed. Electrochemical and -static doping will be presented in the next chapter (**Chapter 2.4**) in the context of electrolyte-gated transistors.

2.3.1 Fundamentals of Chemical Doping

To achieve chemical doping, strong electron-withdrawing (p-type doping) or electron-donating (n-type doping) agents (dopants) are brought in contact with a semiconductor, which leads to charge transfer and thus introduction of holes for p-type doping or electrons for n-type doping. This results in an increase in conductivity due to the introduction of an excess of mobile charge carriers. This chapter will focus on p-type doping, as it is more common than n-type doping, due to a higher stability under ambient conditions.

The addition of oxidizing agents to a semiconductor can lead to charge transfer doping which manifests in either full electron transfer - known as integer charge transfer (ICT) doping - or charge transfer complex formation (CTC doping).[216,217] For ICT, an electron is transferred from the highest occupied molecular orbital (HOMO) of the semiconductor to the lowest unoccupied molecular orbital (LUMO) of the dopant (**Figure 13A**). Within a simplified picture, effective electron transfer occurs if the electron affinity (EA, LUMO energy) of the dopant exceeds the ionization energy (IE, HOMO energy) of the semiconductor.[216-218] While this model can qualitatively describe the doping process for the interaction of strong dopants with organic many semiconductors like conjugated polymers, it fails to explain the occurrence of semiconductor doping if the EA of the dopant is lower than the IE of the semiconductor. CTC, on the other hand, assumes a formally partial charge transfer process and leads to the formation of new states *via* hybridization of the frontier orbitals of dopant and semiconductor.[217] This is schematically shown in **Figure 13B**. It should be noted that CTC can also occur if the EA of the dopant is significantly smaller than the IE of the semiconductor.

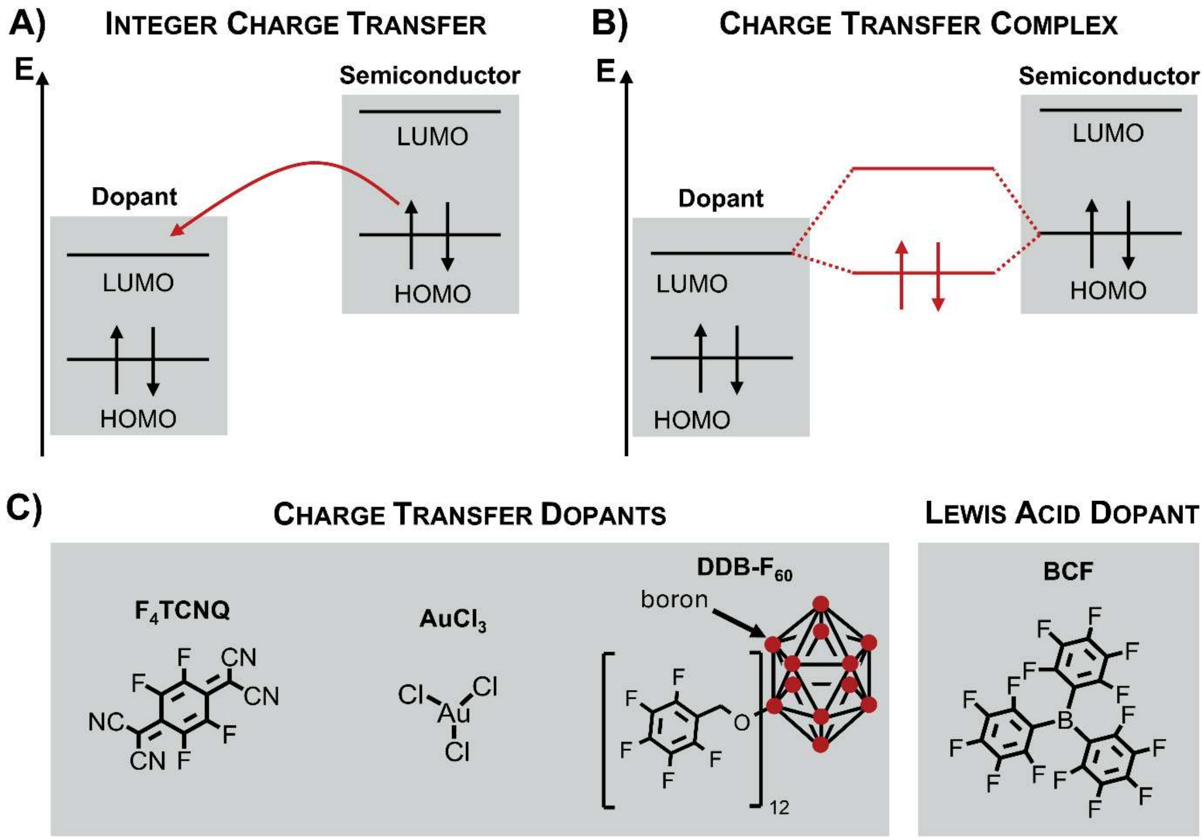

Figure 13. A) Integer charge transfer between a electron-accepting dopant and a molecular semiconductor. The red arrow schematically depicts full electron transfer from the highest occupied molecular orbital HOMO of the semiconductor to the LUMO of the dopant. **B)** Charge transfer complex formation between a p-type dopant and a semiconductor. The HOMO of the semiconductor and the LUMO of the dopant interact to form new local HOMO and LUMO states (red lines). **C)** Commonly used dopants for either charge transfer or Lewis acid-base doping.

Dopants that typically induce charge transfer doping are small molecules with high electron affinities such as $FeCl_3$, $AuCl_3$, and F_4TCNQ (structures of the last two are shown in **Figure 13C**). These dopants, however, often suffer from drawbacks including limited solubility in nonpolar solvents[219,220] or high reactivity that leads to unwanted side reactions and issues with doping stability.[221-223] Furthermore, the doping efficiency is limited by the dopant's LUMO energy. For instance, small-diameter SWCNTs with high IE are only weakly doped by F_4TCNQ.[224] After doping, the small counterions result in localization of charge carriers in the semiconductor due to strong Coulomb interactions, which decrease the their mobility and thus limit the gain in conductivity.[217,225] Although larger dopants, such as dodecaborane clusters (*e.g.*, DDB-F_{60}, see **Figure 13C**) only weakly localize holes due to a larger spatial separation between counterion and semiconductor, they are not commercially available and synthetically demanding.[226]

Brønsted acids, such as hydrochloric acid or toluene sulfonic acid, have also proven to be effective dopants for organic semiconductors and have been extensively applied to dope polymers[227-229] and carbon nanotubes[132,224,230] in solid and liquid phase. Although the mechanism of Brønsted acid doping is not yet fully understood, it is assumed that the acid protonates the organic semiconductor, followed by electron transfer between a charged and uncharged semiconductor species.[228]

A relatively new approach to doping was presented by Welch *et al.* in 2009, who modified the optical properties of a Lewis basic organic chromophore by addition of Lewis acids, thus introducing the concept of Lewis acid-base doping.[231] Lewis acid-base doping involves the coordination of non-oxidative Lewis acids to Lewis basic moieties, which in turn changes the charge carrier density in the semiconductor. Since then, especially tris(pentafluorophenyl)borane (BCF, structure shown in **Figure 13C**) – a strong Lewis acid – has been extensively used as a dopant for semiconducting polymers.[232-238] Due to its commercial availability, high doping efficiency even towards high IE polymers, and a good solubility in nonpolar organic solvents, it is also a promising dopant for carbon-based nanomaterials.

2.3.2 Chemical Doping of Carbon Nanotubes

Inspired by the doping of polyacetylene by halogens in 1977[239], first doping experiments on SWCNTs also utilized elemental bromine and potassium for p- and n-type doping, respectively, and found an increase in SWCNT conductivity upon introduction of additional charge carriers.[240-242] Since then, a plethora of charge transfer dopants and Brønsted acid dopants have been applied to SWCNTs to improve their performance in thermoelectric power generators, reduce contact resistance or modulate their ambipolar charge transport behaviour.[11,222,243-246] Aside from changes of the electrical performance of SWCNTs, doping also influences the optical properties of SWCNTs.

Chemical doping leads to a bleach of E_{11} absorption, as well as a quenching of E_{11} emission. The bleaching can be attributed to the change of electron density from the SWCNT valence band and hence a reduction in transition probability.[247] As such, the E_{11} bleach can be used as a qualitative measure for the doping level of SWCNTs. Additionally, asymmetric broadening and a blueshift of the excitonic E_{11} absorption is observed. This has been interpreted as a sign of inhomogeneous doping, where counterions are randomly distributed along the SWCNT and thereby segment it. The exciton wave functions are then confined to the segments between two doping sites, leading to the observed blueshift of excitonic transitions.[128,247,248] The photoluminescence quenching can be explained by additional relaxation channels such as Auger quenching of excitons and trion formation.[128]

In addition to the effects outlined above, a new red-shifted feature emerges in absorption and emission spectra upon doping (see **Figure 14A**).

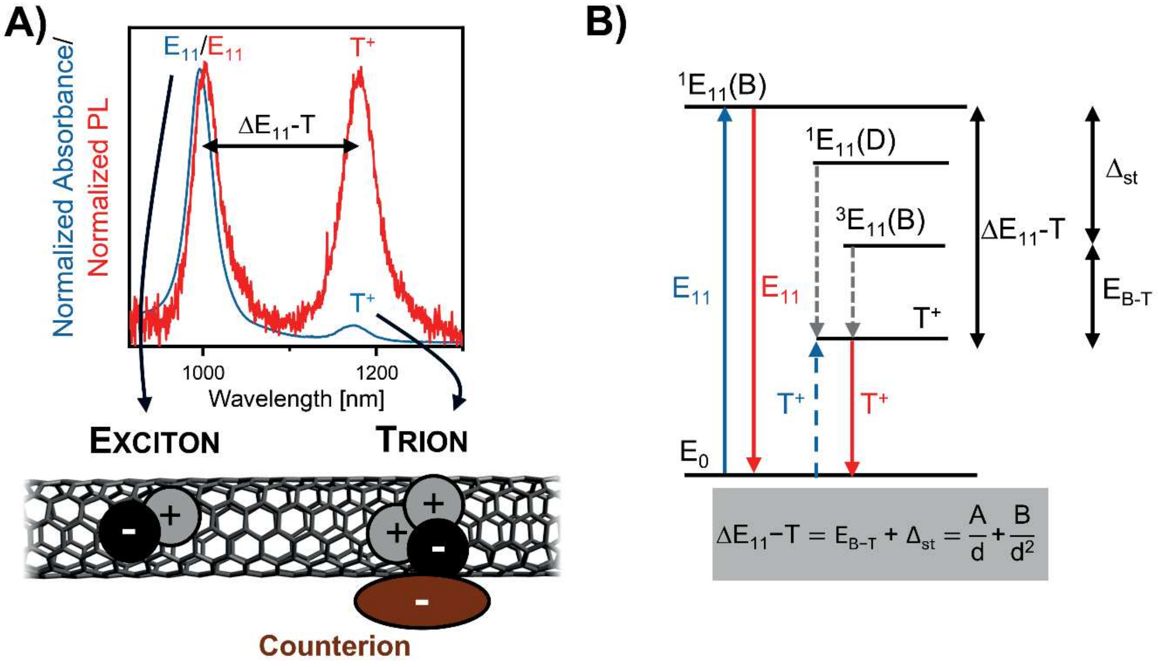

Figure 14. A) Absorption and photoluminescence spectra of chemically p-type doped (6,5) SWCNTs. Excitonic and trionic transitions are labelled by E_{11} and T^{+}, respectively. The bottom panel shows a schematic depiction of an exciton and a trion at a dopant site on a (6,5) SWCNT. **B)** Optical transitions and population processes of the trionic state T^{+} in a p-type doped SWCNT. Electronic transitions corresponding to absorption and emission processes are shown in blue and red, respectively. Potential population processes of the trionic state via dark and triplet excitons are depicted as grey dashed arrows. The charge-induced absorption process is depicted with a dashed blue arrow, as it is debated whether it is actually trionic or polaronic in origin. The exciton-trion energy separation ΔE_{11}-T, the energy splitting between bright singlet and triplet state Δ_{st} and the trion binding energy $E_{B\text{-}T}$ are shown on the right.

In 2009, Rønnow *et al.* predicted the formation of trions – quasiparticles consisting of an exciton and an additional positive or negative charge – in SWCNTs, if an imbalance of charges is present under optical excitation.[249] This prediction was experimentally confirmed in 2011 by Matsunaga *et al.* and Santos *et al.* who observed charge-induced red-shifted absorption and photoluminescence bands $T^{(+)}$ in SWCNTs under optical excitation Matsunaga used chemical p-type doping to create the necessary charge imbalance, while Santos used an all-optical approach with photogenerated carriers at high excitation densities. Since then, optical features associated with trions have been observed in spectra of optically exited chemically[247,250], electrochemically[251-253] and electrostatically[254,255] doped SWCNTs, as well as in electroluminescence spectra of SWCNTs.[123,256] Note that trion formation also competes with Auger quenching of excitons, which results in a significant reduction of observed photoluminescence intensities.[257] For high doping levels, the rate of Auger quenching surpasses the rate of trion formation and the trion emission is quenched.[252]

Trions primarily form *via* combination of diffusive excitons with (localized) charges. It is still debated whether dark excitonic states or triplet excitonic states are involved in this process.[257-260] It has also been proposed that trions can be directly excited from the ground state, which explains the red-shifted absorption band.[224,251,253,259,261-263] Recent studies, however, indicate that the red-shifted absorption is not trionic but polaronic in origin.[264-266] An overview of these processes is given in **Figure 14B**.

The experimentally observed energy difference between excitonic and trionic absorption and emission peaks ΔE_{11}-T is significantly larger than the predicted values for the trion binding energy $E_{B\text{-}T}$.[249] This has been explained by an increased singlet-triplet splitting Δ_{st} due to strong short-ranged Coulomb interactions, which contributes to the energy separation between excitonic and trionic states (see **Figure 14B**).[224] Both trion binding energies as well as the induced singlet-triplet splitting scale inversely with the tube diameter and the square of the tube diameter, respectively (see formula **Figure 14B**). Experimentally determined values range from 40-105 meV nm for A and 48-70 meV nm^2 for B.[224,251,254,267-269] Hence, trions show a stronger red-shift for small diameter SWCNTs.

2.3.3 Chemical Doping of Graphene Nanoribbons

So far, only little is known about the changes in optical spectra of GNRs upon doping. As they are structurally similar to rigid conjugated polymers, the optical spectra of doped polymers will be discussed here instead. Upon chemical doping of conjugated polymers, an absorption bleach and photoluminescence quenching can be observed.[217] Absorption spectra of undoped and p-doped PFO-BPy are shown as an example in **Figure 15A**. Similar as in SWCNTs a bleaching of excitonic absorption and quenching of photoluminescence can be observed upon doping of conjugated polymers. Additionally, a red-shifted absorption feature emerges upon doping. In contrast to SWCNTs, this feature is not trionic in origin but is associated with polaronic states. Polarons are quasiparticles emerging upon crystal lattice relaxation around a charge due to strong electron-phonon coupling.[270] This relaxation results in polaronic states (P* and P**) located within the band gap of the semiconductor (see **Figure 15B**).[270]

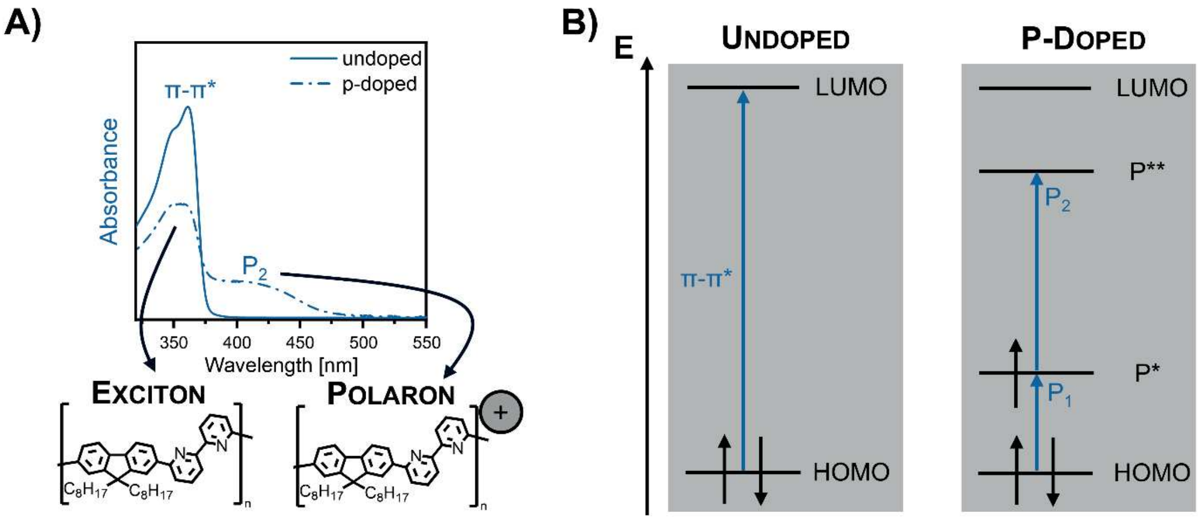

Figure 15. A) . UV-Vis absorption spectrum of a solution of undoped and p-doped PFO-BPy. The excitonic π-π*-transition, as well as the polaronic P_2 transition are labelled. **B)** States and optical transitions in an undoped and p-doped semiconductor with strong electron-phonon coupling

These new states also lead to new polaronic transitions (P_1 and P_2) that can be identified with absorption spectroscopy.[271] For PFO-BPy, only the P_2 transition is visible (**Figure 15A**), as the P_1 transition appears at substantially larger wavelengths. Polaronic states are not emissive, hence polaronic transitions only appear in absorption spectra in contrast to trionic states that also have an optical signature in emission spectra.[271]

For GNRs, only two studies which investigate the impact of chemical doping on their optical properties exist so far: A theoretical study by Deilmann *et al.* predicted large trion binding energies on the order of several hundreds of meV for n = 4-13 n-aGNRs.[272] Similar to the electronic band gap, the trion binding energy was predicted to be inversely proportional to the width of the GNR. Experimentally, only one study investigated the chemical doping of aGNRs so far. In this study, F_4TCNQ was used to p-dope on-surface synthesized 7-aGNRs which showed red-shifted photoluminescence upon increasing doping levels.[273] While the authors assigned this spectroscopic feature to emission from trionic states, the low emission intensity, the presence of dark states in the 3q+1 n-aGNR family, and the presence of zigzag end-states that were shown to also emit light at lower energies than the excitonic transitions[203,207] were not discussed. Additionally, a theoretical study from 2019 predicted considerably stronger interactions of charge carriers and phonons in GNRs than in SWCNTs.[274] Furthermore, sterically demanding side chains in solution-synthesized GNRs lead to a significant distortion of the GNR backbone – a fact that was not considered in the theoretical study by Deilmann *et al.*[272] Hence, the question whether charges in GNRs rather couple with excitons to form trions or with phonons to form polaronic states, as observed in polymers, arises.

2.4 Field-Effect Transistors

Field-effect transistors (FETs) enable controlled electrostatic or -chemical doping of semiconductors, as well as modulation of the current that flows through the semiconductor *via* application of an external electrical gate field. Hence, they are perfectly suited for investigation of the charge transport properties of semiconductors. The first FET with bottom-up synthesized GNRs as channel material has been presented by Bennett *et al.* in 2013 who used on-surface synthesized 7-aGNRs.[275] Since then, research focused on improving the charge transport in GNR-based FETs and identified several challenges that must be addressed to realize better performing devices. The following chapters will briefly explain the working principles of ambipolar FETs in general and of electrolyte-gated FETs. Additionally, an overview of charge transport in GNRs will be given. Finally, remaining challenges for GNR-based devices will be discussed.

2.4.1 Fundamentals of Ambipolar Field-Effect Transistors

In a field-effect transistor, the current flowing through a semiconductor deposited between two electrodes (i.e., source and drain) can be modulated by an external electrical field which is regulated by the gate electrode separated from the semiconductor by a dielectric layer. The device layout of a bottom-contact, top-gate and a top-contact bottom-gate FET is shown in **Figure 16**.

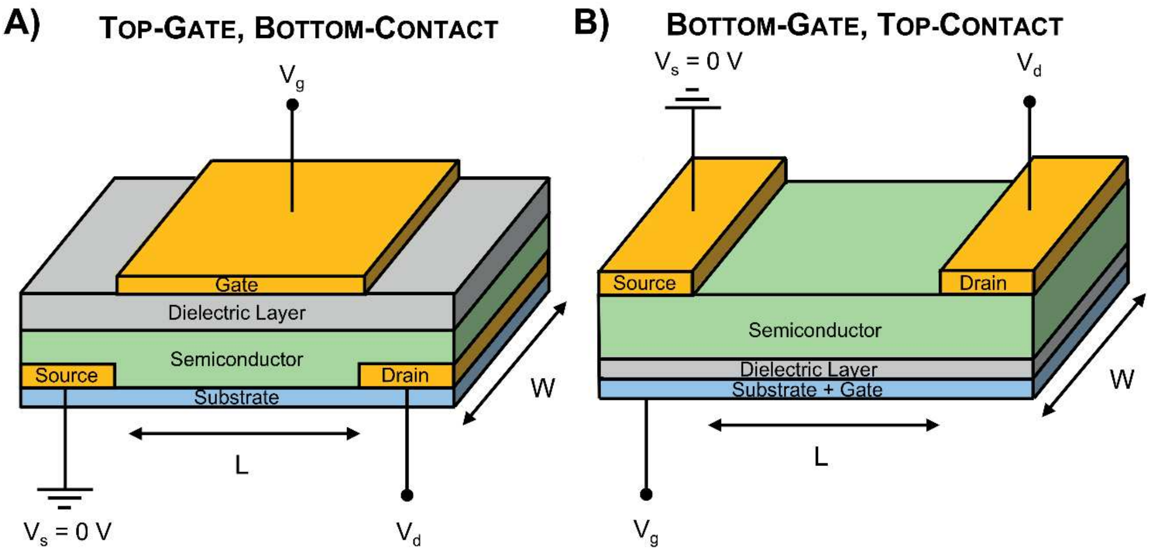

Figure 16. Schematic layout of a **A**) bottom-contact, top-gate FET **B**) top-contact, bottom-gate FET with channel length L and channel width W. During device operation, the source electrode is grounded and a drain voltage V_d and gate voltage V_g are applied to drain and gate electrodes.

'Bottom/top-contact' and 'top/bottom-gate' indicate the relative positions of source/drain and gate electrodes within the device. The device geometry influences the device performance[276,277], but the general working-principle of the FET stays the same. Many GNR-based devices adopt a bottom-gate, top-contact architecture, primarily due to a straightforward and efficient fabrication process. For top-contact, bottom-gate GNR based devices, the substrate typically consists of a silicon oxide layer (which serves as the dielectric) on top of a heavily doped silicon layer, which can serve as the gate electrode.[165,281,301] Thus, only transfer of the GNRs and evaporation of source and drain electrodes are necessary.

The dielectric in the FET plays an important role, as its properties influence the voltage range and switching frequency the device can be operated at and generally affect device performance. Commonly used dielectrics consist of metal oxides with high dielectric constants or a bilayer of a metal oxide and a polymer which can help to prevent trap state formation at the metal oxide/semiconductor interface.[2,278,279] working principle of electrolyte-gated transistors (EGTs), which were used within this thesis, is explored within the next chapter after the general discussion of the working principle of an ambipolar FET.

While unipolar FETs only allow for the transport of one type of charge carrier, ambipolar FETs enable the transport of electrons and holes. Whether a transistor is ambipolar or unipolar depends on the employed semiconductor, the electrode work functions and the presence of (un)intentionally introduced dopants.[277] Since SWCNTs and GNRs are ambipolar semiconductors, this chapter will focus on ambipolar FETs.[266,280,281]

Ambipolar FETs typically have four operating regimes which are depicted in **Figure 17A**. Which regime the device is operated in depends on the threshold voltage V_{th}, the gate voltage V_g and the drain voltage V_d.

For application of a gate voltage V_g without a drain voltage V_d, the transistor operates in the accumulation regime and can be seen as a capacitor. Below the threshold voltage V_{th}, accumulated charges fill trap states that originate from the semiconductor or are induced by impurities or the semiconductor morphology. Note that the threshold voltage varies, depending on the type of charge carriers. As soon as V_g exceeds V_{th}, charges are accumulated at the dielectric/semiconductor interface, which results in doping of the semiconductor and creation of a conductive channel (**Figure 17A**).[282,283] For a dielectric, the density of accumulated charge carriers per unit area Q can be calculated *via*

$$Q = C_i(V_g - V_{th}) \tag{2.17}$$

with C_i as the areal capacitance of the device. It should be noted that the actual experimental determination of charge carrier density is not trivial, as the areal capacitance of the device is dependent on operating frequency and gate voltage.[284]

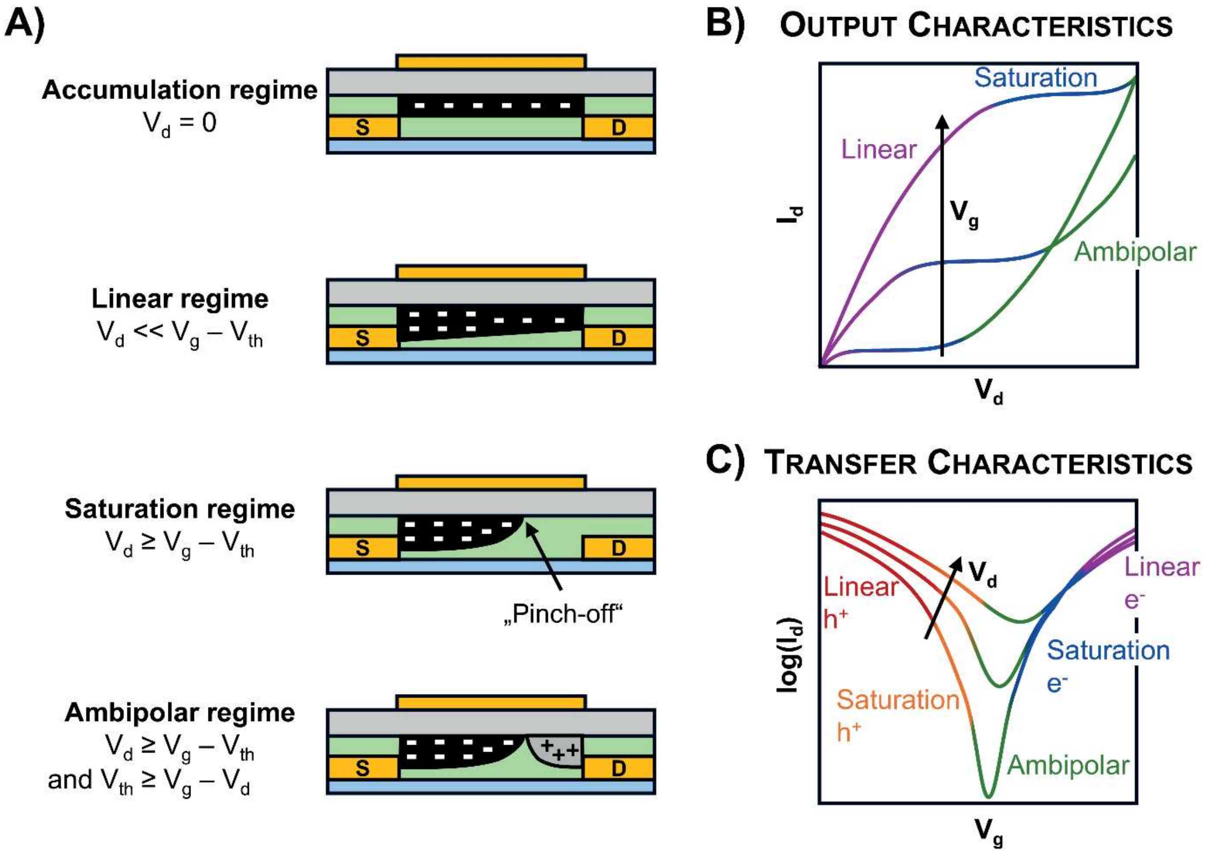

Figure 17. A) Operation regimes of an ambipolar bottom-contact, top-gate transistor. **B)** Output characteristics of an ambipolar transistor at different gate voltages V_g. **C)** Transfer characteristics of an ambipolar transistor at different drain voltages V_d. Differently colored parts of the output and transfer curves indicate the different operation/transport regimes.

The application of a small drain voltage $V_d << V_g - V_{th}$ leads to the formation of an electric potential gradient between source and drain electrode within the conductive channel, which induces a current flow (**Figure 17A**). Within the graduate channel approximation[277], which assumes that the gate field greatly exceeds the lateral electric field between source and drain electrodes and that the channel length L is significantly larger than the thickness of the dielectric layer, the current between source and drain electrode I_d can be calculated as

$$I_d = \frac{WC_i}{L}\mu\left(\left(V_g - V_{th}\right)V_d - \frac{V_d^2}{2}\right) \tag{2.18}$$

where μ is the charge carrier mobility. This also assumes that μ is independent of carrier density and neglects any diffusion currents. In the case of $V_d \ll V_g - V_{th}$, **Equation (2.18)** can be simplified to

$$I_d = \frac{WC_i}{L}\mu_{lin}\left(V_g - V_{th}\right)V_d. \tag{2.19}$$

Equation (2.19) shows that, in this case, the drain current linearly depends on the applied drain voltage, which is why this operating regime is termed ‘linear regime’. This can also be observed in **Figure 17B** which depicts the output curves (*i.e.*, a plot of I_d *vs.* V_d at constant V_g) for three different gate voltages V_g. In the purple-colored part of the curve $V_d \ll V_g - V_{th}$ and I_d increases linearly with V_d.

If the drain voltage is further increased so that $V_d \geq V_g - V_{th}$, the saturation regime is reached, and a carrier depletion zone is formed at the so-called pinch-off position (see **Figure 17A**). In this regime, the drain current can be determined by

$$I_d = \frac{WC_i}{2L}\mu_{sat}\left(V_g - V_{th}\right)^2. \tag{2.20}$$

Here, the drain current is independent of the drain voltage, as is shown by the blue segments of the output curves depicted in **Figure 17B**.

The linear and saturation regimes also exist for unipolar FETs, but further increasing V_d does not have any effect. For ambipolar FETs, however, further increasing V_d so that $V_d \geq V_g - V_{th}$ and $V_{th} \geq V_g - V_d$ leads to injection of carriers of opposite charge (here holes) from the drain electrode into the channel (**Figure 17A**).[285] This regime, in which both types of charge carriers are present in the channel is termed ‘ambipolar regime’. The drain current in this regime increases superlinearly with the drain voltage (**Figure 17B**, green segment).

By keeping V_d constant and varying V_g the device can also be cycled through the different operation regimes as becomes evident from the transfer curves (I_d *vs.* V_g at constant V_d) depicted in **Figure 17C**. The characteristic V-shape of the transfer curves in an ambipolar transistor can be explained by a superposition of the electron and hole transport branch. The ambipolar regime is the region in which the hole and electron transport branch overlap. From the transfer curves, several figures of merit such as on-currents and on/off current ratios can be extracted. The on-current is defined as the maximum of the drain current (*i.e.*, the current after which the drain current does not increase with increasing V_g anymore). The on/off current ratio can then be calculated by dividing the on-current by the current that flows through the transistor in the off-state (typically the drain current minimum).

Additionally, the charge carrier mobilities of the device can be extracted. By rearranging **Equations 2.19** and **2.20**, the charge carrier mobilities in the linear and saturation regime can be calculated. For the carrier mobility in the linear regime μ_{lin} rearranging **Equation 2.19** gives

$$\mu_{lin} = \frac{\partial I_d}{\partial V_g} \frac{L}{W C_i V_d}, \tag{2.21}$$

The derivative of the drain current with respect to the gate voltage is also called transconductance g_m and determines how effectively the device can amplify a voltage signal at the gate.[286] If the capacitance of a device is unknown, it can be used instead of the carrier mobility to compare carrier transport between devices with the same L and W. It should be noted that the transconductance and carrier mobility are not material constants but strongly dependent on carrier density, device layout, semiconductor film morphology and measurement conditions.

2.4.2 Electrolyte-Gated FETs

Instead of solid dielectrics, which only contain immobile dipoles, electrolytes such as ionic liquids, salt-containing water or ion gels (ionic liquids + polymer) with mobile ions can be used as a dielectric.[284] Resulting devices are often referred to as organic electrochemical transistors (OECTs). In this work the term electrolyte-gated transistors (EGTs) is used.

When a positive (negative) gate voltage is applied, cations (anions) accumulate at the electrolyte/semiconductor interface or even penetrate the semiconductor film if it is permeable, while anions (cations) accumulate at the gate electrode (**Figure 18**). This leads to the formation of an electrochemical double layer in the channel and accumulation of opposite charge carriers within the semiconductor (*i.e.*, electrochemical doping).[284]

Bernard *et al.* presented a model to describe these processes within an EGT with a separated ionic and electronic circuit (**Figure 18**).[286,287] The ionic circuit consists of two capacitors at the electrolyte/semiconductor ($C_{Channel}$) and the electrolyte/gate electrode (C_{Gate}) interface which are connected *via* a resistor ($R_{Electrolyte}$) represented by the electrolyte. Charging of the channel capacitor by applying a gate voltage then modulates the resistance of the channel resistor $R_{Channel}$

in the electronic circuit and consequently leads to a change in the drain current.[286,287] Note that the capacitance of C_{Gate} in the ionic circuit is significantly than that of $C_{Channel}$. Since the two capacitors are connected in series, the capacitance in the ionic circuit is dominated by that of $C_{Channel}$.[286]

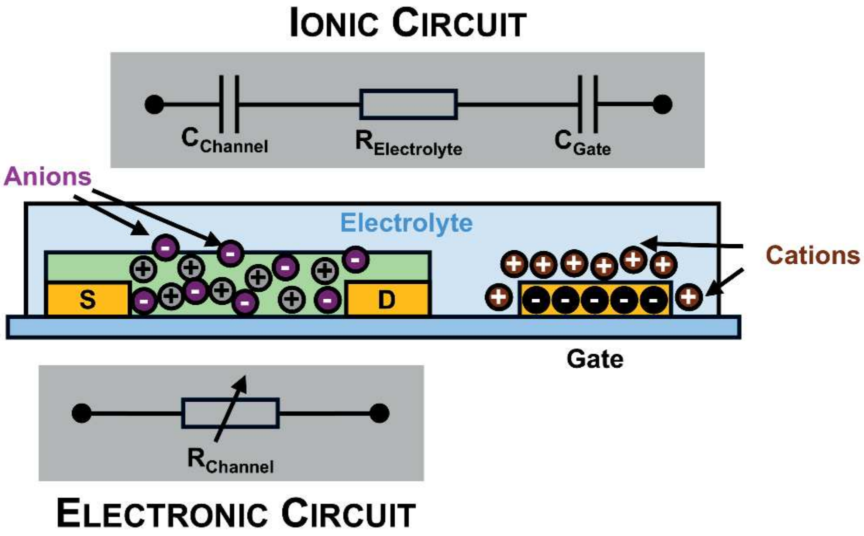

Figure 18. Schematic depiction of an EGT with a side gate structure and an ion-permeable semiconductor film in hole accumulation mode. Application of a negative gate potential leads to accumulation of cations at the gate electrode and anions within the semiconductor. This induces charge injection of opposite charges (*i.e.*, holes) into the semiconductor film.

For an impermeable semiconductor, the $C_{Channel}$ can be treated as a plate capacitor (similar to devices with solid dielectrics), but if the ions are able to permeate the semiconductor (as schematically depicted in **Figure 18**), the volumetric capacitance of the channel has to be considered.[286] This means that the device capacitance C_i in **Equations 2.18-2.21** has to be replaced by C^*d, where C^* is the volumetric capacitance of the channel and d the thickness of the channel material to correctly describe the charge transport in EGTs.[286]

The charge accumulation throughout the whole channel is responsible for the resulting high electric fields in EGTs that reach values of several μF cm^{-2} which significantly exceeds values that can be reached using solid dielectrics and thus enables device operation at low voltages (V_g is typically within ± 3 V).[288] Additionally, the permeation of the semiconductor film by the electrolyte allows for doping of thick (>100 nm) semiconductor films, which cannot be achieved using electrostatic doping.[284] Electrolyte gating also enables a larger variety of device geometries, as the gate electrode does not have to be located directly above or below the channel area and devices can be made fully flexible, which is not possible with rigid oxide dielectrics.[289,290] Finally, gating of rough semiconductor films is no problem with EGTs, while film roughness needs to be controlled in FETs with solid dielectrics to optimize device performance.[291]

The achievable high electric fields by volumetric gating come at the disadvantage of slow response times, which result from a limited ionic conductivity and thus slow ion movement within the electrolyte.[284,286] This prevents application of EGTs in fields where high-frequency switching is necessary. Additionally, when using EGTs to characterize charge carrier transport in semiconductors, transfer characteristics have to be recorded with a low gate voltage sweep rate to minimize hysteresis. In EGTs the employed electrolyte also dictates the measurement window, as high applied voltages can lead to electrolysis or unwanted side reactions within the electrolyte. Ionic liquids, that are frequently used as electrolytes in EGTs are typically stable between $V_g = \pm 2.5$ V.[284] Lastly, depending on the semiconductor, ion migration might lead to swelling of semiconductor films which alters film morphology and device performance.[292]

The low ion mobilities in EGTs can however also be used for example in neuromorphic devices. As ions that migrated into the channel area during application of a gate voltage do not immediately diffuse after that, the device remains conductive, thus exhibiting a memory function. Generally, EGTs support a wide range of potential applications. The flexible electrolyte layer can be structured when an ion gel is used, which enables production of synaptic pressure sensors.[293] Additionally, EGTs are sensitive toward changes in electrolyte composition (e.g., introduction of an analyte), making them suitable for electrical sensing applications.[289,294]

2.4.3 GNRs as Channel Material in FETs

In 2013, Bennett *et al.* reported the first bottom-up synthesized GNR FET with on-surface synthesized 7-aGNRs as channel material.[275] The successful integration of on-surface synthesized GNRs into devices was enabled by the development of a transfer process from the metallic growth substrate (typically gold) to an insulating substrate. This transfer process involves spin-coating of a PMMA layer on top of the as-synthesized GNR film, delamination of the support mica substrate by hydrofluoric acid, etching of the gold by a mixture of potassium iodide and iodine and transfer of the free-floating PMMA/GNR film to the insulating substrate, where the PMMA is removed by soaking in acetone. It has since become the standard process for device integration of on-surface synthesized GNRs.[158,165,168,275,295-298] The top-contact, bottom-gate structure, which used silicon dioxide as a dielectric layer, only had a channel length of 20-30 nm, resulting in single-GNR FETs. Bennett *et al.* reported hole transport for unannealed devices which switched to electron transport once devices were annealed at 300 °C in vacuum with on/off-ratios of 3×10^3. This was attributed to a change in contact metal work function due to removal of adsorbed oxygen.[275,299]

Since then, n = 5, 7, 9, 13 on-surface synthesized n-aGNRs[158,165,168,275,295-297,300,301] and n = 3, 5, 7, 13 solution-synthesized n-aGNRs[280,281,295] have been integrated in short-channel single-GNR FETs as well as long-channel (L > 100 nm) FETs based on GNR networks. Interestingly, only few studies that used on-surface synthesized GNRs reported FETs with ambipolar charge transport, with most of the devices exhibiting only hole transport. Mutlu *et al.* demonstrated in 2021, that on-surface synthesized 7-aGNRs transferred with the above-described wet-transfer process only resulted in devices exhibiting p-type transport, while using a transfer-free device fabrication method yielded ambipolar FETs.[158] This points towards unintentional doping during the transfer process of on-surface synthesized GNRs. FETs built from solution-synthesized aGNRs typically showed ambipolar charge transport.[280,281]

Reported hole and electron mobilities for GNR-FETs are on the order of 10^{-3}-10^{-2} $cm^2V^{-1}s^{-1}$, and on/off-ratios range from two to 3×10^5.[168,280,297,300,301] The highest carrier mobilities and on/off-ratios were recorded for single-ribbon FETs with channel lengths of ~20 nm.[295,297] An increase in channel length (*i.e.*, going from a single-ribbon FET to a GNR-network FET) resulted in a strong decrease of observed drain currents and on/off ratios. Hence, several studies concluded that the inter-ribbon charge transport is one of the limiting factors in GNR-based FETs.[24,297,301] Charge transport in GNR networks is suggested to occur via temperature-activated hopping and polaron-assisted tunneling.[297,301] The reported carrier mobilities for single-ribbon FETs do, however, also not align with the high intrinsic carrier mobilities of 100-25000 $cm^2(Vs)^{-1}$ estimated *via* optical-probe, terahertz-pump spectroscopy.[142,170,175,302] Charge scattering at defect sites in the GNR lattice provides a possible explanation for this discrepancy. As described in **Chapter 2.2.2**, incomplete Scholl graphitization in solution-based synthesis or carbon-carbon bond cleavage during thermal cyclodehydrogenation in on-surface synthesis lead to defects in the form of unclosed bonds or missing phenyl rings (so-called ‘bite-defects’) at the GNR edges. These defects inevitably occur in GNR synthesis and are, consequentially, present in GNRs employed in FETs. Several theoretical studies predict that they result in a severe reduction of conductivities (up to 98 %) in narrow graphene nanoribbons.[303,304] This has, however, not been confirmed experimentally thus far.

There are several other parameters that were found to limit GNR device performance: The type of material used for source and drain electrodes determines the contact resistance (*i.e.*, the resistance charge carriers experience upon injection from the electrodes into the semiconductor). High Schottky barriers (potential barriers due to energy band misalignment between metal and semiconductor) and poor GNR-electrode contact are the main contributors to contact resistance in GNR devices.[24] It was shown that replacing platinum with indium as the electrode material enabled a better GNR-metal contact and reduced contact resistance.[305] Graphene and SWCNTs are also explored as electrode materials to reduce Schottky barriers.[296,306,307] Furthermore it was found that the dielectric layer has an impact on GNR device performance, possibly due to introduction of short and long-range disorder.[24,295] Future studies must resolve these challenges and help understand the impact of parameters such as defects and processing conditions on charge transport in GNRs.

CHAPTER 3

PUBLICATION P1

A Hands-On Guide to Shear Force Mixing of Single-Walled Carbon Nanotubes with Conjugated Polymers

Lindenthal, S.; Settele, S.; Hellmann, J.; Schmitt, K.; Zaumseil, J.

arXiv **2023,** *arXiv:2311.11654v1*
https://doi.org/10.48550/arXiv.2311.11654

While this publication has not been peer-reviewed, it summarizes important details on the optimization of the dispersion of different chiralities of SWCNTs by the method of shear-force mixing. The optimized procedure described within the guide enables large-scale, reproducible dispersion of semiconducting SWCNTs.

I optimized the method for dispersion of (6,5) SWCNTs with PFO-BPy, which was originally reported by Graf *et al.*[20] and applied it to selectively disperse other chiralities, namely (7,5) and semiconducting, large-diameter Plasma Torch SWCNTs. Through constant review of process parameters over more than three years and input from student assistants who performed the dispersion process, I identified potential pitfalls, developed solution strategies and optimized the process.

A Hands-On Guide

to

Shear Force Mixing of Single-Walled Carbon Nanotubes with Conjugated Polymers

Sebastian Lindenthal, Simon Settele, Joshua Hellmann, Klaus Schmitt,

and Jana Zaumseil

Institute for Physical Chemistry, Universität Heidelberg, D-69120 Heidelberg, Germany

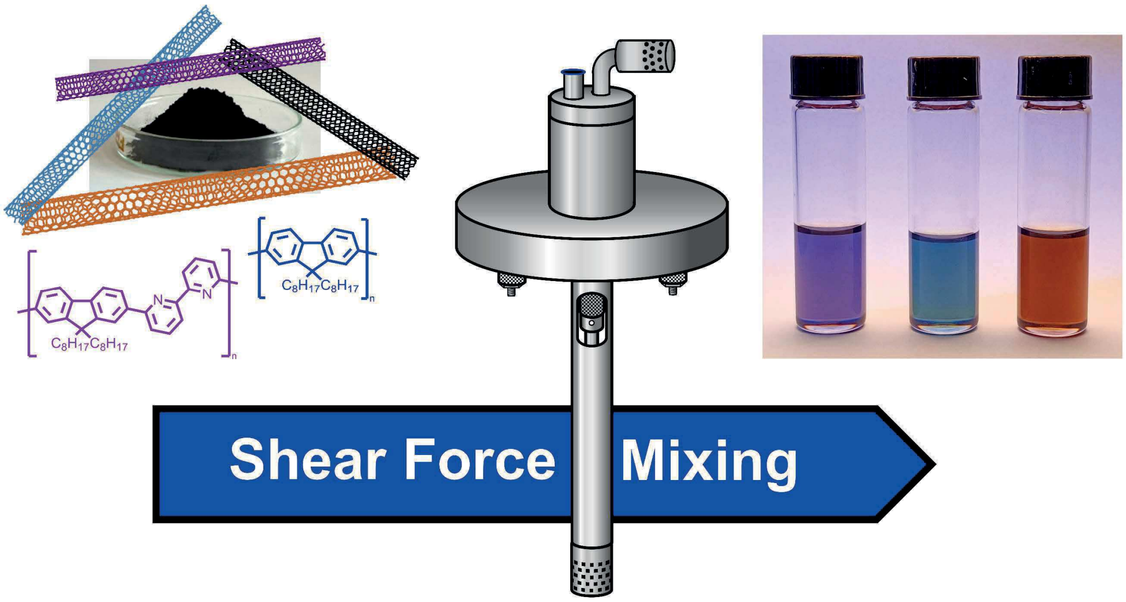

Version 1.0 / 12.11.2023

ABSTRACT

This guide provides a detailed step-by-step procedure for the dispersion of (6,5) single-walled carbon nanotubes by shear force mixing with the conjugated polymer PFO-BPy in organic solvents. All processes presented here were developed in the Zaumseil group at Heidelberg University since 2015 and represent best practices to the best of our knowledge. In addition to the detailed instructions, we discuss potential pitfalls and problems, that we have encountered over eight years of operation and show how to solve them. This also includes a detailed description of how to maintain and service a shear force mixer to ensure long operation lifetime. Finally, we show how to expand our process to the dispersion other nanotube chiralities in electronic-grade quality and how to treat dispersions for subsequent processing (*e.g.*, thin film deposition or functionalization).

If you use this guide please cite it as:

https://doi.org/10.11588/heidok.00033977

as well as the original publication:

Graf, A.; Zakharko, Y.; Schießl, S. P.; Backes, C.; Pfohl, M.; Flavel, B. S.; Zaumseil, J., Large scale, selective dispersion of long single-walled carbon nanotubes with high photoluminescence quantum yield by shear force mixing. *Carbon* **2016**, *105*, 593-599.

Acknowledgements: We thank Arko Graf and Jan Lüttgens for the initial development and optimization of the Shear Force Mixing process. Special thanks go to the dedicated undergraduate students who ran the Shear Force Mixing process within our group over the past years. Our deepest gratitude is reserved for our mechanical workshop team, led by Klaus Schmitt, whose support was indispensable whenever challenges arose with our Shear Force Mixers.

Funding: This work was financially supported by the European Research Council (ERC) under the European Union's Seventh Framework Programme (FP/2007–2013) (Grant Agreement No. 306298 "EN-LUMINATE") and under the European Union's Horizon 2020 research and innovation programme (Grant Agreement No. 817494 "TRIFECTs").

CONTENTS

INTRODUCTION TO SWNT DISPERSION

The optical and electronic properties (metallic or semiconducting, bandgap) of single-wall carbon nanotubes (SWNTs) are determined by their chiral indices (n,m) (see **Figure 1a**). Commercial growth methods such as CoMoCAT®, HiPco® or the Plasma Torch process always yield a mixture of different nanotube chiralities with different diameter distributions and metallic nanotube content.[1, 2] To integrate SWNTs in useful devices, methods to form stable dispersions and select desired chiralities are required. De-bundling of the as-synthesized SWNTs is achieved by applying sufficient mechanical force *via* sonication or shear force mixing in a solvent followed by stabilization through surfactants or polymers. Stable dispersions in water have been achieved by addition of surfactants such as sodium cholate or sodium dodecyl sulfate[3, 4] or single-stranded DNA and RNA.[5, 6] These dispersants are, however, mostly unspecific toward nanotube chirality, which makes sorting of the SWNTs *via* methods such as aqueous two-phase extraction[7, 8], density gradient ultracentrifugation[9] or column chromatography[10] necessary.

Selective dispersions of nanotubes with suitable conjugated polymers in organic solvents provides a direct route to certain nanotube types (semiconducting) and even single chiralities. Fluorene-based polymers and copolymers show especially high selectivities. **Figure 1b** shows the preferentially selected (n,m) chiralities for a few combinations of polyfluorene polymer and SWNT raw material.[11-16] In addition, polymer-related (molecular weight, concentration, polymer to nanotube ratio),[14, 17, 18] solvent-related (polarity, viscosity)[14, 19, 20] and process-related (sonication time, temperature)[14, 21-23] parameters have an impact on the yield and selectivity of the dispersion process. For more details, we refer the reader to two review articles by Samanta *et al.*[24] and Fong *et al.*[25] which discuss the influence of these parameters extensively.

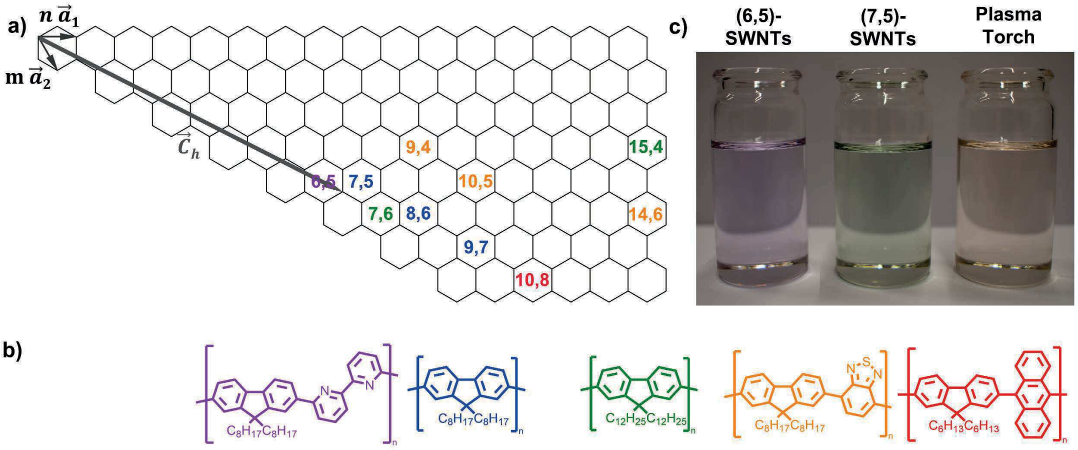

	PFO-BPy	PFO	PFDD	PFO-BT	PFH-A
CoMoCAT	(6,5)[11]	(7,5)[12]			
HiPco		(8,6)[11]	(7,6)[12]	(10,5)[14] (9,4)[14]	
Laser vaporization		(9,7)[12]			(10,8)[15]
Arc discharge (Meijo Carbon)			(15,4)[13]	(14,6)[13]	
Plasma Torch	Plasma Torch[16]				

Figure 1. a) Schematic depiction of a graphene sheet with the chiral vector $\vec{C}_h$ for a (6,5) SWNT. Chiral indices of nanotube chiralities that can be selected by polymer-wrapping are shown on the honeycomb lattice. **b)** Structures of highly-selective wrapping polymers and an overview of their selectivity for dispersion of different starting materials in toluene. In this work we provide a protocol for shear force mixing of the grey-shaded chiralities. **c)** Photographs of purified dispersions of (6,5), (7,5) and semiconducting Plasma Torch SWNTs in toluene obtained by Shear Force Mixing with polyfluorene polymers.

SHEAR FORCE MIXING as an EXFOLIATION METHOD

The quality of a nanotube dispersion (*i.e.*, the defectiveness and length of the contained nanotubes) is strongly influenced by the applied dispersion method. Structural defects and open tube ends will act as quenching sites for excitons (strongly bound electron-hole pairs that are highly mobile on carbon nanotubes), thus decreasing their emission efficiency.[26] Additionally, defects and inter-tube junctions in SWNT thin film devices, can act as charge-carrier scattering sites and will reduce charge-carrier mobilities.[27, 28] Both effects significantly influence the performance of SWNTs in photonic, electronic, and optoelectronic devices, which makes long and defect-free SWNTs highly desirable.

Sonication with a bath or tip sonicator damages and shortens nanotubes due to highly localized friction and pressure, created by sonication-induced cavitation.[29, 30] In contrast to that, Shear Force Mixing, provides energy for exfoliation continuously without locally creating highly turbulent and damaging regions. A basic explanation of the working principle of a Shear Force Mixer in the context of nanotube exfoliation is given in **Figure S1**.

Shear force mixing was previously shown to be a mild dispersion method for 2D materials (*e.g.*, graphene, MoS_2)[31, 32] and for SWNTs in aqueous dispersions[33] that enables larger flakes and longer nanotubes than sonication methods. Graf *et al.* showed that using shear force mixing of CoMoCAT® nanotubes with a polyfluorene copolymer (PFO-BPy) in toluene results in long nanotubes (> 1 µm) with low defect densities.[34] The average values for nanotube length, Raman D/G$^+$-ratios (as a metric for defect density) and photoluminescence quantum yields (PLQY) for different exfoliation methods are shown in **Table 1**. While Graf *et al.* reported a comparatively high D/G$^+$-ratio of 0.10 for shear force mixing in their original paper, we nowadays observe values of <0.05 for dispersions obtained by shear force mixing.

Table 1. Average lengths, D/G$^+$-ratios and PLQY for PFO-BPy wrapped (6,5) SWNTs exfoliated by Shear Force Mixing, Bath Sonication, Tip Sonication and (6,5) SWNTs sorted by Gel Chromatography + Density Gradient Ultracentrifugation (GC-DGU). All values were taken from Graf *et al.* [34]

	SFM	**Bath Sonication**	**Tip Sonication**	**GC-DGU**
Length (µm) Mean/Median	1.82/1.55	1.12/1.01	0.61/0.50	0.62/0.58
D/G$^+$-ratio	0.10	0.11	0.08	0.10
PLQY (%)	2.3	1.8	1.3	0.2

In addition to the superior nanotube quality, shear force mixing offers a scalable approach to exfoliate large quantities of nanotubes in one batch. Exfoliation of SWNTs and other nanomaterials by Shear Force Mixing is possible in large volumes up to 300 L.[31]

In the following we provide a step-by-step protocol for the dispersion of long, defect-free (6,5) and (7,5) SWNTs from CoMoCAT® raw material and purely semiconducting Plasma Torch-SWNTs from Plasma Torch (Raymor Nanotech) raw material by shear force mixing (resulting dispersions shown in **Figure 1c**).

WORKFLOW OVERVIEW

The workflow for Shear Force Mixing is shown in **Figure 2**. In a first step, SWNTs are weighed and dried (**steps 1-9**), as air humidity and moisture in the material significantly reduce the dispersion yield. The dried raw material is then dispersed in toluene with a suitable wrapping polymer (**steps 10-21**). The exfoliation is followed by centrifugation (**steps 22-30**) to remove unexfoliated material. Since a single SFM run usually does not disperse all (6,5) SWNTs that are contained in the raw material, the pellet from the centrifugation can be recycled (**steps 36-41**) to increase the yield. The supernatant after centrifugation is the final (6,5) SWNT dispersion, which is characterized by absorption and Raman spectroscopy (**steps 42-43**) to determine the yield and the quality of the dispersion.

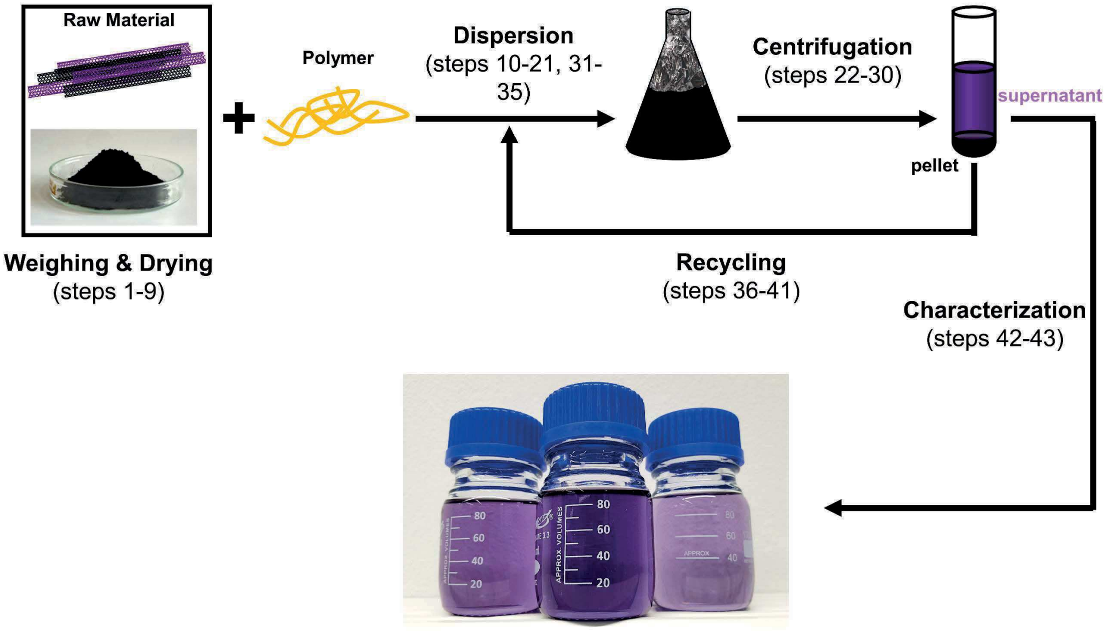

Figure 2. Workflow of the Shear Force Mixing process. Nanotube raw material is weighed and dried. Shear Force Mixing with a suitable wrapping-polymer and toluene yields a dispersion that must be purified by centrifugation. The resulting supernatant is characterized while the pellet can be recycled several times to maximize the yield.

In the following we present a step-by-step protocol for the monochiral dispersion of (6,5) SWNTs *via* Shear Force Mixing. While the dispersion protocol is similar for other chiralities, there are some important differences. The experimental variations are explained in the Supporting Information (**Appendix I** for (7,5) and **Appendix II** for Plasma Torch SWNTs).

In case excess polymer is problematic (*e.g.*, for functionalization or thin film deposition experiments), you can remove the polymer either by filtration or ultracentrifugation. We added an explanation for both processes in **Appendix III**.

EQUIPMENT

Here we list the materials, consumables and the equipment that is necessary for the dispersion of (6,5) SWNTs with PFO-BPy in toluene. For other chiralities see the Supporting Information. Specific companies or brands are named to describe our process as detailed as possible and do not represent any endorsement and recommendation.

Required Raw Materials / Polymers / Solvents

- **CoMoCAT® raw material** from CHASM (SG65i, *e.g.*, Sigma-Aldrich, 773735, (6,5) chirality, ≥95% carbon basis (≥95% as carbon nanotubes), 0.78 nm average diameter)
- **Poly[(9,9-dioctylfluorenyl-2,7-diyl)-alt-(6,6′-[2,2′-bipyridine])]** (American Dye Source, PFO-BPy, ADS153UV, $M_w \sim 34\,000$ g/mol, note that the molecular weight range is critical and always should be between 30 000 and 40 000 g/mol)
- **Toluene** (purity >99.7 %)
- **Isopropanol**

Required Equipment for Nanotube Weighing and Drying (steps 1-9)

- **High precision scale (**e.g. A&D Weighing HR-250AZ Galaxy Analytical Balance**)**
- **Polyimide-tape** (3M™, 5419 high temperature polyimide tape)
- **PTFE filter** (Millipore, Omnipore Membrane Filter JHWP02500, hydrophilic PTFE Filter, 25 mm diameter)
- **Snap-cap vials** (VWR, 15 mL, ND22 opening)
- **Spatula**
- **Tweezers**
- **Wipes** (Kimtech Science, Precision Wipes)
- **Hotplate**

Personal protective equipment (PPE):

- **Safety glasses and lab coat** (obviously…)
- **Particle mask** (Dräger, model type: X-plore 3300, equipped with bayonet filter type: A1B1E1K1 Hg P3 R D) or similar
- **Nitrile gloves** (Ansell, Touch N Tuff® 92-600, Length 240 mm)
- **Long-sleeve gloves** (Hygostar, LDPE gloves Softline long)

Required Equipment for Dispersion (steps 10-21)

- **Shear Force Mixer** (L2/Air, Silverson Machines Ltd.) depicted in **Figure 3**.

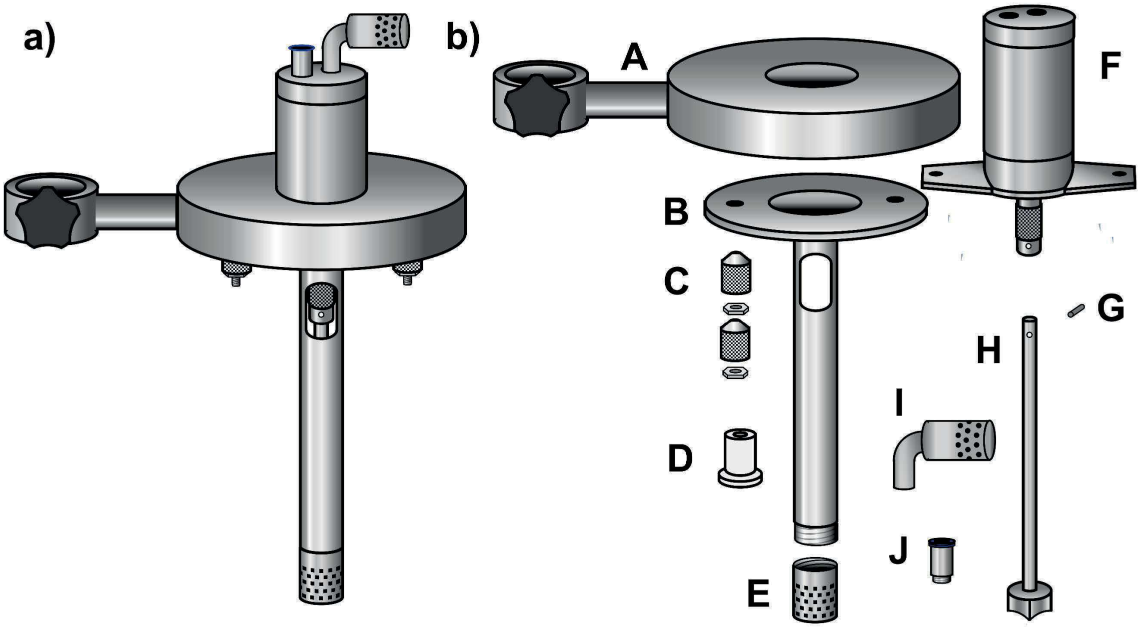

Figure 3. a) Assembled shear force mixer **b)** Explosion drawing of shear force mixer parts with a detailed description given in Table 2.

Table 2. List of the shear force mixer parts.

A	Metal block for attachment of F and B with connection to lab stand
B	Frame for detachable shear heads (in this paper the combination of B and E will be referred to as stator)
C	Conical screws and nuts (for connection between A and B)
D	¾” PTFE Bush (CAB6E10/1)
E	**¾” square hole high shear screen** (here we call the combination of B and E stator)
F	Compressed air motor (**Atlas Copco, LZB 22RL A220-11**, 0.34 HP (0.25 kW) lubrication free stainless-steel air motor (9600 RPM at 5.3 L/s (11.2 cfm))
G	Aglet for connection of F and H
H	Drive shaft with ¾” rotor
I	Exhaust for compressed air motor
J	Push-in fitting for connection to PVC hose (Landefeld, 3/8” IQS straight push-in fitting, diameter 12 mm)

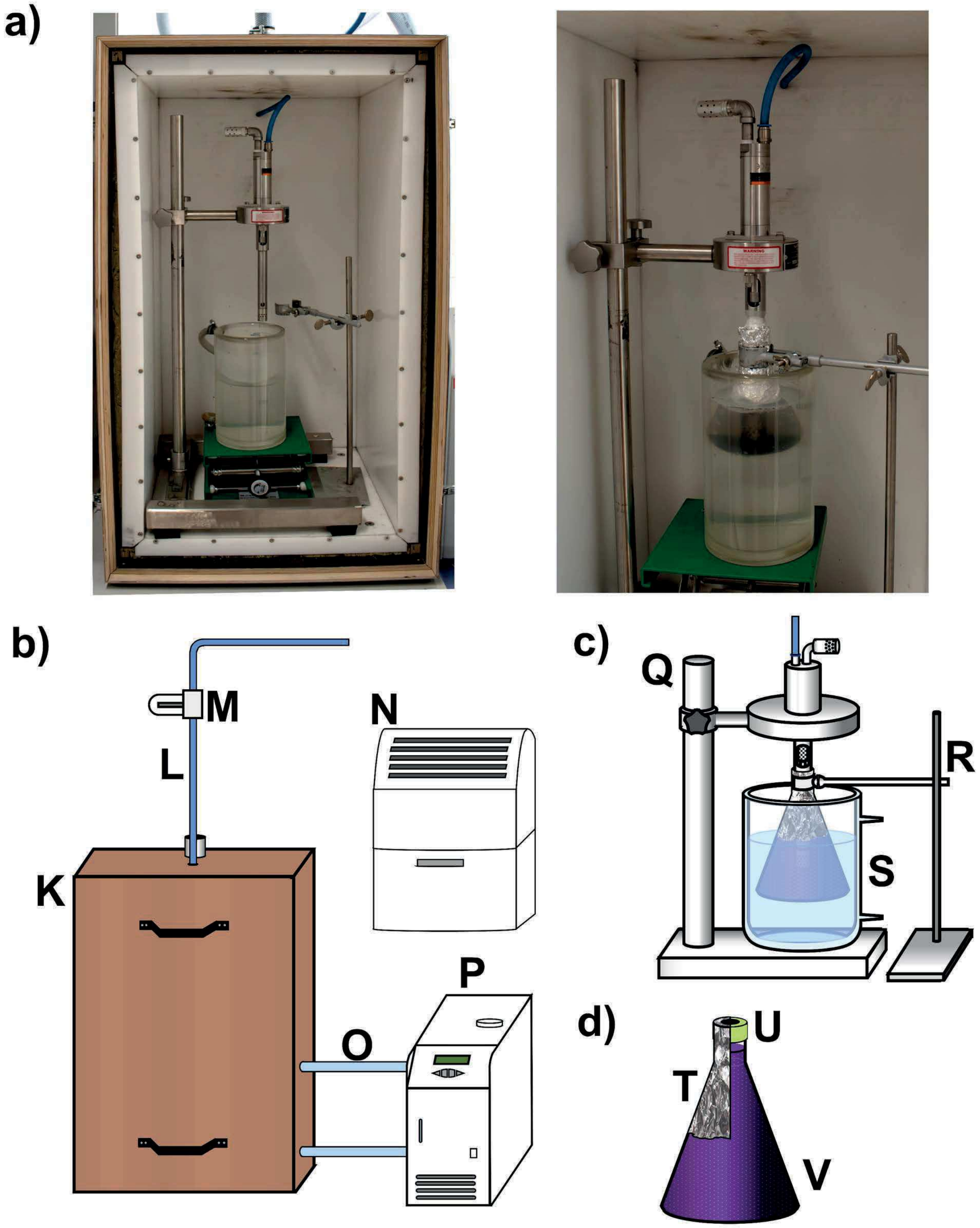

Figure 4. a) Pictures of the Sound proof box that contains the Shear Force Mixer. Left panel only shows the Shear Force Mixer. Right Panel shows how the setup looks when an Erlenmeyer flask is attached to it. **b-d)** Schematic depiction of additional equipment needed for dispersion of SWNTs with Shear Force Mixing.

Table 3. Detailed list of required accessories for the Shear Force Mixing process

K	Soundproof box containing the SFM setup (Homebuilt, Explanation and technical drawing can be found in **Appendix IV** of the **Supporting Information**)
L	Polycarbonate hose (Landefeld, 10.2x8 mm diameter, outside/inside) with connection to pressurized air source with 5 bar pressure
M	Air filter (Landefeld, multifix series 0 - type F014, 1000 l/min)
N	Dehumidifier (Remko, model type: ETF320)
O	PVC hoses for cooling water (Landefeld, 16x10 mm diameter, outside/inside)
P	Chiller (Julabo GmbH, model type: F250)
Q	Stainless steel metal lab stand for the shear force mixer
R	Lab stand for attachment of Erlenmeyer flask
S	Tempering beaker (KGW-Isotherm GmbH, model type: T 2000)
T	Aluminum foil and parafilm
U	Splash protection (Homebuilt, made from PP lid of centrifuge tubes)
V	Erlenmeyer flask (VWR, borosilicate glass, NS29/32, 250 mL)

Required Equipment for Purification (steps 22-30)

- **Ultracentrifuge** (e.g., Beckmann Coulter, Avanti J-26S XP equipped with a JA25.50 fixed-angle rotor, the centrifuge needs to reach RCF values of 60 000 *g*)
- **Centrifuge tubes** (Beckmann, **Polypropylene** Centrifuge Tubes with PE Caps, 50 mL)
- **Eppendorf pipette** (10 mL)
- **Pipette tips**
- **Syringes** (BD, Discardit II, 20 mL)
- **Syringe Filters** (Whatman, Puradisc 13, PTFE filters 5 µm pore size, 13 mm diameter)

Required Equipment for Cleaning of the SFM (steps 31-35)

- **Test tube brush**
- **Measuring cylinder** (must be big enough so that the stator can fit inside)
- **Ultrasonication bath** (here, Branson 2510)

Required Equipment for Characterization (steps 42-43)

- **Absorption spectrometer with detection into the nIR-region** (here, Cary 6000i UV-Vis-NIR absorption spectrometer, Varian, Inc.)
- **Cuvettes for absorption spectroscopy (1 cm pathlength)**
- **Raman spectrometer with suitable excitation wavelengths** (here, Renishaw inVia confocal Raman microscope in backscattering configuration equipped with a 50× long working distance objective (N.A. 0.5, Olympus) and with excitation wavelengths of 532 nm, 633 nm and 785 nm)
- **Glass coverslips, aluminum foil**
- **Hotplate**

PROTOCOL for DISPERSION of (6,5) SWNTs

Here we describe the standard shear force mixing process for the dispersion of 125 mg of CoMoCAT® raw material (SG65i) with 125 mg of PFO-BPy in 250 mL toluene to obtain a nearly monochiral (6,5) SWNT dispersion. You can scale down the process to a volume of 125 mL by simply halving the amount of raw materials and using a smaller Erlenmeyer flask. The process stays the same.

Nanotube weighing ● TIMING 1 h (+ at least 10 h drying time)

▲CRITICAL The CoMoCAT® raw material should be stored in a dry environment, such as a glovebox or dry box, to minimize the influence of humidity on the dispersion process.
▲CRITICAL Use dehumidifiers in the labs (if not air-conditioned and humidity-controlled) where you handle and disperse nanotubes, as high humidity can decrease the dispersion yield and quality.
! CAUTION Dry nanotube raw material can be electrostatically charged and forms particle aerosols that pose a respiratory hazard. Always ensure to work in a fume hood and avoid spills. Clean the equipment that was in touch with nanotube raw material (spatulas, tweezers, fume hood) with IPA-wetted Kimtech wipes until no more black particles can be seen on the wipes.

1 Clean the fume hood in which you will weigh the nanotubes thoroughly by wiping it down with a Kimtech wipe and IPA.

2 Line the fume hood with Kimtech wipes and wet them with IPA. Ensure that the wipes stay wet as long as you work with the nanotubes, so spilled nanotube raw material sticks to the wet wipes.
! CAUTION Ensure to remove any ignition sources (*e.g.* hotplates) from the fume hood where you are working.

3 Cut six stripes of Kapton tape (length ~4-5 cm) and stick them to a surface but ensure they can be removed from it later. You only need four stripes of tape, two are just for backup.

4 Place a snap-cap vial, the container with CoMoCAT® raw material and a long-sleeve glove (will act as a trash can) on the IPA-wetted Kimtech wipes. Place a spatula, tweezers and a PTFE filter on a dry spot in the fume hood.

5 Put on a lab coat, the particle mask and a pair of nitrile gloves. Wear a pair of long-sleeve gloves over the nitrile gloves. Put on a last pair of nitrile gloves on top of the long-sleeve gloves.

Figure 5. Personal protective equipment for weighing of nanotubes. Ensure that the long sleeve gloves extend up to your elbows, so that in case of nanotube spills only the gloves and not the lab coat will be contaminated.

6 Tare (zero) the snap-cap vial and weigh in 125 mg of nanotubes with the spatula.

▲**CRITICAL** The bottom of the snap-cap vial will be wet from the IPA-wet Kimtech wipes during the weighing process. Thus, the mass will change (loss of 1-2 mg) when the IPA starts evaporating on the scale.

▲**CRITICAL** Do not try to weigh the nanotubes directly on the scale. Instead place the snap-cap vial on the Kimtech wipes when you transfer them from the container. Hold the container with the nanotubes as close as possible over the snap-cap vial to minimize the number of nanotubes that fly off the spatula. If the raw material exhibits a high electrostatic charging behaviour try to use an anti-static gun on the nanotube raw material.

▲**CRITICAL** Try to weigh in 125 mg, but anything from 120-130 mg is fine. Do not start to remove nanotubes from the vial again, as it will create more nanoparticle aerosol.

7 Use tweezers to place the PTFE filter membrane on the snap-cap vial (**Figure 6a**) and adhere the PTFE filter to the vial using 4 stripes of Kapton tape leaving a quadratic window uncovered so that water vapour can still escape (**Figure 6b**).

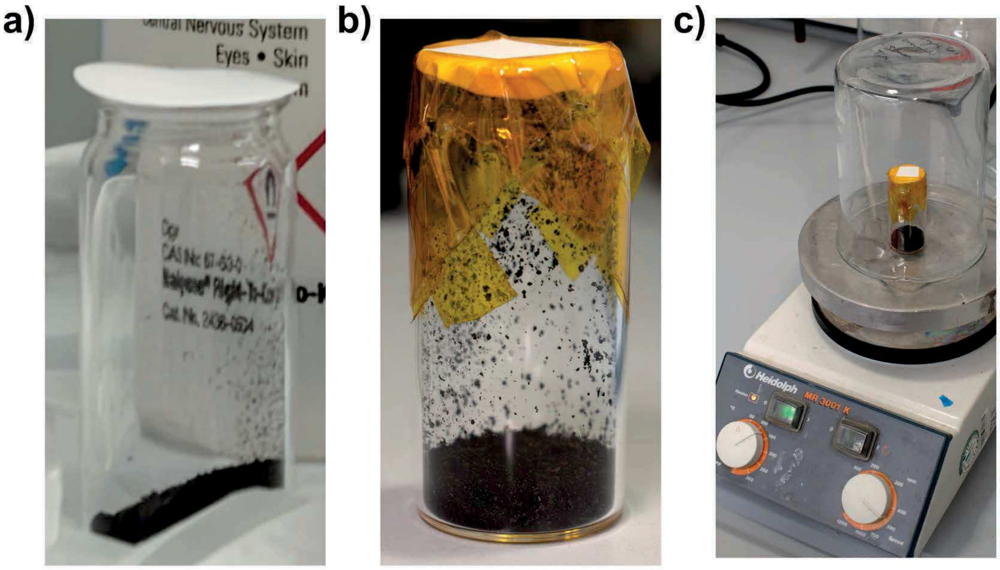

Figure 6. a) Vial with 130 mg CoMoCAT® raw material and loose PTFE filter. **b)** Vial sealed with PTFE filter and Kapton tape. **c)** Vial placed on hotplate for drying. The beaker is placed on top to prevent people from accidentally knocking over the vial with SWNTs.

8 Place the vial on a hotplate and heat it to 130 °C for at least overnight (**Figure 6c**).

▲CRITICAL Drying of the raw material is **not optional!** Not dried material will lead to a significant loss in yield.

■ PAUSE POINT The CoMoCAT® raw material can be dried for up to 3 days without causing any damage to the SWNTs.

9 Thoroughly wipe down the fume hood with IPA and Kimtech wipes until you see no more black particles. Dirty Kimtech wipes, as well as your outer nitrile gloves and the long-sleeve gloves should go into the long-sleeve glove acting as a trash can. When you are finished press out residual air and tie a knot into the long-sleeve glove. This will seal the waste that is contaminated with nanoparticles (→ solid waste container).

Setting up the SFM ● TIMING 1 h (+ at least 72 h dispersion time)

▲CRITICAL The polymer should be stored in a dry environment, such as a glovebox or dry box, to minimize the influence of humidity on the dispersion process.
▲CRITICAL Use dehumidifiers in rooms where you handle and disperse nanotubes, as high humidity can decrease the dispersion yield and quality.

10 In an Erlenmeyer flask, prepare a solution of 125 mg of PFO-BPy in ~200 mL of toluene. If the polymer does not fully dissolve upon stirring, use sonication to break up bigger chunks and heat the solution to 60 °C.
▲CRITICAL The polymer solution must cool down to room temperature again before you add the dried nanotubes.

11 Remove the nanotubes from the hotplate, so they can cool down to room temperature.

12 Put on your personal protective equipment (safety glasses, lab coat, gloves, particle mask).

13 Place a Kimtech wipe in the fume hood and wet it with IPA. Above this wipe, remove the PTFE filter membrane from the snap-cap vial and pour the dried nanotube material into the polymer solution. Rinse out the snap-cap vial with toluene from a squeeze bottle and pour it to the polymer solution. Rinse down any nanotube raw material that sticks to the inner wall of the Erlenmeyer flask and has not yet been in contact with the polymer solution.
! CAUTION Dry nanotube raw material can be electrostatically charged and forms particle aerosols that pose a respiratory hazard. If any nanotube spills happen, thoroughly clean the fume hood with IPA and wipes.

14 Assemble the Shear Force Mixer as shown in **Figure 7**.
▲CRITICAL After assembling the shear force mixer, it must be levelled using a spirit level.
! CAUTION Ensure that the shear force mixer is running in a well-ventilated space. In our case, the soundproof box is connected to an exhaust. You can also place the SFM in a fume hood.

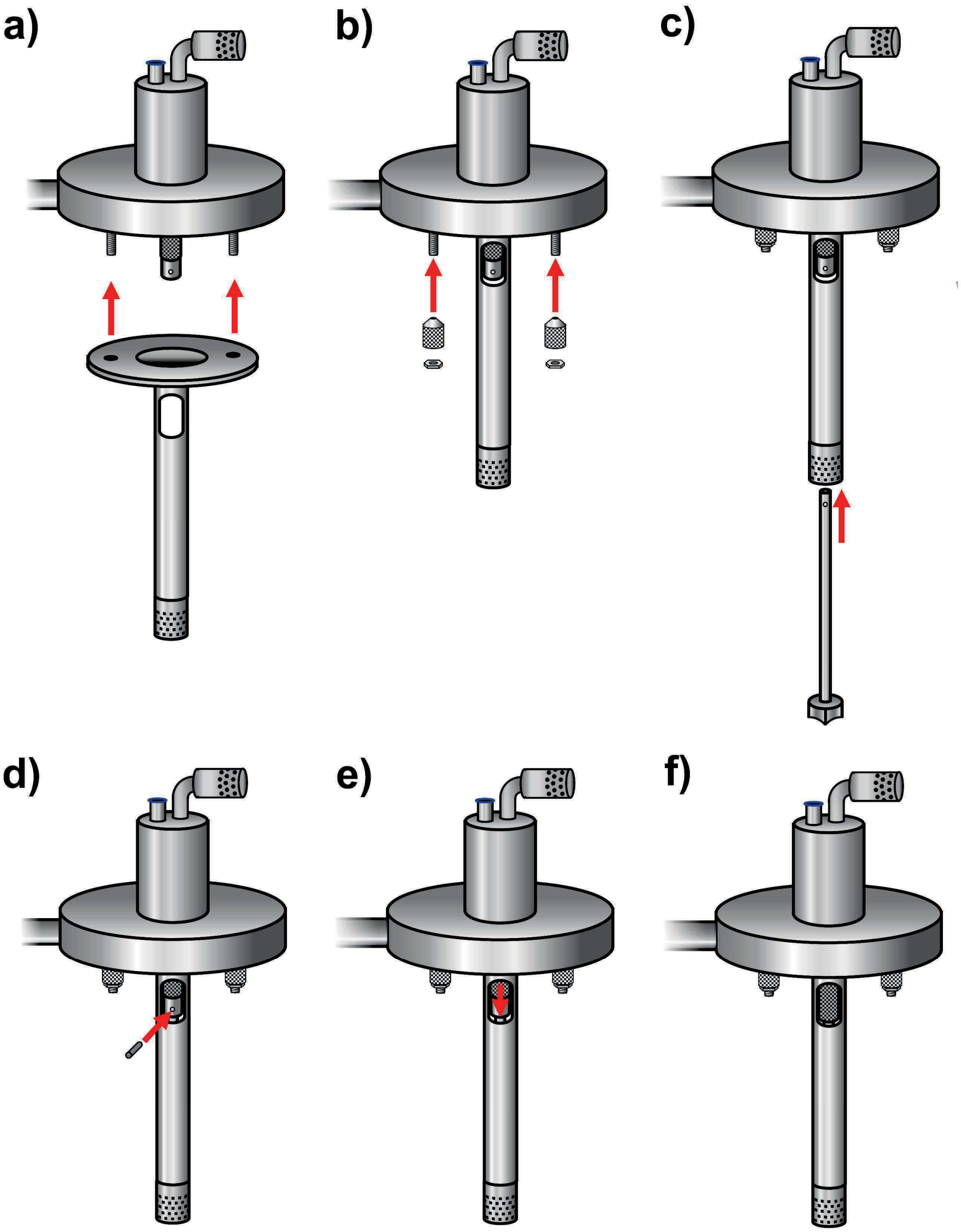

Figure 7. Assembly of the SFM. **a)** Insert the stator into the bolts that come out of the metal block. **b)** Use the conical screws and nuts to fixate it. **c)** Insert the rotor into the stator. Align the hole of the rotor with the hole of the motor unit. **d)** Fixate the rotor by inserting the metal aglet into the aligned holes. **e)** Pull the metal protection cap down. **f)** Assembled SFM.

15 Attach the Erlenmeyer flask to the lab stand. Make sure that the rotor/stator of the SFM is centered in the middle of the flask and resides ~2 cm above the bottom of the Erlenmeyer flask (**Figure 8**).

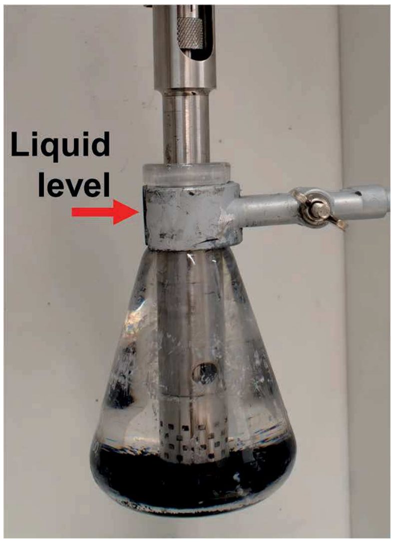

Figure 8. The stator is centred in the Erlenmeyer flask and immersed into the solvent. It resides approximately 2 cm above the bottom of the Erlenmeyer flask. The level of the solvent is at around half the height of the bottleneck.

16 Fill up the flask with toluene until the level of the liquid reaches half the height of the bottleneck (indicated by an arrow in **Figure 8**).

17 Remove the flask again without changing the height of the clamp on the lab stand. Then attach the splash protection (lid of centrifuge tube with hole in it) to the Erlenmeyer flask using aluminum foil and parafilm (see **Figure 9**). The aluminum foil should extend above the splash protection.

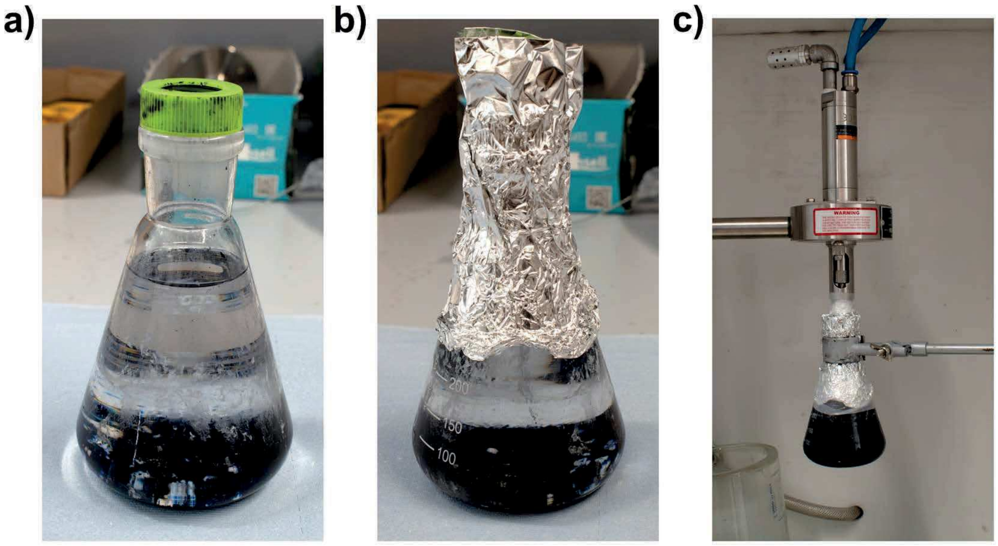

Figure 9. a) Erlenmeyer flask with dispersion with splash protection. **b)** Erlenmeyer flask with splash protection, fixated by aluminum foil. **c)** Erlenmeyer flask attached to the SFM

18 Attach the Erlenmeyer flask to the lab stand with the rotor/stator already inserted in the flask. Seal the extension of the aluminum foil around the SFM frame and wrap the connection between them with parafilm (**Figure 9c**)

! CAUTION Aluminum foil and parafilm must not cover the opening at the top of the stator frame. If loose ends are pulled into the rotor unit, they will damage the SFM.

19 Without closing the soundproof box, slowly open the valve to the pressurized air. We use an overpressure of 4 bar, which enables the motor to run at its maximum speed of 10230 rpm. While opening the valve, closely monitor the movement of the rotor (does it start spinning?) and listen to the sounds the motor makes. The latter should give off a whining noise with a uniform pitch that rises when you increase the air pressure. If everything looks and sounds good, close the valve to the pressurized air again.

! CAUTION Make sure that the protective lid covers the aglet that connects rotor and motor unit. If this is not the case, the aglet will fly out of the setup, becoming a high-speed projectile.

! CAUTION If the SFM makes loud noises or the whining noise is not uniform, immediately close the valve to the pressurized air.

? TROUBLESHOOTING

20 Bring the cooling beaker up to a position in which the water covers around 2/3 of the height of the Erlenmeyer flask. Turn on the chiller, set the temperature to 20 °C and cover the beaker with aluminum foil to minimize evaporation of cooling water.

▲**CRITICAL** As shown by Gomulya *et al.*, temperature is an important parameter that affects dispersion quality and yield, if not controlled precisely.[23] High temperatures can cause gelification of the mixture and lead to unpurifiable dispersion results. Worst case scenario: All of the solvent evaporated and the rotor will be destroyed! Thus, always make sure to turn on your chiller and check the water level in the cooling beaker every two days during the SFM process.

21 Close the soundproof box and fully open the valve to the pressurized air. Let the shear force mixer run for the desired time.

▲**CRITICAL** ■ **PAUSE POINT** As shown by Graf *et al.* the dispersion time impacts the yield (see **Figure S2**).[34] We usually let our SFM run for 72-96 h. Further increasing the dispersion time only leads to a slight increase in yield.

Purification of the stock dispersion ● TIMING 3 h

▲**CRITICAL** Use dehumidifiers in rooms where you handle and disperse nanotubes, as high humidity can decrease the dispersion yield and quality.

▲**CRITICAL** As soon as the dispersion process is stopped, work as quickly as possible. Even well dispersed (6,5) SWNTs will start aggregating after a few hours if the dispersion is not mixed anymore which leads to sedimentation during the centrifugation process.

22 Close the valve to the pressurized air to stop the shear force mixer. Remove the Erlenmeyer flask from the shear force mixer.

23 Distribute the black dispersion from the Erlenmeyer flask equally into the centrifuge tubes and place them in the rotor of the centrifuge.

▲**CRITICAL** As the centrifuge tubes are rather expensive we usually use them several times.

! CAUTION Prior to usage, check the centrifuge tubes and their lids for damage. The polypropylene and polyethylene can withstand the toluene for a limited time, but eventually the material will break. If you see even small cracks or damaged spots, replace the centrifuge tubes.

! CAUTION Make sure to thoroughly balance the centrifuge tubes. Two opposing centrifuge tubes should have a maximum weight difference of ±5 mg.

24 Centrifuge the dispersion at 60,000 *g* for 45 min. During the centrifugation step you have time to clean the Shear Force Mixer.

► REFER TO **Cleaning the Shear Force Mixer** (steps 30-34)

25 Carefully remove the centrifuge tubes from the rotor and place them in a tube rack.

▲CRITICAL Try to move the tubes as little as possible, as any movement might stir up the pelletized, unexfoliated material.

26 Using an Eppendorf pipette, take off the supernatant and fill it into a second set of centrifuge tubes. The supernatant should show a at least slightly purple colour. Again, balance out the centrifuge tubes.

▲CRITICAL This step will have a great impact on the dispersion quality! While taking up the supernatant, work slowly and stay close to the surface with the tip of the Eppendorf pipette. This will prevent any stir up of the pelletized material. Rather leave a little bit of supernatant in the centrifuge tubes than risking to transfer the pelletized material into the new set of centrifuge tubes.

! CAUTION Prior to usage, check the centrifuge tubes and their lids for damage. The polypropylene and polyethylene can withstand the toluene for a limited time, but eventually the material will break. If you see even small cracks or damaged spots, replace the centrifuge tubes.

! CAUTION Make sure to thoroughly balance the centrifuge tubes. Two opposing centrifuge tubes should have a maximum weight difference of ±5 mg.

? TROUBLESHOOTING

27 The pelletized material can be reused for subsequent dispersion steps.

► REFER TO **Recycling** (steps 36-41).

28 Centrifuge the supernatant of the first centrifugation step again at 60,000 *g* for another 45 min. This should pelletize any remaining unexfoliated material

29 Carefully remove the centrifuge tubes from the rotor and place them in a tube rack.

▲**CRITICAL** Try to move the tubes as little as possible, as any movement might stir up the pelletized, unexfoliated material.

30 Use a syringe to take off the supernatant and fill it into a storage container. For nicely dispersed nanotubes, you can use a syringe filter to remove any remaining particles. This is, however, not necessary if you worked carefully and can decrease the yield, if the dispersed nanotubes already started to aggregate.

▲**CRITICAL** Despite being polymer-wrapped, exfoliated SWNTs will start to reaggregate eventually; especially when dispersions have a high nanotube concentration. Before using them, sonicate the dispersion for 10 minutes, using a bath sonicator to break up any formed bundles. As reported by Schneider *et al.*, you can also use 1,10-phenantroline to stabilize your dispersions.[35]

■ **PAUSE POINT** The characterization of the dispersion can be delayed if you do not want to immediately recycle your pellets. Otherwise, you have to at least measure an absorption spectrum.

? TROUBLESHOOTING

Cleaning the Shear Force Mixer ● TIMING 30 min

! CAUTION Wear gloves when handling parts of the Shear Force Mixer that were in direct contact with the nanotube dispersion

31 After the SFM has stopped, remove the metal aglet that connects rotor and stator by pushing it out with a suitable rod-shaped object. The rotor should now fall out. Disassemble the rest of the SFM. You will notice black stains on the parts of stator and rotor that were immersed in the nanotube dispersion. Try to remove them with IPA-wetted wipes. This works very well for the rotor and the outside of the stator.
? TROUBLESHOOTING

32 Clean the inside of the stator with IPA and a test tube brush of suitable thickness.

33 Immerse the stator in a measuring cylinder and fill it with toluene until all nanotube stains are covered. Place the measuring cylinder in an ultrasonication bath and sonicate for 15 mins

34 Remove the stator from the measuring cylinder and discard the dirty toluene. Rinse both, stator and measuring cylinder, with toluene.

35 After letting stator and rotor dry, reassemble the Shear Force Mixer as shown in **Figure 7**.
▲CRITICAL If any IPA is left and gets into the next dispersion, it will cause severe aggregation problems.

Recycling of pelletized material ● TIMING 30 min

▲CRITICAL Running the shear force mixing procedure once does not exfoliate all the (6,5) SWNTs contained in the CoMoCAT® raw material. The pellets will still contain lots of (6,5) SWNTs and can usually be recycled 3-4 times before you have to use fresh SWNT material.

▲CRITICAL For recycling of the pelletized material, you have two options. You can either directly recycle the pellets after centrifugation (see steps 36-38) or you can let them dry (steps 39-41)

36 After step 26, a pellet of unexfoliated material, that still contains (6,5) SWNTs and a few millilitres of supernatant are left in the centrifuge tubes. Pour the remaining supernatant back into the Erlenmeyer flask. With toluene from a squeeze bottle, loosen the pellet and pour it back into the Erlenmeyer flask.

37 The pellet will contain some polymer but new polymer should be added. The extinction coefficient of PFO-BPy for the band at 363 nm is 96.4 ± 0.2 mL(mg cm)$^{-1}$ (see **Figure S3**). An absorption spectrum of the dispersion you obtained from the process that yielded the pellets should be measured.

►REFER TO Characterization (step 42)

38 The amount of to-be-added polymer is now calculated with:

$$m_{Polymer} = \frac{A_{363\ nm} \cdot V_{dispersion}}{\varepsilon_{363\ nm} \cdot d_{cuvette}}$$

▲CRITICAL As PFO-BPy is very selective towards (6,5) SWNTs and small variations of concentration won't influence your selectivity, you can roughly estimate $V_{dispersion}$.

38 Add the calculated amount of PFO-BPy to the Erlenmeyer flask that contains the pellets. Fill it with toluene until you have a total volume of ~200 mL in the flask. From here on, follow steps 14-35.

39 Instead of directly recycling the pelletized material, the pellets can be dried for use at a later point. The remaining supernatant should be removed and the centrifuge tubes with the pellets should be left open for drying for ~3 days.

40 Remove the dried pellets from the centrifuge tubes with a spatula and put them in a container. For longer storage times, store them in a dry environment.

■ PAUSE POINT You can store the pellets for several months before reusing them.

41 To recycle the dried pellets, calculate the amount of polymer you need to add as explained in step 37 and 38. Add the dried pellets, the polymer and ~200 mL of toluene to an Erlenmeyer flask. Follow steps 14-35 from here.

Characterization of dispersions ● TIMING **2 h**

▲CRITICAL UV-vis-NIR absorption and resonant Raman spectroscopy are used to check whether the selective dispersion of (6,5) SWNTs was successful without dispersing any other semiconducting or metallic nanotube species.

42 Measure an absorption spectrum of the dispersion in the range between 300-1600 nm. It should look as shown in **Figure 10** with SWNT-related peaks at 1000 nm (E_{11}), ~900 nm (phonon side band, PSB), 575 nm (E_{22}) and a peak at 363 nm originating from PFO-BPy.

▲CRITICAL To obtain a useful value for the polymer peak at 360 nm, you might have to dilute the dispersion. It should have an absorption of less than 2 cm^{-1} in order to calculate the amount of polymer you need to add during recycling.

? TROUBLESHOOTING

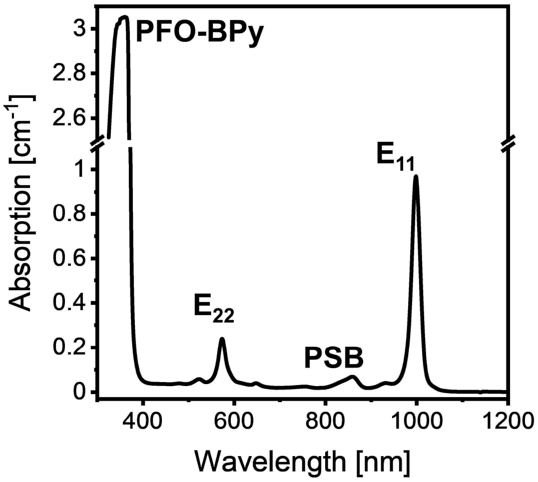

Figure 10. Absorption spectrum of a monochiral (6,5) SWNT dispersion obtained by Shear Force Mixing. The dominant peaks (E_{11}, PSB, E_{22}, PFO-BPy) are marked in the spectrum.

43 For Raman measurements, drop-cast the dispersion onto a coverslip coated with aluminum foil to form a film (**Note**: aluminum-foil shows no Raman signal at all). The film should have a visible purple colour to obtain sufficient signal without too much integration. To avoid a background from excess PFO-BPy, you can remove it by carefully rinsing the film with toluene or THF. To check for other SWNT chiralities, especially metallic nanotubes, the region between 200-320 cm^{-1}, in which SWNTs show the diameter dependent radial breathing mode, has to be investigated. (6,5) SWNTs can be efficiently excited with a 532 or 785 nm laser. To account for spot-to-spot variations in the drop-cast sample, we measure at least 200 spectra at different positions (square grid) and average them. **Figure 11a** shows a spectrum of a drop-cast dispersion that only contains (6,5) SWNTs, while **Figure 11b** was measured on a dispersion that also contained metallic SWNT chiralities.

? TROUBLESHOOTING

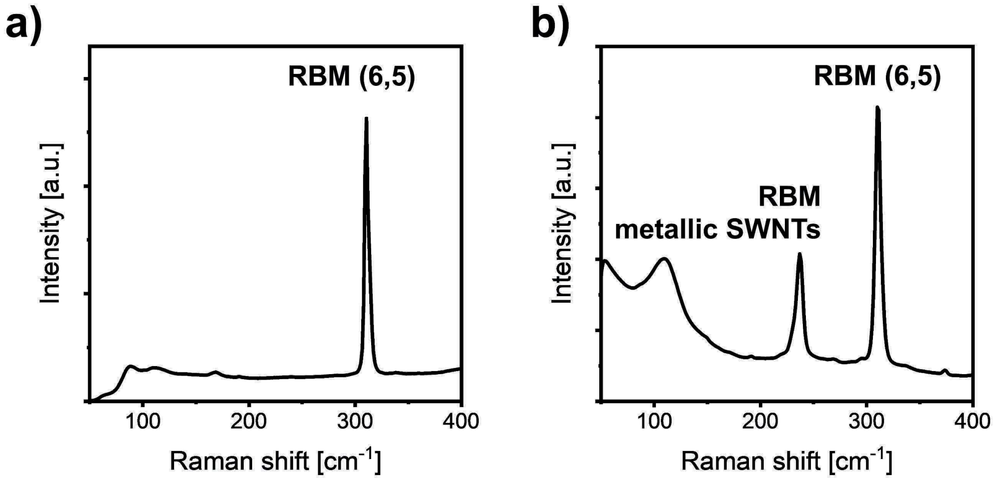

Figure 11. a) Raman spectrum of a monochiral (6,5) SWNT dispersion without contamination of metallic nanotubes as indicated by the absence of peaks aside from the RBM at 310 cm^{-1}. **b)** Raman spectrum of a (6,5) SWNT dispersion with a large content of metallic tubes. Metallic tubes lead to a peak at ~240 cm^{-1} (usually not as pronounced as in this case). Both samples were excited with a 532 nm laser.

TROUBLESHOOTING

TROUBLESHOOTING Step 19

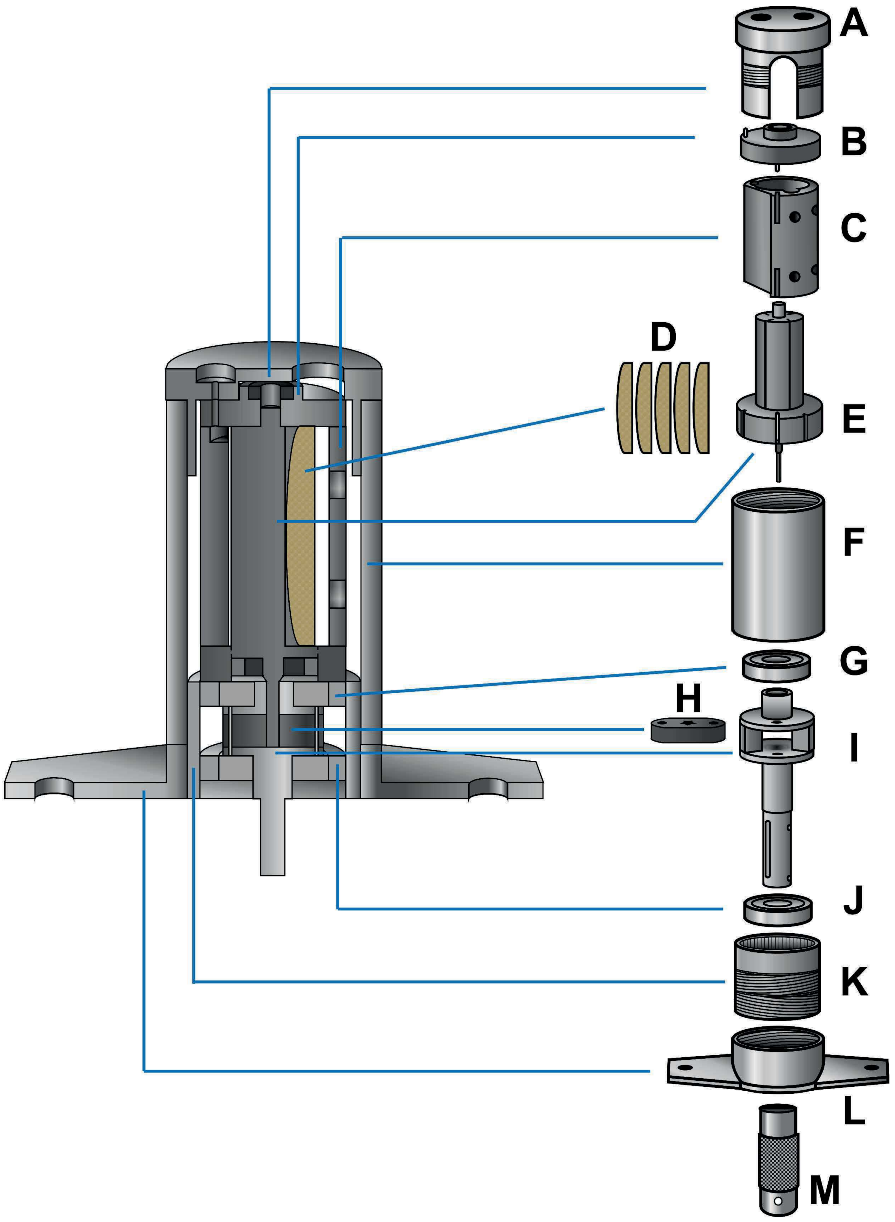

Figure 12. Cross section of the assembled motor unit and explosion drawing. In the explosion drawing all the parts are in the correct order for assembly. The motor unit consists of lid (B), stator (C), vanes (D) and rotor (E). The rounded site of the vanes is oriented towards the centre of the rotor. The rotor is connected to a shaft (I) *via* an aglet (H). To ensure smooth rotation of the shaft, two identical ball bearings (G and J) hold it inside the housing that consists of a lid (A), a housing (F) and a bottom part (K, L). Mounting the adapter (M) to the shaft (I) allows for connection to the rotor of the Shear Force Mixer. Note that all threads in the motor are left-handed threads.

? The pitch of the noise that the motor produces is not uniform.

Most likely origin: The noise is produced by moving parts inside the motor. The air-driven motor of the shear force mixer has five vanes (**D**), that grind down against the motor housing (**C**). Over time, a significant amount of debris builds up inside of the SFM (**Figure 13**). This debris can cause irregular motion of the motor unit, which leads to a non-uniform pitch of the whining noise.

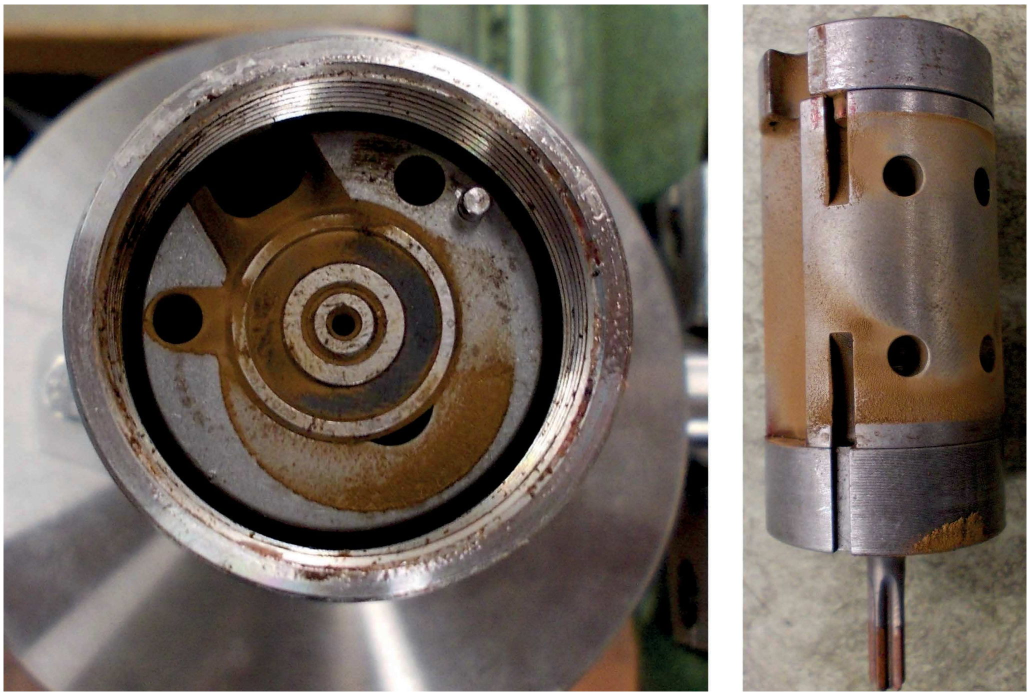

Figure 13. Motor with significant amount of debris (left: after unscrewing lid (A), right: only motor unit (B-E)). The debris can be removed with pressurized air and a damp towel.

Solution: The motor unit must be disassembled and cleaned. **Figure 12** might help to understand the how to disassemble (and later reassemble) the motor unit. Once disassembled, clean dirty parts with pressurized air from the orange-brown debris.

? The shear force mixer does not move at all or gets stuck regularly although you can hear air flushing through it.

Most likely origin: The air-driven motor of the shear force mixer has five vanes, that grind down against the motor housing. After several months of continuous usage, the vanes are significantly smaller than in the beginning (see **Figure 14**) and can fall out of their respective slits which will prevent rotation.

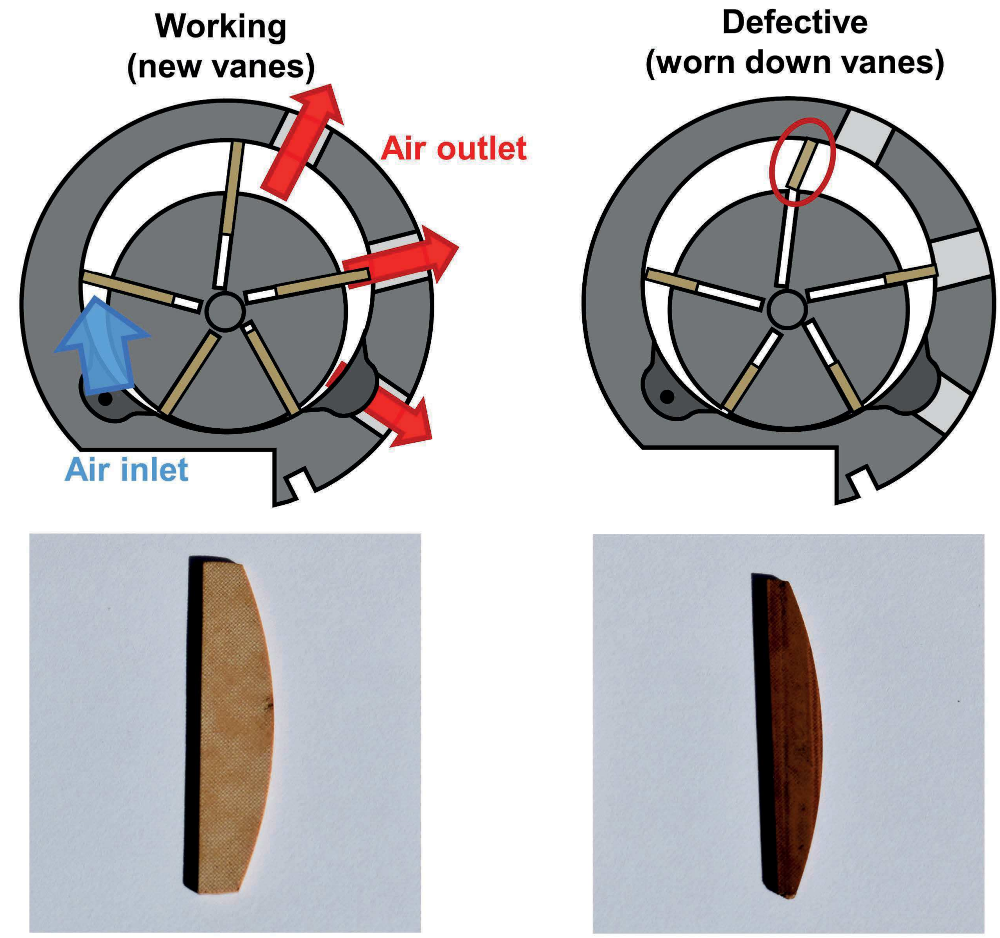

Figure 14. The top panel shows a schematic depiction of the working principle of an air-driven vane motor with new vanes (left) and significantly worn-down vanes (right) that can cause problems during operation. The picture of the vanes (bottom panel) shows a drastic change in vane size and shape.

Additionally, the metal parts will wear down over time. Especially the connection between motor and rotor (Parts E and H/I in **Figure 12**) is prone to failure after intensive use.

Solution: When the vanes are worn-down, you have to exchange them. A **repair kit**, that includes 5 vanes, gaskets and ball bearings can be ordered from Atlas Copco. In case of worn-down metal parts, a new motor unit must be ordered from Silverson.

? **There are “scratching” noises.**

Most likely origin: The rotor grinds against the stator.

Solution: The PTFE bush (**Figure 3b**, **D**) that stabilizes the rotor in the stator must be replaced every few months to prevent this issue from happening. The brushes can be ordered individually from Silverson.

TROUBLESHOOTING Step 26

? **The supernatant does not show any colour.**

Most likely origin: There are no nanotubes dispersed or the dispersion was not stable. This can have several causes:

- High humidity during dispersion
- Too little polymer
- Temperature was not controlled sufficiently

Solution: Check that your chiller works sufficiently and that you regularly empty the dehumidifiers. In case of very humid conditions, even the dehumidifiers might fail. For possible recycling runs, consider adding more polymer.

? **There still is unexfoliated, non-pelletized material floating in the dispersion.**

Most likely origin: The centrifugation process is not yet complete.

Solution: Try to centrifuge for another 15 min. Make sure that you move the centrifuge tubes as little as possible when removing them from the centrifuge.

? **The supernatant is purple but also shows a greyish colour.**

Most likely origin: This indicates either a non-complete sedimentation (see above) or exfoliation of metallic SWNTs.

Solution: Reduce the amount of polymer in the next (recycling) run.

TROUBLESHOOTING Step 30

? **When using a syringe filter, there is significant resistance when pushing the dispersion through it and/or the syringe filter turns purple.**

Most likely origin: The nanotube dispersion has started aggregating and nanotube aggregates clog the PTFE filter.

Solution: If you need to use a syringe filter, try sonicating the dispersion for 5 minutes and filter immediately after sonication.

TROUBLESHOOTING Step 31

? **The rotor gets stuck when trying to remove it from the stator.**

Most likely origin: Debris from the vanes obstructs the rotor movement.

Solution: Remove the rotor together with the stator by removing the metal aglet and the conical screws/nuts that fixate the stator. The rotor can now be pushed out of the stator. Clean both rotor and stator extensively to prevent any future problems.

TROUBLESHOOTING Step 42

? **There are additional peaks in the nIR-region of the absorption spectrum.**

Most likely origin: Additional semiconducting chiralities were dispersed. You will usually disperse very little other chiralities (*e.g.*, (7,5) SWNTs) which will be visible in Raman but should not appear in absorption spectra

Solution: Reduce the amount of polymer in the next SFM run.

? **Over a longer period of time (>3 years), a decrease in yield is observed.**

Most likely origin: During years of continuous usage, the rotor can grind against the stator and thus enlarges the distance between them. This, in turn, leads to a decrease in shear force and thus a lower dispersion efficiency. We saw a substantial decrease after ~4 years of heavy usage (see **Figure 15**)

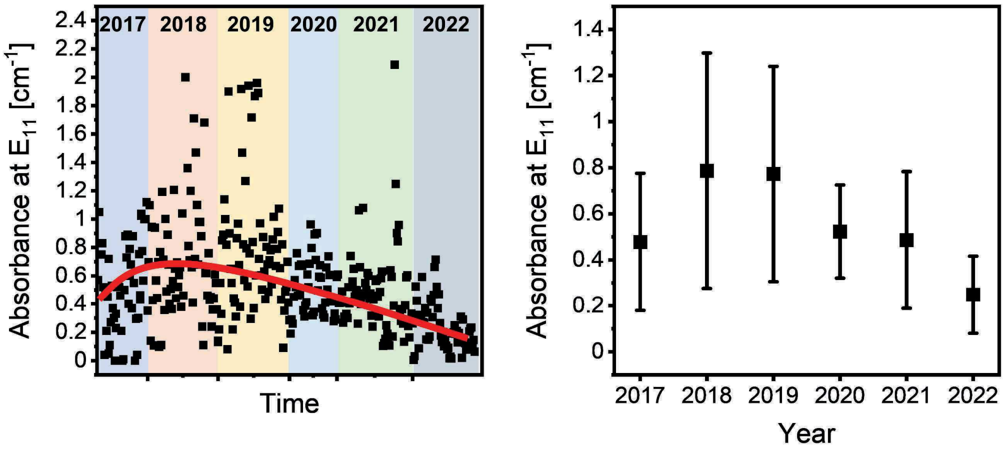

Figure 15. Evolution of the absorbance of (6,5) SWNT dispersions at the E_{11} over several years in the Zaumseil group. The dispersions plotted here were obtained from the same shear force mixer. Left: all data points, right: averaged over the entire year.

Solution: A new rotor and shear head must be bought from Silverson. **Note**, you only have to replace the detachable shear head (E in **Figure 3**) and not the whole stator.

TROUBLESHOOTING Step 43

? **There is only a broad background and no nanotube signals.**

Most likely origin: The sample has a high polymer-to-nanotube ratio.

Solution: Drop-cast a thicker film and carefully wash away excess amounts of polymer with THF.

? **Additional peaks between 200-250 cm^{-1} appear**

Most likely origin: Metallic SWNTs have been exfoliated

Solution: Reduce the amount of polymer in the next SFM run.

? **There is an additional peak at ~280 cm^{-1}**

Most likely origin: (7,5) SWNTs have been exfoliated.

Solution: A small amount of (7,5) SWNTs is usually dispersed. A small peak is nothing to worry about. If the peak is substantial, reduce the amount of polymer in your next run

REFERENCES

1. Chen, Y.; Zhang, Y.; Hu, Y.; Kang, L.; Zhang, S.; Xie, H.; Liu, D.; Zhao, Q.; Li, Q.; Zhang, J., State of the Art of Single-Walled Carbon Nanotube Synthesis on Surfaces. *Advanced Materials* **2014,** *26* (34), 5898-5922.

2. Zhao, X.; Zhang, S.; Zhu, Z.; Zhang, J.; Wei, F.; Li, Y., Catalysts for single-wall carbon nanotube synthesis—From surface growth to bulk preparation. *MRS Bulletin* **2017,** *42* (11), 809-818.

3. Moore, V. C.; Strano, M. S.; Haroz, E. H.; Hauge, R. H.; Smalley, R. E.; Schmidt, J.; Talmon, Y., Individually Suspended Single-Walled Carbon Nanotubes in Various Surfactants. *Nano Letters* **2003,** *3* (10), 1379-1382.

4. Coleman, J. N., Liquid-Phase Exfoliation of Nanotubes and Graphene. *Advanced Functional Materials* **2009,** *19* (23), 3680-3695.

5. Zheng, M.; Jagota, A.; Semke, E. D.; Diner, B. A.; McLean, R. S.; Lustig, S. R.; Richardson, R. E.; Tassi, N. G., DNA-assisted dispersion and separation of carbon nanotubes. *Nature Materials* **2003,** *2* (5), 338-342.

6. Pramanik, D.; Maiti, P. K., DNA-Assisted Dispersion of Carbon Nanotubes and Comparison with Other Dispersing Agents. *ACS Applied Materials & Interfaces* **2017,** *9* (40), 35287-35296.

7. Fagan, J. A., Aqueous two-polymer phase extraction of single-wall carbon nanotubes using surfactants. *Nanoscale Advances* **2019,** *1* (9), 3307-3324.

8. Li, H.; Gordeev, G.; Garrity, O.; Reich, S.; Flavel, B. S., Separation of Small-Diameter Single-Walled Carbon Nanotubes in One to Three Steps with Aqueous Two-Phase Extraction. *ACS Nano* **2019,** *13* (2), 2567-2578.

9. Arnold, M. S.; Green, A. A.; Hulvat, J. F.; Stupp, S. I.; Hersam, M. C., Sorting carbon nanotubes by electronic structure using density differentiation. *Nature Nanotechnology* **2006,** *1* (1), 60-65.

10. Liu, H.; Nishide, D.; Tanaka, T.; Kataura, H., Large-scale single-chirality separation of single-wall carbon nanotubes by simple gel chromatography. *Nature Communications* **2011,** *2* (1), 309.

11. Nish, A.; Hwang, J.-Y.; Doig, J.; Nicholas, R. J., Highly selective dispersion of single-walled carbon nanotubes using aromatic polymers. *Nature Nanotechnology* **2007,** *2* (10), 640-646.

12. Stürzl, N.; Hennrich, F.; Lebedkin, S.; Kappes, M. M., Near Monochiral Single-Walled Carbon Nanotube Dispersions in Organic Solvents. *The Journal of Physical Chemistry C* **2009,** *113* (33), 14628-14632.

13. Tange, M.; Okazaki, T.; Iijima, S., Selective Extraction of Large-Diameter Single-Wall Carbon Nanotubes with Specific Chiral Indices by Poly(9,9-dioctylfluorene-alt-benzothiadiazole). *Journal of the American Chemical Society* **2011,** *133* (31), 11908-11911.

14. Jakubka, F.; Schießl, S. P.; Martin, S.; Englert, J. M.; Hauke, F.; Hirsch, A.; Zaumseil, J., Effect of Polymer Molecular Weight and Solution Parameters on Selective Dispersion of Single-Walled Carbon Nanotubes. *ACS Macro Letters* **2012,** *1* (7), 815-819.

15. Mistry, K. S.; Larsen, B. A.; Blackburn, J. L., High-Yield Dispersions of Large-Diameter Semiconducting Single-Walled Carbon Nanotubes with Tunable Narrow Chirality Distributions. *ACS Nano* **2013,** *7* (3), 2231-2239.

16. Grimm, S.; Schießl, S. P.; Zakharko, Y.; Rother, M.; Brohmann, M.; Zaumseil, J., Doping-dependent G-mode shifts of small diameter semiconducting single-walled carbon nanotubes. *Carbon* **2017,** *118*, 261-267.

17. Imin, P.; Cheng, F.; Adronov, A., The effect of molecular weight on the supramolecular interaction between a conjugated polymer and single-walled carbon nanotubes. *Polymer Chemistry* **2011,** *2* (6), 1404-1408.

18. Ding, J.; Li, Z.; Lefebvre, J.; Cheng, F.; Dubey, G.; Zou, S.; Finnie, P.; Hrdina, A.; Scoles, L.; Lopinski, G. P.; Kingston, C. T.; Simard, B.; Malenfant, P. R. L., Enrichment of large-diameter semiconducting SWCNTs by polyfluorene extraction for high network density thin film transistors. *Nanoscale* **2014,** *6* (4), 2328-2339.

19. Hwang, J.-Y.; Nish, A.; Doig, J.; Douven, S.; Chen, C.-W.; Chen, L.-C.; Nicholas, R. J., Polymer Structure and Solvent Effects on the Selective Dispersion of Single-Walled Carbon Nanotubes. *Journal of the American Chemical Society* **2008,** *130* (11), 3543-3553.

20. Qian, L.; Xu, W.; Fan, X.; Wang, C.; Zhang, J.; Zhao, J.; Cui, Z., Electrical and Photoresponse Properties of Printed Thin-Film Transistors Based on Poly(9,9-dioctylfluorene-co-bithiophene) Sorted Large-Diameter Semiconducting Carbon Nanotubes. *The Journal of Physical Chemistry C* **2013,** *117* (35), 18243-18250.

21. Sun, Z.; O'Connor, I.; Bergin, S. D.; Coleman, J. N., Effects of Ambient Conditions on Solvent−Nanotube Dispersions: Exposure to Water and Temperature Variation. *The Journal of Physical Chemistry C* **2009,** *113* (4), 1260-1266.

22. Lee, H. W.; Yoon, Y.; Park, S.; Oh, J. H.; Hong, S.; Liyanage, L. S.; Wang, H.; Morishita, S.; Patil, N.; Park, Y. J.; Park, J. J.; Spakowitz, A.; Galli, G.; Gygi, F.; Wong, P. H. S.; Tok, J. B. H.; Kim, J. M.; Bao, Z., Selective dispersion of high purity semiconducting single-walled carbon nanotubes with regioregular poly(3-alkylthiophene)s. *Nature Communications* **2011,** *2* (1), 541.

23. Gomulya, W.; Salazar Rios, J. M.; Derenskyi, V.; Bisri, S. Z.; Jung, S.; Fritsch, M.; Allard, S.; Scherf, U.; dos Santos, M. C.; Loi, M. A., Effect of temperature on the selection of semiconducting single walled carbon nanotubes using Poly(3-dodecylthiophene-2,5-diyl). *Carbon* **2015,** *84*, 66-73.

24. Samanta, S. K.; Fritsch, M.; Scherf, U.; Gomulya, W.; Bisri, S. Z.; Loi, M. A., Conjugated Polymer-Assisted Dispersion of Single-Wall Carbon Nanotubes: The Power of Polymer Wrapping. *Accounts of Chemical Research* **2014,** *47* (8), 2446-2456.

25. Fong, D.; Adronov, A., Recent developments in the selective dispersion of single-walled carbon nanotubes using conjugated polymers. *Chemical Science* **2017,** *8* (11), 7292-7305.

26. Hertel, T.; Himmelein, S.; Ackermann, T.; Stich, D.; Crochet, J., Diffusion Limited Photoluminescence Quantum Yields in 1-D Semiconductors: Single-Wall Carbon Nanotubes. *ACS Nano* **2010,** *4* (12), 7161-7168.

27. Zorn, N. F.; Zaumseil, J., Charge transport in semiconducting carbon nanotube networks. *Applied Physics Reviews* **2021,** *8* (4).

28. Zheng, W.; Zorn, N. F.; Bonn, M.; Zaumseil, J.; Wang, H. I., Probing Carrier Dynamics in sp3-Functionalized Single-Walled Carbon Nanotubes with Time-Resolved Terahertz Spectroscopy. *ACS Nano* **2022,** *16* (6), 9401-9409.

29. Hennrich, F.; Krupke, R.; Arnold, K.; Rojas Stütz, J. A.; Lebedkin, S.; Koch, T.; Schimmel, T.; Kappes, M. M., The Mechanism of Cavitation-Induced Scission of Single-Walled Carbon Nanotubes. *The Journal of Physical Chemistry B* **2007,** *111* (8), 1932-1937.

30. Mouri, S.; Miyauchi, Y.; Matsuda, K., Dispersion-Process Effects on the Photoluminescence Quantum Yields of Single-Walled Carbon Nanotubes Dispersed Using Aromatic Polymers. *The Journal of Physical Chemistry C* **2012,** *116* (18), 10282-10286.

31. Paton, K. R.; Varrla, E.; Backes, C.; Smith, R. J.; Khan, U.; O'Neill, A.; Boland, C.; Lotya, M.; Istrate, O. M.; King, P.; Higgins, T.; Barwich, S.; May, P.; Puczkarski, P.; Ahmed, I.; Moebius, M.; Pettersson, H.; Long, E.; Coelho, J.; O'Brien, S. E.; McGuire, E. K.; Sanchez, B. M.; Duesberg, G. S.; McEvoy, N.; Pennycook, T. J.; Downing, C.; Crossley, A.; Nicolosi, V.; Coleman, J. N., Scalable production of large quantities of defect-free few-layer graphene by shear exfoliation in liquids. *Nature Materials* **2014,** *13* (6), 624-630.

32. Varrla, E.; Backes, C.; Paton, K. R.; Harvey, A.; Gholamvand, Z.; McCauley, J.; Coleman, J. N., Large-Scale Production of Size-Controlled MoS2 Nanosheets by Shear Exfoliation. *Chemistry of Materials* **2015,** *27* (3), 1129-1139.

33. Naumov, A. V.; Tsyboulski, D. A.; Bachilo, S. M.; Weisman, R. B., Length-dependent optical properties of single-walled carbon nanotube samples. *Chemical Physics* **2013,** *422*, 255-263.

34. Graf, A.; Zakharko, Y.; Schießl, S. P.; Backes, C.; Pfohl, M.; Flavel, B. S.; Zaumseil, J., Large scale, selective dispersion of long single-walled carbon nanotubes with high photoluminescence quantum yield by shear force mixing. *Carbon* **2016,** *105*, 593-599.

35. Schneider, S.; Lefebvre, J.; Diercks, N. J.; Berger, F. J.; Lapointe, F.; Schleicher, J.; Malenfant, P. R. L.; Zaumseil, J., Phenanthroline Additives for Enhanced Semiconducting Carbon Nanotube Dispersion Stability and Transistor Performance. *ACS Applied Nano Materials* **2020,** *3* (12), 12314-12324.

SUPPORTING INFORMATION

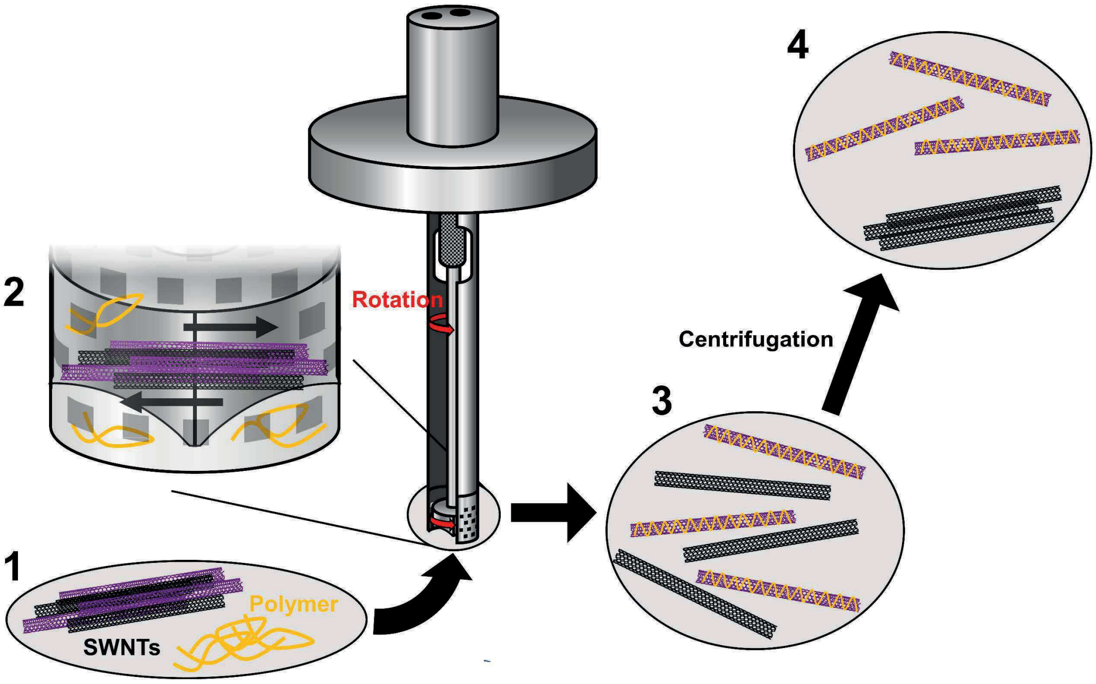

Figure S1. Working principle of a shear force mixer. During operation, the shear force mixer works like a pump. Solvent, unexfoliated SWNT raw material and polymer are sucked into the rotor/stator area where larger chunks are broken down (**1**). The fast rotation of the rotor produces centrifugal forces that push solids and solvent towards the edge of the shear screen. During this process the SWNTs are pushed out of the square holes in the screen, high shear forces act on the nanotube bundles and break them up (**2**). The polymer can now wrap around the exfoliated nanotubes but only stabilizes certain nanotube types, others re-aggregate instantly (**3**). These reaggregated SWNTs will be removed during the centrifugation step (**4**).

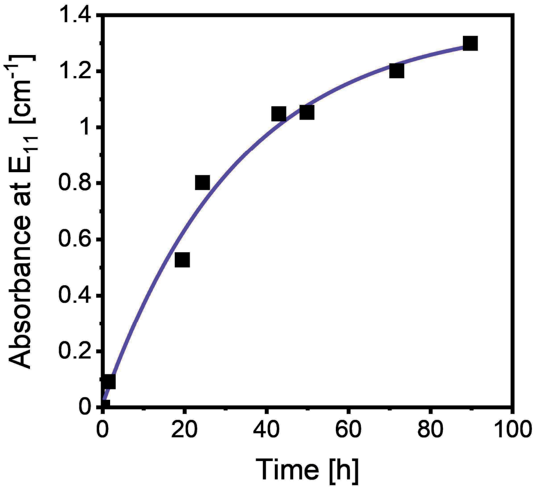

Figure S2. Relationship between duration of shear force mixing and dispersion yield. The data were obtained from Graf *et al.*[S1]

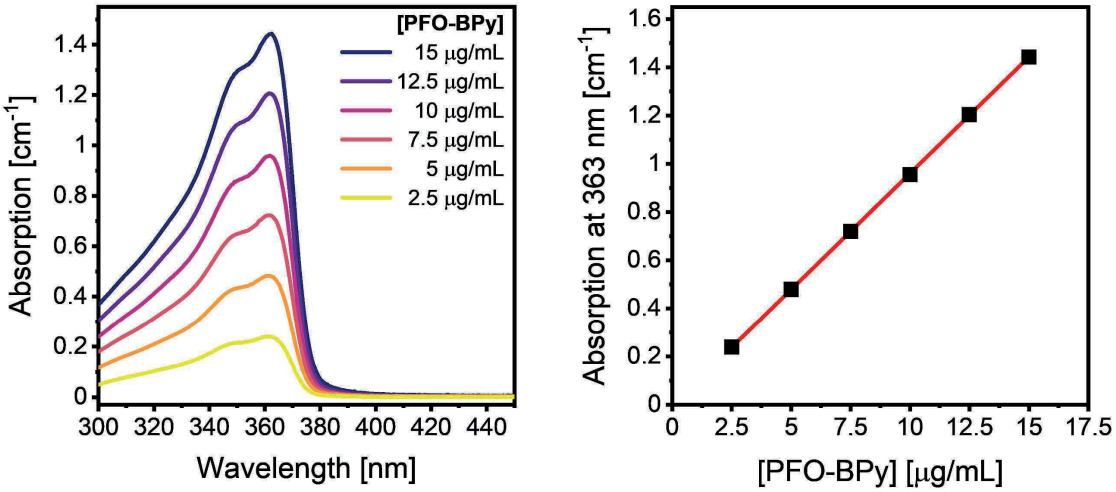

Figure S3. a) UV-Vis absorption spectra of PFO-BPy solutions in toluene. **b)** Lambert-Beer plot of the absorption (1 cm cuvette) at the absorption maximum at 363 nm against PFO-BPy concentration.

APPENDIX I: REQUIRED CHANGES FOR DISPERSION OF (7,5) SWNTs

Raw Materials

For (7,5) SWNTs a combination of CoMoCAT® raw material and poly[9,9-dioctylfluorene-2,7-diyl] (PFO) is used. The raw materials, that we use, are:

- **CoMoCAT® raw material** (Sigma-Aldrich, 773735, (6,5) chirality, ≥95% carbon basis (≥95% as carbon nanotubes), 0.78 nm average diameter)
- **poly[9,9-dioctylfluorenyl-2,7-diyl]** (PFO, Sigma-Aldrich, $M_W > 20$ kg mol^{-1})

Polymer Concentration

Precise control over the polymer concentration is necessary in the dispersion process of (7,5) SWNTs to obtain monochiral dispersions, as shown by the absorption data in **Figure S4a**.

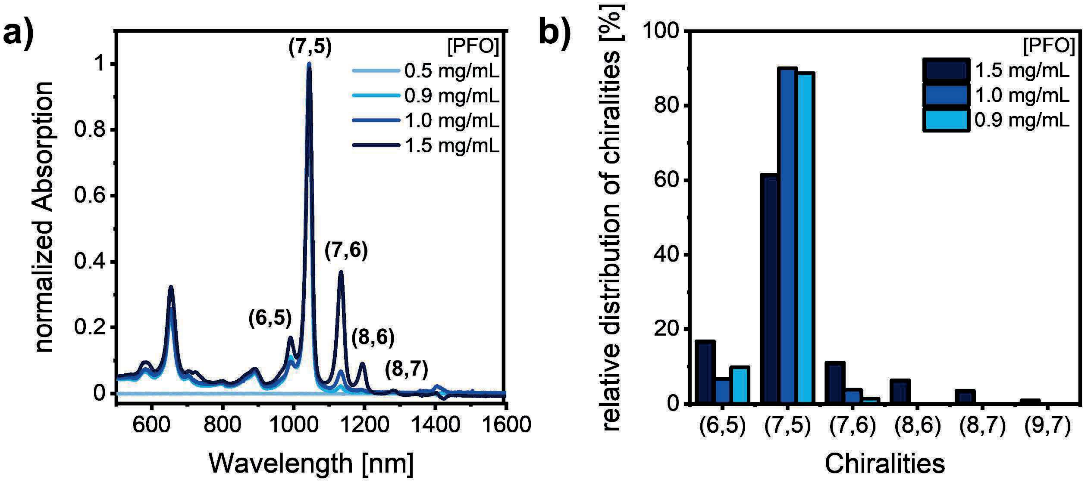

Figure S4. a) Absorption spectra of nanotube dispersions obtained by shear force mixing of CoMoCAT® raw material with varying PFO concentrations. b) Relative distribution of nanotube chiralities for varying PFO concentrations calculated with the script by Pfohl *et al.*[S2] [DOI: 10.1021/acsomega.6b00468] and experimentally determined extinction coefficients.

While insufficient polymer concentration (0.5 mg/mL) prevents any dispersion of nanotubes, a very high concentration (1.5 mg/mL) leads to dispersion of additional nanotube chiralities. Using the script by Pfohl *et al.*[S2] and experimentally determined extinction coefficients,[S3] which vary between nanotube chiralities, the relative chirality distribution can be calculated (see **Figure S4b**). The highest chiral purity (>90 %) is achieved for PFO concentrations of 0.9 and 1.0 mg/mL. Raman spectroscopy, however, reveals that for 1.0 mg/mL some metallic nanotubes are still exfoliated (see **Figure S5**).

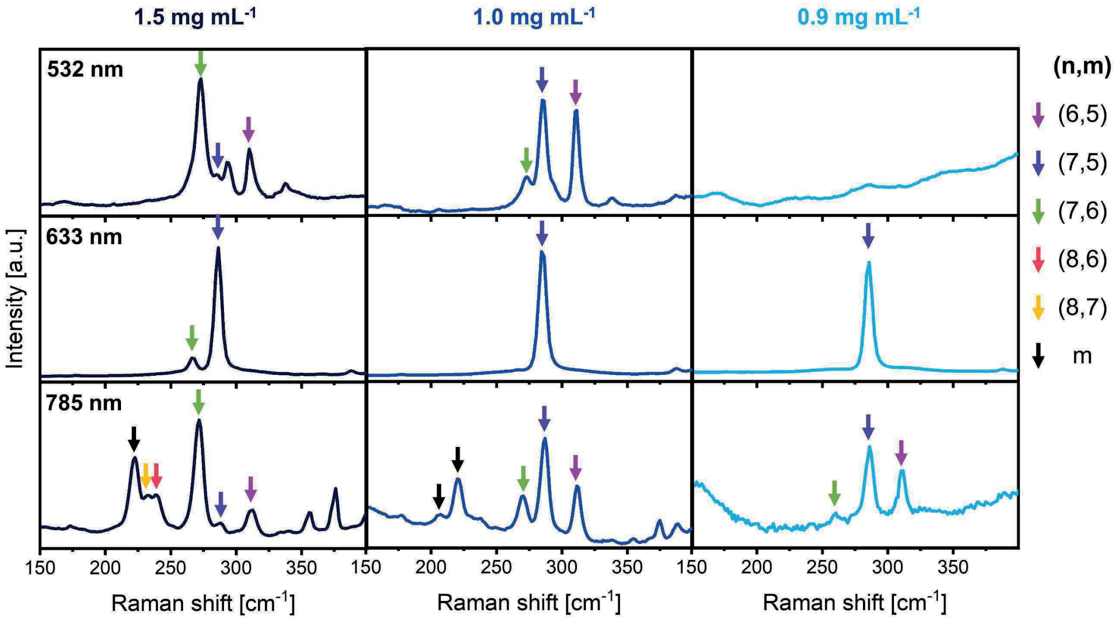

Figure S5. Raman spectra of drop-cast dispersions of CoMoCAT® nanotubes exfoliated with different PFO concentrations (1.5, 1.0 and 0.9 mg/mL) in toluene. Three different excitation lasers (532 nm, 633 nm and 785 nm) were employed to reveal as many chiralities as possible. RBMs of identified chiralities are marked with colored arrows.

Despite the reduced yield, we recommend using 0.9 mg/mL instead of 1.0 mg/mL as the PFO concentration to obtain electronic-grade dispersions with a high chiral purity.

Recycling

As the polymer concentration is such an important parameter for dispersions of (7,5) SWNTs, one has to ensure the addition of the right amount of PFO for recycling. The extinction coefficient of PFO was determined to be 96.1 ± 0.2 mL(mg cm)$^{-1}$ (see **Figure S6**). The amount of polymer to be added is calculated in the same way as described in the protocol for (6,5) SWNTs.

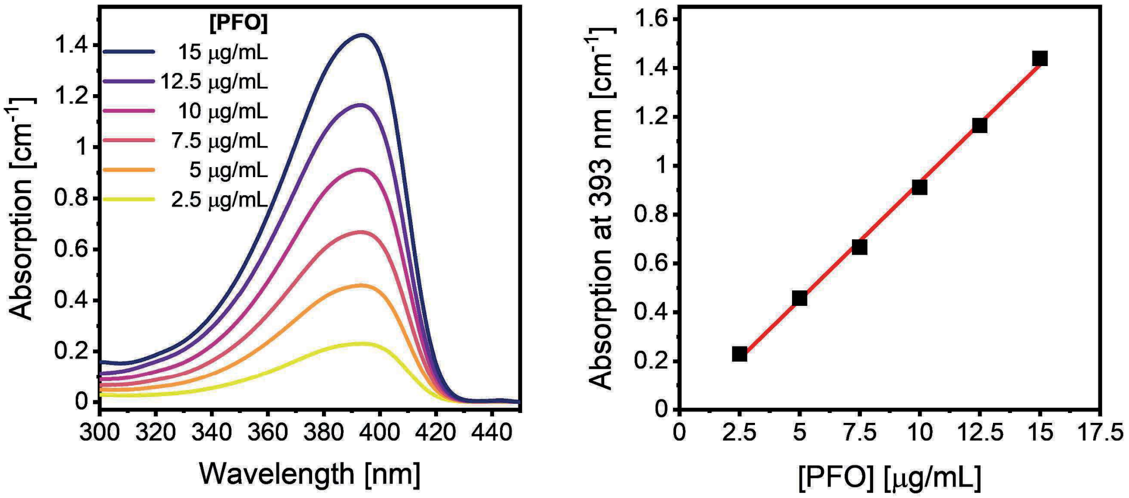

Figure S6. a) UV-vis absorption spectra of PFO solutions in toluene. **b)** Lambert-Beer plot of the absorption (1 cm cuvette) at the absorption maximum at 393 nm against PFO concentration.

Characterization

The CoMoCAT® raw material contains significantly less (7,5) than (6,5) SWNTs. Thus, the overall dispersion yield will be lower than for dispersions for (6,5) SWNTs (usually the absorption at the E_{11} peak is below 0.2 cm^{-1}). To check for other nanotube chiralities or metallic nanotubes in (7,5) SWNT dispersions with Raman spectroscopy, we advise to use at least a 633 nm and a 785 nm laser.

APPENDIX II: REQUIRED CHANGES FOR DISPERSION OF PLASMA TORCH SWNTs

Raw Materials

For the dispersion of only semiconducting Plasma Torch SWNTs, a combination of Plasma Torch nanotubes and PFO-BPy is used:

- **Plasma Torch SWNT raw material** (Raymor Industries Inc., RN-220, diameter 0.9-1.5 nm, batch RNB739-220-161220-A329)
- **Poly[(9,9-dioctylfluorenyl-2,7-diyl)-alt-(6,6′-[2,2′-bipyridine])]** (American Dye Source, PFO-BPy, ADS153UV, M_w ~ 34 000 g/mol)

SWNT concentration

As the Plasma Torch raw material has a lower SWNT content compared to the CoMoCAT® raw material, we use 1.5 mg/mL instead of 0.5 mg/mL of raw material. The polymer concentration remains unaltered at 0.5 mg/mL.

Purification

The higher nanotube concentration will lead to bigger pellets, that tend to break apart more easily. Pay extra attention when removing the supernatant after the first centrifugation step. Additionally, Plasma Torch SWNTs tend to reaggregate quickly. Work fast once you stopped shear force mixing, to prevent sedimentation during the centrifugation. Do not use a syringe filter as it will get clogged almost immediately and the yield is decreased significantly.

Characterization

Absorption spectra of Plasma Torch SWNT dispersions recorded between 400-1600 nm should show an E_{33}-region between 400-600 nm, an E_{22}-region between 800-1000 nm and the onset of an E_{11}-region at 1500 nm (**Figure S7**). Additional peaks between 600-800 nm are an indicator for metallic nanotubes. The residual background in this wavelength range should be as low as possible.

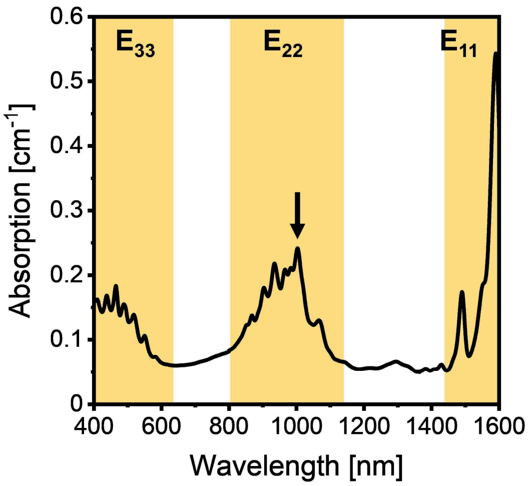

Figure S7. Absorption spectrum of a Plasma Torch SWNT dispersion with PFO-BPy. The absence of peaks in the range of 600-800 nm indicates a high semiconducting purity.

The arrow in **Figure S7** indicates the highest E_{22} transition. The absorption value at this transition multiplied by 10 can be used to roughly compare the concentration of the obtained Plasma Torch dispersions to (6,5) and (7,5) SWNT dispersions.

Raman spectra of Plasma Torch SWNT dispersions must be measured at multiple excitation wavelengths (532 nm, 633 nm and 785 nm) to check for metallic nanotubes Raman spectra of a drop-cast Plasma Torch SWNT dispersion are shown in **Figure S8**. Regions, where RBMs of metallic nanotubes are expected are shaded in grey and marked by ‘**m**’.

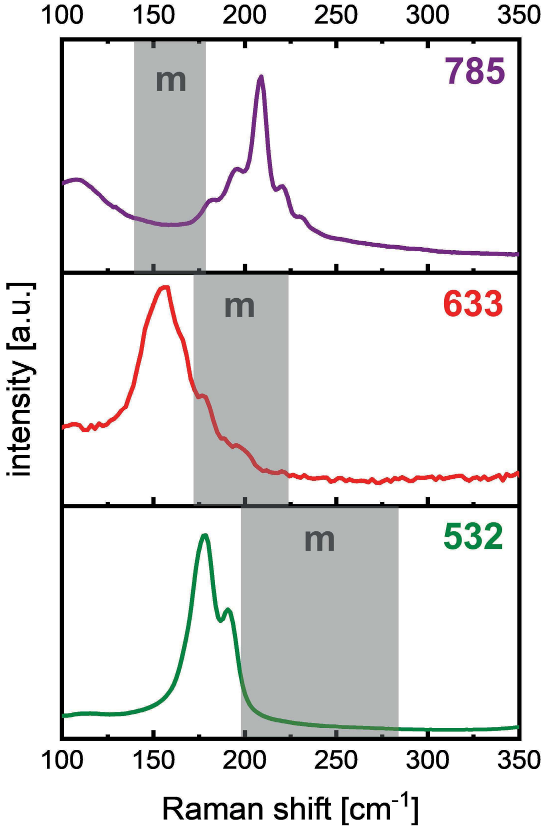

Figure S8. Raman spectra of drop-cast dispersions of semiconducting Plasma Torch SWNTs. Three different lasers (532 nm, 633 nm and 785 nm) were used for excitation to reveal as many chiralities as possible. Grey-shaded areas indicate a region where RBMs of metallic nanotubes would be expected for excitation with the respective laser.

APPENDIX III: REMOVAL OF EXCESS POLYMER

High polymer concentrations (≥ 0.5 mg/mL) are necessary to selectively disperse nanotubes and help to stabilize the resulting dispersions. In processes such as sp^3-functionalization of SWNT dispersions or if clean SWNT films are desired, these polymer concentrations can lead to problems. Thus, we want to briefly describe how excess polymer can be removed *via* filtration (for polymer concentrations up to 1.0 mg/mL) or ultracentrifugation (for polymer concentrations >1.0 mg/mL). Note that removal of polymer will lead to very instable dispersions, that will aggregate quickly. In these cases you can add 1,10-phenantroline to your dispersions to stabilize them.[S4]

Method A: Filtration

Equipment:

- **PTFE filters** (Millipore, Omnipore Membrane Filter JHWP02500, hydrophilic PTFE Filter, 25 mm diameter, 0.1 µm pore size)
- **Glass vial** (4 mL volume)
- **Glass beaker** (250 mL volume)
- **Hotplate**
- **Ultrasonication bath** (here Branson 2510)
- **Membrane pump** (here Millipore vacuum pump WP6122050)
- **Glassware for the filtration setup as shown in Figure S9a**

Chemicals:

- **Toluene** (purity >99.7 %)

Procedure:

Fill toluene into the glass beaker and heat it to ~80°C on the hotplate. Assemble your filtration setup (**Figure S9b**). The filter should be centred above the metal mesh (**Figure S9c**). Test the setup for leaks by filtering a few millilitres of pure toluene through the PTFE membrane. If nothing leaks, fill the glass reservoir with ~25 mL of nanotube dispersion and filter it off. After this, wash the filter with ~10 mL of hot toluene. Repeat the process until you have filtered off the desired amount of nanotubes. The filtration process will get slower with the amount of nanotubes that you have already filtered off. Thus, consider filtering off large amounts of nanotubes onto several filters.

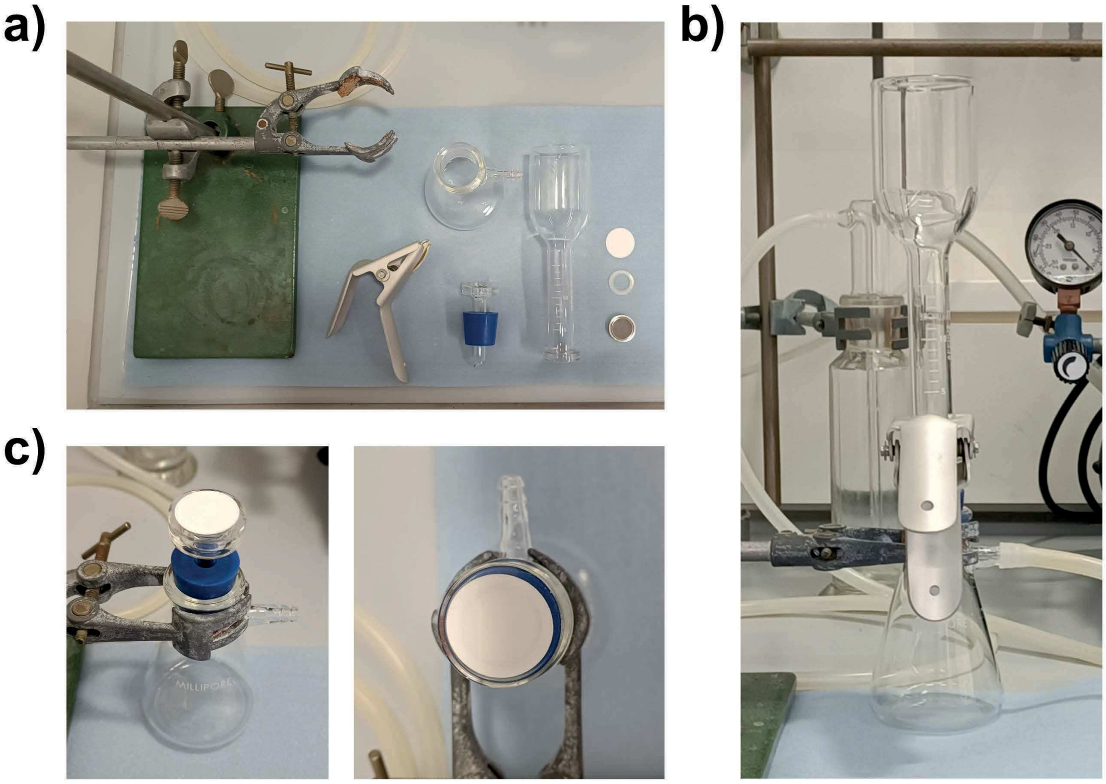

Figure S9. a) Disassembled filtration setup. **b)** Assembled filtration setup. **c)** Picture of ideal PTFE filter placement on the metal mesh.

Figure S10. a) Filter containing filtered off (6,5)-SWNTs and razor blade used for quartering the filter. **b)** Quartered filter submerged in toluene before sonication. **c)** Dark purple dispersion of (6,5)-SWNTs in toluene obtained by sonicating the vial from Figure S10b for 20 min.

Carefully remove the clamp and the glass reservoir and take off the filter. Quarter the filter using a clean razor blade (**Figure S10a**). Transfer the quarters into a 4 mL vial and add 1 – 1.5 mL of solvent. Ensure, that the filter is immersed in solvent (**Figure S10b**). Wrap the lid with parafilm to prevent water from entering the dispersion. Sonicate the vial for 20 min in the ultrasonication bath to obtain a concentrated, polymer-free dispersion of SWNTs (**Figure S10c**).

Method B: Ultracentrifugation

Equipment:

- **Ultracentrifuge** (needs to reach RCF values of at least 250000 *g*, here Optima XPN-80, Beckmann Coulter)
- **Centrifuge Tubes** (need to have acceptable resistance against toluene and THF, here 15 mL Polypropylene Centrifuge Tubes, Beckmann Coulter)
- **Ultrasonication bath** (here Branson 2510)

Chemicals:

- **Toluene** (purity >99.7 %)

Procedure:

For polymer concentrations above 1 mg/mL, PTFE filters will clog very quickly. In these cases, we use ultracentrifugation to pelletize dispersed SWNTs.

Depending on your ultracentrifuge, the sample preparation (including type of centrifuge tubes, filling level, etc.) might vary. We centrifuge our samples at 284000 *g* for 12 h using a swinging-bucket rotor (SW 40 Ti, Beckmann Coulter). The swinging-bucket rotor ensures an ideal pellet shape, which makes an unwanted stir-up less probable. After removing the centrifuge tubes from the buckets, carefully take off the supernatant and wash the pellet with THF and toluene. After washing, you can re-disperse the pelletized SWNTs in fresh solvent using an ultrasonication bath.

APPENDIX IV: TECHNICAL DRAWINGS FOR SOUNDPROOF BOX K in FIGURE 4

The soundproof box consists of an inner box (1), an outer box (2) and a door (3). The inner box is made from polyoxymethylene plates and rests on four rubber feet inside the outer box (made from plywood). The space between the boxes is filled with sound dampening rock wool.

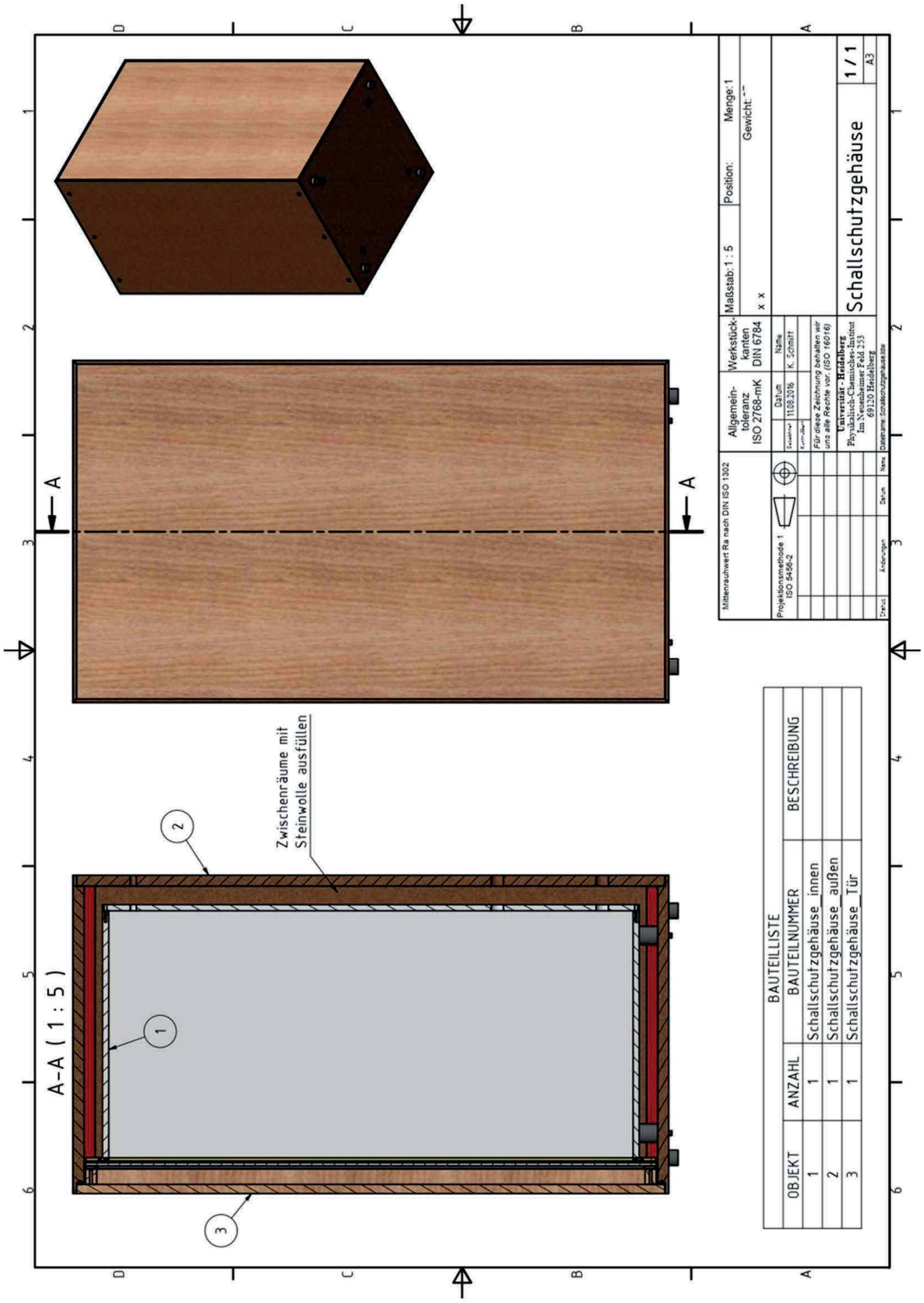

BAUTEILLISTE

OBJEKT	ANZAHL	BAUTEILNUMMER	BESCHREIBUNG
1	1	Schallschutzgehäuse_innen	
2	1	Schallschutzgehäuse_außen	
3	1	Schallschutzgehäuse_Tür	

REFERENCES SUPPORTING INFORMATION

S1. Graf, A.; Zakharko, Y.; Schießl, S. P.; Backes, C.; Pfohl, M.; Flavel, B. S.; Zaumseil, J., Large scale, selective dispersion of long single-walled carbon nanotubes with high photoluminescence quantum yield by shear force mixing. *Carbon* **2016,** *105*, 593-599.

S2. Pfohl, M.; Tune, D. D.; Graf, A.; Zaumseil, J.; Krupke, R.; Flavel, B. S. Fitting Single-Walled Carbon Nanotube Optical Spectra. *ACS Omega* **2017**, 2, 1163-1171.

S3. Sanchez, S. R.; Bachilo, S. M.; Kadria-Vili, Y.; Lin, C. W.; Weisman, R. B. (n,m)-Specific Absorption Cross Sections of Single-Walled Carbon Nanotubes Measured by Variance Spectroscopy. *Nano Lett.* **2016**, 16, 6903-6909.

S4. Schneider, S.; Lefebvre, J.; Diercks, N. J.; Berger, F. J.; Lapointe, F.; Schleicher, J.; Malenfant, P. R. L.; Zaumseil, J., Phenanthroline Additives for Enhanced Semiconducting Carbon Nanotube Dispersion Stability and Transistor Performance. *ACS Applied Nano Materials* **2020,** *3* (12), 12314-12324.

CHAPTER 4

PUBLICATION P2

Synergistic p-Doping of Polymer-Wrapped Small-Diameter Single-Walled Carbon Nanotubes by Tris(pentafluorophenyl)borane

Lindenthal, S.; Rippel, D.; Kistner, L.; Hawkey, A.; Zaumseil, J.

Journal of Physical Chemistry C **2025,** *11*, 5520-5529

https://doi.org/10.1021/acs.jpcc.4c08584

This project explores tris(pentafurophenyl)borane (BCF), which was previously used to p-dope conjugated polymers, as a new dopant for polymer-wrapped SWCNTs. We find that a unique, synergistic interaction between BCF, wrapping polymer and SWCNT enables stable, efficient doping of small diameter SWCNTs.

Formblatt Kumulative Dissertation

1. **Publikation:** Vollständige bibliographische Referenz/*Complete bibliographic reference*:

   Lindenthal, S.; Rippel, D.; Kistner, L.; Hawkey, A.; Zaumseil, J., Synergistic p-Doping of Polymer-Wrapped Small-Diameter Single-Walled Carbon Nanotubes by Tris(pentafluorophenyl)borane. *Journal of Physical Chemistry C* **2025,** *11*, 5520-5529, https://doi.org/10.1021/acs.jpcc.4c08584

2. **Erst- oder gleichberechtigte Autorenschaft/*First or equal authorship*:**

   ☒ Ja/*yes* ☐ Nein/*no*

3. **Status der Veröffentlichung/*Status of publication*:**

   ☒ Veröffentlicht/*Published*
   ☐ Zur Veröffentlichung angenommen/*Accepted*
   ☐ Eingereicht/*Submitted*
   ☐ Noch nicht eingereicht/*Not yet submitted*

4. **Beteiligungen/*Contributions***:**

	Doktorand/in/*Doctoral student*
Name, first name	**Lindenthal, Sebastian**
Methodology	**X**
Software	
Validation	**X**
Formal Analysis	**X**
Investigation	**X**
Resources	
Data Curation	**X**
Writing – Original Draft	**X**
Writing – Review & Editing	**X**
Visualization	**X**
Supervision	**X**
Project Administration	
Funding Acquisition	

****Kategorien des CRediT (*Contributor Roles Taxonomy*, https://credit.niso.org/)**

Hiermit bestätige ich, dass alle obigen Angaben korrekt sind/*I confirm that all declarations made above are correct.*

Unterschrift/*Signature* ____________
Doktorand/in/*Doctoral student*

Betreuungsperson/*Supervisor*:
Hiermit bestätige ich, dass alle obigen Angaben korrekt sind und dass die selbstständigen Arbeitsanteile des Doktoranden an der aufgeführten Publikation hinreichend und signifikant sind/*I confirm that all declarations made above are correct and that the doctoral student's independent contribution to this publication is significant and sufficient to be considered for the cumulative dissertation.*

Prof. Dr. Jana Zaumseil ____________ 27.5.2025
Name/*Name* **Unterschrift/*Signature*** **Datum/*Date***

THE JOURNAL OF
PHYSICAL
CHEMISTRY C
A JOURNAL OF THE AMERICAN CHEMICAL SOCIETY

Synergistic p-Doping of Polymer-Wrapped Small-Diameter Single-Walled Carbon Nanotubes by Tris(pentafluorophenyl)borane

Sebastian Lindenthal, Daniel Rippel, Lucas Kistner, Angus Hawkey, and Jana Zaumseil*

Cite This: *J. Phys. Chem. C* 2025, 129, 5520−5529

Read Online
ACCESS | Metrics & More | Article Recommendations | Supporting Information

ABSTRACT: Despite its comparatively low electron affinity, tris(pentafluorophenyl)borane (BCF) has been widely explored as an efficient molecular p-dopant for semiconducting polymers through the formation of Brønsted acidic complexes as well as its high affinity toward Lewis-basic nitrogen moieties. Many conjugated polymers that are used for selective wrapping and dispersion of semiconducting single-walled carbon nanotubes (SWCNTs) such as poly[(9,9-di-*n*-octylfluorenyl-2,7-diyl)-*alt*-(6,6′-(2,2′-bipyridine))] (PFO-BPy) contain nitrogen moieties that should promote interaction with BCF. Here, we demonstrate that BCF indeed efficiently p-dopes even small-diameter (6,5) SWCNTs that are wrapped with large-bandgap PFO-BPy as corroborated by bleaching of the main absorption peaks and the appearance of red-shifted trion absorption and emission. In contrast, SWCNTs that are wrapped with poly(9,9-di-*n*-octylfluorenyl-2,7-diyl) (PFO) without any Lewis-basic nitrogen moieties are only mildly doped. UV−Vis−NIR absorption, ^{19}F NMR, and ^{11}B NMR spectra confirm that BCF dopes the bipyridine-containing PFO-BPy but not PFO, thus leading to a proposed doping mechanism that relies on the unique interactions between BCF, the bipyridine moieties in PFO-BPy, and the nanotubes. Since BCF doping of PFO-BPy-wrapped (6,5) SWCNTs is more efficient than doping with F_4TCNQ and more stable than doping with $AuCl_3$, it provides a reliable alternative for spectroscopic studies of the interactions of charge carriers and excitons in SWCNTs.

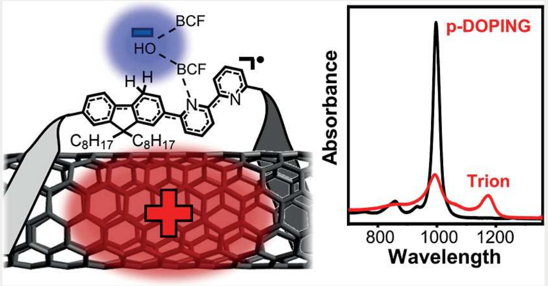

INTRODUCTION

Single-walled carbon nanotubes (SWCNTs) are quasi-one-dimensional carbon allotropes that can be conceptualized as seamlessly rolled-up sheets of graphene. Their structure is defined by two chiral indices (*n*,*m*), which directly determine their diameter as well as their electronic (metallic versus semiconducting)[1] and optical properties (absorption and emission wavelengths).[2] Since nanotube growth produces a mixture of different SWCNT species with different diameters, various methods to separate them such as selective dispersion by polymer-wrapping have been developed.[3−5] Polymer-wrapping of SWCNTs relies on specific interactions between the backbone of the conjugated polymers and the SWCNT lattice.[6] Hence, any changes to the electron density and structure of the polymer can also have a significant impact on the electronic and optical properties of the wrapped nanotubes.[7−9] The most selective and most commonly used wrapping polymers for small-diameter (<1 nm) nanotubes are the polyfluorene copolymers poly(9,9-di-*n*-octylfluorenyl-2,7-diyl) (PFO) and poly[(9,9-di-*n*-octylfluorenyl-2,7-diyl)-*alt*-(6,6′-(2,2′-bipyridine))] (PFO-BPy). They selectively wrap and thus disperse (7,5) and (6,5) nanotubes, respectively, in toluene (see Figure 1a).[3,10] They both have very large optical band gaps (>2.8 eV) and ionization energies (IEs), exceeding those of the respective nanotubes, which leads to the formation of type I heterojunctions.[8]

The control of charge carrier density in semiconducting polymers and SWCNTs through chemical doping is crucial for a wide range of applications, most recently for thermoelectric generators.[11,12] Doping also changes their optical properties by bleaching the ground state absorption and quenching photoluminescence accompanied by the appearance of charge induced absorption and emission (i.e., polaron or trion) bands.[13−15] These spectral changes can give direct insights into the interactions of charge carriers with electronic states or other quasiparticles (e.g., excitons), which strongly depend on the material. For the purpose of this study, we will only consider p-doping.

A variety of molecular dopants and different doping mechanisms have been studied for organic and polymeric semiconductors.[16] Molecular doping can be categorized as charge transfer doping, Brønsted acid doping, or Lewis acid doping. In the first case, the interaction of a molecular oxidant with an organic semiconductor leads to either full electron transfer—i.e., integer charge transfer (ICT) doping—or the

Received: December 19, 2024
Revised: February 20, 2025
Accepted: February 26, 2025
Published: March 5, 2025

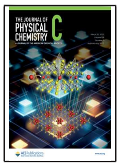

https://doi.org/10.1021/acs.jpcc.4c08584

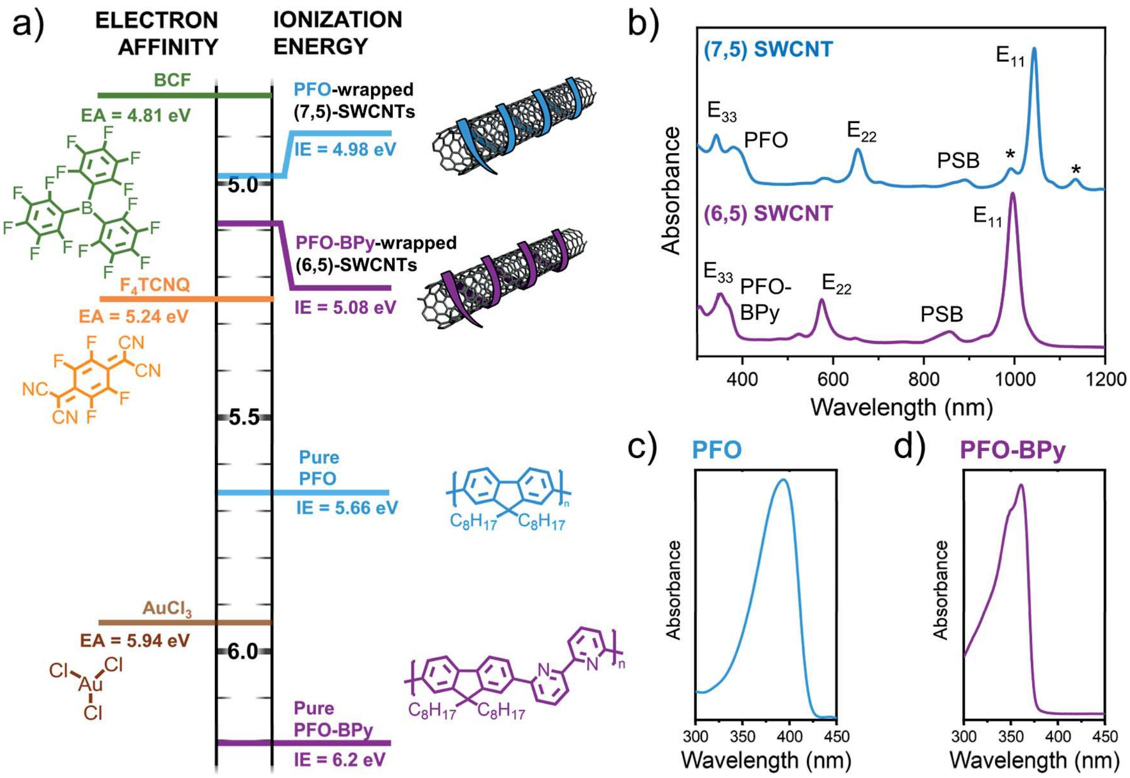

Figure 1. (a) Molecular structures of dopants and semiconductors used in this study and their corresponding EAs and IEs. EAs for dopants were retrieved from Han et al.,[33] Vijayakumar et al.,[39] and Lu et al.[40] IPs of SWCNTs were obtained from Tanaka et al.,[41] and IEs of polymers from Balcı Leinen et al. and Park et al.[8,42] (b) Absorption spectra of dispersions of PFO-wrapped (7,5) SWCNTs (top, blue) and PFO-BPy-wrapped (6,5) SWCNTs (bottom, purple) in toluene. Minority species of other semiconducting nanotubes in the (7,5) SWCNT dispersion are marked with an asterisk; PSB refers to the phonon sideband of the main excitonic E_{11} transition. (c,d) Absorption spectra of pure PFO and PFO-BPy in toluene, respectively.

formation of a charge transfer complex (CTC doping).[17,18] Common oxidants for charge transfer p-type doping of organic semiconductors and SWCNTs include $AuCl_3$, and F_4TCNQ (see Figure 1a). These dopants, however, often exhibit limited solubility in nonpolar solvents[19,20] or high chemical reactivity, which results in unwanted side reactions and limited doping stability.[21,22] Furthermore, effective p-doping by electron transfer generally occurs when the electron affinity (EA) of the dopant exceeds the IE of the semiconductor. For example, F_4TCNQ only induces weak doping in semiconductors with a relatively high IE, such as small-diameter carbon nanotubes.[14] Brønsted acids (e.g., hydrochloric acid and toluene sulfonic acid) are also effective dopants and have been applied extensively to polymers[23,24] and carbon nanotubes.[25,26] The mechanism of Brønsted acid doping is still unclear, but likely involves protonation of the organic semiconductor, followed by electron transfer between a charged and neutral semiconductor species or segment.[27]

While charge transfer doping and Brønsted acid doping have been utilized for organic semiconductors for decades, Lewis acid p-doping is a relatively new approach.[28] It involves the coordination of nonoxidative Lewis acids (e.g., AlX_3, BX_3, with X = F, Cl, Br) to Lewis basic moieties (e.g., pyridinic nitrogen), thus altering their electronic properties.[28,29] In particular, the strong Lewis acid tris(pentafluorophenyl)borane ($B(C_6F_5)_3$ or BCF, see Figure 1a) has been used recently to dope or co-dope organic semiconductors.[30] Its presence significantly enhanced the performance of organic light-emitting diodes,[31] field-effect transistors,[32,33] solar cells,[34,35] and thermoelectric devices.[36] Despite its comparatively low EA of only 4.81 eV, it can p-dope nitrogen-containing Lewis basic polymers with high ionization energies of up to 5.82 eV.[33] However, BCF can also dope polymers without Lewis basic moieties. This effect was recently attributed to the formation of strongly Brønsted acidic complexes of BCF with water ($BCF{:}OH_2$), which are capable of protonating polymer chains without Lewis basic moieties similar to other Brønsted acids.[37,38] However, these $BCF{:}OH_2$ complexes do not form in the presence of highly Lewis-basic moieties as BCF preferentially coordinates to them.[36−38]

Here, we employ BCF as a p-dopant for polymer-wrapped semiconducting carbon nanotubes with small diameters in toluene dispersions. We find that the doping efficiency, and hence impact on the optical properties of (6,5) and (7,5) nanotubes, depends on the presence of Lewis basic bipyridine units in the wrapping-polymer (PFO-BPy or PFO, respectively) and the concentration of the polymer when bipyridine units are present. We propose a possible doping mechanism based on ^{11}B NMR and ^{19}F NMR measurements. Compared with other common dopants for SWCNTs, BCF enables well-controlled, efficient, and stable p-doping of PFO-BPy-wrapped SWCNTs in toluene dispersions. It is thus an excellent choice for detailed spectroscopic studies of charge carriers in semiconducting nanotubes.

■ METHODS

Materials. All chemicals were used as purchased. Dopants were stored in a dry nitrogen glovebox, and doping solutions were freshly prepared on the day of usage. Doping experiments

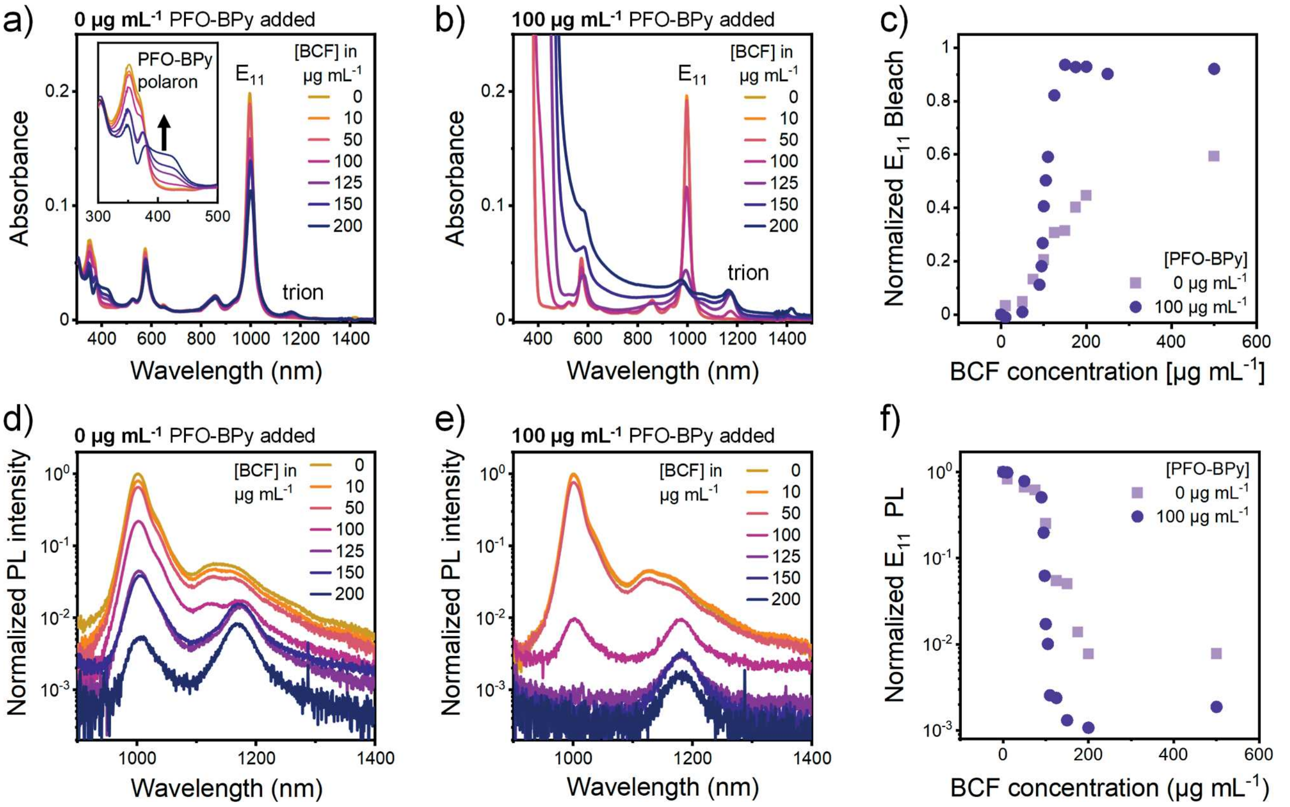

Figure 2. (a) Absorption spectra of PFO-BPy-wrapped (6,5) SWCNTs redispersed in pure toluene and doped with different concentrations of BCF, inset: PFO-BPy polaron absorption. (b) Absorption spectra of (6,5) SWCNTs, redispersed in a 100 μg mL^{-1} solution of PFO-BPy in toluene, doped with different amounts of BCF. (c) E_{11} absorption bleach values, extracted from extended data shown in Figure S4. (d) Normalized PL spectra of (6,5) SWCNTs redispersed in pure toluene and doped with different amounts of BCF. (e) Normalized PL spectra of (6,5) SWCNTs, redispersed in a 100 μg mL^{-1} solution of PFO-BPy in toluene and doped with different amounts of BCF. (f) Normalized E_{11} PL intensity plotted against the BCF concentration.

were performed under atmospheric conditions and with non-dried solvents. $AuCl_3$ (≥99.99%) and 2,3,5,6-tetrafluoro-7,7,8,8-tetracyanoquinodimethane (>97%) were purchased from Sigma-Aldrich. Tris(pentafluorophenyl)borane (>98%) was purchased from Tokyo Chemical Industries (TCI) and 2,2′-bipyridine (>99.94%) was acquired from BLD Pharmatech.

Selective Dispersion of SWCNTs. Dispersions of (6,5) SWCNTs or (7,5) SWCNTs were produced by shear force mixing (Silverson L2/Air, 10,230 rpm, 20 °C, at least 72 h) of CoMoCAT raw material (Sigma-Aldrich, SG65i, 0.5 g L^{-1}) in a solution of poly[(9,9-dioctylfluorenyl-2,7-diyl)-*alt*-(6,6′-(2,2′-bipyridine))] (PFO-BPy, American Dye Source, $M_W \sim$ 38 kDa, 0.5 g L^{-1}) or poly(9,9-dioctylfluorenyl-2,7-diyl) (PFO, Sigma-Aldrich, $M_W >$ 20 kDa, 0.9 g L^{-1}) in toluene. The resulting slurry was centrifuged twice at 60,000*g* for 45 min (Beckman Coulter Avanti J26SXP centrifuge). Finally, the supernatant was filtered through a poly(tetrafluoroethylene) (PTFE) syringe filter (Whatman, pore size of 5 μm). Further details can be found in Graf et al. and Lindenthal et al.[43,44]

Controlling the Polymer Concentration in SWCNT Dispersions. (6,5) or (7,5) SWCNT-dispersions were filtered through a poly(tetrafluorethylene) (PTFE) membrane filter (Merck Omnipore, JVWP, pore size 0.1 μm). The resulting filter cakes were submerged in hot toluene (80 °C, 8 times for 10 min) to wash away residual free polymer. Small parts of the filter cake were sonicated (Branson 2510, 30 min at 20 °C) in either pure toluene or a solution of the respective wrapping polymer in toluene to yield SWCNT dispersions with a controlled polymer concentration.

Doping of Polymers. Stock solutions of PFO and PFO-BPy were created by dissolving 1 mg mL^{-1} of the respective polymer in either toluene (for absorption measurements) or d^8-toluene (for NMR measurements). Stock solutions of the polymers were then mixed with (d^8-)toluene and a freshly prepared stock solution of BCF (1 mg mL^{-1}) in (d^8-)toluene to achieve the desired doping levels.

BCF and F_4TCNQ Doping Procedure. Stock solutions of either BCF (1 mg mL^{-1}) or F_4TCNQ (0.5 mg mL^{-1}) and wrapping polymer (PFO or PFO-BPy, 1 mg mL^{-1}) in toluene were mixed with freshly sonicated SWCNT dispersions and pure toluene, such that the resulting samples contained a SWCNT concentration corresponding to an optical density of 0.2 cm^{-1} at the E_{11} transition and the desired concentrations of wrapping polymer and BCF. Absorption and photoluminescence (PL) spectra were recorded within 15 min of preparing each sample to minimize effects of dedoping or doping-induced aggregation.

$AuCl_3$ Doping Procedure. Stock solutions of $AuCl_3$ (0.5 mg mL^{-1}) and wrapping polymer (1 mg mL^{-1}) in a volumetric 5:1 mixture toluene/acetonitrile were combined with SWCNT dispersions and pure toluene and acetonitrile. The resulting samples contained a SWCNT concentration corresponding to an optical density of 0.2 cm^{-1} at the E_{11} transition, the desired concentrations of wrapping polymer and $AuCl_3$, while maintaining a volumetric ratio of 5:1 toluene/acetonitrile.

NMR Spectroscopy. NMR spectra were recorded with a Bruker Avance III 600 (field intensity of 14.1 T, ^{1}H: 600.18 MHz) with d^{8}-toluene as the solvent. Chemical shifts (δ) are reported in parts per million in relation to $CFCl_3$ for ^{19}F NMR spectra and BF_3−Et_2O for ^{11}B NMR spectra. Note that no standard was used to avoid possible interactions with BCF. Analysis of the spectra was performed with MestReNova x64. The molar ratios of PFO-BPy/BCF mixtures are expressed as the ratio of polymer monomer units/BCF. Since the molar weights of PFO-BPy monomers and BCF are quite similar, the molar ratio roughly resembles the mass ratio of BCF/PFO-BPy.

Absorption Spectroscopy. Absorption spectra were recorded with a Cary 6000i UV−vis−NIR absorption spectrometer (Varian, Inc.) and quartz cuvettes with either a 0.1 or 1 cm path length. For SWCNTs, the resulting spectra were fitted with the Fityk 1.3.1 software by subtracting a Naumov background and fitting the peaks with Gaussian line profiles to obtain absorbances (A) for the E_{11} absorbance peaks; for details see Pfohl et al.[45] The normalized bleach was calculated as $1 - A(E_{11})/A(E_{11})_{\text{reference}}$.

Photoluminescence Spectroscopy. PL spectra were acquired from (6,5) SWCNT dispersions by excitation at 575 nm with a picosecond-pulsed supercontinuum laser (NKT) Photonics SuperK Extreme. Emitted photons were collected by a NIR-optimized 50× objective (N.A. 0.65, Olympus) and spectra were recorded with an Acton SpectraPro SP2358 spectrometer with a liquid-nitrogen-cooled InGaAs line camera (Princeton Instruments, OMA-V:1024). A lamp spectrum of a stabilized tungsten halogen lamp (Thorlabs SLS201/M, 300−2600 nm) was recorded at regular intervals to perform detection efficiency corrections.

RESULTS AND DISCUSSION

Doping of PFO-BPy-Wrapped (6,5) SWCNTs with BCF.

Dispersions of PFO-BPy-wrapped (6,5) SWCNTs and PFO-wrapped (7,5) SWCNTs in toluene were obtained via shear-force mixing (for details, see Methods). Figure 1b shows the corresponding absorption spectra with their characteristic E_{11} and E_{22} absorption peaks for the sorted nanotube species and a few minority species that were present. Raman spectra, recorded on drop-cast films of SWCNTs (Figure S1), indicated small amounts of other semiconducting SWCNTs but no metallic nanotubes. Arnold and co-workers had shown previously that the coverage of different nanotube species with polyfluorene wrapping polymer depends strongly on the concentration of the latter in solution.[46] Hence, we controlled the concentration of the polymer (PFO-BPy or PFO) for all doping experiments (see Methods) by removal of excess polymer from the initially obtained dispersions via filtration and subsequent dispersion in pure toluene (0 μg mL^{-1}) or in a polymer solution (100 μg mL^{-1}) to adjust its concentration (see Figure S2a−c). Note that it is not possible to remove all of the wrapping polymer, hence the diluted dispersions as used for doping studies still contained about 1 μg mL^{-1} PFO-BPy (see Figure S2d), which should lead to submonolayer coverage of the SWCNTs (around 50%).[46] The same applies to (7,5) SWCNTs dispersions with PFO (Figure S3).

Doping experiments with BCF were performed at an absorbance of 0.2 at the E_{11} transition of the SWCNTs (corresponding to ∼0.36 μg mL^{-1} of SWCNTs) and a constant PFO-BPy concentration of either 0 or 100 μg mL^{-1}. At a polymer concentration of 100 μg mL^{-1} (PFO-BPy/SWCNTs ≈ 280:1), we expect full coverage of the SWCNTs by PFO-BPy.[46] All dispersions were sonicated prior to each doping experiment to minimize the influence of aggregation. Absorption spectra of BCF-doped (6,5) SWCNTs with and without added PFO-BPy are shown in Figure 2a,b. Upon addition of increasing amounts of BCF, the (6,5) SWCNT E_{11} transition is bleached and a red-shifted absorption between 1160 and 1180 nm appears, which is ascribed to a trion (charged exciton).[14] These spectral changes are typical for p-doping of SWCNTs and have been reported for several different dopants.[47−49]

The evolution of the normalized bleach of the E_{11} absorption with increasing BCF concentration for (6,5) SWCNTs without additional PFO-BPy is shown in Figure 2c. For BCF concentrations of less than 100 μg mL^{-1} only a slight bleach (∼15%) can be observed. At BCF concentrations above 100 μg mL^{-1} the SWCNTs are increasingly doped and E_{11} bleaching reaches ∼60% for the highest BCF concentration of 500 μg mL^{-1}. This behavior is similar to chemical doping with common oxidants such as F_4TCNQ and $AuCl_3$.[50]

For low PFO-BPy concentrations (Figure 2a), it is also possible to follow the doping process of the residual PFO-BPy in the (6,5) SWCNT dispersion (see Figure S4 for a complete set of spectra with BCF concentrations up to 500 μg mL^{-1}). Interestingly, the PFO-BPy polaron at 420 nm (for spectra of BCF-doped PFO-BPy without SWCNTs see Figure S5a) emerges at exactly the same BCF concentration as the SWCNT trion (i.e., at 100 μg mL^{-1}). The PFO-BPy polaron, the E_{11} bleach and the SWCNTs trion absorption all follow the same trend as a function of the BCF concentration (Figure S6). This is not the case for other dopants (e.g., $AuCl_3$), which strongly dope (6,5) SWCNTs but not the wrapping polymer[48] and indicates a synergistic interaction between BCF, PFO-BPy and the SWCNTs.

Since a higher PFO-BPy concentration should result in higher polymer coverage of the SWCNTs,[46] we also expect a stronger BCF doping effect for (6,5) SWCNT dispersions doped at a PFO-BPy concentration of 100 μg mL^{-1}. Absorption spectra of these dispersions (Figure 2b) exhibit the same general trends for increasing BCF concentrations and indeed a significantly stronger doping at the same BCF concentrations. Up to a BCF concentration of 90 μg mL^{-1}, no bleaching occurs at all; however, between 90 and 110 μg mL^{-1} of BCF, the E_{11} bleach reaches more than 80% (Figure 2c). At even higher BCF concentrations, the E_{11} absorption peak nearly vanishes and the normalized bleach reaches ∼95%. These values are significantly higher than those for the (6,5) SWCNT dispersion without extra PFO-BPy.

Figure S7 gives a more detailed representation of the data in Figure 2c together with the corresponding absorption spectra. They show a strong blueshift (up to 20 nm) of the E_{11} absorption as previously discussed by Eckstein et al.[15] The peak position of the PFO-BPy polaron shifts from roughly 420 to 450 nm (Figure S8), thus indicating a higher doping level of the polymer. Again, the PFO-BPy polaron absorption, the SWCNT E_{11} bleach, and the SWCNT trion absorption for different BCF concentrations (Figure S9) follow the same trend, similar to the 0 μg mL^{-1} PFO-BPy sample (Figure S6).

As photoluminescence (PL) of SWCNTs is even more sensitive toward doping than absorption, we also recorded PL spectra of BCF-doped (6,5) SWCNT samples with and without added PFO-BPy (Figure 2d,e). For better comparability, the spectra were normalized to the E_{11} emission of the

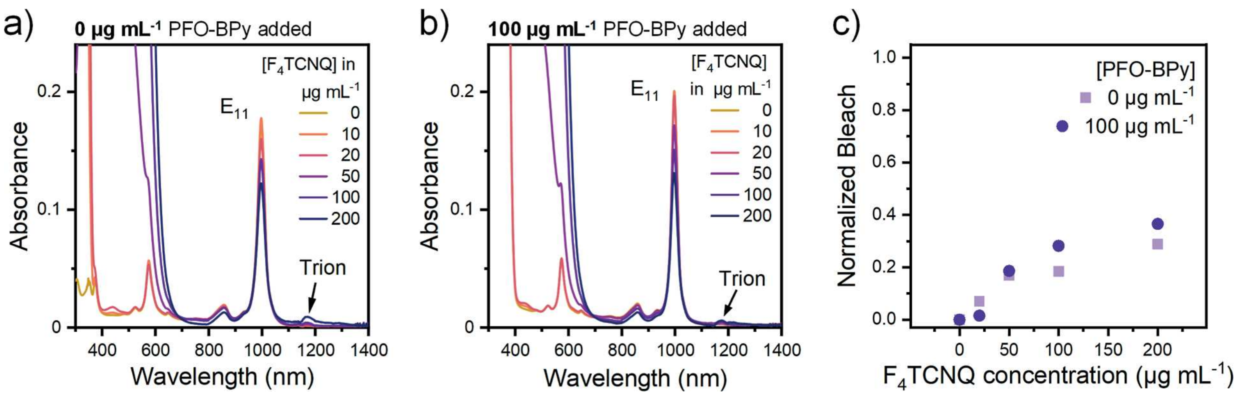

Figure 3. (a) Absorption spectra of (6,5) SWCNTs redispersed in pure toluene and doped with different amounts of F_4TCNQ. (b) Absorption spectra of (6,5) SWCNTs redispersed in a 100 μg mL^{-1} solution of PFO-BPy in toluene and doped with different amounts of F_4TCNQ. (c) Normalized E_{11} bleach values for both dispersions depending on the F_4TCNQ concentration.

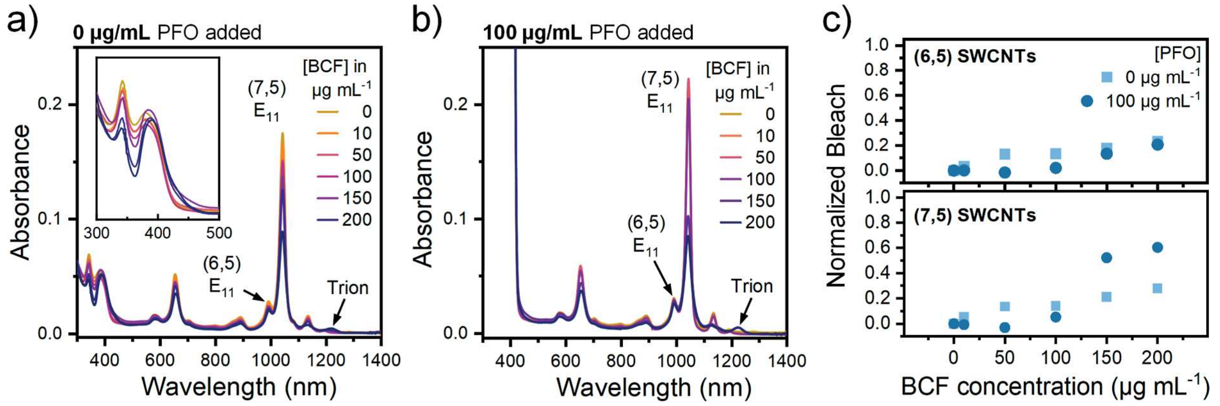

Figure 4. (a) Absorption spectra of PFO-wrapped (7,5) SWCNTs (with residual (6,5) SWCNTs) redispersed in pure toluene and doped with different amounts of BCF. (b) Absorption spectra of (7,5) SWCNTs redispersed in a 100 μg mL^{-1} solution of PFO in toluene and doped with different amounts of BCF. (c) Normalized E_{11} bleach values for PFO-wrapped (6,5) and (7,5) SWCNTs.

undoped sample, and the PL intensities were plotted on a logarithmic scale. Both types of samples showed very strong quenching of the E_{11} emission upon addition of BCF. Trion emission (at 1180 nm) also appeared as expected from previous reports on doped (6,5) SWCNTs.[50] Again, a clear difference in the degree of doping can be observed. While E_{11} emission remained visible for the 0 μg mL^{-1} PFO-BPy sample when doped with 200 μg mL^{-1} BCF, it was completely quenched in the 100 μg mL^{-1} PFO-BPy sample. Plotting the normalized E_{11} emission for both experiments against the BCF concentration (Figure 2f) further shows that a higher PFO-BPy concentration leads to overall stronger quenching compared to samples without additional PFO-BPy.

This significantly stronger doping of the (6,5) SWCNTs by BCF when additional PFO-BPy is present and the simultaneous and similar doping trends of the wrapping polymer strongly indicate a synergistic effect between BCF and PFO-BPy with its bipyridine units in the doping process of the SWCNTs. However, the possibility of simultaneous but nevertheless independent doping of PFO-BPy and (6,5) SWCNTs cannot be excluded yet.

The observed doping of PFO-BPy wrapped (6,5) SWCNTs with BCF can be compared to the well-known molecular p-dopant F_4TCNQ at the same polymer concentrations. Corresponding absorption spectra and normalized bleaching values at different F_4TCNQ concentrations are presented in Figure 3a−c. The E_{11} bleach and trion absorption that are associated with increasing p-doping levels are observed again. The normalized bleach values of samples with 0 and 100 μg mL^{-1} PFO-BPy are very similar to each other and correspond to the levels obtained by BCF for 0 μg mL^{-1} PFO-BPy (see Figure 2a). Due to the strong absorption of F_4TCNQ in the same range as the PFO-BPy, a direct comparison between doping of the wrapping polymer and SWCNTs is not possible. Overall, there seems to be no specific interaction between PFO-BPy and molecular dopants in general, but the interaction between BCF and PFO-BPy appears to be crucial.

Doping of PFO-Wrapped (7,5) SWCNTs with BCF. To corroborate that PFO-BPy and its bipyridine unit indeed play an integral role in the BCF-doping of nanotubes, we tested the doping of PFO-wrapped (7,5) SWCNTs with BCF at PFO concentrations of 0 and 100 μg mL^{-1}. Due to the slightly smaller bandgap and lower ionization energy of the (7,5) SWCNTs compared to (6,5) SWCNTs (Figure 1a), we would expect even stronger doping of the (7,5) SWCNTs by BCF if solely Brønsted acid doping took place. Additionally, PFO does not wrap (7,5) SWCNTs as tightly as PFO-BPy wraps (6,5) SWCNTs,[51] which would facilitate access of a BCF:OH_2 complex[37,38] to the nanotube surface.

PFO is less selective toward (7,5) SWCNTs than PFO-BPy is toward (6,5) SWCNTs. Hence, depending on the polymer concentration, other semiconducting nanotube species such as (6,5) SWCNTs will also be dispersed by PFO from the CoMoCat nanotube source material. This is evident from the

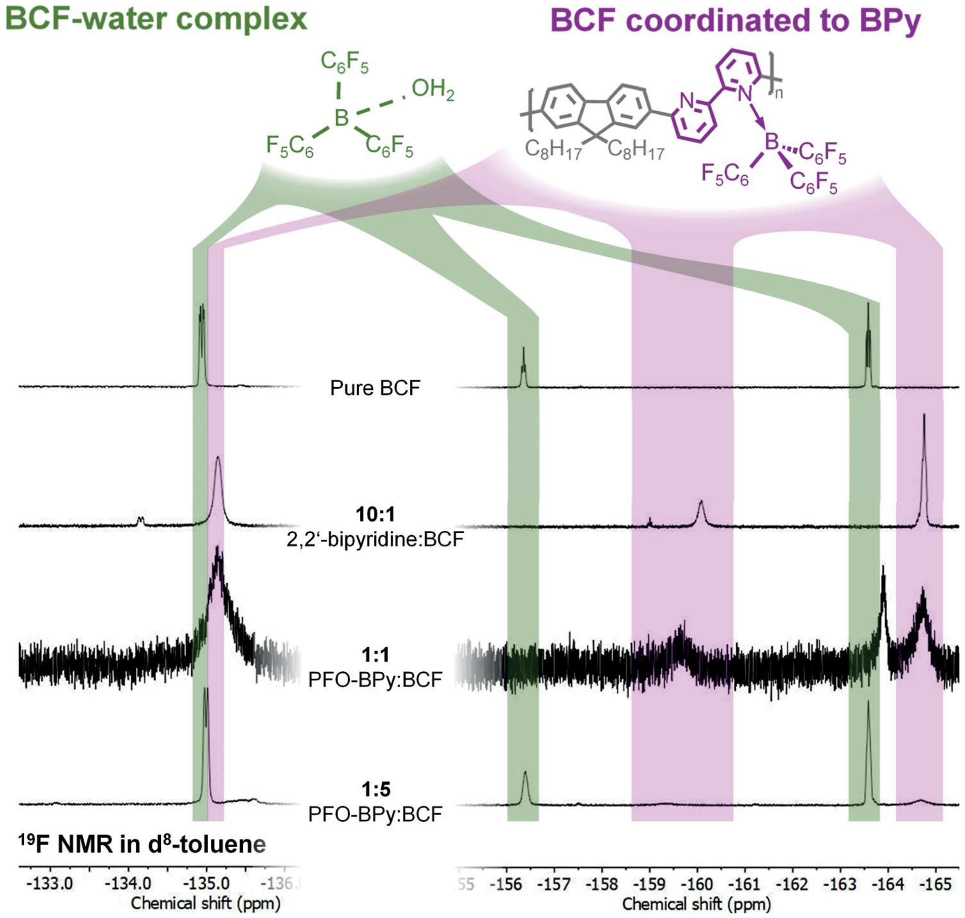

Figure 5. ^{19}F NMR spectra (546.73 MHz, d^8-toluene) of pure BCF, a 10:1 molar ratio of 2,2′-bipyridine/BCF, a 1:1 molar ratio PFO-BPy/BCF, and a 1:5 molar ratio of PFO-BPy/BCF (top to bottom). Green shaded areas indicate peaks associated with BCF:OH_2 complexes, and purple regions refer to peaks associated with BCF:BPy complexes. Schematic depictions of complexes are shown above the NMR spectra.

E_{11} absorption of (6,5) SWCNTs at around 990 nm in the absorption spectra (Figure 4a,b) and the radial breathing modes in the Raman spectra (Figure S1b). While usually undesired, these residual PFO-wrapped (6,5) SWCNTs enable a direct comparison to BCF-doping of the PFO-BPy-wrapped (6,5) SWCNTs.

Upon addition of up to 100 μg mL^{-1} of BCF to the dispersions, we observe similarly low bleaching of the (6,5) and (7,5) SWCNTs E_{11} absorption with or without additional PFO (see Figure 4a,b). For higher BCF concentrations, the (7,5) SWCNTs with 100 μg mL^{-1} PFO showed a stronger bleach than the (7,5) SWCNTs without added PFO. For the highest BCF concentration of 200 μg mL^{-1}, the trion absorption of the (7,5) SWCNTs at 1220 nm emerges. Overall, the bleaching remains below 60% and the E_{11} absorption peak remains well-defined with only a small blue-shift of 1 nm. In contrast to PFO-BPy (see inset in Figure 2a), PFO does not show any spectral signs of doping (see inset in Figure 4a) even for the highest BCF concentration of 200 μg mL^{-1}, which is consistent with the lack of doping of pure PFO solutions shown in Figure S5b,c as well as PFO film data by Zapata-Arteaga et al.[30]

The normalized bleaching values of the E_{11} absorption of (6,5) and (7,5) SWCNTs are shown in Figure 4c. While there is a stronger bleach of around 60% for the (7,5) SWCNTs at higher PFO concentrations (compared to ~30% for the sample at lower PFO concentration), the differences for the PFO-wrapped (6,5) SWCNTs are negligible. Overall, these absorption spectra indicate only very limited doping of PFO-wrapped SWCNTs compared with PFO-BPy-wrapped SWCNTs under otherwise identical experimental conditions. Given the smaller bandgap of (7,5) SWCNTs compared to (6,5) SWCNTs, this experiment provides further evidence for a specific interaction of BCF with PFO-BPy and with PFO-BPy-wrapped SWCNTs.

BCF Doping Mechanism. The presented evidence for a synergistic interaction between BCF and PFO-BPy-wrapped nanotubes raises the question of a possible doping mechanism. Hence, we investigated the interaction and doping of pure PFO-BPy and PFO with BCF in more detail. Solutions of both polymers (100 μg mL^{-1} in toluene) were exposed to increasing amounts of BCF (see Figure S5a,b). While PFO showed no signs of bleaching or polaron formation, not even at much higher BCF/PFO ratios (50:1, Figure S5c), PFO-BPy was clearly p-doped as indicated by significant bleaching and red-shifted polaron absorption at BCF/PFO-BPy molar ratios above 1:1 (for calculation of molar ratios, see Methods). BCF only has an electron affinity of 4.81 eV (Figure 1a) and should not be able to dope any of the polymers via ICT or CTC. Previous studies also showed that PFO is not doped by the BCF:OH_2 complex.[30] Hence, the bipyridine unit of PFO-BPy must play a crucial role in doping the polymer.

To understand this behavior, we performed ^{19}F and ^{11}B NMR spectroscopy on solutions of PFO-BPy and the model

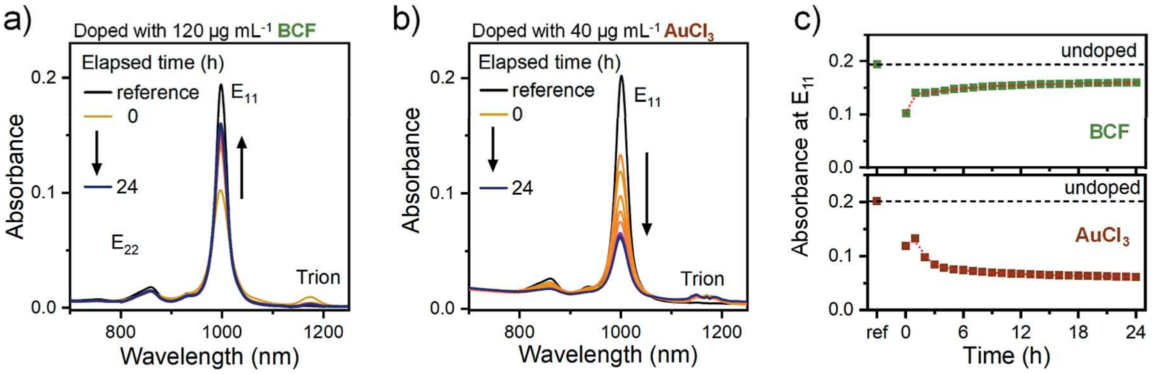

Figure 6. (a) Absorption spectra of (6,5) SWCNTs at a polymer concentration of 100 μg mL^{-1} doped with 120 μg mL^{-1} BCF over the course of 24 h. (b) Absorption spectra of (6,5) SWCNTs at a polymer concentration of 100 μg mL^{-1} doped with 40 μg mL^{-1} $AuCl_3$ over the course of 24 h. (c) E_{11} absorption of (6,5) SWCNTs doped with either BCF (top) or $AuCl_3$ (bottom) plotted against time after doping. The absorption of an undoped dispersion is indicated by a dashed line. The red dotted line serves as a guide to the eye.

compound 2,2′-bipyridine (BPy) in d^8-toluene that were doped with various amounts of BCF (Figures 5 and S10, S11). It is well-known that ^{11}B and ^{19}F NMR chemical shifts (δ) of organoboron compounds are especially sensitive to changes of the coordination state and ligand electronegativity. Trivalent organoboranes exhibit ^{11}B NMR shifts between 30 and 60 ppm, whereas tetravalent organoborates display significantly upfield-shifted ^{11}B NMR signals, typically in the range of −30 to 0 ppm.[52] In its pristine trivalent form BCF shows a single broad ^{11}B NMR peak at δ = 56 ppm,[53] as well as three ^{19}F NMR signals at δ = −129.5, −140.5, and −161.5 ppm.[54] When subjected to moisture (such as atmospheric humidity or trace amounts of water in solvents), BCF forms tetravalent complexes with water, as schematically shown in Figure 5. Hence, we only observe upfield-shifted ^{11}B NMR signals at δ = −1.6 ppm (Figure S10, top) and ^{19}F NMR signals at δ = −134.9, −156.4, and −163.6 ppm (Figure S11, top), confirming the presence of the tetravalent BCF:OH_2 complex.[53,54]

Since the only structural difference between the two wrapping polymers is a bipyridine unit, we used 2,2′-bipyridine (BPy) as a model compound to examine Lewis acid−base complexation in this system, as schematically shown in Figure 5. Providing a large excess of BPy (10:1 BPy/BCF) to achieve complete complexation of the BCF leads to a slight upfield shift of 1−4 ppm for the ^{19}F NMR signals and 2 ppm for the ^{11}B NMR signals. This is in agreement with previous reports of stronger shielding upon coordination of BCF to pyridinic nitrogen moieties and indicates a higher complexation strength compared to the BCF:OH_2 complex.[36]

For a 1:1 mixture of PFO-BPy/BCF (Figures 5 and S10, third trace), which does not yet show any signs of doping (Figure S5a), only the ^{19}F NMR and ^{11}B NMR signals of the complexed BCF are present. The small change in chemical shift of 0.5−1 ppm compared to the BCF:BPy complex can be explained by a slightly different chemical environment within the BCF:PFO-BPy complex. We also observe a significant line broadening compared to the BCF:OH_2 and BCF:BPy complex, which can be attributed to reduced molecular tumbling of the BCF molecules when complexed to the polymer.[55]

In contrast, the ^{19}F NMR spectrum of the 1:5 mixture of PFO-BPy/BCF (Figure 5, bottom trace) shows sharp peaks that can be assigned to the BCF:OH_2 complex. 10-fold magnification of the ^{19}F NMR spectrum (Figure S11), however, reveals that the broad signals of the BCF:PFO-BPy complex are still present. This is similar to the ^{11}B NMR spectrum, in which a sharp peak for the BCF:OH_2 complex and an underlying broad peak for the BCF:PFO-BPy complex is visible (Figure S10, bottom trace).

The NMR data together with the UV−vis absorption data strongly indicate that doping of PFO-BPy occurs via the Brønsted acidic BCF:OH_2 complex, which only forms after saturation of all polymer BPy units with BCF, and not via Lewis acid−base complexation. Despite having two possible coordination sites in a single BPy unit, one BCF molecule occupies both, as the addition of two mol equivalents of BCF already leads to substantial doping (Figure S5a). Applying these insights to the PFO-BPy-wrapped SWCNTs, we propose that the SWCNTs are not simply doped by BCF:OH_2 but through a unique interaction between BCF:OH_2 and the BCF:PFO-BPy complex. Such interaction also explains the dependence of the doping efficiency on the PFO-BPy concentration and the fact that significant doping occurred only above a 1:1 molar ratio of PFO-BPy/BCF for a PFO-BPy concentration of 100 μg mL^{-1}.

A possible doping mechanism for the SWCNTs might be inferred from previous work on the BCF-doping of polymers. For semiconducting polymers, Yurash et al. found a two-step doping mechanism with the first step being the protonation of a polymer chain by a BCF:OH_2 complex to create a positively charged chain segment and a $[\mathrm{BCF(OH)BCF}]^-$ anion stabilized by a second BCF molecule.[38] The doping process is completed by intra- or interchain electron transfer from a neutral chain segment to the protonation site.[37,38] For the PFO-BPy-wrapped SWCNTs, we propose a similar three-step mechanism: (1) Lewis acid−base complexation of BCF by the PFO-BPy bipyridine units up to a 1:1 molar ratio. (2) Protonation of the PFO-BPy wrapped around the SWCNTs by BCF:OH_2 and formation of a $[\mathrm{BCF(OH)BCF}]^-$ anion. (3) Electron transfer from the SWCNT (instead of a neutral polymer chain segment) to the doped PFO-BPy polymer segments leading to p-doping of the SWCNT. The proposed steps are visualized in Figure S12. Note that this process would not be possible with PFO-wrapped SWCNTs because the polymer would not be doped without the presence of the bipyridine units and the resulting BCF complex. Although this mechanism is consistent with the available experimental data, further theoretical studies are needed to resolve the details.

BCF versus Other Common p-Dopants. Regardless of the precise doping mechanism, one of the main questions is whether BCF-doping provides any advantages compared with other common molecular dopants for SWCNTs. Various oxidants have been applied to obtain p-doped (6,5) or other SWCNTs.[48,50,56] Due to their large bandgap, (6,5) SWCNTs usually require fairly strong p-dopants compared to larger diameter nanotubes. Typical dopants include F_4TCNQ but also $AuCl_3$. F_4TCNQ suffers from several disadvantages as a p-dopant for polymer-wrapped small-diameter SWCNTs. It is barely soluble in nonpolar solvents such as toluene, while BCF is highly soluble. Despite an EA of 5.26 eV, F_4TCNQ is not able to induce strong doping in small diameter nanotubes as shown in Figure 3. The maximum E_{11} bleach values are below 40%. Furthermore, the intense absorption of F_4TCNQ and F_4TCNQ anions[56] between 400 and 700 nm makes analysis of any changes in E_{22} or PFO-BPy absorption impossible. In contrast to that, BCF does not have any absorption bands in the visible range.[29]

$AuCl_3$ is a very strong dopant that is often used for spectroscopic studies of small-diameter SWCNTs.[47,48,50] Only low concentrations of $AuCl_3$ are required for efficient doping, and it has no absorption features that would obstruct spectral analysis. However, $AuCl_3$ is essentially insoluble in nonpolar solvents such as toluene. Hence, a mixture of acetonitrile and toluene is usually used for doping in a dispersion, which reduces the dispersion stability significantly.

The difference in long-term stability between doping of (6,5) SWCNTs with BCF and $AuCl_3$ is demonstrated in Figure 6. A (6,5) SWCNT dispersion with 100 μg mL^{-1} PFO-BPy in a 1:5 mixture of acetonitrile/toluene was doped with 40 μg mL^{-1} $AuCl_3$ and compared to a similar dispersion with only toluene as the solvent doped with 120 μg mL^{-1} of BCF. Doping with BCF results in an initial absorption bleach of E_{11} of around 50%. The absorption increases again within the first hour and then stabilizes at around 75−80% of the initial absorption value (Figure 6a,c). The PFO-BPy polaron absorption is decreasing simultaneously (see Figure S13), which points toward slight dedoping of the polymer and the SWCNTs. The same dedoping behavior can be observed for a BCF concentration of 200 μg mL^{-1}, which led to higher initial doping level of the (6,5) SWCNT (Figure S14). In this case, the E_{11} absorption stabilizes after 6 h at 25% of the original absorption. These observations indicate a loss of BCF possibly due to side reactions, e.g., with residual water. While this means that samples should be measured instantly to correlate doping concentration with doping level, the intrinsic dedoping over time also provides an opportunity to measure the same sample at various doping levels without additional sample preparation. Importantly, there are no signs of aggregation (Figure S15), which makes BCF an interesting dopant for spectroscopic studies of doped (6,5) SWCNTs in dispersion.

In contrast to that, the (6,5) SWCNT dispersion in toluene/acetonitrile shows an increased scattering background (see Figure 6b), indicating SWCNT aggregation despite previous sonication. Upon addition of $AuCl_3$, the E_{11} absorption is bleached to ∼60% of its initial value. Within the first hour, $AuCl_3$ the E_{11} absorption starts to increase again, indicating dedoping but then decreases (Figure 6c). This loss of absorption is due to strong nanotube aggregation[57] not increased doping as the corresponding absorption spectra do not show higher trion absorption but the scattering background increases. Indeed, visual inspection of the cuvette reveals clouds of aggregated SWCNTs for $AuCl_3$ doping (Figure S15). This renders $AuCl_3$ a less-than-ideal dopant for extended doping experiments on SWCNTs and shows the potential of BCF as a dopant for detailed spectroscopic studies of SWCNT dispersions.

■ CONCLUSIONS

In this study, we explored the unique p-doping of PFO-BPy-wrapped (6,5) SWCNTs by BCF. Despite its comparatively low electron affinity, BCF is able to induce efficient p-doping of small-diameter PFO-BPy-wrapped (6,5) SWCNTs, while it does not dope PFO-wrapped (7,5) SWCNTs. The increase of BCF doping strength with higher PFO-BPy concentrations, an effect that is not observed for other dopants such as F_4TCNQ, as well as the simultaneous doping of the PFO-BPy and the (6,5) SWCNTs indicate a specific interaction between BCF, the bipyridine groups of the PFO-BPy and the nanotubes. Based on the proposed BCF-doping mechanism for semiconducting polymers, we suggest a three-step process that involves the complexation of BCF by the bipyridine of the polymer, protonation of the PFO-BPy that is wrapped around the SWCNTs by BCF:OH_2 and formation of a $[BCF(OH)BCF]^-$ anion, and finally electron transfer from the SWCNT to the protonated PFO-BPy polymer. The applicability of BCF as an efficient dopant should not be limited to PFO-BPy-wrapped SWCNTs as there are several conjugated polymers, which are applied for nanotube sorting and contain Lewis-basic nitrogen.[58,59] Overall, BCF is an excellent dopant for small-diameter, polymer-wrapped SWCNTs in toluene dispersions with a higher doping efficiency than F_4TCNQ and much better long-term dispersion stability than doping with $AuCl_3$. These properties are especially important for fundamental spectroscopic studies of the interactions of charge carriers with excitons in one-dimensional nanotubes without any spectral broadening or energy transfer, which are usually observed for aggregates, networks, or dense films.

■ ASSOCIATED CONTENT

Supporting Information

The Supporting Information is available free of charge at https://pubs.acs.org/doi/10.1021/acs.jpcc.4c08584.

Raman and absorption spectra of undoped polymer-wrapped (6,5) and (7,5) SWCNTs, ^{11}B and ^{19}F NMR and absorption spectra of BCF-doped wrapping polymers, additional data on BCF doping of polymer-wrapped SWCNTs (absorption spectra of additional BCF concentrations, analysis of E_{11}, polaron and trion bands as a function of BCF concentration, analysis of PFO-BPy polaron position for BCF doping), schematic illustration of the proposed doping mechanism, and photographs of SWCNT dispersions doped with $AuCl_3$ or BCF after 24 h (PDF)

■ AUTHOR INFORMATION

Corresponding Author

Jana Zaumseil − *Institute for Physical Chemistry, Heidelberg University, D-69120 Heidelberg, Germany;* orcid.org/0000-0002-2048-217X; Email: zaumseil@uni-heidelberg.de

Authors

Sebastian Lindenthal − *Institute for Physical Chemistry, Heidelberg University, D-69120 Heidelberg, Germany*

Daniel Rippel − *Institute for Physical Chemistry, Heidelberg University, D-69120 Heidelberg, Germany*
Lucas Kistner − *Institute for Inorganic Chemistry, Heidelberg University, D-69120 Heidelberg, Germany*
Angus Hawkey − *Institute for Physical Chemistry, Heidelberg University, D-69120 Heidelberg, Germany*

Complete contact information is available at:
https://pubs.acs.org/10.1021/acs.jpcc.4c08584

Author Contributions

S.L. processed and measured all samples and analyzed the data with help from D.R. and A.H. L.K. assisted in measuring and analyzing NMR data. J.Z. conceived and supervised the project. S.L. and J.Z. wrote the manuscript with input from all authors. All authors have given approval to the final version of the manuscript.

Notes

The authors declare no competing financial interest.

■ ACKNOWLEDGMENTS

The authors acknowledge financial support by the Deutsche Forschungsgemeinschaft (DFG, German Research Foundation) via SFB 1225/3 (Isoquant). A.H. received funding from the European Union's Horizon 2020 research and innovation program under the Marie Skłodowska-Curie grant agreement no. 955837 (HORATES). The authors also thank Prof. H.-J. Himmel and J. Doll for assistance with NMR measurements.

■ REFERENCES

(1) Charlier, J. C.; Blase, X.; Roche, S. Electronic and transport properties of nanotubes. *Rev. Mod. Phys.* **2007**, *79*, 677−732.

(2) Weisman, R. B.; Bachilo, S. M. Dependence of Optical Transition Energies on Structure for Single-Walled Carbon Nanotubes in Aqueous Suspension: An Empirical Kataura Plot. *Nano Lett.* **2003**, *3*, 1235−1238.

(3) Nish, A.; Hwang, J.-Y.; Doig, J.; Nicholas, R. J. Highly selective dispersion of single-walled carbon nanotubes using aromatic polymers. *Nat. Nanotechnol.* **2007**, *2*, 640−646.

(4) Mistry, K. S.; Larsen, B. A.; Blackburn, J. L. High-Yield Dispersions of Large-Diameter Semiconducting Single-Walled Carbon Nanotubes with Tunable Narrow Chirality Distributions. *ACS Nano* **2013**, *7*, 2231−2239.

(5) Salazar-Rios, J. M.; Talsma, W.; Derenskyi, V.; Gomulya, W.; Keller, T.; Fritsch, M.; Kowalski, S.; Preis, E.; Wang, M.; Allard, S.; Bazan, G. C.; Scherf, U.; dos Santos, M. C.; Loi, M. A. Understanding the Selection Mechanism of the Polymer Wrapping Technique toward Semiconducting Carbon Nanotubes. *Small Methods* **2018**, *2*, 1700335.

(6) Gao, J.; Loi, M. A.; de Carvalho, E. J. F.; dos Santos, M. C. Selective Wrapping and Supramolecular Structures of Polyfluorene−Carbon Nanotube Hybrids. *ACS Nano* **2011**, *5*, 3993−3999.

(7) Kahmann, S.; Salazar Rios, J. M.; Zink, M.; Allard, S.; Scherf, U.; dos Santos, M. C.; Brabec, C. J.; Loi, M. A. Excited-State Interaction of Semiconducting Single-Walled Carbon Nanotubes with Their Wrapping Polymers. *J. Phys. Chem. Lett.* **2017**, *8*, 5666−5672.

(8) Balcı Leinen, M.; Berger, F. J.; Klein, P.; Mühlinghaus, M.; Zorn, N. F.; Settele, S.; Allard, S.; Scherf, U.; Zaumseil, J. Doping-Dependent Energy Transfer from Conjugated Polyelectrolytes to (6,5) Single-Walled Carbon Nanotubes. *J. Phys. Chem. C* **2019**, *123*, 22680−22689.

(9) Guo, C.; Ouyang, J.; Shin, H.; Ding, J.; Li, Z.; Lapointe, F.; Lefebvre, J.; Kell, A. J.; Malenfant, P. R. L. Enrichment of Semiconducting Single-Walled Carbon Nanotubes with Indigo-Fluorene-Based Copolymers and Their Use in Printed Thin-Film Transistors and Carbon Dioxide Gas Sensors. *ACS Sens.* **2020**, *5*, 2136−2145.

(10) Ozawa, H.; Ide, N.; Fujigaya, T.; Niidome, Y.; Nakashima, N. One-pot Separation of Highly Enriched (6,5)-Single-walled Carbon Nanotubes Using a Fluorene-based Copolymer. *Chem. Lett.* **2011**, *40*, 239−241.

(11) Zhao, W.; Ding, J.; Zou, Y.; Di, C.-a.; Zhu, D. Chemical doping of organic semiconductors for thermoelectric applications. *Chem. Soc. Rev.* **2020**, *49*, 7210−7228.

(12) Blackburn, J. L.; Ferguson, A. J.; Cho, C.; Grunlan, J. C. Carbon-Nanotube-Based Thermoelectric Materials and Devices. *Adv. Mater.* **2018**, *30*, 1704386.

(13) Hofmann, A. I.; Kroon, R.; Zokaei, S.; Järsvall, E.; Malacrida, C.; Ludwigs, S.; Biskup, T.; Müller, C. Chemical Doping of Conjugated Polymers with the Strong Oxidant Magic Blue. *Adv. Electron. Mater.* **2020**, *6*, 2000249.

(14) Matsunaga, R.; Matsuda, K.; Kanemitsu, Y. Observation of Charged Excitons in Hole-Doped Carbon Nanotubes Using Photoluminescence and Absorption Spectroscopy. *Phys. Rev. Lett.* **2011**, *106*, 037404.

(15) Eckstein, K. H.; Hartleb, H.; Achsnich, M. M.; Schöppler, F.; Hertel, T. Localized Charges Control Exciton Energetics and Energy Dissipation in Doped Carbon Nanotubes. *ACS Nano* **2017**, *11*, 10401−10408.

(16) Salzmann, I.; Heimel, G.; Oehzelt, M.; Winkler, S.; Koch, N. Molecular Electrical Doping of Organic Semiconductors: Fundamental Mechanisms and Emerging Dopant Design Rules. *Acc. Chem. Res.* **2016**, *49*, 370−378.

(17) Lüssem, B.; Keum, C.-M.; Kasemann, D.; Naab, B.; Bao, Z.; Leo, K. Doped Organic Transistors. *Chem. Rev.* **2016**, *116*, 13714−13751.

(18) Jacobs, I. E.; Moulé, A. J. Controlling Molecular Doping in Organic Semiconductors. *Adv. Mater.* **2017**, *29*, 1703063.

(19) Arias, A. C.; MacKenzie, J. D.; McCulloch, I.; Rivnay, J.; Salleo, A. Materials and Applications for Large Area Electronics: Solution-Based Approaches. *Chem. Rev.* **2010**, *110*, 3−24.

(20) Li, J.; Zhang, G.; Holm, D. M.; Jacobs, I. E.; Yin, B.; Stroeve, P.; Mascal, M.; Moulé, A. J. Introducing Solubility Control for Improved Organic P-Type Dopants. *Chem. Mater.* **2015**, *27*, 5765−5774.

(21) Kumar, J.; Singh, R. K.; Singh, R.; Rastogi, R. C.; Kumar, V. Effect of FeCl3 on the stability of π-conjugation of electronic polymer. *Corros. Sci.* **2008**, *50*, 301−308.

(22) Jha, M.; Mogollon Santiana, J.; Jacob, A. A.; Light, K.; Hong, M. L.; Lau, M. R.; Filardi, L. R.; Miao, H.; Gurses, S. M.; Kronawitter, C. X.; Mascal, M.; Moulé, A. J. Stability Study of Molecularly Doped Semiconducting Polymers. *J. Phys. Chem. C* **2024**, *128*, 1258−1266.

(23) Han, C. C.; Elsenbaumer, R. L. Protonic acids: Generally applicable dopants for conducting polymers. *Synth. Met.* **1989**, *30*, 123−131.

(24) Polk, B. J.; Potje-Kamloth, K.; Josowicz, M.; Janata, J. Role of Protonic and Charge Transfer Doping in Solid-State Polyaniline. *J. Phys. Chem. B* **2002**, *106*, 11457−11462.

(25) Strano, M. S.; Huffman, C. B.; Moore, V. C.; O'Connell, M. J.; Haroz, E. H.; Hubbard, J.; Miller, M.; Rialon, K.; Kittrell, C.; Ramesh, S.; Hauge, R. H.; Smalley, R. E. Reversible, Band-Gap-Selective Protonation of Single-Walled Carbon Nanotubes in Solution. *J. Phys. Chem. B* **2003**, *107*, 6979−6985.

(26) Kim, S. M.; Jo, Y. W.; Kim, K. K.; Duong, D. L.; Shin, H.-J.; Han, J. H.; Choi, J.-Y.; Kong, J.; Lee, Y. H. Transparent Organic P-Dopant in Carbon Nanotubes: Bis(trifluoromethanesulfonyl)imide. *ACS Nano* **2010**, *4*, 6998−7004.

(27) Ausserlechner, S. J.; Gruber, M.; Hetzel, R.; Flesch, H.-G.; Ladinig, L.; Hauser, L.; Haase, A.; Buchner, M.; Resel, R.; Schürrer, F.; Stadlober, B.; Trimmel, G.; Zojer, K.; Zojer, E. Mechanism of surface proton transfer doping in pentacene based organic thin-film transistors. *Phys. Status Solidi A* **2012**, *209*, 181−192.

(28) Bridges, C. R.; Baumgartner, T. Lewis acids and bases as molecular dopants for organic semiconductors. *J. Phys. Org. Chem.* **2020**, *33*, No. e4077.

(29) Welch, G. C.; Coffin, R.; Peet, J.; Bazan, G. C. Band Gap Control in Conjugated Oligomers via Lewis Acids. *J. Am. Chem. Soc.* **2009**, *131*, 10802−10803.

(30) Zapata-Arteaga, O.; Perevedentsev, A.; Prete, M.; Busato, S.; Floris, P. S.; Asatryan, J.; Rurali, R.; Martín, J.; Campoy-Quiles, M. A Universal, Highly Stable Dopant System for Organic Semiconductors Based on Lewis-Paired Dopant Complexes. *ACS Energy Lett.* **2024**, *9*, 3567−3577.

(31) Zalar, P.; Henson, Z. B.; Welch, G. C.; Bazan, G. C.; Nguyen, T.-Q. Color Tuning in Polymer Light-Emitting Diodes with Lewis Acids. *Angew. Chem., Int. Ed.* **2012**, *51*, 7495−7498.

(32) Zalar, P.; Kuik, M.; Henson, Z. B.; Woellner, C.; Zhang, Y.; Sharenko, A.; Bazan, G. C.; Nguyen, T.-Q. Increased Mobility Induced by Addition of a Lewis Acid to a Lewis Basic Conjugated Polymer. *Adv. Mater.* **2014**, *26*, 724−727.

(33) Han, Y.; Barnes, G.; Lin, Y.-H.; Martin, J.; Al-Hashimi, M.; AlQaradawi, S. Y.; Anthopoulos, T. D.; Heeney, M. Doping of Large Ionization Potential Indenopyrazine Polymers via Lewis Acid Complexation with Tris(pentafluorophenyl)borane: A Simple Method for Improving the Performance of Organic Thin-Film Transistors. *Chem. Mater.* **2016**, *28*, 8016−8024.

(34) Yan, H.; Chen, J.; Zhou, K.; Tang, Y.; Meng, X.; Xu, X.; Ma, W. Lewis Acid Doping Induced Synergistic Effects on Electronic and Morphological Structure for Donor and Acceptor in Polymer Solar Cells. *Adv. Energy Mater.* **2018**, *8*, 1703672.

(35) Yan, H.; Tang, Y.; Sui, X.; Liu, Y.; Gao, B.; Liu, X.; Liu, S. F.; Hou, J.; Ma, W. Increasing Quantum Efficiency of Polymer Solar Cells with Efficient Exciton Splitting and Long Carrier Lifetime by Molecular Doping at Heterojunctions. *ACS Energy Lett.* **2019**, *4*, 1356−1363.

(36) Suh, E. H.; Kim, S. B.; Yang, H. S.; Jang, J. Regulating Competitive Doping in Solution-Mixed Conjugated Polymers for Dramatically Improving Thermoelectric Properties. *Adv. Funct. Mater.* **2022**, *32*, 2207413.

(37) Yurash, B.; Cao, D. X.; Brus, V. V.; Leifert, D.; Wang, M.; Dixon, A.; Seifrid, M.; Mansour, A. E.; Lungwitz, D.; Liu, T.; Santiago, P. J.; Graham, K. R.; Koch, N.; Bazan, G. C.; Nguyen, T.-Q. Towards understanding the doping mechanism of organic semiconductors by Lewis acids. *Nat. Mater.* **2019**, *18*, 1327−1334.

(38) Marqués, P. S.; Londi, G.; Yurash, B.; Nguyen, T.-Q.; Barlow, S.; Marder, S. R.; Beljonne, D. Understanding how Lewis acids dope organic semiconductors: a "complex" story. *Chem. Sci.* **2021**, *12*, 7012−7022.

(39) Vijayakumar, V.; Durand, P.; Zeng, H.; Untilova, V.; Herrmann, L.; Algayer, P.; Leclerc, N.; Brinkmann, M. Influence of dopant size and doping method on the structure and thermoelectric properties of PBTTT films doped with F6TCNNQ and F4TCNQ. *J. Mater. Chem. C* **2020**, *8*, 16470−16482.

(40) Lu, H.; Guo, Y.; Robertson, J. Charge transfer doping of graphene without degrading carrier mobility. *J. Appl. Phys.* **2017**, *121*, 224304.

(41) Tanaka, Y.; Hirana, Y.; Niidome, Y.; Kato, K.; Saito, S.; Nakashima, N. Experimentally Determined Redox Potentials of Individual (n,m) Single-Walled Carbon Nanotubes. *Angew. Chem., Int. Ed.* **2009**, *48*, 7655−7659.

(42) Park, K. H.; Lee, S.-H.; Toshimitsu, F.; Lee, J.; Park, S. H.; Tsuyohiko, F.; Jang, J.-W. Gate-enhanced photocurrent of (6,5) single-walled carbon nanotube based field effect transistor. *Carbon* **2018**, *139*, 709−715.

(43) Graf, A.; Zakharko, Y.; Schießl, S. P.; Backes, C.; Pfohl, M.; Flavel, B. S.; Zaumseil, J. Large scale, selective dispersion of long single-walled carbon nanotubes with high photoluminescence quantum yield by shear force mixing. *Carbon* **2016**, *105*, 593−599.

(44) Lindenthal, S.; Settele, S.; Hellmann, J.; Schmitt, K.; Zaumseil, J. A Hands-On Guide to Shear Force Mixing of Single-Walled Carbon Nanotubes with Conjugated Polymers. *arXiv* **2023**, arXiv:2311.11654v1.

(45) Pfohl, M.; Tune, D. D.; Graf, A.; Zaumseil, J.; Krupke, R.; Flavel, B. S. Fitting Single-Walled Carbon Nanotube Optical Spectra. *ACS Omega* **2017**, *2*, 1163−1171.

(46) Shea, M. J.; Mehlenbacher, R. D.; Zanni, M. T.; Arnold, M. S. Experimental Measurement of the Binding Configuration and Coverage of Chirality-Sorting Polyfluorenes on Carbon Nanotubes. *J. Phys. Chem. Lett.* **2014**, *5*, 3742−3749.

(47) Eckstein, K. H.; Oberndorfer, F.; Achsnich, M. M.; Schöppler, F.; Hertel, T. Quantifying Doping Levels in Carbon Nanotubes by Optical Spectroscopy. *J. Phys. Chem. C* **2019**, *123*, 30001−30006.

(48) Hawkey, A.; Dash, A.; Rodríguez-Martínez, X.; Zhao, Z.; Champ, A.; Lindenthal, S.; Zharnikov, M.; Kemerink, M.; Zaumseil, J. Ion-Exchange Doping of Semiconducting Single-Walled Carbon Nanotubes. *Adv. Mater.* **2024**, *36*, 2404554.

(49) Liu, Y.; Zhao, Z.; Kang, L.; Qiu, S.; Li, Q. Molecular Doping Modulation and Applications of Structure-Sorted Single-Walled Carbon Nanotubes: A Review. *Small* **2024**, *20*, 2304075.

(50) Eckstein, K. H.; Kunkel, P.; Voelckel, M.; Schöppler, F.; Hertel, T. Trions, Exciton Dynamics, and Spectral Modifications in Doped Carbon Nanotubes: A Singular Defect-Driven Mechanism. *J. Phys. Chem. C* **2023**, *127*, 19659−19667.

(51) Hartmann, N. F.; Pramanik, R.; Dowgiallo, A.-M.; Ihly, R.; Blackburn, J. L.; Doorn, S. K. Photoluminescence Imaging of Polyfluorene Surface Structures on Semiconducting Carbon Nanotubes: Implications for Thin Film Exciton Transport. *ACS Nano* **2016**, *10*, 11449−11458.

(52) Wrackmeyer, B. Organoboranes and tetraorganoborates studied by 11B and 13C NMR spectroscopy and DFT calculations. *Z. Naturforsch., B* **2015**, *70*, 421−424.

(53) Yurash, B.; Leifert, D.; Reddy, G. N. M.; Cao, D. X.; Biberger, S.; Brus, V. V.; Seifrid, M.; Santiago, P. J.; Köhler, A.; Chmelka, B. F.; Bazan, G. C.; Nguyen, T.-Q. Atomic-Level Insight into the Postsynthesis Band Gap Engineering of a Lewis Base Polymer Using Lewis Acid Tris(pentafluorophenyl)borane. *Chem. Mater.* **2019**, *31*, 6715−6725.

(54) Beringhelli, T.; Maggioni, D.; D'Alfonso, G. 1H and 19F NMR Investigation of the Reaction of B(C6F5)3 with Water in Toluene Solution. *Organometallics* **2001**, *20*, 4927−4938.

(55) Bovey, F. A. The high resolution NMR spectroscopy of polymers. *Prog. Polym. Sci.* **1971**, *3*, 1−108.

(56) Stanton, N. J.; Ihly, R.; Norton-Baker, B.; Ferguson, A. J.; Blackburn, J. L. Solution-phase p-type doping of highly enriched semiconducting single-walled carbon nanotubes for thermoelectric thin films. *Appl. Phys. Lett.* **2021**, *119*, 023302.

(57) Schneider, S.; Lefebvre, J.; Diercks, N. J.; Berger, F. J.; Lapointe, F.; Schleicher, J.; Malenfant, P. R. L.; Zaumseil, J. Phenanthroline Additives for Enhanced Semiconducting Carbon Nanotube Dispersion Stability and Transistor Performance. *ACS Appl. Nano Mater.* **2020**, *3*, 12314−12324.

(58) Berton, N.; Lemasson, F.; Poschlad, A.; Meded, V.; Tristram, F.; Wenzel, W.; Hennrich, F.; Kappes, M. M.; Mayor, M. Selective Dispersion of Large-Diameter Semiconducting Single-Walled Carbon Nanotubes with Pyridine-Containing Copolymers. *Small* **2014**, *10*, 360−367.

(59) Gu, J.; Han, J.; Liu, D.; Yu, X.; Kang, L.; Qiu, S.; Jin, H.; Li, H.; Li, Q.; Zhang, J. Solution-Processable High-Purity Semiconducting SWCNTs for Large-Area Fabrication of High-Performance Thin-Film Transistors. *Small* **2016**, *12*, 4993−4999.

SUPPLEMENTARY INFORMATION

Synergistic p-Doping of Polymer-Wrapped Small-Diameter Single-Walled Carbon Nanotubes by Tris(pentafluorophenyl)borane

Sebastian Lindenthal[1], Daniel Rippel[1], Lukas Kistner[2], Angus Hawkey[1], Jana Zaumseil,[1]*

[1]Institute for Physical Chemistry, Heidelberg University, D-69120 Heidelberg, Germany

[2]Institute for Inorganic Chemistry, Heidelberg University, D-69120 Heidelberg, Germany

*E-mail: zaumseil@uni-heidelberg.de

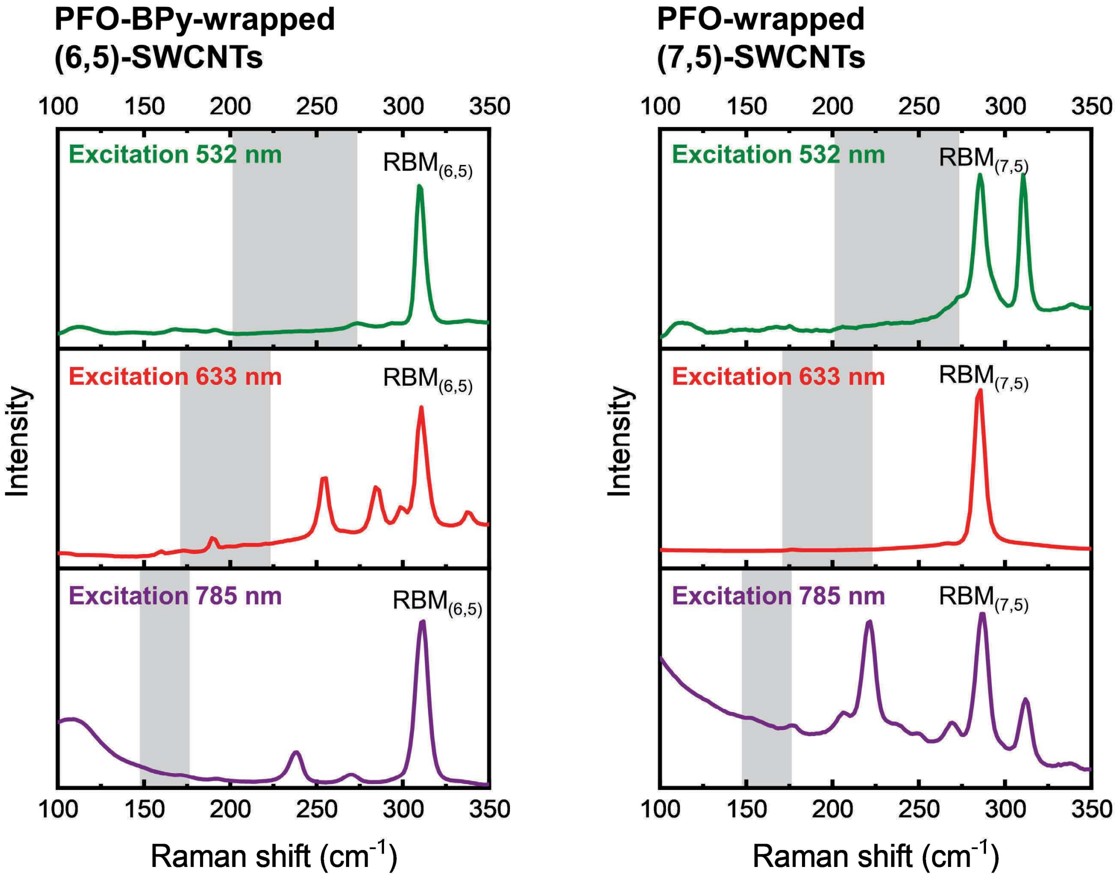

Figure S1. Raman spectra of drop-cast films of polymer-wrapped SWCNT dispersions, measured with three different excitation wavelengths (532 nm, 633 nm, and 785 nm). Radial breathing modes of (6,5) SWCNTs and (7,5) SWCNTs are labelled. Areas highlighted in grey indicate regions in which RBM modes of metallic SWCNTs would be expected. Due to different resonance conditions, RBM modes of additional semiconducting SWCNTs are also visible. Raman spectra were acquired with a Renishaw inVia confocal Raman microscope in backscattering configuration equipped with a 50× long working distance objective (N.A. 0.5, Olympus). To minimize the influence of spot-to-spot variations, maps with >500 spectra were recorded and averaged.

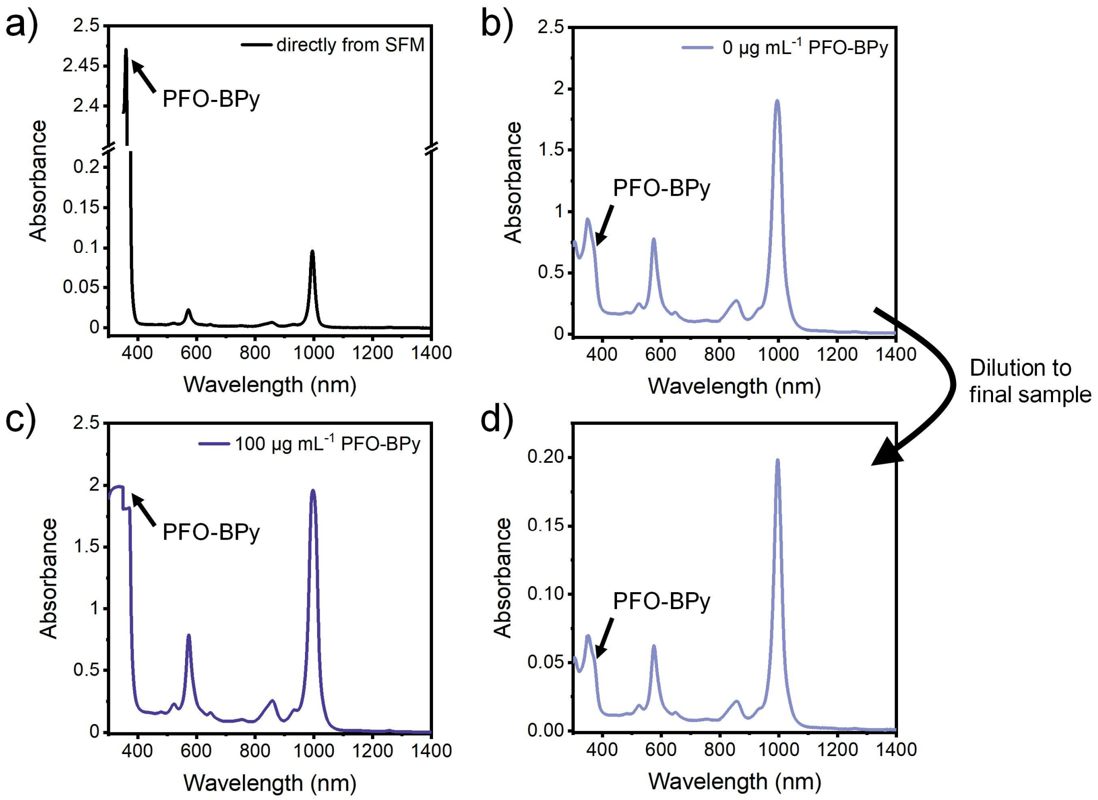

Figure S2. a) Absorption spectrum of (6,5) SWCNTs as obtained from shear force mixing (SFM) after centrifugation. **b)** Absorption spectrum of (6,5) SWCNTs after polymer removal and redispersion in pure toluene. **c)** Absorption spectrum of (6,5) SWCNTs after polymer removal and redispersion in a solution of 100 µg mL^{-1} PFO-BPy in toluene. **d)** Absorption spectrum of a (6,5) SWCNT dispersion that was obtained from the dispersion shown in Figure S2b *via* dilution. Note, that the dilution leads to a further decrease of PFO-BPy absorption (*i.e.*, concentration).

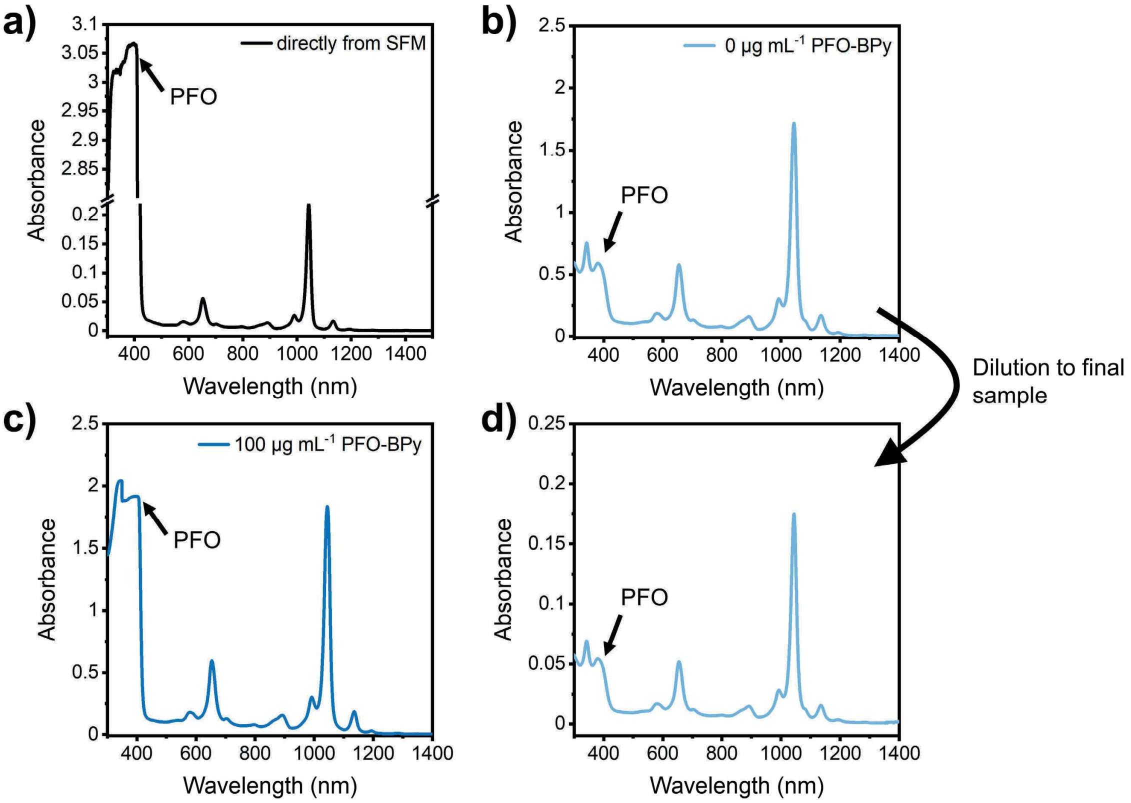

Figure S3. a) Absorption spectrum of (7,5) SWCNTs as obtained from shear force mixing and centrifugation. **b)** Absorption spectrum of (7,5) SWCNTs after polymer removal and redispersion in pure toluene. **c)** Absorption spectrum of (7,5) SWCNTs after polymer removal and redispersion in a solution of 100 µg mL^{-1} PFO in toluene. **d)** Absorption spectrum of a (7,5) SWCNT dispersion that was obtained from the dispersion shown in Figure S3b *via* dilution. Note, that the dilution leads to a further decrease of PFO absorption (*i.e.*, concentration).

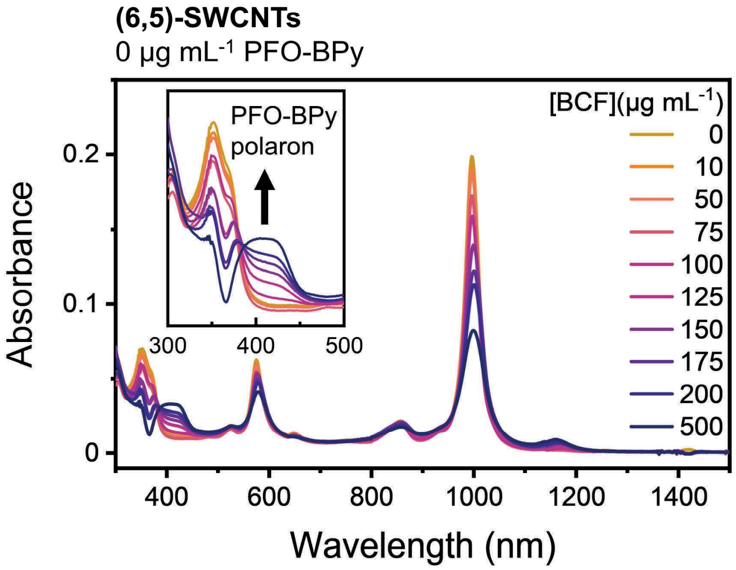

Figure S4. Absorption spectra of (6,5) SWCNTs, redispersed in pure toluene, doped with a wide range of BCF concentrations.

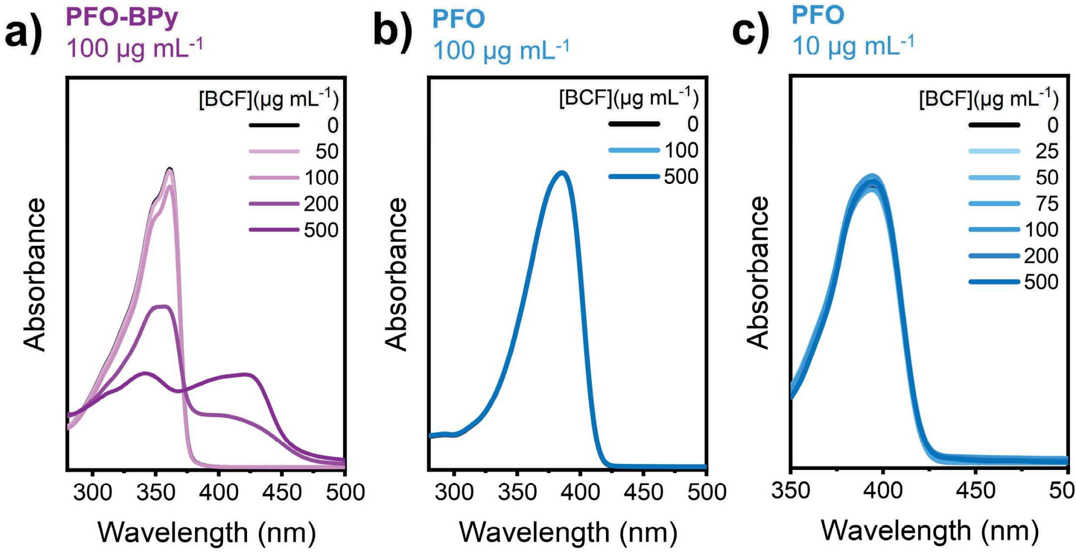

Figure S5. a) Absorption spectra of a 100 µg mL^{-1} solution of PFO-BPy in toluene, doped with different amounts of BCF. **b)** Absorption spectra of a 100 µg mL^{-1} solution of PFO in toluene, doped with different amounts of BCF. **c)** Absorption spectra of a 10 µg mL^{-1} solution of PFO in toluene, doped with different amounts of BCF.

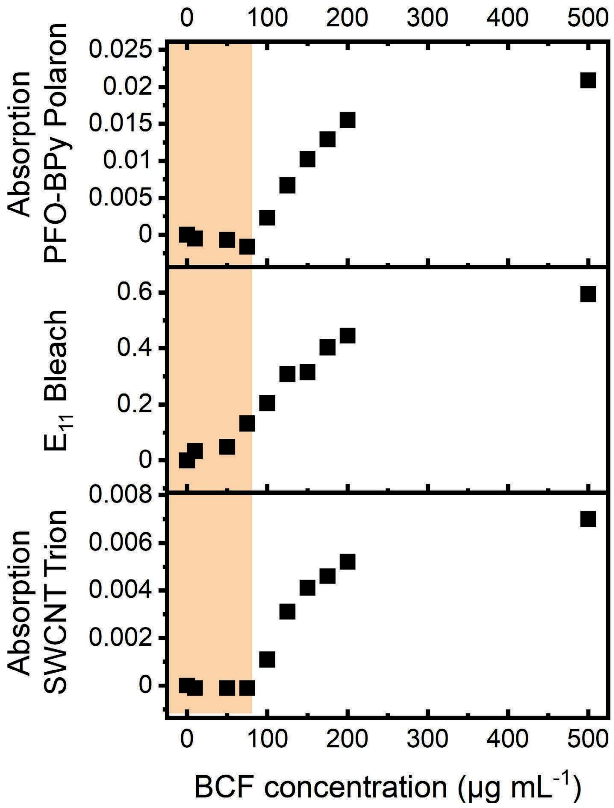

Figure S6. PFO-BPy polaron absorption, E_{11} bleach and SWCNT trion absorption against BCF doping concentration for doping of (6,5) SWCNTs at a PFO-BPy concentration of 0 µg mL^{-1}. The highlighted area indicates the region in which the polymer is not yet doped.

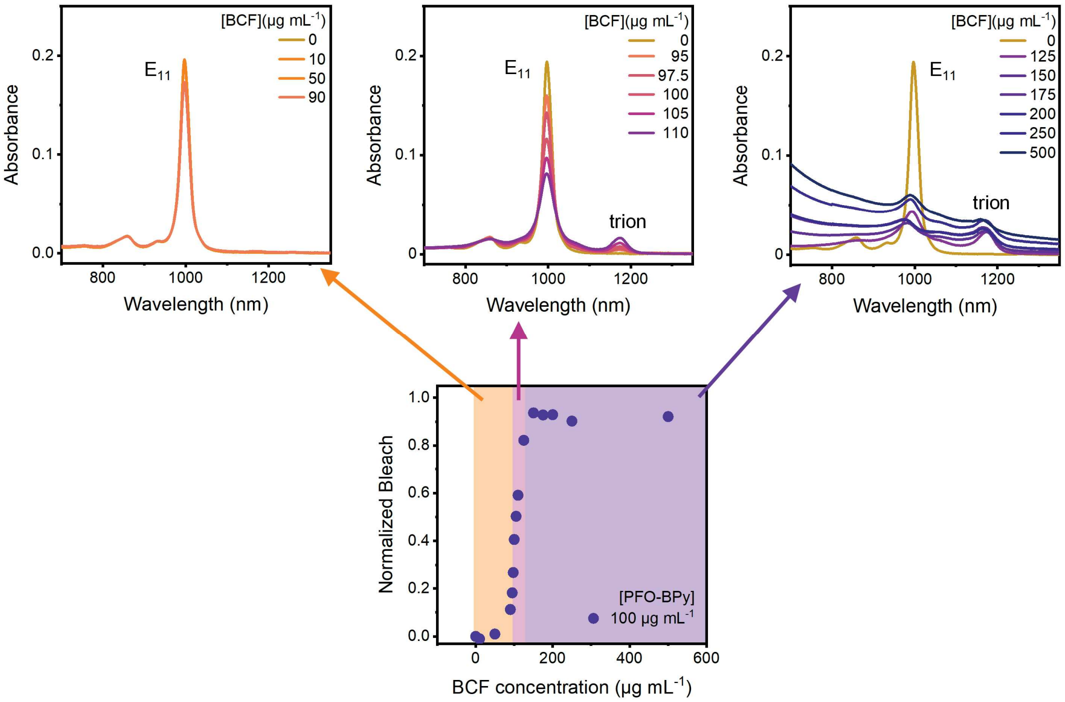

Figure S7. Analysis of absorption spectra for BCF doping of (6,5) SWCNTs at a PFO-BPy concentration of 100 µg mL^{-1}. The lower graph depicts the calculated bleaching as a function of BCF concentration. It is divided into three regions representing different doping behavior: no doping (orange), rapid onset of doping (pink), and a strongly doped region (purple). Corresponding absorption spectra are shown above. The upper graphs show absorption spectra for 0-90 µg mL^{-1} (left), 95-110 µg mL^{-1} (middle) and 125-500 µg mL^{-1} (right) BCF. The absorption spectrum of the undoped sample (dark yellow) is shown as a reference in all spectra.

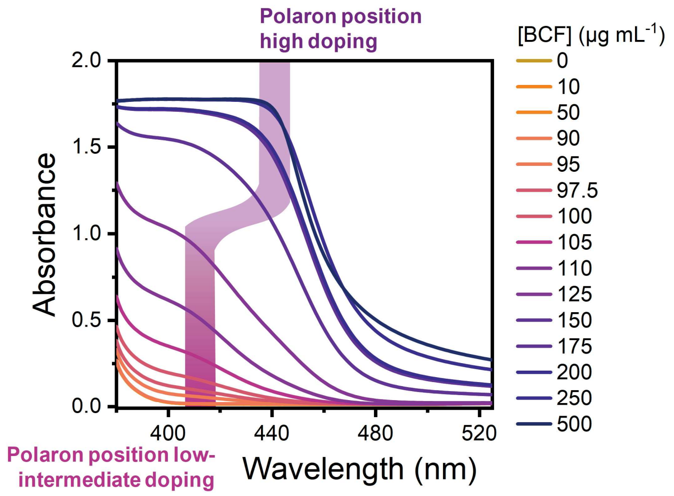

Figure S8. Zoom in on the PFO-BPy polaron peak for BCF doping of (6,5) SWCNTs at a PFO-BPy concentration of 100 µg mL^{-1} The change in polaron peak position from 410 nm to 445 nm for a BCF concentration from 110 to 150 µg mL^{-1} is indicated by the highlighted area.

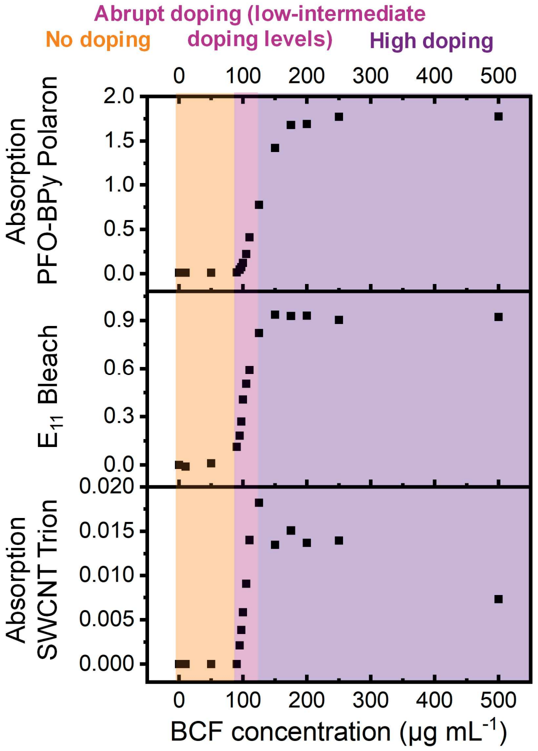

Figure S9. PFO-BPy polaron absorption, E_{11} bleach and SWCNT trion absorption (from Figures S7, S8) against BCF doping concentration for doping of (6,5) SWCNTs at a PFO-BPy concentration of 100 µg mL^{-1}. The highlighted areas indicate regions of no doping (orange), low-intermediate doping (pink) and high doping levels (purple).

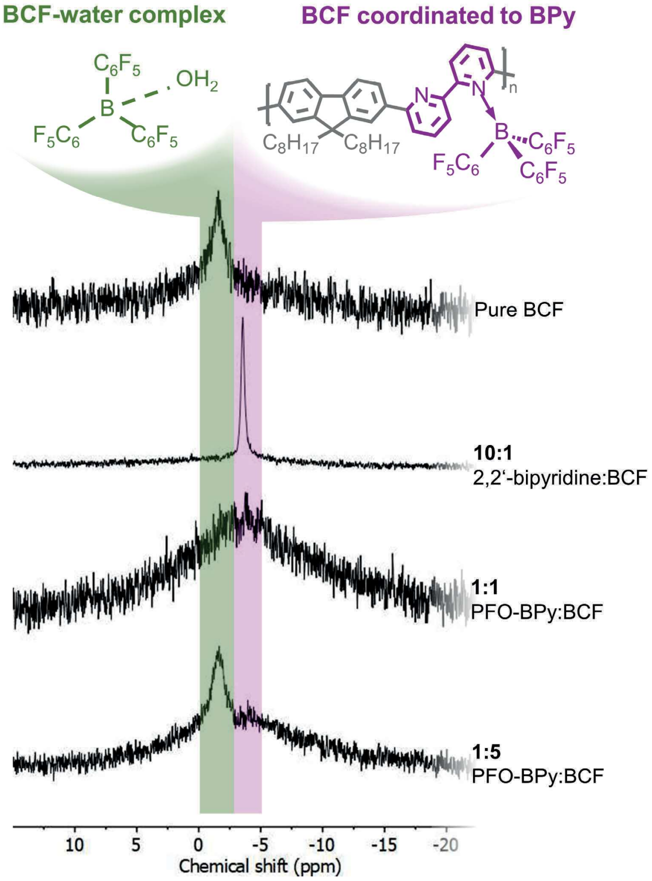

Figure S10. ^{11}B-NMR spectra (192.56 MHz, d^8-toluene) of pure BCF, a 10:1 molar ratio of 2,2'-bipyridine:BCF, a 1:1 molar ratio of PFO-BPy:BCF and a 1:5 molar ratio of PFO-BPy:BCF (top to bottom). Green highlighted regions mark peaks associated with BCF:water complexes, purple regions peaks associated with BCF:BPy complexes. Schematic depictions of complexes are shown above the NMR spectra.

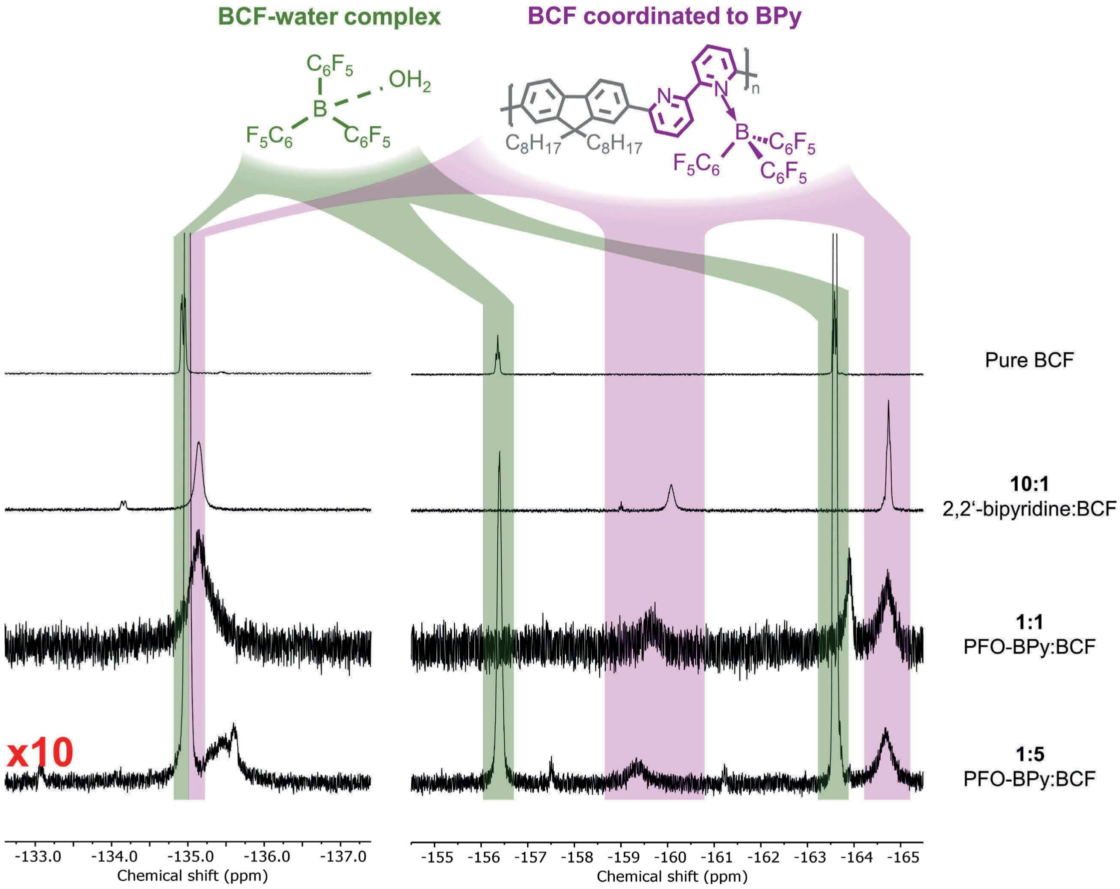

Figure S11. ^{19}F-NMR spectra of pure BCF, a 10:1 molar ratio of 2,2'-bipyridine:BCF, a 1:1 molar ratio of PFO-BPy:BCF and a 1:5 molar ratio of PFO-BPy:BCF (top to bottom). The intensity of the latter spectrum is scaled up by a factor of 10 to show the broad peaks associated with the BCF:PFO-BPy complex. Green highlighted regions indicate peaks associated with BCF:water complexes, purple regions correspond to peaks associated with BCF:BPy complexes. Schematic depictions of complexes are shown above the NMR spectra.

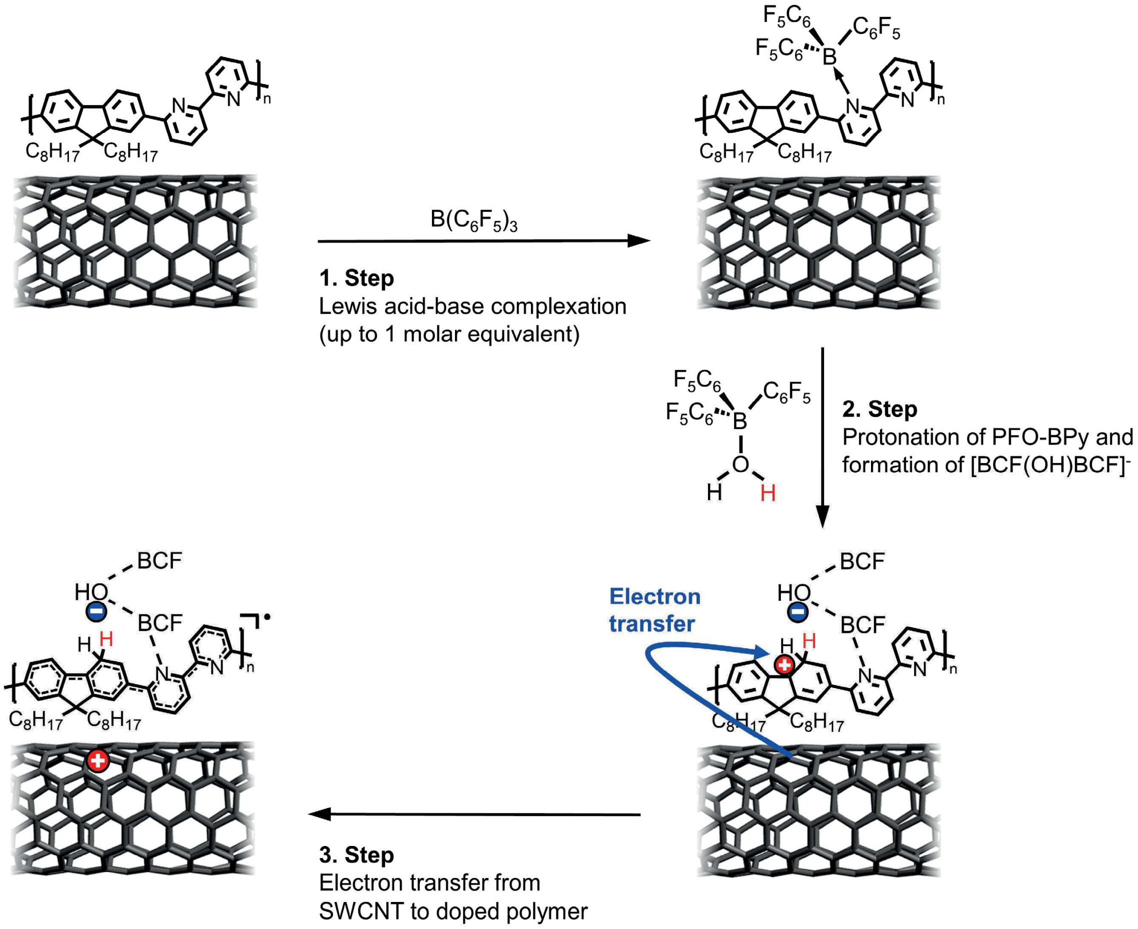

Figure S12. Proposed mechanism for p-doping of PFO-BPy-wrapped (6,5)-SWCNTs with BCF. In a first step, BCF is complexed by the bipyridine moieties of the PFO-BPy, which wraps the SWCNT (for clarity the polymer is just shown adjacent to the SWCNT). Upon addition of further BCF, Brønsted acidic $BCF(OH)_2$ complexes are formed (with residual water in the solvent) that protonate the wrapping polymer and form $[BCF(OH)BCF]^-$ anions with the BCF molecule complexed to the BPy moieties. In a final step, an electron is transferred from the nanotube to the protonated wrapping polymer. The electron transfer from the SWCNT to the polymer is favourable due to the much lower ionization energy of the nanotube compared to PFO-BPy and the stabilization of the hole on the SWCNT by delocalization.

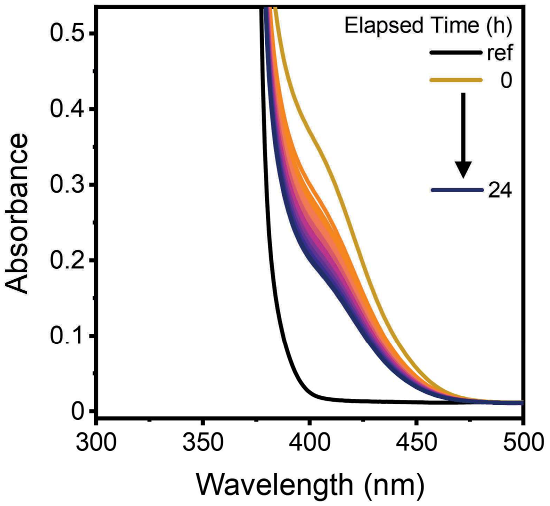

Figure S13. Zoom in on the PFO-BPy polaron peak for BCF doping (120 µg mL^{-1}) of (6,5) SWCNTs at a PFO-BPy concentration of 100 µg mL^{-1}, showing a clear decrease of PFO-BPy polaron over time.

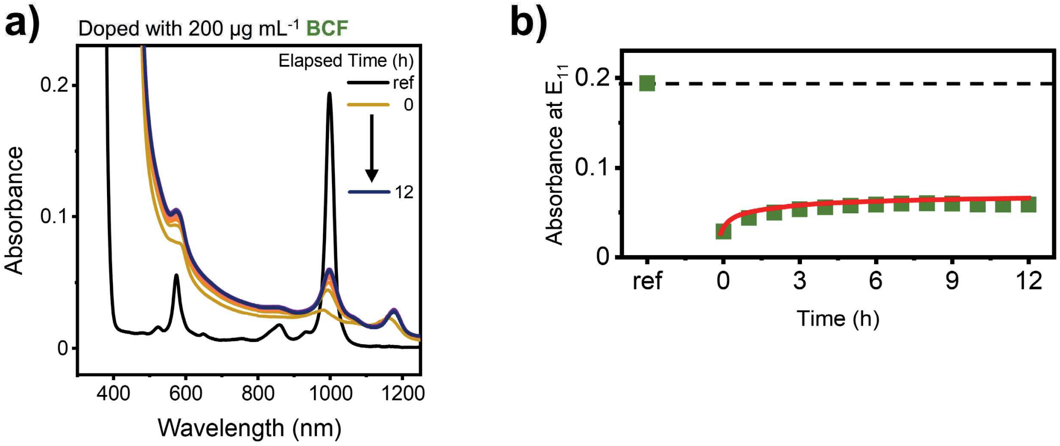

Figure S14. a) Absorption spectra of (6,5) SWCNTs at a polymer concentration of 100 µg mL^{-1} doped with 200 µg mL^{-1} BCF over the course of 12 h. **b)** E_{11} absorption of (6,5) SWCNTs doped with 200 µg mL^{-1} BCF plotted against elapsed time. The absorbance of the undoped sample is marked by a dashed line. The red line serves as a guide to the eye.

Figure S15. Photographs of cuvettes, filled with a (6,5) SWCNT dispersion at a PFO-BPy concentration of 100 µg mL^{-1} and doped with 40 µg mL^{-1} $AuCl_3$ (left) or with 120 µg mL^{-1} BCF (right). The images were taken after not moving the cuvettes for 24 h. The left image shows severe aggregation of the SWCNTs for $AuCl_3$ doping. No visible aggregation is observed for BCF doping (right image). Note that in the right image, a cuvette with sidewalls made of black glass was used.

CHAPTER 5

PUBLICATION P3

Understanding the Optical Properties of Doped and Undoped 9-Armchair Graphene Nanoribbons in Dispersion

Lindenthal, S.; Fazzi, D.; Zorn, N. F.; El Yumin, A. A.; Settele, S.; Weidinger, B.; Blasco, E.; Zaumseil, J.

ACS Nano **2023,** *17*, 18240-18252

https://doi.org/10.1021/acsnano.3c05246

In this project, the optical properties of undoped and p-doped solution-synthesized 9-aGNRs in dispersion are investigated. For this, a method to disperse and sort GNRs by defectiveness is developed. The optical properties of pristine and defective GNRs are investigated by absorption, (single-ribbon) photoluminescence and Raman spectroscopy. Additionally, DFT calculations are performed to corroborate findings from spectroscopic experiments. Finally, GNRs are chemically doped using the strong electron acceptor F_4TCNQ which leads to polaronic features in their absorption spectra.

Formblatt Kumulative Dissertation

1. **Publikation:** Vollständige bibliographische Referenz/*Complete bibliographic reference*:

Lindenthal, S.; Fazzi, D.; Zorn, N. F.; El Yumin, A. A.; Settele, S.; Weidinger, B.; Blasco, E.; Zaumseil, J., Understanding the Optical Properties of Doped and Undoped 9-Armchair Graphene Nanoribbons in Dispersion. *ACS Nano* **2023,** *17*, 18240-18252, https://doi.org/10.1021/acsnano.3c05246.

2. **Erst- oder gleichberechtigte Autorenschaft/*First or equal authorship*:**

☒ Ja/*yes* ☐ Nein/*no*

3. **Status der Veröffentlichung/*Status of publication*:**

☒ Veröffentlicht/*Published*
☐ Zur Veröffentlichung angenommen/*Accepted*
☐ Eingereicht/*Submitted*
☐ Noch nicht eingereicht/*Not yet submitted*

4. **Beteiligungen/*Contributions***:**

	Doktorand/in/*Doctoral student*
Name, first name	**Lindenthal, Sebastian**
Methodology	X
Software	
Validation	X
Formal Analysis	X
Investigation	X
Resources	
Data Curation	X
Writing – Original Draft	X
Writing – Review & Editing	X
Visualization	X
Supervision	
Project Administration	
Funding Acquisition	

****Kategorien des CRediT (*Contributor Roles Taxonomy*, https://credit.niso.org/)**

Hiermit bestätige ich, dass alle obigen Angaben korrekt sind/*I confirm that all declarations made above are correct.*

Unterschrift/*Signature* ____________
Doktorand/in/*Doctoral student*

Betreuungsperson/*Supervisor*:
Hiermit bestätige ich, dass alle obigen Angaben korrekt sind und dass die selbstständigen Arbeitsanteile des Doktoranden an der aufgeführten Publikation hinreichend und signifikant sind/*I confirm that all declarations made above are correct and that the doctoral student's independent contribution to this publication is significant and sufficient to be considered for the cumulative dissertation.*

Prof. Dr. Jana Zaumseil
Name/*Name*

Unterschrift/*Signature*

22.5.2025
Datum/*Date*

ACS NANO

Open Access

www.acsnano.org

ARTICLE

Understanding the Optical Properties of Doped and Undoped 9-Armchair Graphene Nanoribbons in Dispersion

Sebastian Lindenthal, Daniele Fazzi, Nicolas F. Zorn, Abdurrahman Ali El Yumin, Simon Settele, Britta Weidinger, Eva Blasco, and Jana Zaumseil*

Cite This: *ACS Nano* 2023, 17, 18240−18252

Read Online

ACCESS | Metrics & More | Article Recommendations | Supporting Information

ABSTRACT: Graphene nanoribbons are one-dimensional stripes of graphene with width- and edge-structure-dependent electronic properties. They can be synthesized bottom-up in solution to obtain precise ribbon geometries. Here we investigate the optical properties of solution-synthesized 9-armchair graphene nanoribbons (9-aGNRs) that are stabilized as dispersions in organic solvents and further fractionated by liquid cascade centrifugation (LCC). Absorption and photoluminescence spectroscopy reveal two near-infrared absorption and emission peaks whose ratios depend on the LCC fraction. Low-temperature single-nanoribbon photoluminescence spectra suggest the presence of two different nanoribbon species. Based on density functional theory (DFT) and time-dependent DFT calculations, the lowest energy transition can be assigned to pristine 9-aGNRs, while 9-aGNRs with edge-defects, caused by incomplete graphitization, result in more blue-shifted transitions and higher Raman D/G-mode ratios. Hole doping of 9-aGNR dispersions with the electron acceptor F_4TCNQ leads to concentration dependent bleaching and quenching of the main absorption and emission bands and the appearance of red-shifted, charge-induced absorption features but no additional emission peaks, thus indicating the formation of polarons instead of the predicted trions (charged excitons) in doped 9-aGNRs.

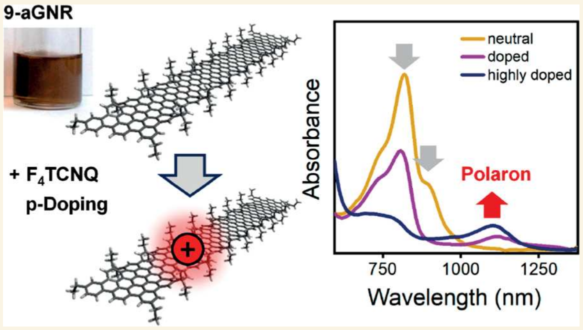

KEYWORDS: *nanoribbons, bottom-up synthesis, doping, trion, polaron*

INTRODUCTION

Graphene nanoribbons (GNRs) are quasi-one-dimensional, nanometer-wide stripes of graphene with an electronic band structure that directly depends on their width and edge geometry.[1−3] Graphene nanoribbons with zigzag edges (zGNRs) show metallic behavior, while nanoribbons with armchair edges (n-aGNRs) are semiconductors. Here, n stands for the number of carbon dimer lines perpendicular to the long axis of the GNR and thus indicates the width. Semiconducting aGNRs are interesting as alternatives to graphene and carbon nanotubes for nanoscale optoelectronic devices. Similar to nanotubes, precise control over the structure of GNRs is required to take advantage of their intrinsic electronic and optical properties.

GNRs can be created by different methods. While top-down techniques, such as electron beam lithography[4] and plasma etching[5] of graphene or unzipping of multiwalled carbon nanotubes,[6] only yield GNRs with a broad width distributions and undefined edge geometries, bottom-up synthesis enables the creation of atomically precise GNRs with a distinct electronic structure. Two different bottom-up approaches are commonly used. The first approach utilizes Ullmann-type coupling of molecular precursors on suitable metal surfaces.[7,8] This method produces pristine GNRs with high precision but the yield is limited by the substrate surface, and subsequent transfer to another substrate is necessary to investigate optical properties or to create nanoelectronic devices.[9,10] In contrast to that, solution-mediated synthesis can produce large amounts of a wide variety of GNRs with precise width and edge geometry.[11,12] However, the resulting GNRs are usually polydisperse in length and, due to strong intermolecular

Received: June 10, 2023
Accepted: September 7, 2023
Published: September 11, 2023

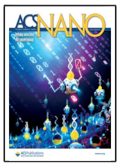

https://doi.org/10.1021/acsnano.3c05246

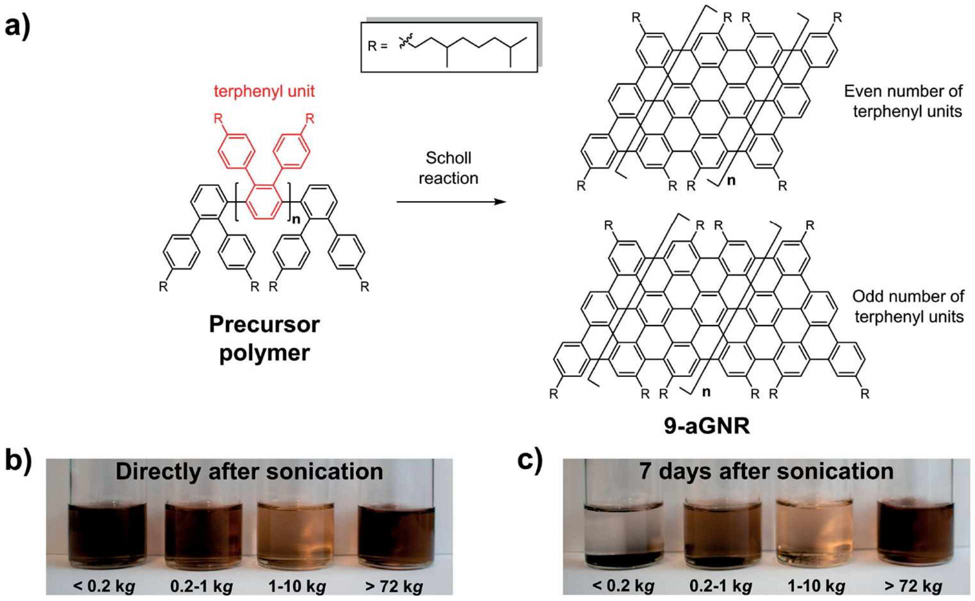

Figure 1. (a) Bottom-up synthesis of 9-aGNRs via a Scholl reaction of the precursor polymer. The precise shape of the 9-aGNRs depends on the number (odd or even) of terphenyl units (red) in the precursor polymer. (b) Photograph of size-selected dispersions of 9-aGNRs directly after sonication in THF. (c) Same dispersions of 9-aGNRs left undisturbed for 7 days after sonication.

interactions, tend to aggregate quickly.[13] Bulky side groups, e.g., branched alkyl chains, along the GNR edges help to prevent aggregation and improve solution processability but can also alter their intrinsic properties.[14−16] Sonication or shear force mixing of GNRs in suitable solvents, e.g., *N*-methylpyrrolidone (NMP), can help to create dispersions with good stability,[17,18] although film deposition from NMP is difficult due to its high boiling point.

Despite these challenges, the bottom-up synthesis of GNRs has facilitated a number of studies of their electronic and optical properties. The predicted dependence of the bandgap on width was confirmed by scanning tunneling spectroscopy of different on-surface-synthesized aGNRs.[19] Theoretical and experimental studies revealed that their optical spectra are dominated by excitonic transitions.[20−22] Additionally, photoluminescence (PL) lifetimes on the order of nanoseconds and good photoluminescence quantum yields (PLQY) of up to 80% were reported.[16,23]

Furthermore, ambipolar charge transport and electroluminescence were observed from bottom-up synthesized aGNRs,[24−26] which raises the question of the impact of charge carriers on the spectroscopic properties of GNRs. Similar low-dimensional materials, such as one-dimensional single-walled carbon nanotubes (SWNTs) or two-dimensional transition metal dichalcogenides (TMDs), exhibit additional optical transitions upon chemical, electrochemical or electrostatic doping.[27−31] Characteristic transitions emerge from the interaction of charges (electrons or holes) with excitonic states in these nanomaterials, thus forming quasiparticles—called trions or charged excitons—with red-shifted emission. The trion binding energy (roughly the energy offset between exciton and trion) increases when the dimensionality of the nanomaterial is reduced.[32] Reported values are in the range of a few tens of meV for TMDs[29,31,33] and 100−150 meV for SWNTs.[27,28,30]

Deilmann et al. predicted large trion binding energies on the order of several hundreds of meV for freestanding GNRs.[32] Consequently, the corresponding optical transitions should be observable for doped GNRs. However, the spectroscopic investigation of doped nanoribbons has been hindered by substrate-induced photoluminescence quenching and low yields for on-surface synthesized aGNRs, as well as aggregation issues for solution-synthesized aGNRs. It remains unclear whether solution-synthesized aGNRs can show trionic features upon doping similar to rigid SWNTs or rather exhibit charge-induced quenching and polaron formation due to strong electron−phonon coupling. Polarons are ground state quasiparticles consisting of a charge coupled to a lattice distortion and are typically observed in the absorption spectra of doped polymers.[34,35]

Here we create stable dispersions of solution-synthesized 9-aGNRs through exfoliation in common and easy-to-process organic solvents. Further purification by liquid cascade centrifugation (LCC) yields dispersion fractions with slightly different absorption, photoluminescence, and Raman spectra, indicating the presence of more than one 9-aGNR species. Low-temperature single-nanoribbon spectroscopy and quantum-chemical calculations are used to gain further insights into the structural and optoelectronic properties of these 9-aGNRs and to propose a possible origin of these different species. Finally, the impact of chemical doping with a strong molecular electron acceptor (F_4-TCNQ) on the absorption and emission spectra of 9-aGNRs in dispersion is demonstrated and discussed.

RESULTS AND DISCUSSION

Synthesis, Dispersion, and Liquid Cascade Centrifugation of 9-aGNRs. 9-aGNRs (see Figure 1a) were selected for this study based on their reported bandgap values ranging from 1.1 to 1.4 eV,[19,36,37] resulting in near-infrared (nIR) absorption and emission bands that should still enable the resolution of strongly red-shifted doping-induced features with common InGaAs detectors. The nanoribbons were synthesized via a solution-based method previously reported by Li et al. (for details see Supporting Information, Scheme S1).[36] Briefly, a terphenyl derivative was polymerized in an AB-type Suzuki

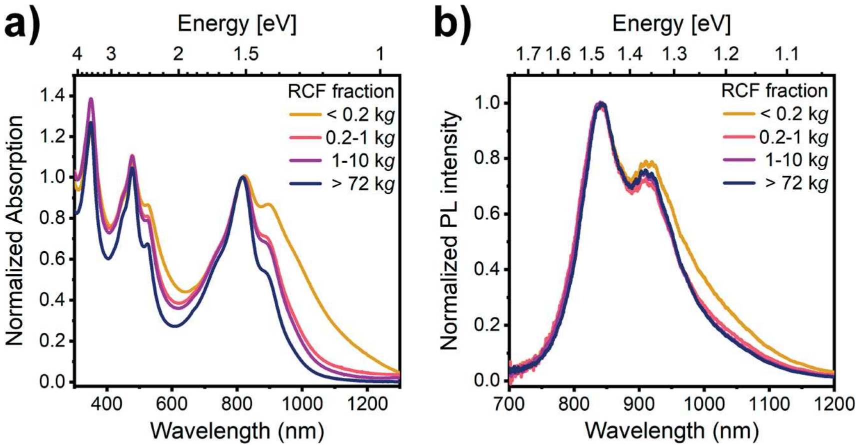

Figure 2. (a) Absorption spectra of size-selected 9-aGNR dispersions in THF normalized to the absorption band at 817 nm. (b) PL spectra of size selected 9-aGNR dispersions in THF (excited with a pulsed laser at 535 nm) normalized to the emission peak at 840 nm.

reaction to yield the precursor polymer for 9-aGNR (see Figure 1a). The length of the polymer and thus the length of the GNR depend on the number of terphenyl units (marked in red in Figure 1a) that are coupled during the polymerization reaction. Size exclusion chromatography (SEC) of the precursor polymer using a polystyrene standard revealed a molecular weight of 30.8 kDa with a polydispersity of 1.46 (see Supporting Information and Figure S1a). These values are in good agreement with reports by Li et al.[36] and would correspond to an average precursor length of ∼25 nm. However, SEC is likely to overestimate the molecular weight of the precursor polymer. Matrix-assisted laser-desorption ionization time-of-flight (MALDI-TOF) mass spectrometry of the precursor polymer showed peaks up to only 17 kDa (see Supporting Information and Figure S1b), corresponding to a length of up to 15 nm. Mass spectrometry typically underestimates the molecular weight of polymers, as longer polymer chains are less likely to desorb into the sample chamber and have a higher probability of undergoing fragmentation reactions. Nevertheless, both measurements show that the precursor is polydisperse with a length between 15 and 25 nm. This polydispersity should be retained when the polymer is converted into the 9-aGNR by a Scholl reaction. Atomic force microscopy images of self-assembled 9-aGNR islands on highly ordered pyrolytic graphite (HOPG) show small gaps and reveal that these islands consist of GNRs with different lengths (Supporting Information and Figure S2).

One way to reduce the polydispersity of a nanomaterial dispersion is liquid cascade centrifugation (LCC).[38] In LCC, a stock dispersion is prepared from raw material by sonication in a suitable solvent. It is then subjected to centrifugation steps at increasing rotational centrifugal fields (RCF). Particles that were sedimented during one centrifugation step are collected and redispersed in fresh solvent for the next centrifugation step. Backes et al. showed that for 2D materials such as graphene nanosheets or TMDs, LCC leads to a decrease in size and layer number in the sediments for increasing RCF values.[38−40]

Despite previous reports about the instability of dispersions of GNRs without bulky side chains, the as-synthesized 9-aGNR powder could be readily dispersed in tetrahydrofuran (THF) or toluene by a simple bath sonication. The resulting stock dispersions were then subjected to centrifugation steps at increasing RCF values of 200, 1000, 10000, and 72000*g*, yielding five different fractions, which will be referred to by their RCF values (<0.2 kg, 0.2−1 kg, 1−10 kg, 10−72 kg, >72 kg). For a detailed explanation of the LCC process, see Figure S3 (Supporting Information). The 10−72 kg fraction was discarded, as it barely contained any exfoliated material. Photographs of the other fractions in THF directly after sonication are shown in Figure 1b. The colors indicate the amount of exfoliated GNRs in the different fractions, with large quantities in the <0.2 kg, 0.2−1 kg, and >72 kg fractions. The dispersion stability depends highly on the RCF values during LCC. Differences in dispersion stability and aggregation behavior become apparent when dispersions are left undisturbed for 7 days (see Figure 1c). While the <0.2 kg fraction shows almost complete discoloration and a large amount of aggregated GNRs at the bottom of the vial, the appearance of the >72 kg fraction remains unaltered. The latter showed a dispersion stability of up to one year with no changes in appearance or spectroscopic properties.

Spectroscopic Characterization of 9-aGNR Dispersions. Due to the challenges of exfoliation and stabilization of solution-synthesized GNRs, little is known about their spectroscopic properties in dispersion. Here, we employed absorption and PL spectroscopy to investigate the influence of LCC on the optical properties of the 9-aGNR dispersions in the neutral state. Baseline-corrected absorption spectra of the different LCC fractions in THF are shown in Figure 2a. Strong absorption bands at 350, 477, 526, 817, and 900 nm are apparent that are similar to previously reported absorption spectra of 9-aGNR films[36] but substantially narrower. Absorption spectra of dispersions in toluene showed the same transitions and are presented in Figure S4 (Supporting Information). The uncorrected spectrum for the <0.2 kg fraction shows a large scattering background (Figure S5, Supporting Information), indicating a significant amount of unexfoliated material. A high content of unexfoliated material in the first fraction of LCC is also observed for other nanomaterials, such as TMDs, where it is usually discarded.[40] Absorption spectra measured over 10 h for the 0.2−1 kg and the >72 kg fractions (Figure S6) showed no changes of the observed peaks or the scattering background, thus demonstrating the high dispersion stability of the fractions obtained by LCC.

Interestingly, absorption spectra normalized to the band at 817 nm show a decreasing contribution of the absorption band

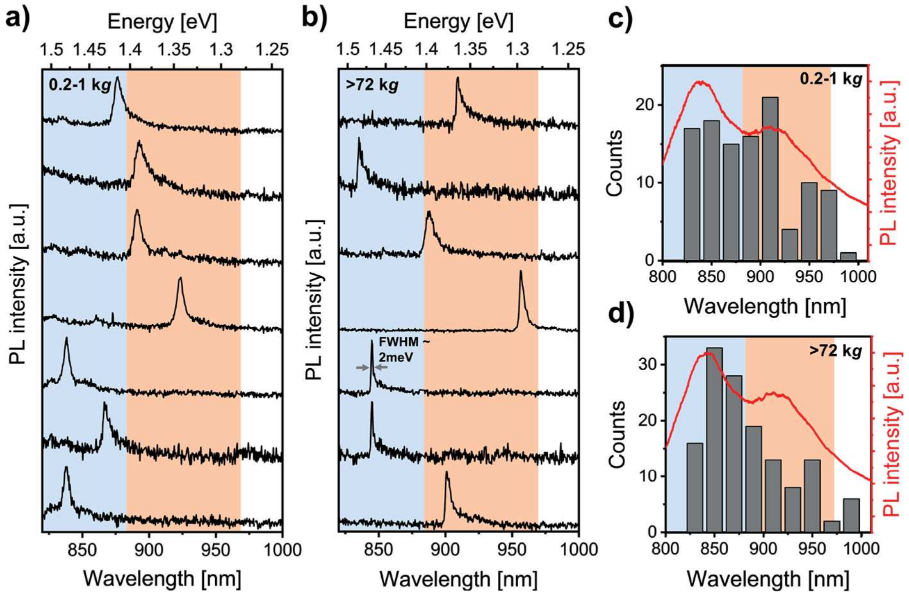

Figure 3. PL spectra at 4.6 K of 7 individual 9-aGNRs from the (a) 0.2−1 kg and (b) >72 kg fractions embedded in a polystyrene matrix (excitation wavelength 532 nm). Blue and orange areas highlight the spectral regions associated with the broader emission peaks at 840 and 910 nm of the corresponding dispersion at room temperature. (c) Histogram of peak positions extracted from 108 spectra for the 0.2−1 kg fraction. (d) Histogram of peak positions extracted from 133 spectra for the >72 kg fraction. The red lines represent the ensemble PL spectrum of the corresponding 0.2−1 kg and >72 kg 9-aGNR dispersions.

at 900 nm for increasing RCF values. The two lowest energy transitions could originate from two different populations of GNRs that exhibit different sedimentation behavior, or they could be intrinsic to a single GNR species and its aggregates. An absorption spectrum with several different transition bands within an energy range of 100−200 meV could be the result of vibronic coupling, as reported for polymers or polycyclic aromatic hydrocarbons. However, the ratios of the individual vibronic transitions are determined by the molecular structure and should not change, except when aggregates are present. Stronger blue-shifted absorption peaks may indicate the presence of H-aggregates that should be formed by GNRs (see below). LCC usually sorts nanomaterials by their sedimentation coefficients, which are influenced by structural parameters such as size, shape, defectiveness, layer number for TMDs and aggregation tendency.[38,39] Aggregates should sediment faster and thus should be more prominent in the low RCF fraction, which is the opposite of the observed trend here. Clearly, there is a separation of material with different sedimentation properties between RCF fractions, but it is not yet clear what these differences might be.

Normalized PL spectra of 9-aGNR dispersions in THF excited at 535 nm (see Figure 2b) exhibit two emission features at 840 and 910 nm. PL spectra of dispersions in toluene are shown in Figure S7 (Supporting Information). The corresponding photoluminescence excitation−emission (PLE) map (Figure S8) also shows two emission features at 840 and 910 nm that reach their maximum intensity when excited at 535 nm, corresponding well to the observed absorption band at 526 nm. Note that the general shape of the PL spectrum resembles the most red-shifted absorption features and is not a mirror image, as would be expected for a vibronic progression. The Stokes shifts of 40 meV for the emission peak at 840 nm and 15 meV for the peak at 910 nm indicate intrinsic PL originating from radiative exciton relaxation (i.e., no excimer emission such as from aggregates). This observation is further corroborated by the fact that time-correlated single photon counting (TCSPC) traces can be fitted with a simple monoexponential decay to determine the PL lifetime (Figure S9 and Supporting Information). The two different emission features exhibit very similar PL lifetimes between 1.0 and 1.2 ns (measured at 840 and 920 nm, see Figure S9, Supporting Information) that vary slightly but not significantly with RCF values and solvent. The RCF values also do not influence the intensity ratios of the two emission bands, in contrast to the absorption bands. However, there is a clear trend of increasing PLQY for increasing RCF fractions (Figure S10). The highest PLQYs are reached for the >72 kg fractions with 39% for dispersions in THF and 71% for dispersions in toluene. These PLQY values are quite good for organic near-infrared emitters in a wavelength range above 800 nm.[41] The increasing PLQY may also explain the similarities between the PL spectra of the different LCC fractions in Figure 2b compared to the differences in the absorption spectra. The PL spectra are likely dominated by the more emissive species and their distribution.

Low-Temperature Single-GNR Spectroscopy. A technique that can help to determine whether the two emission features at 840 and 910 nm originate from two different GNR populations or both peaks are intrinsic to a single GNR species is low-temperature single molecule spectroscopy. For the case of two different GNR populations with each contributing to only one emission feature, one would expect single-GNR spectra with only one emission peak in the corresponding spectral region. Alternatively, if the two main emission peaks are intrinsic to the 9-aGNR they should always appear together. Measurements at cryogenic temperatures simplify the differentiation between single nanoribbons and aggregates by decreasing line widths and increasing PL intensities of single fluorophores.[42]

Background-corrected PL spectra collected at 4.6 K from several individual 9-aGNRs embedded in a polystyrene matrix

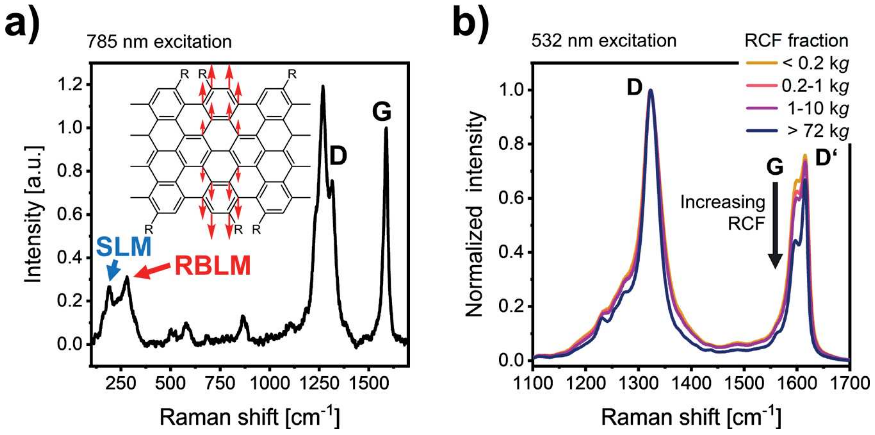

Figure 4. (a) Baseline-corrected Raman spectrum of a drop-cast film of a >0.2−1 kg 9-aGNR dispersion in THF on glass (excitation 785 nm). The inset shows the atomic displacement for the RBLM of 9-aGNRs. The alkyl chains are represented by −R. (b) Raman spectra of drop-cast films of different LCC fractions of 9-aGNRs normalized to the D-peak (excitation 532 nm).

(for details see Experimental Methods) are shown in Figure 3a for the 0.2−1 kg fraction and in Figure 3b for the >72 kg fraction. The highlighted areas indicate the spectral regions associated with the peaks at 840 nm (blue) and 920 nm (orange).

For low excitation densities, only one peak per spectrum is observed independent of the LCC fraction. The observed emission features are very narrow, with the narrowest peaks exhibiting a full-width-at-half-maximum of 2 meV (spectral resolution limit of the setup). Emission spectra measured on the same sample but at room temperature are significantly broader but still show single peaks with substantial variations in position (see Figure S11, Supporting Information). The occurrence of only one emission peak for a single nanoribbon indicates that there are indeed different 9-aGNR species that correspond to the two absorption (817 and 900 nm) and emission features (840 and 910 nm) observed for dispersions.

To ensure that the observed PL signals indeed originated from 9-aGNRs, we recorded over a hundred low-temperature PL spectra (for details, see Experimental Methods) and determined the positions of the peak maxima. The occurrence of peak maxima at certain wavelengths is plotted in Figure 3c and Figure 3d. Both histograms show that the majority of peaks are observed in the range between 820 and 940 nm, thus roughly resembling the features of the ensemble PL spectra.

Raman Spectroscopy on 9-aGNR Dispersions. Raman spectroscopy can help to corroborate that all of the fractions obtained by LCC contain structurally intact 9-aGNRs. It might also give further insights into the nature of the two GNR populations implied by the single-GNR PL measurements (see above). In addition to the D- and G-modes that are intrinsic to sp^2-carbon lattices, graphene nanoribbons exhibit a radial breathing-like mode (RBLM), that decreases in frequency with increasing ribbon width.[43,44] A width-dependent shear-like mode (SLM) has also been reported for on-surface synthesized 9-aGNRs.[45,46] Figure 4a shows a background-corrected Raman spectrum (excitation laser 785 nm; see Figure S12a for spectra without background correction) of a drop-cast film of a 9-aGNR dispersion (for details, see Experimental Methods). The inset schematically shows the atomic displacement for the RBLM. While wavenumbers between 310 and 316 cm^{-1} have been reported for RBLMs of 9-aGNRs,[10,37,45] we observe RBLM at ∼280 cm^{-1} (red arrow). This discrepancy might be explained by the presence of the alkyl side chains that were shown to move in phase with the nanoribbon atoms, thus increasing the effective width of the GNR and decreasing the RBLM frequency.[47,48] Since the RBLM is observed independent of RCF (Figure S12b, Supporting Information), all fractions resulting from LCC contain 9-aGNRs. Additionally, a SLM at 188 cm^{-1} is observed for all fractions (blue arrow), which is in good agreement with previously reported experimental (179 cm^{-1}) and theoretical (206 cm^{-1}) values for 9-aGNRs.[45,46]

Raman spectra of different drop-cast LCC fractions of 9-aGNRs in the wavenumber region above 1000 cm^{-1} show three major peaks at 1322, 1597, and 1615 cm^{-1} (Figure 4b) that can be assigned to the D-, G-, and D′-mode (for extended Raman spectra up to 3000 cm^{-1} including second order peaks see Figure S13, Supporting Information). When normalized to the D-peak, a decrease in the G-peak intensity for increasing RCF can be observed. Since the G-mode is intrinsic to the sp^2-carbon lattice and the D-mode is activated only near defects, the D/G ratio is often used as a measure for defect density or disorder. High D/G ratios indicate a structurally defective carbon lattice.[49] For aGNRs this correlation is complicated by the fact that armchair edges also activate the D-mode.[49] A high D/G ratio (as in the >72 kg fraction) could be the result of a larger edge-to-basal plane ratio for shorter GNRs or indeed indicate more defects within the GNR.

Both parameters, GNR length and number of structural defects, may also influence the sedimentation behavior of the nanoribbons. The attractive forces between graphitic nanomaterials increase with their size, for example, the length for SWNTs or the surface area for graphene.[50] Thus, longer GNRs should have an increased aggregation tendency and sediment faster in LCC. Defects in GNRs that cause structural distortion may prevent aggregation similar to defects in graphene flakes.[51] Assuming similar length distributions, GNRs with structural defects should thus exhibit a higher dispersion stability and slower sedimentation than defect-free GNRs, i.e., they should be more prevalent in higher RCF fractions as indeed observed in the Raman spectra of the different 9-aGNR fractions.

Quantum Chemical Calculations Regarding Shape, Size, and Defects of 9-aGNRs. The absorption and photoluminescence spectra of the different LCC fractions of 9-aGNRs indicate different populations. Further, the Raman data suggest that these GNR species may exhibit different lengths, shapes, or defect densities. To gain deeper insights

https://doi.org/10.1021/acsnano.3c05246
ACS Nano 2023, 17, 18240−18252

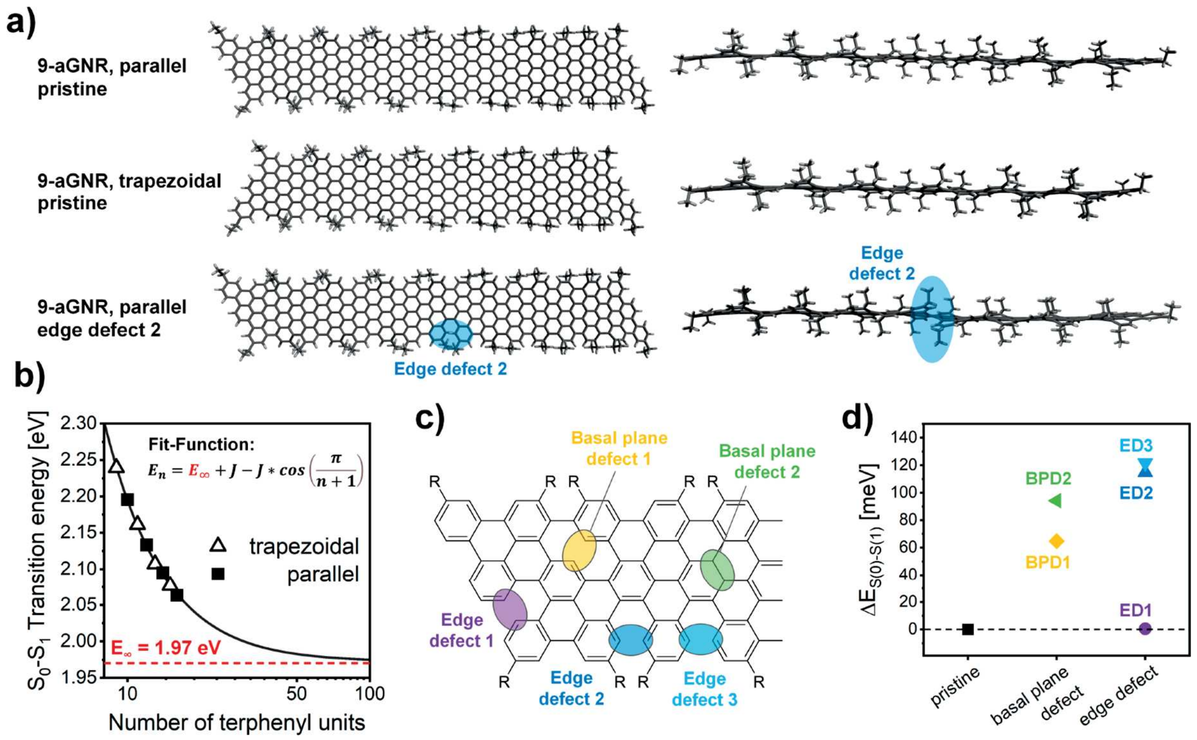

Figure 5. (a) GFN2-xTB optimized structures for pristine (top and middle) 9-aGNRs with 16 and 15 terphenyl units, respectively, and a defected (ED2) 9-aGNR (bottom). (b) Unscaled TD-DFT energies for the lowest bright transition (S_0−S_1) versus oligomer length (parallel shape: filled squares; trapezoidal shape: open triangles) and corresponding fit. (c) Schematic depiction of structural defects that can occur during a Scholl reaction. (d) Energy difference (TD-DFT data) between the S_0−S_1 transition energy computed for the defected 9-aGNR species and the pristine case (parallel shape, 16 terphenyl units). See Supporting Information for the corresponding values for the trapezoidal shape.

into the structural and optical properties of 9-aGNRs at the molecular level and to investigate the impact of length, shape and defects, we performed a range of quantum chemical calculations including tight-binding density functional (DFT) semiempirical methods (GFN2-xTB), DFT and time-dependent DFT (TD-DFT) calculations (for details see Computational Methods). In the following, we will refer to the electronic ground state of the GNRs as S_0 and to the n-th excited electronic state of the GNR as S_n. Transitions between these states are labeled as S_0−S_n.

First, an oligomer approach was applied by varying the number of repeat units (i.e., terphenyl units) of the 9-aGNRs to examine the dependence of the excited state energies on the length of the nanoribbon and thus to identify the structural model that represents the real system best. For each oligomer, different 9-aGNR shapes were considered, as well as the presence of various types of structural defects. Figure 5a shows the optimized structures (GFN2-xTB data; see Computational Methods) of the longest oligomers considered in this computational study for two different shapes of 9-aGNRs, i.e., trapezoidal (15 terphenyl units) and parallel (16 terphenyl units.) Trapezoidal and parallel shapes are created by coupling an odd or even number of terphenyl units, respectively. In both cases, the 9-aGNRs are characterized by a flat core structure.

Excited state (singlet) vertical excitation energies were computed at the TD-DFT level for each oligomer length. The strongest dipole-allowed electronic transition, i.e., the one with the highest oscillator strength (f), was the S_0−S_1 transition for each oligomer and for each shape of the nanoribbons, also indicating that the first singlet excited state (S_1) is the brightest. Furthermore, there are no dark states (as described at the single-reference TD-DFT level) at energies lower than S_1. The S_0−S_1 transition can be characterized in terms of the one-particle approximation as the HOMO−LUMO excitation (see Figure S14, Supporting Information).

By increasing the oligomer length, the computed S_0−S_1 transition shifts to lower energies, decreasing from 2.19 eV (short oligomer) to 2.06 eV (longest oligomer, ~600 nm, f = 7.8) for the parallel shape 9-aGNR, and from 2.23 to 2.07 eV (~596 nm, f = 7.13) for the trapezoidal species (see Figure 5b). Both types of 9-aGNRs show very similar S_0−S_1 vertical transition energies, regardless of their shape. By fitting the S_0−S_1 transition energies of the entire 9-aGNR oligomer series with a model function as previously proposed by Gierschner et al.[52] and Kowalczyk et al.[53] we obtain an extrapolated *infinite-chain* value of about 1.97 eV (629 nm). This value is very close to the S_0−S_1 transition energies computed for the longest oligomers considered here (~600 nm), thus suggesting that the structural models already reflect electronic properties (e.g., electron delocalization) quite close to the asymptotic (large size) limit. Hence, they can be considered as good representations of the real 9-aGNRs.

Note that the computed S_0−S_1 transition energies and the extrapolated data refer to unscaled TD-DFT values. It is well-known that depending on the choice of the exchange correlation functional and basis set adopted for the calculations (here ωB97X-D/6-31G*, see Computational Methods), the TD-DFT transition energies are overestimated compared to the experimental values (usually by 0.2−0.6 eV).[54] By rescaling the extrapolated (*infinite-chain*) value (1.97 eV) with respect to the energy of the lowest energy absorption band at 1.37 eV (900 nm, see Figure 2a), which is presumably related to the longest 9-aGNR within the sample, we obtain a scaling factor of about 0.70 for the electronic transition energies.

As suggested by quantum-chemical calculations, the shape of the nanoribbon (i.e., parallel vs trapezoidal) does not affect the S_0-S_1 optical gap significantly and thus cannot explain the two observed absorption bands (817 and 900 nm, Figure 2a). Furthermore, if a substantial length distribution of 9-aGNRs were present in the sample, then a spectral broadening should be observed. A very narrow and well-separated bimodal length distribution would be necessary to observe two well-defined peaks instead of a broad absorption and emission feature. Such a bimodal distribution is, however, not apparent in SEC or mass spectra of the precursor polymer (see Figure S1), indicating that the two different transitions are most likely not the result of GNR populations with different lengths. Hence, other possible factors should be considered.

Several studies have attributed the emergence of two distinct peaks in absorption and PL spectra to GNR aggregation and inter-GNR energy transfer.[16,55,56] Thus, we also calculated the ground to excited state (singlet) transition energies for a 9-aGNR monomer, consisting of 10 terphenyl units, and its van-der-Waals dimer. Given the large size of the dimer (>600 atoms), a full geometry optimization was possible only at the GFN2-xTB level of theory, while the excited state energies were computed at the semiempirical sTD-DFT level. According to these dimer-based calculations, 9-aGNRs should form H-type aggregates resulting in blue-shifted transition energies (see Figure S15, Supporting Information). Since aggregates sediment at lower RCF values than monomers,[39,40] larger amounts of H-aggregates should be found in low RCF fractions and lead to an increase in optical density of the peak at 817 nm. However, Figure 2a shows the opposite trend. The relative contribution of the absorption band at 817 nm is lower for lower RCF values, thus rendering aggregates improbable as the origin of the peak at 817 nm.

Another possible cause for the different transition energies might be defects within the 9-aGNR core. The graphitization of the precursor polymer to the 9-aGNR was achieved by a Scholl reaction with 2,3-dichloro-5,6-dicyano-3,4-benzoquinone (DDQ) as an oxidative agent. Scholl reactions can be highly efficient with yields near 100% under ideal conditions.[57] However, small amounts of incompletely graphitized GNRs are possible and will remain undetected by the usual analytical techniques. Based on the estimated length of the precursor polymer, the final 9-aGNR should contain at least ~25 terphenyl units. Four bonds must be closed for each terphenyl unit during the Scholl reaction. Thus, in a GNR with 25 terphenyl units, 100 additional bonds have to be formed. With an efficiency of 99% as determined by Li et al. for this reaction,[36] a typical GNR may still contain one unclosed bond, which would constitute a defect in the sp^2-hybridized lattice.

Consequently, we investigated the presence of different structural defects in our model systems and their effect on the electronic transition energies. For the longest 9-aGNR oligomers (parallel and trapezoidal shapes), we considered five defect types. The molecular structures that could result from missing bonds at different positions and hence different defect types are shown in Figure 5c. Note that edge defects (ED) are more probable than basal plane defects (BPD) as Scholl reactions are more efficient for preoriented precursors.[57] The optimized molecular structures (GFN2-xTB level) for each defected 9-aGNR species are reported in the Supporting Information (Figure S16). Generally, the introduction of an edge defect has a more substantial impact on the structure of the nanoribbon, as it induces a significant twist to the backbone. This twist is particularly evident for ED2 and ED3, which are located on the longitudinal edge of the nanoribbon and thus perturb the effective conjugation along the GNR core. The presence of a basal plane defect (BPD1 and BPD2), on the other hand, is less detrimental and does not induce large structural distortions.

The structural reorganizations introduced by each defect affect the electron delocalization and thus also the S_0-S_1 optical gap. For each defect-type and for both parallel and trapezoidal 9-aGNR species, we computed the excited state energies at the TD-DFT level (see Figure 5d for parallel GNRs and Figure S17 for trapezoidal GNRs). As already implied by the structural deformations, the defected 9-aGNRs show larger S_0-S_1 transition energies in comparison to the pristine species. Edge defects, in particular ED2 and ED3, induce an increase of the optical gap of ca. 0.11−0.13 eV with respect to the pristine ribbons. ED1, being located on the terminal edge, does not perturb the electron conjugation of the plane as much as ED2 and ED3 and the optical gap remains similar to the pristine species. BPD1 and BPD2 defects also induce a blue-shift of the S_0-S_1 transition, which is however lower in magnitude (about 0.06−0.1 eV) than for ED2 and ED3. The S_0-S_1 transitions exhibit similar oscillator strengths for pristine and defected 9-aGNRs (Figure S17 and S18, and Supporting Information).

Our calculations show that the presence of defects changes the electronic transition energies, modulating the optical gap and possibly causing the shift of the absorption and emission bands of 9-aGNRs. These results imply that the strong transition observed at 817 nm (1.5 eV, Figure 2a) may originate mostly from defective 9-aGNRs with presumably ED2 or ED3 type defects, while the transition at 900 nm (1.37 eV) could be assigned to defect-free or ED1-containing 9-aGNRs. The experimentally observed energy difference between the two absorption bands is 0.13 eV, which is close to the computed S_0-S_1 energy offset (Figure 5d).

Similar to defects in graphene[49] and SWNTs,[58] ED2 and ED3 defects could also act as additional electron-defect scattering sites. They should lead to a higher efficiency of one-phonon defect-assisted processes and an increase in relative intensities of the D- and D′-bands in Raman spectra. LCC fractions with higher D/G-ratios also exhibit a higher relative contribution of the absorption peak at 820 nm (Figure 4b), which is consistent with the proposed assignment. Note that the G- and D′-bands are nicely separated even in the >72 kg fraction indicating that a large fraction of the graphene lattice is still defect-free. Thus, in contrast to SWNTs and graphene, the steady increase in D/G ratios for increasing RCF values should not be interpreted as a larger number of defects per GNR but rather as an increasing number of GNRs that contain ED2 or ED3 defects.

In summary, the combination of experimental data and quantum chemical calculations clearly points toward defective nanoribbons (most likely containing edge defects) as one major population within our dispersions in addition to pristine 9-aGNRs. These different GNR species can explain the dependence of the two absorption and emission peaks as well as the Raman D/G ratios on LCC fractions (i.e., different RCF values).

Chemical Doping of 9-aGNR Dispersions with F_4TCNQ. After gaining a better understanding of the optical properties of undoped 9-aGNRs in dispersion, we now

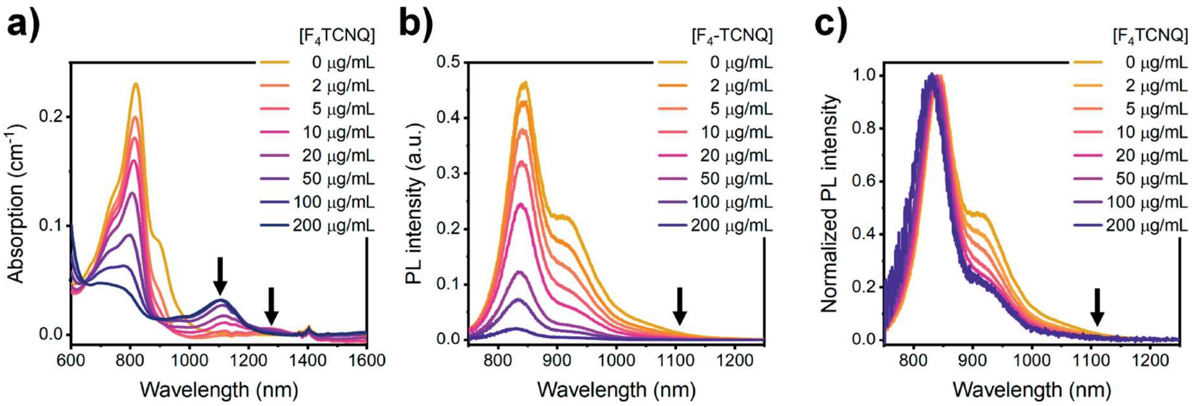

Figure 6. (a) Absorption spectra of a >72 kg 9-aGNR dispersion doped with different concentrations of F_4TCNQ. Positions of charge-induced absorption peaks are marked by arrows. (b) PL spectra (absolute values) of a 9-aGNR dispersion doped with F_4TCNQ and (c) normalized PL spectra. Arrows indicate the position where trion emission would be expected, according to the charge-induced features in the absorption spectra.

investigated the impact of excess charge carriers on these properties. Chemically doped SWNTs show relatively narrow charge-induced absorption and emission features typically associated with trions.[27] However, when conjugated polymers are chemically or electrochemically doped, very broad red-shifted polaron transitions appear in their absorption spectra, reflecting changes in the electronic structure of the polymer upon charging.[34,35,59,60]

2,3,5,6-Tetrafluoro-7,7,8,8-tetracyanoquinodimethane (F_4TCNQ) is a strong molecular electron acceptor that has been used previously to induce p-doping in polymers,[61] semiconducting SWNTs,[62] and graphene[63] by forming charge-transfer complexes and was chosen here for direct doping of nanoribbons in dispersion. As F_4TCNQ quickly decomposes in THF, only 9-aGNR dispersions in toluene could be doped with this method (for details, see Experimental Methods). Figure 6a shows absorption spectra of a >72 kg fraction with increasing concentrations of F_4TCNQ. For low F_4TCNQ concentrations (2 and 5 $\mu g\ mL^{-1}$) the absorption band at 900 nm starts to be bleached and an additional red-shifted charge-induced absorption feature at 1300 nm emerges (indicated by the arrow in Figure 6a). While this feature is fairly weak for the >72 kg fraction, it appears stronger for doping of the 0.2−1 kg fraction (see Figure S19a, Supporting Information). Since the undoped 0.2−1 kg fraction in toluene also shows a stronger absorption band at 900 nm than the >72 kg fraction, it is reasonable to assume that the additional red-shifted absorption feature at 1300 nm is correlated with this transition. For higher dopant concentrations, bleaching of the absorption band at 817 nm commences and another charge-induced red-shifted absorption feature at 1100 nm appears. The presence of an isosbestic point (at ∼900 nm) clearly shows that the two features are connected. Interestingly, for the highest doping concentrations, the feature at 1300 nm bleaches again. For the 0.2−1 kg fraction, we observe an even further red-shifted absorption at 1600 nm and above (see Figure S20a, Supporting Information). Note that the absorption band at 900 nm shows stronger bleaching than that at 817 nm for the same F_4TCNQ concentrations, indicating again that there must be two different 9-aGNR species with different redox potentials.

To differentiate between trions and polarons as the origin of the red-shifted, charge-induced absorption, PL spectra of the F_4TCNQ-doped 9-aGNR dispersions were recorded. As the trion is an emissive excited state (charged exciton), we would expect to observe red-shifted emission peaks at 1100 and 1300 nm. Figure 6b shows the PL spectra of a >72 kg fraction doped with increasing amounts of F_4TCNQ. The arrow indicates the position of the observed charge-induced absorption band. However, for increasing dopant concentrations, we observe only the expected quenching of the main emission and no additional emission features. Spectra showing the region up to 1400 nm are depicted in Figures S19b and S20 (Supporting Information) and also do not show any further red-shifted emission. In PL spectra normalized to the emission peak at 840 nm (Figure 6c), a blue-shift with increasing doping levels is apparent, which is reminiscent of the blue-shift observed for SWNTs upon doping.[64] In addition, we find that the emission at 910 nm is quenched more strongly than that at 840 nm for the same dopant concentration, again indicating the presence of two different species with different redox potentials.

These findings strongly suggest polaron formation upon doping of solution-synthesized 9-aGNRs in dispersion and seem to exclude the possibility of trion formation. This is in stark contrast to the recently reported trionic PL by Fedotov et al. for on-surface synthesized 7-aGNRs.[65] A possible explanation could be the stronger deformation of solution-synthesized 9-aGNRs due to the sterically demanding branched alkyl side chains that may promote charge localization and stronger electron−phonon coupling.

To further understand the observed spectra of p-doped nanoribbons, quantum chemical calculations were also performed for the charged 9-aGNRs. The singly charged states (radical cation, +1) of both parallel and trapezoidal 9-aGNRs were optimized at the GFN2-xTB level. The electronic transitions were further computed at the TD-DFT level by adopting a spin-polarized unrestricted (UωB97XD) functional. Furthermore, a comparison between pristine and defected 9-aGNRs is reported in the Supporting Information (Figure S21). For each species, electronic transitions at lower energies (red-shifted) than the S_0-S_1 optical gap of the undoped nanoribbon appeared. The charge-induced (dipole allowed) electronic transitions are computed at about 0.5−0.8 eV below the S_0-S_1 transition of the undoped species. This energy offset is comparable (within the approximations of GFN2-xTB and TD-DFT methods) to the experimental values (0.38 and 0.42 eV). The presence of defects or different nanoribbon shapes slightly affects the transition energies of the charged species (Figure S21), suggesting a localization of the polaron spin density over the plane of the nanoribbon. As shown above, the nanoribbon shape and defects influence the conjugation length, thus also changing the delocalization of the polaron spin density.

Note that the presence of defects also alters the energy of the frontier molecular orbitals (e.g., HOMO and LUMO levels), thus affecting in a first approximation (i.e., following Koopman's theorem, $\mathrm{IP(EA)} = -\varepsilon_{\mathrm{HOMO}}(-\varepsilon_{\mathrm{LUMO}})$) the redox potentials as well. For example, the DFT-computed HOMO energy for 9-aGNRs with ED2 and ED3 defects (−5.6 eV) is lower than that of the pristine species (−5.5 eV). BPD1 and BPD2 behave similarly to EDs, however, with a reduced energy shift of only 0.08 eV instead of 0.1 eV. These calculations again can help to understand the experimental doping data. Efficient p-doping takes place if the energy difference ΔE between the HOMO of the GNR and the LUMO of the dopant (here F_4TCNQ) is large. Thus, pristine 9-aGNRs (assumed to correspond to the absorption band at 900 nm) with a higher-lying HOMO level (larger ΔE) should be oxidized (p-doped), and thus bleached at lower F_4TCNQ concentrations than the defective 9-aGNRs (which are assigned to the band at 817 nm). The defective 9-aGNRs are oxidized at higher F_4TCNQ concentrations due to their lower-lying HOMO (smaller ΔE) compared to the LUMO of F_4TCNQ. Thus, the computed HOMO energies of defective and pristine 9-aGNRs further corroborate the corresponding assignment of the two absorption and emission peaks as described above.

CONCLUSION

In this study, we created stable dispersions of solution-synthesized 9-aGNRs in organic solvents and revealed the origin of their absorption and emission features in the neutral and hole-doped state. We found that the as-synthesized raw material contains two species of 9-aGNRs that result in two different absorption and emission bands in the near-infrared. Based on semiempirical and DFT/TD-DFT calculations, we could assign the lowest energy band to 9-aGNRs without defects and the dominant blue-shifted band to 9-aGNRs with edge-defects. The ratio of the two nanoribbon populations varies among different LCC fractions. Molecular p-doping of these 9-aGNR dispersions with F_4TCNQ resulted in fairly narrow red-shifted charge-induced absorption features and PL quenching but no charge-induced emission that would indicate the existence of trions. We conclude that solution-synthesized 9-aGNRs in dispersion favor polaron formation similar to conjugated polymers. In contrast to theoretical predictions, the flexibility and torsion of GNRs with alkyl side chains in dispersion seem to prevent the formation of stable and emissive trion states.

EXPERIMENTAL METHODS

Synthesis of 9-aGNR. Atomically precise 9-aGNRs were synthesized according to an adapted protocol by Li et al.[36] and described in detail in the Supporting Information (see Figure S1 for reaction scheme).

Preparation of 9-aGNR Dispersions. 10 mg of 9-aGNR powder was added to 10 mL of solvent (THF or toluene) in a 25 mL round flask, which was then sealed with a septum. This mixture was ultrasonicated for 4 h in a Branson 2510 sonication bath during which the temperature was held constant at room temperature.

Sorting of 9-aGNRs by LCC. A freshly prepared 9-aGNR dispersion was exposed to increasing rotational centrifugal forces (RCF). The samples were centrifuged at 200*g*, 1000*g*, and 10000*g* in a Hettich Mikro 220R centrifuge, equipped with a 11.95A fixed-angle rotor. The supernatant of the 10000*g* centrifugation step was centrifuged at 72000*g* using a Beckmann Coulter Avanti J-26S XP centrifuge, equipped with a JA25.50 fixed-angle rotor. This process yields 5 fractions of GNRs (<200*g*, 200−1000*g*, 1000−10000*g*, 10000−72000*g*, and >72000*g*).

Chemical Doping with F_4TCNQ. A stock solution of F_4TCNQ in toluene with a concentration of 1 mg mL^{-1} was prepared. To achieve the desired doping level, a suitable amount of F_4TCNQ stock solution and pure toluene were added to a size-selected 9-aGNR dispersion in toluene so that in the final mixture the optical density of the absorption peak at 817 nm was 0.2 cm^{-1}.

Raman Spectroscopy. Raman spectra of drop-cast GNR dispersions were acquired with a Renishaw inVia confocal Raman microscope in backscattering configuration equipped with a 50× long working distance objective (N.A. 0.5, Olympus). To minimize the influence of spot-to-spot variations, maps with >500 spectra were recorded and averaged. For excitation at 785 nm, the obtained Raman spectra were baseline-corrected to account for the PL background.

Absorption Spectroscopy. Baseline-corrected absorption spectra were recorded using a Cary 6000i UV−vis−NIR absorption spectrometer (Varian, Inc.) and cuvettes with a 1 cm path length.

Photoluminescence Spectroscopy. PL spectra were acquired from dispersion by excitation at 532 nm (picosecond-pulsed supercontinuum laser (NKT Photonics SuperK Extreme). Emitted photons were collected by a NIR-optimized 50× objective (N.A. 0.65, Olympus) and spectra were recorded with an Acton SpectraPro SP2358 spectrometer with a liquid-nitrogen-cooled InGaAs line camera (Princeton Instruments, OMA-V:1024).

PL Quantum Yield Measurements. The PLQY of the sample was determined by an absolute method using an integrating sphere as described in detail elsewhere.[66] The dispersion (with optical density of ~0.1 cm^{-1} at 817 nm) in a quartz cuvette was placed inside the integrating sphere and excited at 535 nm by the spectrally filtered output of a picosecond pulsed supercontinuum laser source. The absorption of laser light and the fluorescence were transmitted to the spectrograph via an optical fiber. The measurement was repeated with pure solvent to account for scattering and absorption of the solvent and the cuvette.

Lifetime Measurements. Photoluminescence lifetimes were measured by time-correlated single photon counting (TCSPC). The emission from the dispersion (excited at 535 nm) was spectrally filtered by an Acton SpectraPro SP2358 spectrograph and focused onto a gated silicon avalanche photodiode (Micro Photon Devices). Arrival times of photons were recorded with a time-correlated single photon module (Picoharp 300, Picoquant). The fluorescence decay histograms were fitted by a monoexponential fit procedure.

Low-Temperature Single GNR Spectroscopy. For low-temperature single GNR spectroscopy, a GNR dispersion in THF was diluted to an optical density of 0.002 at 817 nm and mixed with the same volume of a 40 mg mL^{-1} polystyrene solution in THF. A volume of 15 μL of this mixture was then spin-coated (2000 rpm, 1 min) onto a glass slide coated with 150 nm gold. The resulting samples were mounted inside a liquid helium-cooled closed-cycle cryostat (Montana Instruments Cryostation s50) and cooled to 4.6 K under high vacuum conditions (10^{-5}−10^{-6} bar). The output of a continuous wave laser diode (Coherent, Inc. OBIS 532 nm) was focused onto the sample using a 50× long working distance objective (Mitutoyo, N.A. 0.42). Scattered laser light was blocked by using the appropriate long-pass filters. Spectra were recorded with a 1340 × 400 Si CCD Camera (Princeton Instruments, PIXIS:400) coupled to a grating spectrograph (Princeton Instruments IsoPlane SCT 320) using a grating with 150 grooves mm^{-1} and 800 nm blaze. For each spot at least 5 spectra with an integration time of one min were recorded and averaged. To record individual spectra for the creation of histograms, an area of 99 μm × 99 μm was scanned with a step width of 3 μm. Emission peaks were observed for 108 (0.2−1 kg fraction) or 133 (>72 kg fraction) spectra out of a total of 1156 measured spots.

COMPUTATIONAL METHODS

Semiempirical (GFNn-xTB) and DFT Calculations. 9-aGNR species were modeled by adopting an oligomer approach and changing the chain length, that is, the number of terphenyl units, of the nanoribbons. Oligomers containing 8 to 16 terphenyl units were considered. Different shapes of the 9-aGNRs were investigated, namely parallel and trapezoidal, featuring an even or an odd number of terphenyl units, respectively. For each oligomer and for each shape, the molecular structure, the electronic structure and the optical transitions (i.e., the ground to excited state (singlet) vertical excitations) were calculated at the semiempirical (i.e., GFN2-xTB, sTD-DFT), and DFT, TD-DFT levels of theory (see below). To reach an effective balance between computational cost and accuracy, the longest 9-aGNRs investigated here comprised 16 (parallel shape) or 15 terphenyl units (trapezoidal shape), respectively. For both of them, various structural defects were further considered, i.e., edge defects (three different types, ED1, ED2, and ED3, see Figure 5) and basal defects (two kinds, BPD1 and BPD2, see Figure 5). The presence of alkyl side chains was included; however, the length of each chain was reduced with respect to the synthesized 9-aGNRs in order to limit the computational costs.

All geometries were fully optimized at the GFN2-xTB level by adopting very tight thresholds for energy and gradients convergence.[67,68] For some oligomers, extra DFT geometry optimizations were performed, leading to results very similar to those of the GFN2-xTB structures. Vertical electronic transitions from ground to singlet excited states were computed both with the semiempirical sTD-DFT approach[67] and TD-DFT. Vibronic effects were not considered in these calculations.

For DFT and TD-DFT calculations, the range-separated functional with the inclusion of dispersion corrections ωB97X-D and the Pople double split-valence basis set with diffusion functions (6-31G*) were used.

The molecular and electronic structures of charged species, i.e., radical-cations (+1), were optimized at the GFN2-xTB level, while the vertical electronic excited state energies were computed at the TD-UDFT level by adopting the spin polarized unrestricted approach. Charged species were computed for the longest 9-aGNR oligomers (parallel and trapezoidal shape) without (pristine) and with structural defects.

GFN2-xTB calculations were performed with the open-source code xTB (v 6.4.1),[68] while DFT and TD-DFT calculations were carried out with Gaussian 16[69] or ORCA[70] (v.5.0.3) programs.

The model function used to extrapolate the oligomer S_0−S_1 (TD-DFT) unscaled excitation energies (Figure 5b) was proposed by Kowalczyk et al.[53] It refers to the Frenkel exciton model and reads as

$$E_n = E_\infty + J\left(1 - \cos\left(\frac{\pi}{n+1}\right)\right)$$

with E_∞ as the extrapolated value for an infinite chain length (n) and J as the coupling constant.

ASSOCIATED CONTENT

Supporting Information

The Supporting Information is available free of charge at https://pubs.acs.org/doi/10.1021/acsnano.3c05246.

> Detailed description of synthesis of 9-aGNRs with NMR spectra of all compounds, size exclusion chromatogram and MALDI-TOF mass spectrum of precursor polymer, atomic force micrograph or drop-cast GNRs, further spectroscopic characterization of 9-aGNRs in other LCC fractions or solvents (absorption, photoluminescence, fluorescence lifetime, and yield measurements), additional single-nanoribbon and Raman spectra, quantum chemical calculations of neutral 9-aGNRs, additional absorption and PL spectra of doped 9-aGNRs, quantum chemical calculations of charged 9-aGNRs (PDF)

AUTHOR INFORMATION

Corresponding Author

Jana Zaumseil − *Institute for Physical Chemistry, Heidelberg University, D-69120 Heidelberg, Germany*; orcid.org/0000-0002-2048-217X; Email: zaumseil@uni-heidelberg.de

Authors

Sebastian Lindenthal − *Institute for Physical Chemistry, Heidelberg University, D-69120 Heidelberg, Germany*
Daniele Fazzi − *Department of Chemistry "Giacomo Ciamician", University of Bologna, 40126 Bologna, Italy*; orcid.org/0000-0002-8515-4214
Nicolas F. Zorn − *Institute for Physical Chemistry, Heidelberg University, D-69120 Heidelberg, Germany*; orcid.org/0000-0001-9651-5612
Abdurrahman Ali El Yumin − *Institute for Physical Chemistry, Heidelberg University, D-69120 Heidelberg, Germany*
Simon Settele − *Institute for Physical Chemistry, Heidelberg University, D-69120 Heidelberg, Germany*; orcid.org/0000-0002-0082-2587
Britta Weidinger − *Institute for Molecular Systems Engineering and Advanced Materials and Institute of Organic Chemistry, Heidelberg University, D-69120 Heidelberg, Germany*
Eva Blasco − *Institute for Molecular Systems Engineering and Advanced Materials and Institute of Organic Chemistry, Heidelberg University, D-69120 Heidelberg, Germany*; orcid.org/0000-0002-0849-4223

Complete contact information is available at: https://pubs.acs.org/10.1021/acsnano.3c05246

Author Contributions

S.L. synthesized the 9-aGNRs, processed and measured all samples, and analyzed the data. D.F. performed and analyzed the quantum-chemical calculations. S.S. and N.F.Z. contributed to the characterization of dispersions and films. A.A.E.Y. and N.F.Z. contributed to low-temperature PL measurements and data analysis. B.W. supervised by E.B. performed size-exclusion chromatography on the precursor polymer. J.Z. conceived and supervised the project. S.L., D.F., and J.Z. wrote the manuscript with input from all authors. All authors have given approval to the final version of the manuscript.

Notes

The authors declare no competing financial interest.

ACKNOWLEDGMENTS

This project has received funding from the European Research Council (ERC) under the European Union's Horizon 2020 research and innovation programme (Grant Agreement No. 817494 "TRIFECTs"). D.F. acknowledges partial funding from the National Recovery and Resilience Plan (NRRP), Mission 04 Component 2, Investment 1.5 − NextGenerationEU, Call for tender no. 3277 dated 12/30/2021, Award Number: 0001052 dated 6/23/2022. E.B. acknowledges funding from the Deutsche Forschungsgemeinschaft (DFG, German Research Foundation) via the Excellence Cluster "3D Matter Made to Order" (EXC-2082/1-390761711) and the Carl Zeiss Foundation through the Carl-Zeiss-Foundation-Focus@HEiKA. S.L. and J.Z. warmly thank Milan Kivala and his team for providing laboratory space and advice on the GNR synthesis.

REFERENCES

(1) Barone, V.; Hod, O.; Scuseria, G. E. Electronic Structure and Stability of Semiconducting Graphene Nanoribbons. *Nano Lett.* **2006**, *6*, 2748−2754.

(2) Ezawa, M. Peculiar Width Dependence of the Electronic Properties of Carbon Nanoribbons. *Phys. Rev. B* **2006**, *73*, 045432.

(3) Son, Y. W.; Cohen, M. L.; Louie, S. G. Energy Gaps in Graphene Nanoribbons. *Phys. Rev. Lett.* **2006**, *97*, 216803.

(4) Tapaszto, L.; Dobrik, G.; Lambin, P.; Biro, L. P. Tailoring the Atomic Structure of Graphene Nanoribbons by Scanning Tunnelling Microscope Lithography. *Nat. Nanotechnol.* **2008**, *3*, 397−401.

(5) Bai, J.; Duan, X.; Huang, Y. Rational Fabrication of Graphene Nanoribbons Using a Nanowire Etch Mask. *Nano Lett.* **2009**, *9*, 2083−2087.

(6) Jiao, L.; Wang, X.; Diankov, G.; Wang, H.; Dai, H. Facile Synthesis of High-Quality Graphene Nanoribbons. *Nat. Nanotechnol.* **2010**, *5*, 321−325.

(7) Cai, J.; Ruffieux, P.; Jaafar, R.; Bieri, M.; Braun, T.; Blankenburg, S.; Muoth, M.; Seitsonen, A. P.; Saleh, M.; Feng, X.; Mullen, K.; Fasel, R. Atomically Precise Bottom-up Fabrication of Graphene Nanoribbons. *Nature* **2010**, *466*, 470−473.

(8) Chen, Y. C.; de Oteyza, D. G.; Pedramrazi, Z.; Chen, C.; Fischer, F. R.; Crommie, M. F. Tuning the Band Gap of Graphene Nanoribbons Synthesized from Molecular Precursors. *ACS Nano* **2013**, *7*, 6123−6128.

(9) Bennett, P. B.; Pedramrazi, Z.; Madani, A.; Chen, Y.-C.; de Oteyza, D. G.; Chen, C.; Fischer, F. R.; Crommie, M. F.; Bokor, J. Bottom-up Graphene Nanoribbon Field-Effect Transistors. *Appl. Phys. Lett.* **2013**, *103*, 253114.

(10) Borin Barin, G.; Fairbrother, A.; Rotach, L.; Bayle, M.; Paillet, M.; Liang, L.; Meunier, V.; Hauert, R.; Dumslaff, T.; Narita, A.; Müllen, K.; Sahabudeen, H.; Berger, R.; Feng, X.; Fasel, R.; Ruffieux, P. Surface-Synthesized Graphene Nanoribbons for Room Temperature Switching Devices: Substrate Transfer and Ex Situ Characterization. *ACS Appl. Nano Mater.* **2019**, *2*, 2184−2192.

(11) Yoon, K.-Y.; Dong, G. Liquid-Phase Bottom-up Synthesis of Graphene Nanoribbons. *Mater. Chem. Front.* **2020**, *4*, 29−45.

(12) Narita, A.; Feng, X.; Hernandez, Y.; Jensen, S. A.; Bonn, M.; Yang, H.; Verzhbitskiy, I. A.; Casiraghi, C.; Hansen, M. R.; Koch, A. H. R.; Fytas, G.; Ivasenko, O.; Li, B.; Mali, K. S.; Balandina, T.; Mahesh, S.; De Feyter, S.; Müllen, K. Synthesis of Structurally Well-Defined and Liquid-Phase-Processable Graphene Nanoribbons. *Nat. Chem.* **2014**, *6*, 126−132.

(13) Shekhirev, M.; Vo, T. H.; Kunkel, D. A.; Lipatov, A.; Enders, A.; Sinitskii, A. Aggregation of Atomically Precise Graphene Nanoribbons. *RSC Adv.* **2017**, *7*, 54491−54499.

(14) Huang, Y.; Mai, Y.; Beser, U.; Teyssandier, J.; Velpula, G.; van Gorp, H.; Straaso, L. A.; Hansen, M. R.; Rizzo, D.; Casiraghi, C.; Yang, R.; Zhang, G.; Wu, D.; Zhang, F.; Yan, D.; De Feyter, S.; Mullen, K.; Feng, X. Poly(Ethylene Oxide) Functionalized Graphene Nanoribbons with Excellent Solution Processability. *J. Am. Chem. Soc.* **2016**, *138*, 10136−10139.

(15) Yang, W.; Lucotti, A.; Tommasini, M.; Chalifoux, W. A. Bottom-up Synthesis of Soluble and Narrow Graphene Nanoribbons Using Alkyne Benzannulations. *J. Am. Chem. Soc.* **2016**, *138*, 9137−9144.

(16) Huang, Y.; Xu, F.; Ganzer, L.; Camargo, F. V. A.; Nagahara, T.; Teyssandier, J.; Van Gorp, H.; Basse, K.; Straaso, L. A.; Nagyte, V.; Casiraghi, C.; Hansen, M. R.; De Feyter, S.; Yan, D.; Mullen, K.; Feng, X.; Cerullo, G.; Mai, Y. Intrinsic Properties of Single Graphene Nanoribbons in Solution: Synthetic and Spectroscopic Studies. *J. Am. Chem. Soc.* **2018**, *140*, 10416−10420.

(17) Liu, Z.; Hu, Y.; Zheng, W.; Wang, C.; Baaziz, W.; Richard, F.; Ersen, O.; Bonn, M.; Wang, H. I.; Narita, A.; Ciesielski, A.; Müllen, K.; Samorì, P. Untying the Bundles of Solution Synthesized Graphene Nanoribbons for Highly Capacitive Micro Supercapacitors. *Adv. Funct. Mater.* **2022**, *32*, 2109543.

(18) Hernandez, Y.; Nicolosi, V.; Lotya, M.; Blighe, F. M.; Sun, Z.; De, S.; McGovern, I. T.; Holland, B.; Byrne, M.; Gun'Ko, Y. K.; Boland, J. J.; Niraj, P.; Duesberg, G.; Krishnamurthy, S.; Goodhue, R.; Hutchison, J.; Scardaci, V.; Ferrari, A. C.; Coleman, J. N. High-Yield Production of Graphene by Liquid-Phase Exfoliation of Graphite. *Nat. Nanotechnol.* **2008**, *3*, 563−568.

(19) Merino-Diez, N.; Garcia-Lekue, A.; Carbonell-Sanroma, E.; Li, J.; Corso, M.; Colazzo, L.; Sedona, F.; Sanchez-Portal, D.; Pascual, J. I.; de Oteyza, D. G. Width-Dependent Band Gap in Armchair Graphene Nanoribbons Reveals Fermi Level Pinning on Au(111). *ACS Nano* **2017**, *11*, 11661−11668.

(20) Prezzi, D.; Varsano, D.; Ruini, A.; Marini, A.; Molinari, E. Optical Properties of Graphene Nanoribbons: The Role of Many-Body Effects. *Phys. Rev. B* **2008**, *77*, 041404.

(21) Fedotov, P. V.; Rybkovskiy, D. V.; Chernov, A. I.; Obraztsova, E. A.; Obraztsova, E. D. Excitonic Photoluminescence of Ultra-Narrow 7-Armchair Graphene Nanoribbons Grown by a New "Bottom-up" Approach on a Ni Substrate under Low Vacuum. *J. Phys. Chem. C* **2020**, *124*, 25984−25991.

(22) Tries, A.; Osella, S.; Zhang, P.; Xu, F.; Ramanan, C.; Klaui, M.; Mai, Y.; Beljonne, D.; Wang, H. I. Experimental Observation of Strong Exciton Effects in Graphene Nanoribbons. *Nano Lett.* **2020**, *20*, 2993−3002.

(23) Gao, Y.; Hua, X.; Jiang, W.; Sun, C. L.; Yuan, C.; Liu, Z.; Zhang, H. L.; Shao, X. Bottom-up Preparation of Twisted Graphene Nanoribbons by Cu-Catalyzed Deoxygenative Coupling. *Angew. Chem., Int. Ed.* **2022**, *61*, No. e202210924.

(24) Gao, J.; Uribe-Romo, F. J.; Saathoff, J. D.; Arslan, H.; Crick, C. R.; Hein, S. J.; Itin, B.; Clancy, P.; Dichtel, W. R.; Loo, Y. L. Ambipolar Transport in Solution-Synthesized Graphene Nanoribbons. *ACS Nano* **2016**, *10*, 4847−4856.

(25) Chong, M. C.; Afshar-Imani, N.; Scheurer, F.; Cardoso, C.; Ferretti, A.; Prezzi, D.; Schull, G. Bright Electroluminescence from Single Graphene Nanoribbon Junctions. *Nano Lett.* **2018**, *18*, 175−181.

(26) Mutlu, Z.; Llinas, J. P.; Jacobse, P. H.; Piskun, I.; Blackwell, R.; Crommie, M. F.; Fischer, F. R.; Bokor, J. Transfer-Free Synthesis of Atomically Precise Graphene Nanoribbons on Insulating Substrates. *ACS Nano* **2021**, *15*, 2635−2642.

(27) Matsunaga, R.; Matsuda, K.; Kanemitsu, Y. Observation of Charged Excitons in Hole-Doped Carbon Nanotubes Using Photoluminescence and Absorption Spectroscopy. *Phys. Rev. Lett.* **2011**, *106*, 037404.

(28) Park, J. S.; Hirana, Y.; Mouri, S.; Miyauchi, Y.; Nakashima, N.; Matsuda, K. Observation of Negative and Positive Trions in the Electrochemically Carrier-Doped Single-Walled Carbon Nanotubes. *J. Am. Chem. Soc.* **2012**, *134*, 14461−14466.

(29) Mak, K. F.; He, K.; Lee, C.; Lee, G. H.; Hone, J.; Heinz, T. F.; Shan, J. Tightly Bound Trions in Monolayer MoS_2. *Nat. Mater.* **2013**, *12*, 207−211.

(30) Jakubka, F.; Grimm, S. B.; Zakharko, Y.; Gannott, F.; Zaumseil, J. Trion Electroluminescence from Semiconducting Carbon Nanotubes. *ACS Nano* **2014**, *8*, 8477−8486.

(31) Zhang, Y.; Li, H.; Wang, H.; Liu, R.; Zhang, S. L.; Qiu, Z. J. On Valence-Band Splitting in Layered MoS_2. *ACS Nano* **2015**, *9*, 8514−8519.

(32) Deilmann, T.; Rohlfing, M. Huge Trionic Effects in Graphene Nanoribbons. *Nano Lett.* **2017**, *17*, 6833−6837.

(33) Berkelbach, T. C.; Hybertsen, M. S.; Reichman, D. R. Theory of Neutral and Charged Excitons in Monolayer Transition Metal Dichalcogenides. *Phys. Rev. B* **2013**, *88*, 045318.

(34) Ghosh, R.; Spano, F. C. Excitons and Polarons in Organic Materials. *Acc. Chem. Res.* **2020**, *53*, 2201−2211.

(35) Beljonne, D.; Cornil, J.; Sirringhaus, H.; Brown, P. J.; Shkunov, M.; Friend, R. H.; Brédas, J. L. Optical Signature of Delocalized Polarons in Conjugated Polymers. *Adv. Funct. Mater.* **2001**, *11*, 229−234.

(36) Li, G.; Yoon, K. Y.; Zhong, X.; Zhu, X.; Dong, G. Efficient Bottom-up Preparation of Graphene Nanoribbons by Mild Suzuki-Miyaura Polymerization of Simple Triaryl Monomers. *Chem. Eur. J.* **2016**, *22*, 9116−20.

(37) Talirz, L.; Sode, H.; Dumslaff, T.; Wang, S.; Sanchez-Valencia, J. R.; Liu, J.; Shinde, P.; Pignedoli, C. A.; Liang, L.; Meunier, V.; Plumb, N. C.; Shi, M.; Feng, X.; Narita, A.; Mullen, K.; Fasel, R.; Ruffieux, P. On-Surface Synthesis and Characterization of 9-Atom Wide Armchair Graphene Nanoribbons. *ACS Nano* **2017**, *11*, 1380−1388.

(38) Backes, C.; Higgins, T. M.; Kelly, A.; Boland, C.; Harvey, A.; Hanlon, D.; Coleman, J. N. Guidelines for Exfoliation, Characterization and Processing of Layered Materials Produced by Liquid Exfoliation. *Chem. Mater.* **2017**, *29*, 243−255.

(39) Backes, C.; Paton, K. R.; Hanlon, D.; Yuan, S.; Katsnelson, M. I.; Houston, J.; Smith, R. J.; McCloskey, D.; Donegan, J. F.; Coleman, J. N. Spectroscopic Metrics Allow in situ Measurement of Mean Size and Thickness of Liquid-Exfoliated Few-Layer Graphene Nanosheets. *Nanoscale* **2016**, *8*, 4311−4323.

(40) Backes, C.; Szydlowska, B. M.; Harvey, A.; Yuan, S.; Vega-Mayoral, V.; Davies, B. R.; Zhao, P. L.; Hanlon, D.; Santos, E. J.; Katsnelson, M. I.; Blau, W. J.; Gadermaier, C.; Coleman, J. N. Production of Highly Monolayer Enriched Dispersions of Liquid-Exfoliated Nanosheets by Liquid Cascade Centrifugation. *ACS Nano* **2016**, *10*, 1589−1601.

(41) Zhuo, M.-P.; Wang, X.-D.; Liao, L.-S. Recent Progress of Novel Organic near Infrared Emitting Materials. *Small Sci.* **2022**, DOI: 10.1002/smsc.202200029.

(42) Schindler, F.; Lupton, J. M.; Feldmann, J.; Scherf, U. A Universal Picture of Chromophores in Pi-Conjugated Polymers Derived from Single-Molecule Spectroscopy. *Proc. Natl. Acad. Sci. U.S.A.* **2004**, *101*, 14695−700.

(43) Vandescuren, M.; Hermet, P.; Meunier, V.; Henrard, L.; Lambin, P. Theoretical Study of the Vibrational Edge Modes in Graphene Nanoribbons. *Phys. Rev. B* **2008**, *78*, 195401.

(44) Yamada, M.; Yamakita, Y.; Ohno, K. Phonon Dispersions of Hydrogenated and Dehydrogenated Carbon Nanoribbons. *Phys. Rev. B* **2008**, *77*, 054302.

(45) Overbeck, J.; Barin, G. B.; Daniels, C.; Perrin, M. L.; Braun, O.; Sun, Q.; Darawish, R.; De Luca, M.; Wang, X. Y.; Dumslaff, T.; Narita, A.; Mullen, K.; Ruffieux, P.; Meunier, V.; Fasel, R.; Calame, M. A Universal Length-Dependent Vibrational Mode in Graphene Nanoribbons. *ACS Nano* **2019**, *13*, 13083−13091.

(46) Overbeck, J.; Borin Barin, G.; Daniels, C.; Perrin, M. L.; Liang, L.; Braun, O.; Darawish, R.; Burkhardt, B.; Dumslaff, T.; Wang, X.-Y.; Narita, A.; Müllen, K.; Meunier, V.; Fasel, R.; Calame, M.; Ruffieux, P. Optimized Substrates and Measurement Approaches for Raman Spectroscopy of Graphene Nanoribbons. *Physica Status Solidi (b)* **2019**, *256*, 1900343.

(47) Verzhbitskiy, I. A.; Corato, M. D.; Ruini, A.; Molinari, E.; Narita, A.; Hu, Y.; Schwab, M. G.; Bruna, M.; Yoon, D.; Milana, S.; Feng, X.; Mullen, K.; Ferrari, A. C.; Casiraghi, C.; Prezzi, D. Raman Fingerprints of Atomically Precise Graphene Nanoribbons. *Nano Lett.* **2016**, *16*, 3442−3447.

(48) Rizzo, D.; Prezzi, D.; Ruini, A.; Nagyte, V.; Keerthi, A.; Narita, A.; Beser, U.; Xu, F.; Mai, Y.; Feng, X.; Müllen, K.; Molinari, E.; Casiraghi, C. Multiwavelength Raman Spectroscopy of Ultranarrow Nanoribbons Made by Solution-Mediated Bottom-up Approach. *Phys. Rev. B* **2019**, *100*, 045406.

(49) Ferrari, A. C.; Basko, D. M. Raman Spectroscopy as a Versatile Tool for Studying the Properties of Graphene. *Nat. Nanotechnol.* **2013**, *8*, 235−246.

(50) Girifalco, L. A.; Hodak, M.; Lee, R. S. Carbon Nanotubes, Buckyballs, Ropes, and a Universal Graphitic Potential. *Phys. Rev. B* **2000**, *62*, 13104−13110.

(51) Kuila, T.; Bose, S.; Mishra, A. K.; Khanra, P.; Kim, N. H.; Lee, J. H. Chemical Functionalization of Graphene and Its Applications. *Prog. Mater. Sci.* **2012**, *57*, 1061−1105.

(52) Gierschner, J.; Cornil, J.; Egelhaaf, H. J. Optical Bandgaps of π-Conjugated Organic Materials at the Polymer Limit: Experiment and Theory. *Adv. Mater.* **2007**, *19*, 173−191.

(53) Kowalczyk, M.; Chen, N.; Jang, S. J. Comparative Computational Study of Electronic Excitations of Neutral and Charged Small Oligothiophenes and Their Extrapolations Based on Simple Models. *ACS Omega* **2019**, *4*, 5758−5767.

(54) Jacquemin, D.; Mennucci, B.; Adamo, C. Excited-State Calculations with TD-DFT: From Benchmarks to Simulations in Complex Environments. *Phys. Chem. Chem. Phys.* **2011**, *13*, 16987−98.

(55) Zhao, S.; Rondin, L.; Delport, G.; Voisin, C.; Beser, U.; Hu, Y.; Feng, X.; Müllen, K.; Narita, A.; Campidelli, S.; Lauret, J. S. Fluorescence from Graphene Nanoribbons of Well-Defined Structure. *Carbon* **2017**, *119*, 235−240.

(56) Niu, W.; Sopp, S.; Lodi, A.; Gee, A.; Kong, F.; Pei, T.; Gehring, P.; Nagele, J.; Lau, C. S.; Ma, J.; Liu, J.; Narita, A.; Mol, J.; Burghard, M.; Mullen, K.; Mai, Y.; Feng, X.; Bogani, L. Exceptionally Clean Single-Electron Transistors from Solutions of Molecular Graphene Nanoribbons. *Nat. Mater.* **2023**, *22*, 180−185.

(57) Jassas, R. S.; Mughal, E. U.; Sadiq, A.; Alsantali, R. I.; Al-Rooqi, M. M.; Naeem, N.; Moussa, Z.; Ahmed, S. A. Scholl Reaction as a Powerful Tool for the Synthesis of Nanographenes: A Systematic Review. *RSC Adv.* **2021**, *11*, 32158−32202.

(58) Sebastian, F. L.; Zorn, N. F.; Settele, S.; Lindenthal, S.; Berger, F. J.; Bendel, C.; Li, H.; Flavel, B. S.; Zaumseil, J. Absolute Quantification of sp^3 Defects in Semiconducting Single-Wall Carbon Nanotubes by Raman Spectroscopy. *J. Phys. Chem. Lett.* **2022**, *13*, 3542−3548.

(59) Francis, C.; Fazzi, D.; Grimm, S. B.; Paulus, F.; Beck, S.; Hillebrandt, S.; Pucci, A.; Zaumseil, J. Raman Spectroscopy and Microscopy of Electrochemically and Chemically Doped High-Mobility Semiconducting Polymers. *J. Mater. Chem. C* **2017**, *5*, 6176−6184.

(60) Vijayakumar, V.; Durand, P.; Zeng, H.; Untilova, V.; Herrmann, L.; Algayer, P.; Leclerc, N.; Brinkmann, M. Influence of Dopant Size and Doping Method on the Structure and Thermoelectric Properties of Pbttt Films Doped with F6tcnnq and F4tcnq. *J. Mater. Chem. C* **2020**, *8*, 16470−16482.

(61) Wang, C.; Duong, D. T.; Vandewal, K.; Rivnay, J.; Salleo, A. Optical Measurement of Doping Efficiency in Poly(3-Hexylthiophene) Solutions and Thin Films. *Phys. Rev. B* **2015**, *91*, 085205.

(62) Stanton, N. J.; Ihly, R.; Norton-Baker, B.; Ferguson, A. J.; Blackburn, J. L. Solution-Phase p-Type Doping of Highly Enriched Semiconducting Single-Walled Carbon Nanotubes for Thermoelectric Thin Films. *Appl. Phys. Lett.* **2021**, *119*, 023302.

(63) Chen, W.; Chen, S.; Qi, D. C.; Gao, X. Y.; Wee, A. T. S. Surface Transfer P-Type Doping of Epitaxial Graphene. *J. Am. Chem. Soc.* **2007**, *129*, 10418−10422.

(64) Eckstein, K. H.; Oberndorfer, F.; Achsnich, M. M.; Schöppler, F.; Hertel, T. Quantifying Doping Levels in Carbon Nanotubes by Optical Spectroscopy. *J. Phys. Chem. C* **2019**, *123*, 30001−30006.

(65) Fedotov, P. V.; Obraztsova, E. D. Near Infrared Photoluminescence of the Bottom-up Produced 7-Armchair Graphene Nanoribbons. *Appl. Phys. Lett.* **2023**, *122*, 013101.

(66) Graf, A.; Zakharko, Y.; Schießl, S. P.; Backes, C.; Pfohl, M.; Flavel, B. S.; Zaumseil, J. Large Scale, Selective Dispersion of Long Single-Walled Carbon Nanotubes with High Photoluminescence Quantum Yield by Shear Force Mixing. *Carbon* **2016**, *105*, 593−599.

(67) Grimme, S.; Bannwarth, C.; Shushkov, P. A Robust and Accurate Tight-Binding Quantum Chemical Method for Structures, Vibrational Frequencies, and Noncovalent Interactions of Large Molecular Systems Parametrized for All spd-Block Elements (Z = 1−86). *J. Chem. Theory. Comput.* **2017**, *13*, 1989−2009.

(68) Bannwarth, C.; Caldeweyher, E.; Ehlert, S.; Hansen, A.; Pracht, P.; Seibert, J.; Spicher, S.; Grimme, S. Extended Tight Binding Quantum Chemistry Methods. *WIREs Comput. Mol. Sci.* **2021**, *11*, No. e1493.

(69) Frisch, M. J.; Trucks, G. W.; Schlegel, H. B.; Scuseria, G. E.; Robb, M. A.; Cheeseman, J. R.; Scalmani, G.; Barone, V.; Petersson, G. A.; Nakatsuji, H.; Li, X.; Caricato, M.; Marenich, A. V.; Bloino, J.; Janesko, B. G.; Gomperts, R.; Mennucci, B.; Hratchian, H. P.; Ortiz, J. V.; Izmaylov, A. F.; Sonnenberg, J. L.; Williams Ding, F.; Lipparini, F.; Egidi, F.; Goings, J.; Peng, B.; Petrone, A.; Henderson, T.; Ranasinghe, D.; Zakrzewski, V. G.; Gao, J.; Rega, N.; Zheng, G.; Liang, W.; Hada, M.; Ehara, M.; Toyota, K.; Fukuda, R.; Hasegawa, J.; Ishida, M.; Nakajima, T.; Honda, Y.; Kitao, O.; Nakai, H.; Vreven, T.; Throssell, K.; Montgomery, J. A., Jr.; Peralta, J. E.; Ogliaro, F.; Bearpark, M. J.; Heyd, J. J.; Brothers, E. N.; Kudin, K. N.; Staroverov, V. N.; Keith, T. A.; Kobayashi, R.; Normand, J.; Raghavachari, K.; Rendell, A. P.; Burant, J. C.; Iyengar, S. S.; Tomasi, J.; Cossi, M.; Millam, J. M.; Klene, M.; Adamo, C.; Cammi, R.; Ochterski, J. W.; Martin, R. L.; Morokuma, K.; Farkas, O.; Foresman, J. B.; Fox, D. J. *Gaussian 16*, Rev. C.01; Gaussian Inc.: Wallingford, CT, 2016.

(70) Neese, F. Software Update: The Orca Program System—Version 5.0. *WIREs Comput. Mol. Sci.* **2022**, *12*, No. e1606.

SUPPORTING INFORMATION

Understanding the optical properties of doped and undoped 9-armchair graphene nanoribbons in dispersion

Sebastian Lindenthal[1], Daniele Fazzi[2], Nicolas F. Zorn[1], Abdurrahman Ali El Yumin[1], Simon Settele[1], Britta Weidinger[3], Eva Blasco[3], Jana Zaumseil,[1]*

[1]Institute for Physical Chemistry, Heidelberg University, D-69120 Heidelberg, Germany E-mail: zaumseil@uni-heidelberg.de

[2] University of Bologna, Department of Chemistry, 40126, Bologna, Italy

[3] Institute for Molecular Systems Engineering and Advanced Materials and Institute of Organic Chemistry, Heidelberg University, D-69120 Heidelberg, Germany

*E-mail: zaumseil@uni-heidelberg.de

Contents

Synthesis of 9-aGNRs

General

The synthesis of 9-aGNRs follows the published method by Li *et al.*[1] with some minor modifications.

Reagent grade chemicals were purchased from Sigma Aldrich, Alfa Aesar, Tokio Chemical Industries or Fisher Scientific and used without further purification. Anhydrous solvents were obtained from an MBraun MB SPS-800 solvent purification system, with the exception of dry THF, which was freshly distilled over sodium prior to usage. All reactions containing moisture or air-sensitive components were carried out in inert atmosphere and in dry reaction vessels with standard Schlenk techniques unless noted otherwise.

For analytical thin-layer chromatography (TLC) aluminum plates coated with 0.2 mm of silica gel and fluorescent indicator (Macherey-Nagel, ALUGRAM®, SIL G/UV$_{254}$) were used. Spots on TLC plates were observed by exposure to UV light (λ = 254 nm and 366 nm). Column chromatography was performed on silica gel (Macherey-Nagel, M-N Silica Gel 60A, 230-400 mesh).

^{1}H and ^{13}C NMR spectra were recorded either on a Bruker Avance DRX 300 (300 MHz for ^{1}H and 75 MHz for ^{13}C), Bruker Avance III 400 (400 MHz for ^{1}H and 100 MHz for ^{13}C) or Bruker Avance III 600 (600 MHz for ^{1}H and 150 MHz for ^{13}C) spectrometer. Chemical shifts δ are reported in ppm and referenced to the residual solvent signal ($\delta_H(CHCl_3)$ = 7.26 ppm, $\delta_C(CHCl_3)$ = 77.2 ppm). Coupling constants (J) are given in Hz. To report the multiplicity the following abbreviations were used: s = singlet, d = doublet and m = multiplet for the ^{1}H NMR and s = primary, d = secondary, t = tertiary and q = quarternary for ^{13}C NMR.

GPC measurements were performed on a Shimadzu Nexera LC-40 system (with LC-40D pump, autosampler SIL-40C, DGU-403 (degasser), CBM-40 (controlling unit), column oven CTO-40C, UV-detector SPD40 and RI-detector RID-20A). The system was equipped with 4 analytical GPC-columns (PSS): 1 x SDV precolumn 3 µm 8x50 mm, 2 x SDV column 3 µm 1000Å 8x300 mm, 1 x SDV column 3 µm 10^4Å 8x300 mm. The measurements were performed in THF at a flow speed of 1 mL/min at a temperature of 40 °C. Chromatograms were analyzed using the LabSolutions (Shimadzu) software. Calibration was performed against different or polystyrene standards (370 - 2 520 000 Da, PSS).

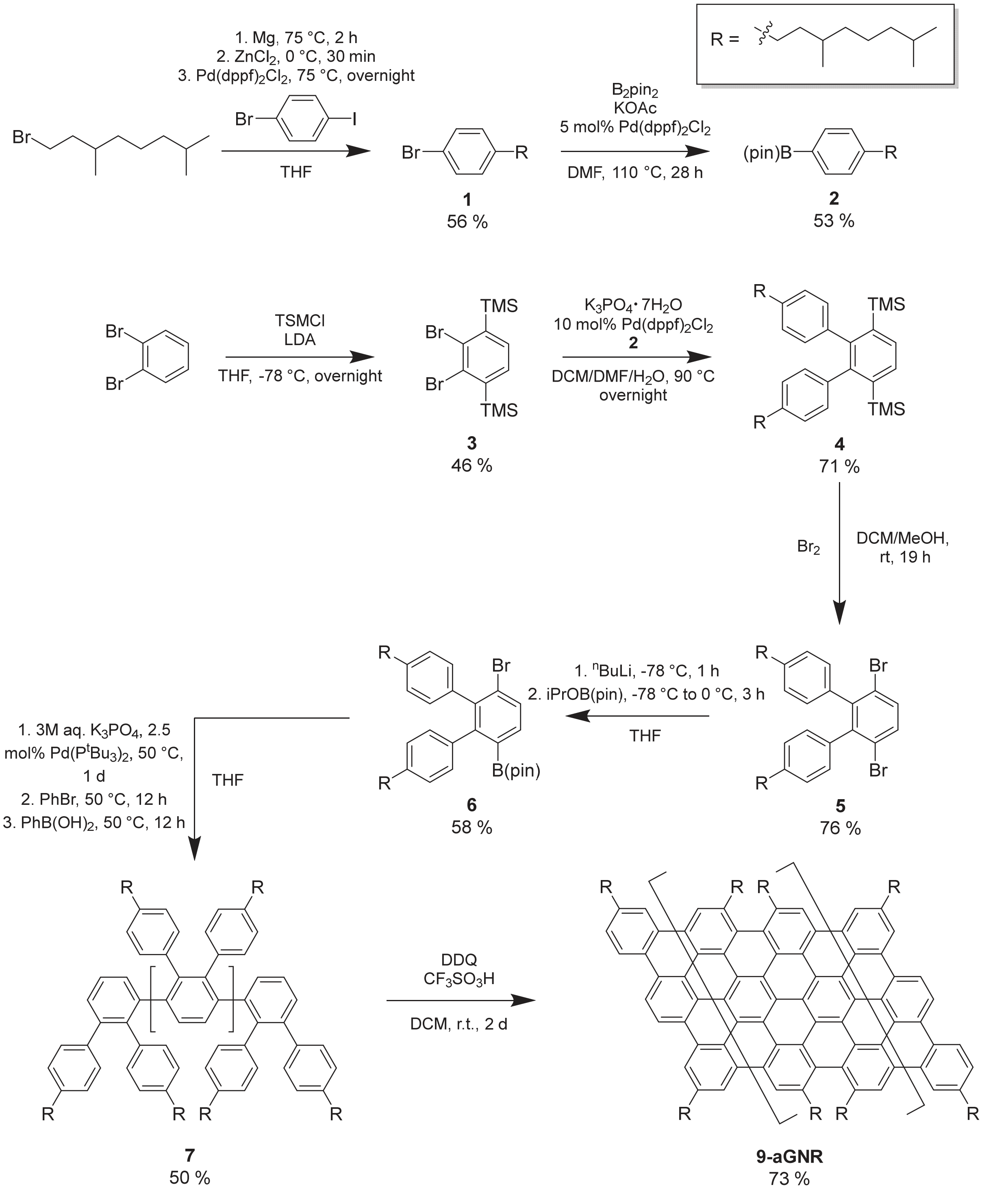

Scheme S1. Synthesis of the 9-aGNR according to Li *et al.*[1] Reaction conditions were kept constant. Yields of each reaction step are denoted under the respective molecule.

1-bromo-4-(3,7-dimethyloctyl)benzene (1)

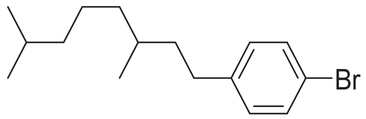

Magnesium shavings (1.47 g, 63.6 mmol) were added to a solution of 1-bromo-3,7-dimethyloctane (4.81 g, 21.7 mmol) in 10 mL dry, degassed THF and stirred at 70 °C for 2 h. The Grignard reagent was slowly added to a solution of dried $ZnCl_2$ (2.89 g, 21.2 mmol) in 20 mL of dry, degassed THF at 0 °C and stirred for 30 min. After addition of 1-bromo-4-iodobenzene (5.00 g, 17.7 mmol) and $Pd(dppf)Cl_2$ (388 mg, 0.53 mmol) the reaction mixture was heated to reflux overnight. When heating up the reaction mixture, addition of more THF was necessary as the reaction mixture used to solidify in the reaction vessel. After cooling to room temperature, 50 mL of diethyl ether and 50 mL of 1 M HCl were added to the reaction mixture. The organic phase was separated and the aqueous phase was extracted with 3 x 100 mL of diethyl ether. The combined organic phases were washed with brine and water, dried over Na_2SO_4 and the solvent was removed by rotary evaporation. The crude product was purified by flash column chromatography ($R_f = 0.9$, pure petroleum ether (PE)) to yield **1** as a colorless oil (3.11 g, 59 %).

^{1}H NMR ($CDCl_3$, 300 MHz): δ 7.38 (m, 2H, Ar-H), 7.05 (m, 2H, Ar-H), 2.65-2.46 (m, 2H), 1.66-1.06 (m, 10H), 0.91 (d, J = 6 Hz, 3H, CH_3), 0.86 (d, J = 7 Hz, 6H, CH_3) ppm.

^{13}C NMR ($CDCl_3$, 300 MHz): δ 142.32, 131.46, 130.31, 119.38, 39.49, 38.99, 37.29, 33.09, 32.59, 28.15, 24.86, 22.89, 22.80, 19.75 ppm.

2-(4-(3,7-dimethyloctyl)phenyl)-4,4,5,5-tetramethyl-1,3,2-dioxaborolane (2)

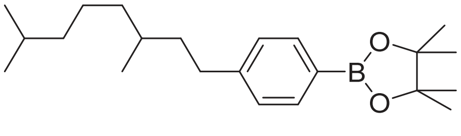

1-bromo-4-(3,7-dimethyloctyl)benzene (5.00 g, 16.8 mmol), 4,4,4',4',5,5,5',5'octamethyl-2,2'-bi-(1,3,2-dioxaborolane) (4.70 g, 18.5 mmol), potassium acetate (4.95 g, 50.5 mmol) and

Pd(dppf)$_2$Cl$_2$ complex with DCM (dichloromethane, 687 mg, 0.84 mmol) were added to 35 mL of degassed, dry DMF and stirred at 110 °C for 28 h. After cooling down to room temperature 100 mL water and 100 mL ethyl acetate were added to the reaction mixture. The organic phase was separated and the aqueous phase was extracted with 3 x 100 mL of diethyl ether. The combined organic phases were washed with brine and water, dried over Na_2SO_4 and the solvent was removed under reduced pressure. The crude product was purified by flash column chromatography ($R_f = 0.4$, DCM:PE 1:4) to yield **2** as a yellow oil (3.24 g, 56 %).

^{1}H NMR (CDCl$_3$, 300 MHz): δ 7.72 (m, 2H, Ar-H), 7.20 (m, 2H, Ar-H), 2.72-2.50 (m, 2H), 1.70-1.04 (m, 10H), 1.34 (s, 12H, CH$_3$) 0.91 (d, J = 6 Hz, 3H, CH$_3$), 0.86 (d, J = 7 Hz, 6H, CH$_3$) ppm.

(2,3-dibromo-1,4-phenylene)bis(trimethylsilane) (3)

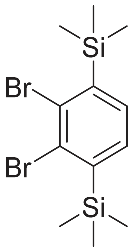

A mixture of dry, degassed THF (3.77 mL, 46.5 mmol), hexane (12.14 mL, 93.0 mmol) and toluene (4.92 mL, 46.5 mmol) was slowly added to solid lithium diisopropylamide (4.98 g, 46.5 mmol) at -78 °C. The slightly yellow LDA solution was then added dropwise to a solution of 1,2-dibromobenzene (5.00 g, 19.7 mmol) and trimethylsilylchloride (5.05 g, 46.5 mmol) at -78 °C. The reaction was stirred at -78 °C overnight. The reaction mixture was then hydrolysed with 50 mL of 0.1M H_2SO_4. The yellow organic phase was separated and the aqueous phase was extracted with 3 x 100 mL of diethyl ether. The combined organic phases were washed with brine and water, dried over Na_2SO_4 and the solvent was removed under reduced pressure. The crude product was purified by flash column chromatography ($R_f = 0.95$, pure PE) and recrystallized from a 1:1 mixture of acetone and methanol to yield **3** as colorless crystals (3.43 g, 46 %).

^{1}H NMR (CDCl$_3$, 600 MHz): δ 7.33 (s, 2H, Ar-H), 0.39 (s, 18H, CH$_3$) ppm.

^{13}C NMR (CDCl$_3$, 150 MHz): δ 145.93, 134.10, 133.52, -0.24 ppm.

(4,4''-bis(3,7-dimethyloctyl)-[1,1':2',1''-terphenyl]-3',6'-diyl)bis(trimethylsilane) (4)

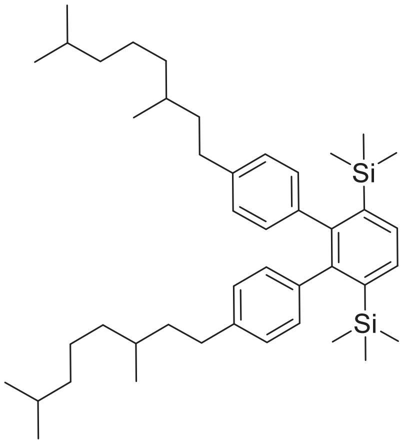

2 (5.16 g, 15.0 mmol), **3** (1.90 g, 5.00 mmol), Pd(dppf)$_2$Cl$_2$ complex with DCM (408 mg, 0.50 mmol) and $K_3PO_4 \cdot 7\,H_2O$ (6.36 g, 30.0 mmol) were dissolved in a mixture of 15 mL degassed DMF and 4 mL of degassed H_2O. The reaction mixture was stirred at 90 °C overnight. After cooling down to room temperature, 100 mL of ethyl acetate and 50 mL of water were added. The organic phase was separated and the aqueous phase was extracted with 3 x 100 mL of diethyl ether. The combined organic phases were washed with brine and water, dried over Na_2SO_4 and the solvent was removed by rotary evaporation. The crude product was purified by flash column chromatography ($R_f = 0.65$, pure PE) to yield **4** as a slightly yellow oil (2.30 g, 69 %).

^{1}H NMR (CDCl$_3$, 400 MHz): δ 7.61 (s, 2H, Ar-H), 6.87-6.81 (m, 8H, Ar-H), 2.55-2.41 (m, 4H, CH$_2$), 1.56-1.06 (m, 20H, CH and CH$_2$), 0.88-0.85 (m, 18H, CH$_3$), -0.07 (s, 18H, CH$_3$) ppm.

^{13}C NMR (CDCl$_3$, 100 MHz): δ 147.74, 140.91, 140.29, 139.80, 132.66, 131.01, 130.98, 126.86, 126.82, 39.54, 39.06, 37.33, 33.20, 32.29, 28.16, 24.93, 22.90, 22.82, 19.78, 0.66 ppm.

3',6'-dibromo-4,4''-bis(3,7-dimethyloctyl)-1,1':2',1''-terphenyl (5)

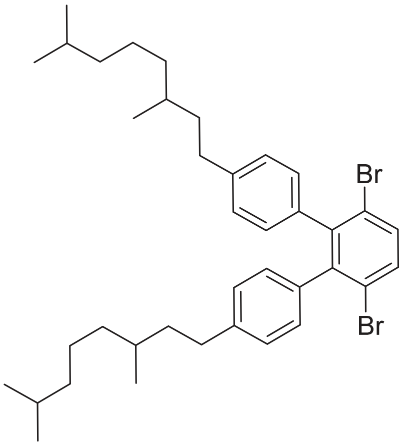

A solution of bromine (1.43 g, 0.46 mL, 8.94 mmol) in 2mL of DCM was slowly added to a solution of **4** (1.70 g, 2.56 mmol) in 3 mL of dry, degassed DCM and 5 mL of MeOH, which was held at 0 °C. The mixture was then stirred at room temperature overnight. After addition of 50 mL aqueous sodium sulphite solution and 50 mL of DCM, the organic phase was separated and the aqueous phase was extracted with 3 x 100 mL DCM. The combined organic phases were washed with brine and water, dried over Na_2SO_4 and the solvent was removed by rotary evaporation. The crude product was purified by flash column chromatography ($R_f = 0.35$, pure PE) to yield **5** as a yellow oil (1.33 g, 78 %).

^{1}H NMR ($CDCl_3$, 400 MHz): δ 7.51 (s, 2H, Ar-H), 6.96-6.93 (m, 4H, Ar-H), 6.86-6.82 (m, 4H, Ar-H), 2.57-2.42 (m, 4H, CH_2), 1.58-1.06 (m, 20H, CH and CH_2), 0.88-0.86 (m, 18H, CH_3) ppm.

^{13}C NMR ($CDCl_3$, 100 MHz): δ 144.39, 142.02, 137.53, 132.71, 129.90, 129.88, 127.53, 123.60, 39.54, 38.76, 37.32, 33.32, 32.58, 28.17, 24.90, 22.91, 22.83, 19.83 ppm.

2-(6'-bromo-4,4''-bis(3,7-dimethyloctyl)-[1,1':2',1''-terphenyl]-3'-yl)-4,4,5,5-tetramethyl-1,3,2-dioxaborolane (6)

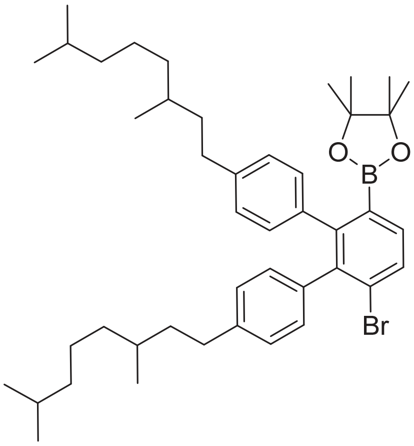

A 2.5 M n-Butyllithium solution in hexane (0.89 mL, 2.22 mmol) was added dropwise to a solution of **5** (1.35 g, 2.02 mmol) in 7 mL dry, degassed THF at -78 °C. The yellow reaction mixture was stirred at -78 °C for 1 h after which 2-isopropoxy-4,4,5,5-tetramethyl-1,3,2-dioxaborolane (0.52 g, 0.57 mL, 2.80 mmol) was added. The white reaction mixture was then stirred for 3 h, during which it was allowed to warm up to 0 °C. After this 50 mL of water and 50 mL of ethyl acetate were added. The organic phase was separated and the aqueous phase was extracted with 3 x 100 mL DCM. The combined organic phases were washed with brine and water, dried over Na_2SO_4 and the solvent was removed by rotary evaporation. The crude product was purified by flash column chromatography (R_f = 0.3, 1:4 DCM:PE) to yield **5** as colorless oil (0.83 g, 57 %).

^{1}H NMR ($CDCl_3$, 400 MHz): δ 7.64 (d, J = 8 Hz, 1H, Ar-H), 7.44 (d, J = 8 Hz, 1H, Ar-H) 6.99-6.81 (m, 8H, Ar-H)), 2.64-2.43 (m, 4H, CH_2), 1.61-1.09 (m, 20H, CH and CH_2), 1.08 (s, 12H, CH_3), 0.91-0.81 (m, 18H, CH_3) ppm.

^{13}C NMR ($CDCl_3$, 100 MHz): δ 148.57, 141.74, 141.54, 141.15, 139.17, 137.70, 133.60, 131.02, 130.37, 130.33, 130.13, 127.45, 127.10, 126.81, 83.87, 39.58, 39.55, 39.30, 38.74, 37.35, 33.34, 33.24, 32.55, 32.42, 28.16, 24.91, 24.89, 24.68, 22.91, 22.89, 22.83, 22.79, 19.84, 19.73 ppm.

Synthesis of precursor polymer (7)

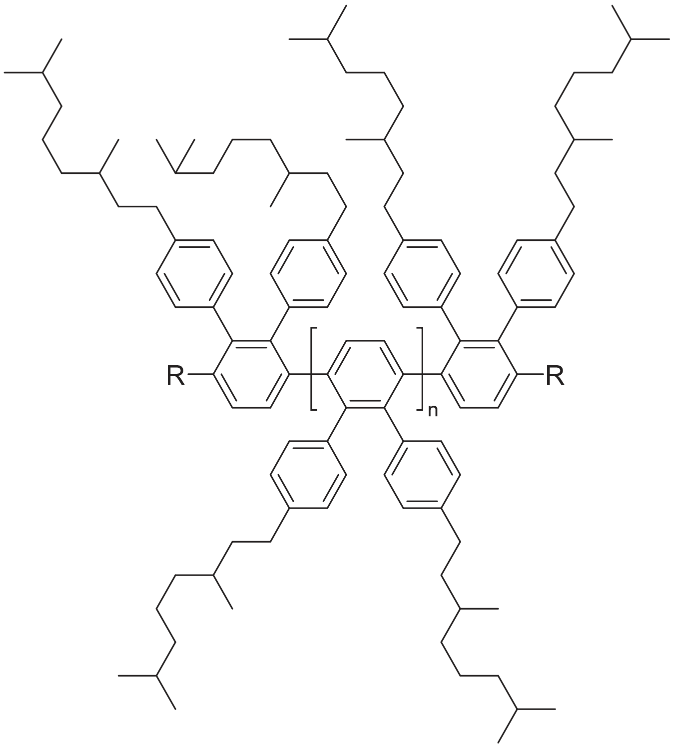

Inside of a nitrogen glovebox, the AB-type monomer **6** (102 mg, 0.14 mmol) and Pd(P^{t}Bu$_3$)$_2$ (4 mg, 2.5 mol%) were combined in a Schlenk flask. Under inert atmosphere, 3 mL of degassed THF and 0.7 mL of a 3M K_3PO_4 solution in degassed water were added to the reaction mixture. The mixture was stirred at 50 °C for 24h. After that, bromobenzene (21 mg, 0.14 mmol) was added and the reaction was stirred at 50 °C for 8 h. Finally, phenyboronic acid (17 mg, 0.14 mmol) was added and the reaction was stirred at 50 °C for another 8 h. After cooling down to room temperature 10 mL of water and 10 mL of DCM were added to the reaction mixture. The organic phase was separated and the aqueous phase was extracted with 3 x 10 mL DCM. The volume of the combined organic phases was reduced to ~2 mL under reduced pressure and the resulting solution was added to 20 mL of MeOH at room temperature. During this process the polymer precipitates as a white solid. After stirring at room temperature for 1 h, the polymer was filtered and dried under vacuum overnight. To remove impurities and smaller polymer strands, the crude polymer was washed by Soxhlet extraction with acetone for 2 days.

Note that the chemical nature of the end groups R was not determined here. According to Li *et al.* the synthesis usually results in H/H and sometimes H/Phenyl end groups.[1]

Synthesis of 9-aGNR

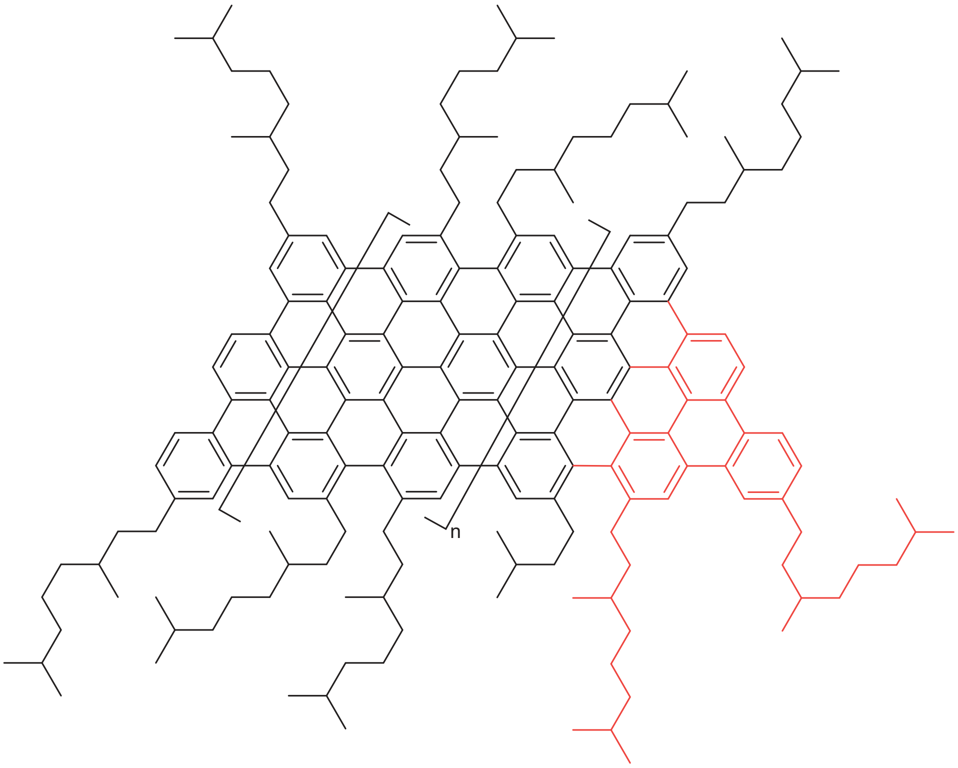

Precursor polymer **7** (202 mg) and DDQ (459 mg) were dissolved in dry, degassed DCM. Dropwise addition of triflic acid (8.6 mL) at 0 °C led to a color change of the reaction mixture from yellow to black. The reaction mixture was stirred at room temperature for 2 days. Subsequently, the reaction mixture was quenched with saturated $NaHCO_3$ solution until no more CO_2 emerged upon addition (after ~30 mL). The black precipitate was filtered off and washed thoroughly with 200 mL of water, methanol and acetone each. The crude product was then purified by Soxhlet extraction with acetone for 2 days.

Note that depending on the number of terphenyl units in the precursor polymer, the resulting 9-aGNR can either have a parallel shape (black structure, even number of terphenyl units) or a trapezoidal shape (black + red structure, odd number of terphenyl units).

NMR spectra

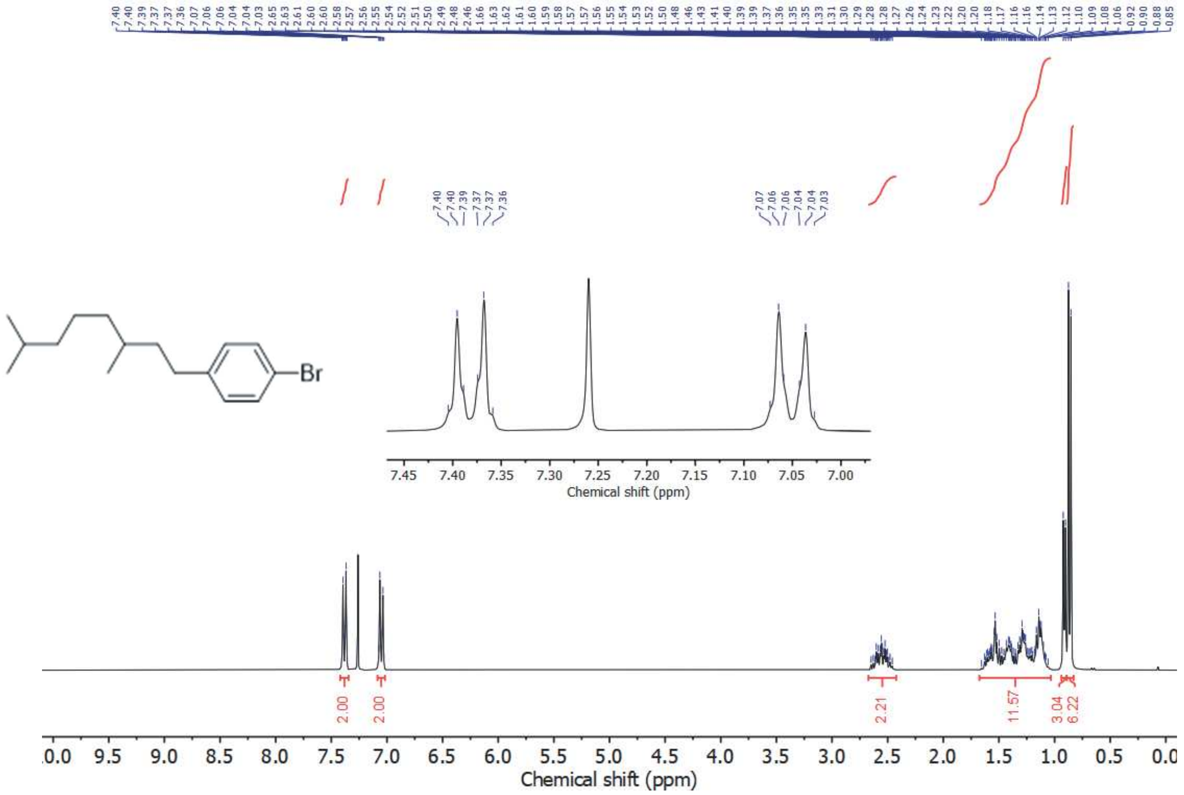

^{1}H NMR spectrum of **1** (CDCl$_3$, 300 MHz, 25°C)

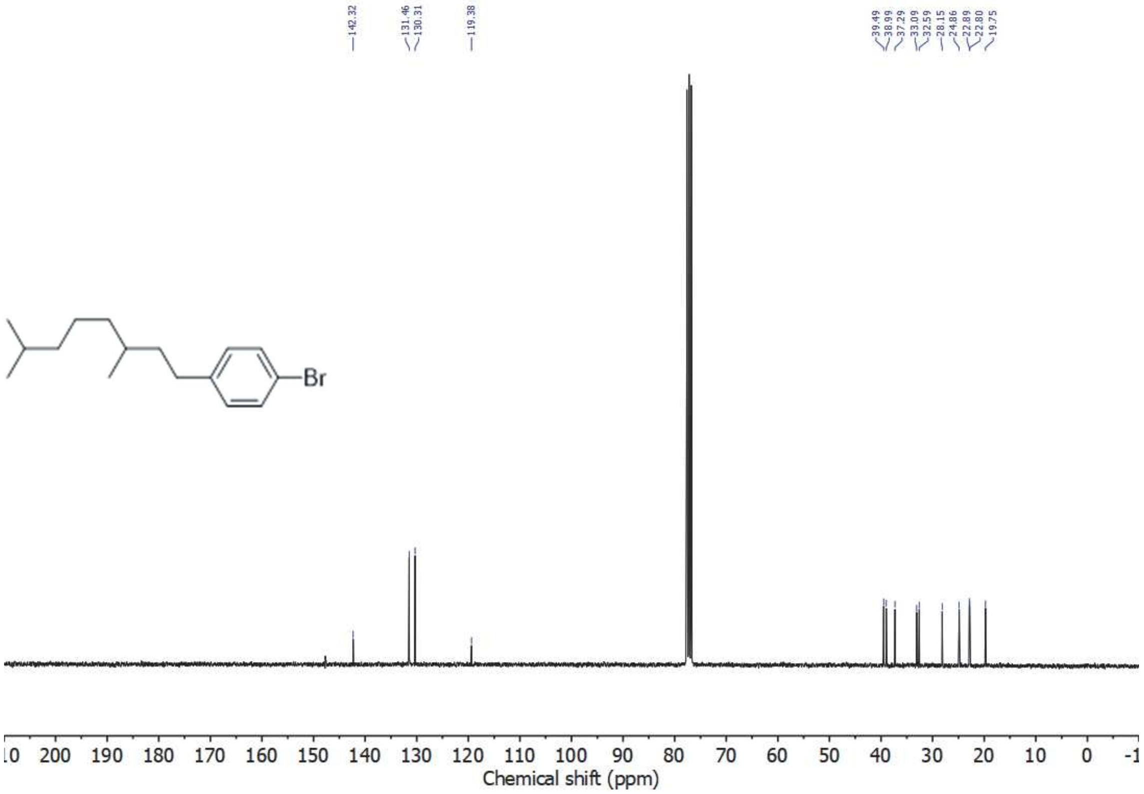

^{13}C NMR spectrum of **1** (CDCl$_3$, 75 MHz, 25°C)

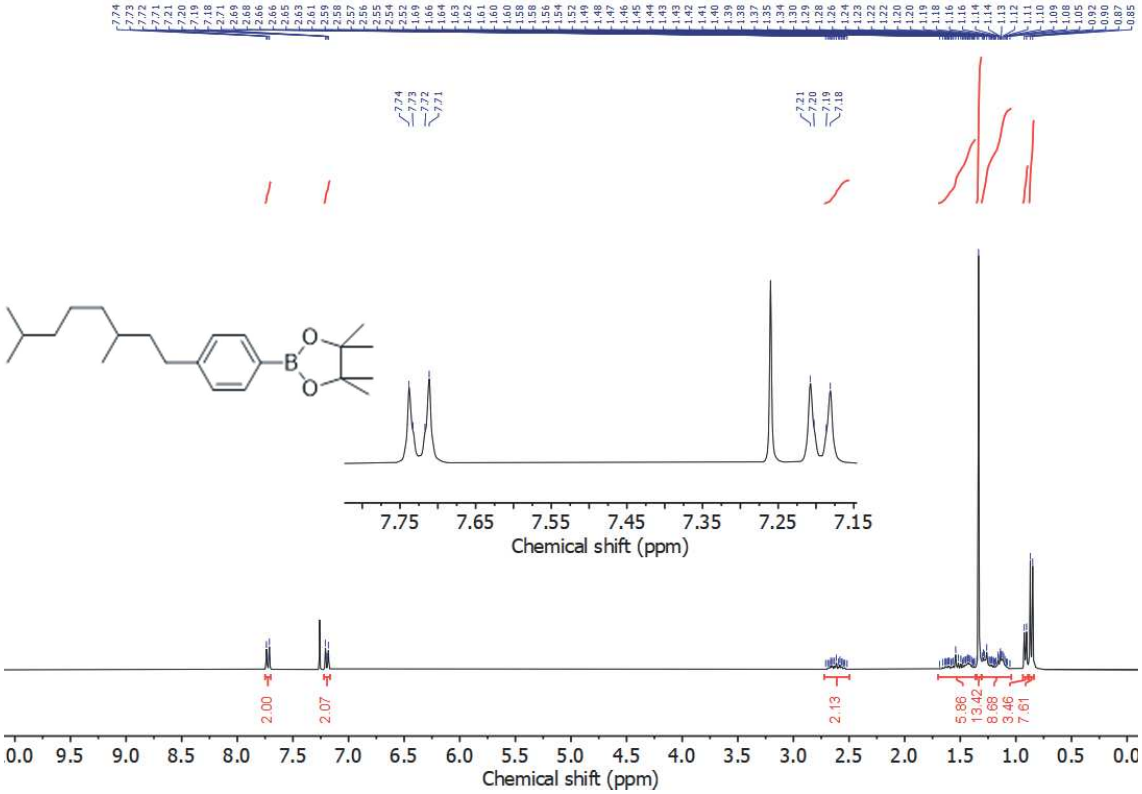

^{1}H NMR spectrum of **2** ($CDCl_3$, 300 MHz, 25°C)

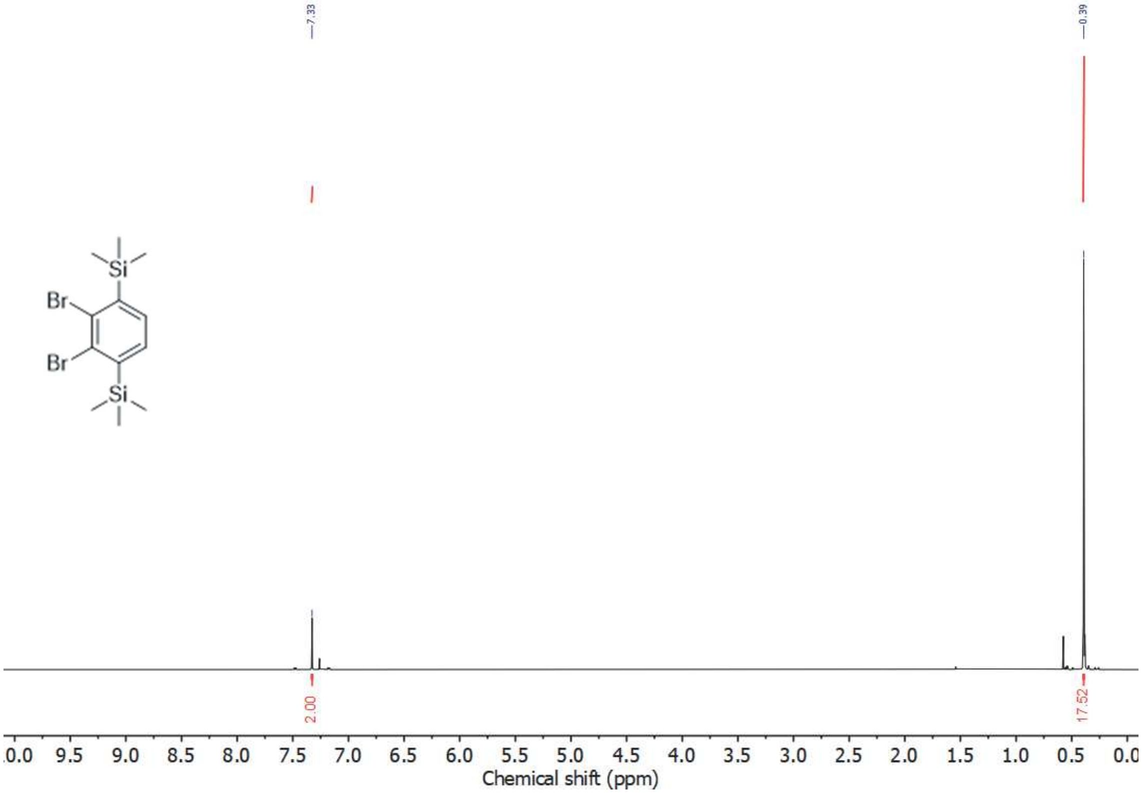

^{1}H NMR spectrum of **3** ($CDCl_3$, 600 MHz, 25°C)

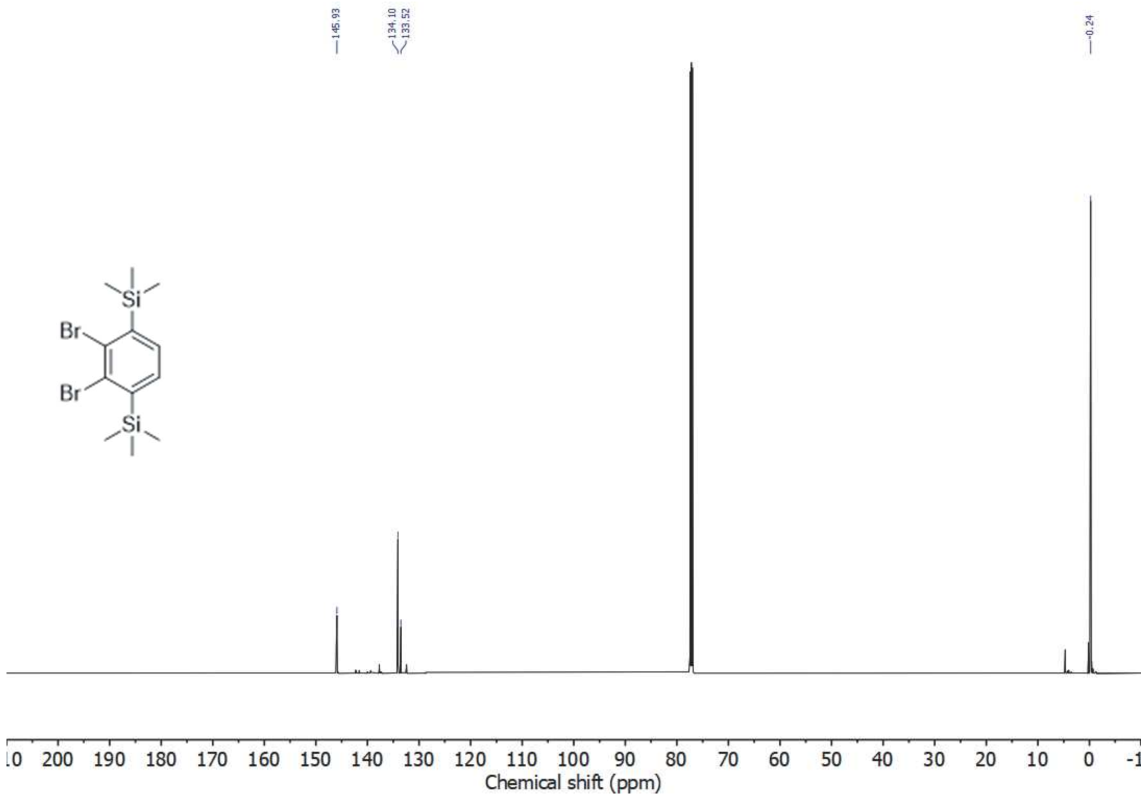

^{13}C NMR spectrum of **3** (CDCl$_3$, 150 MHz, 25°C)

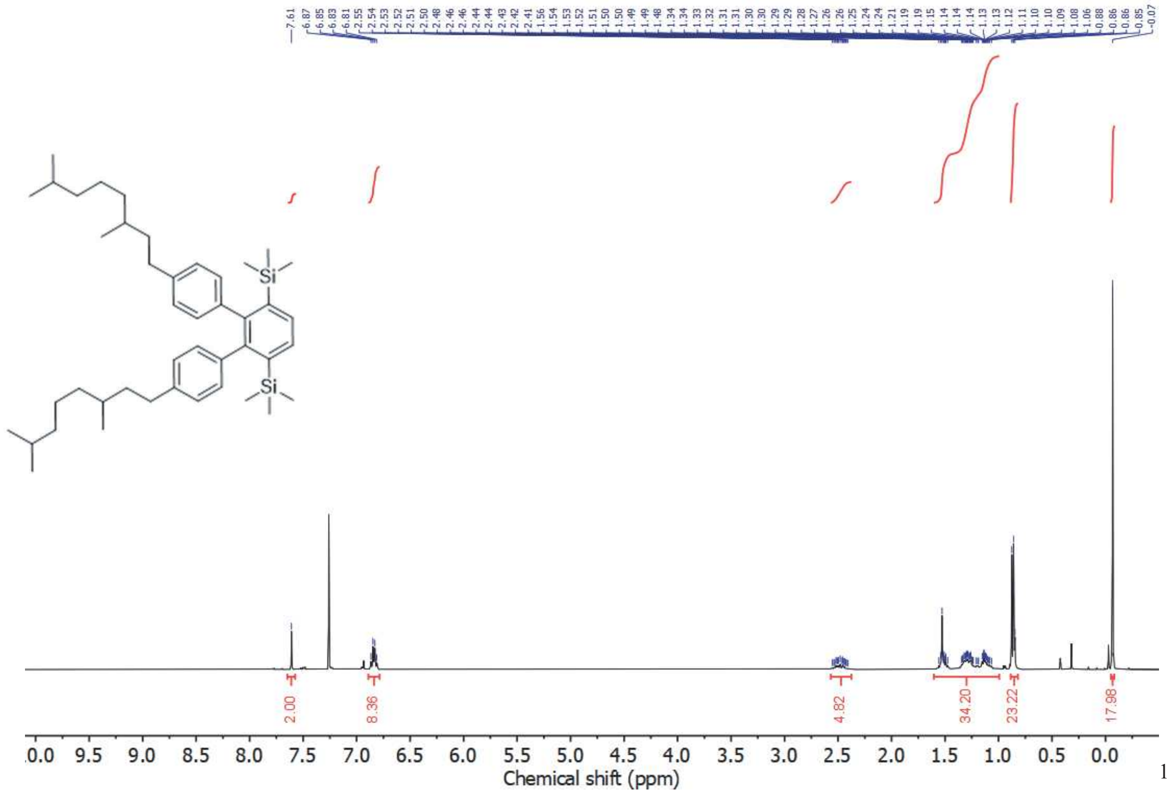

^{1}H NMR spectrum of **4** (CDCl$_3$, 400 MHz, 25°C)

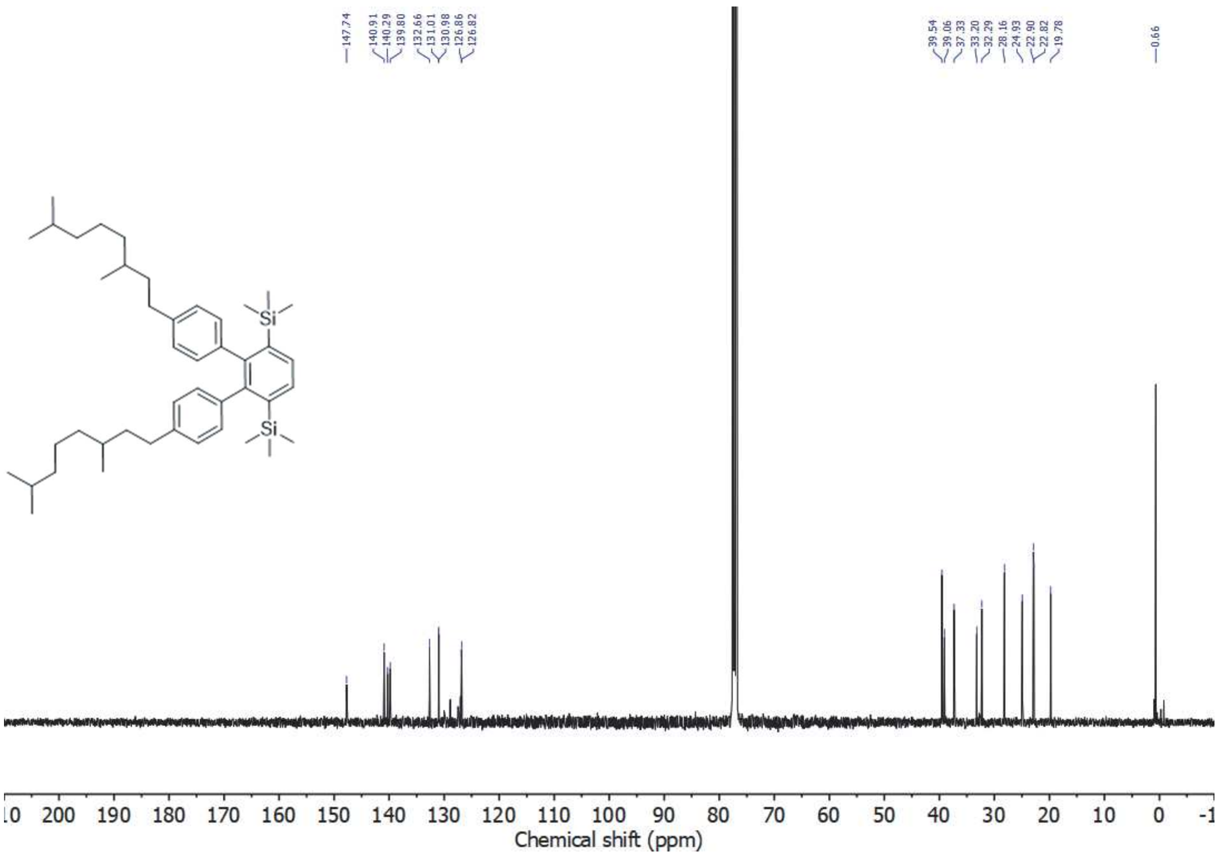

^{13}C NMR spectrum of **4** ($CDCl_3$, 100 MHz, 25°C)

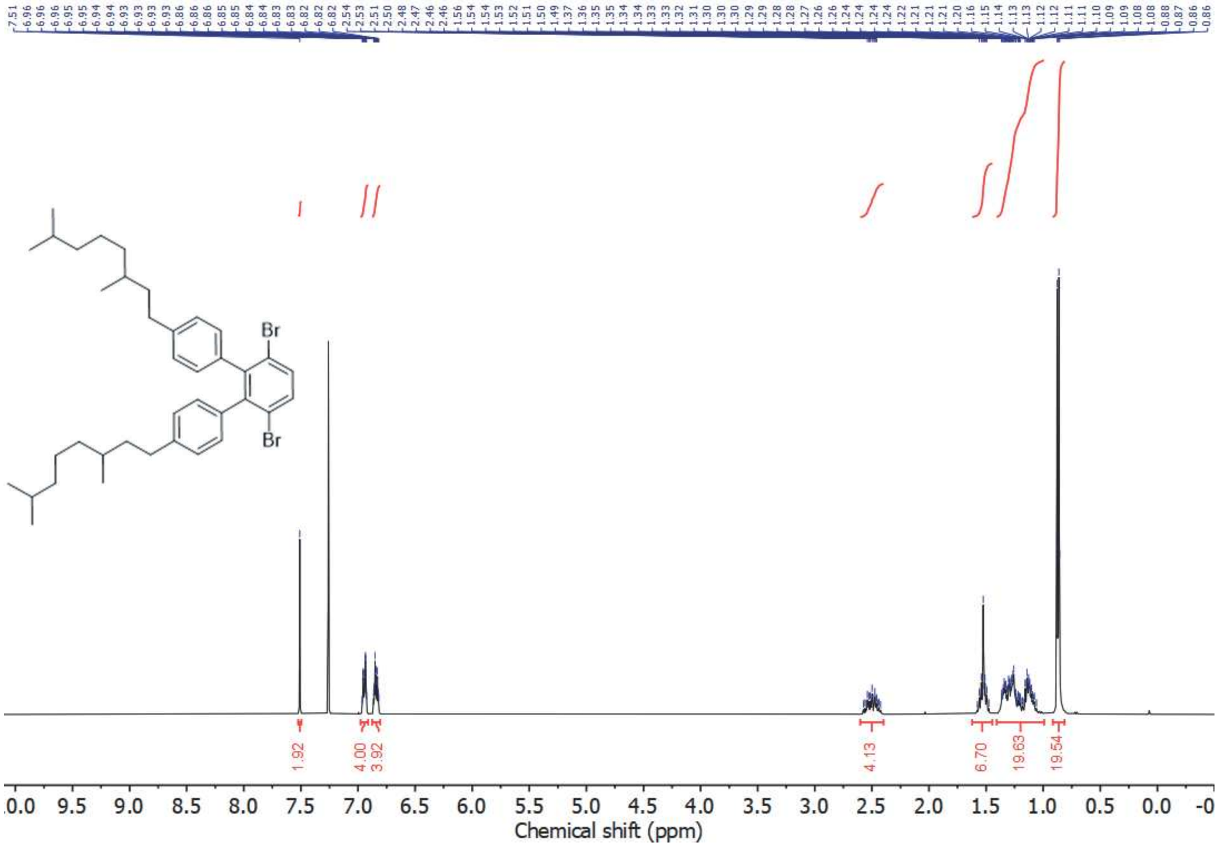

^{1}H NMR spectrum of **5** (CDCl$_3$, 400 MHz, 25°C)

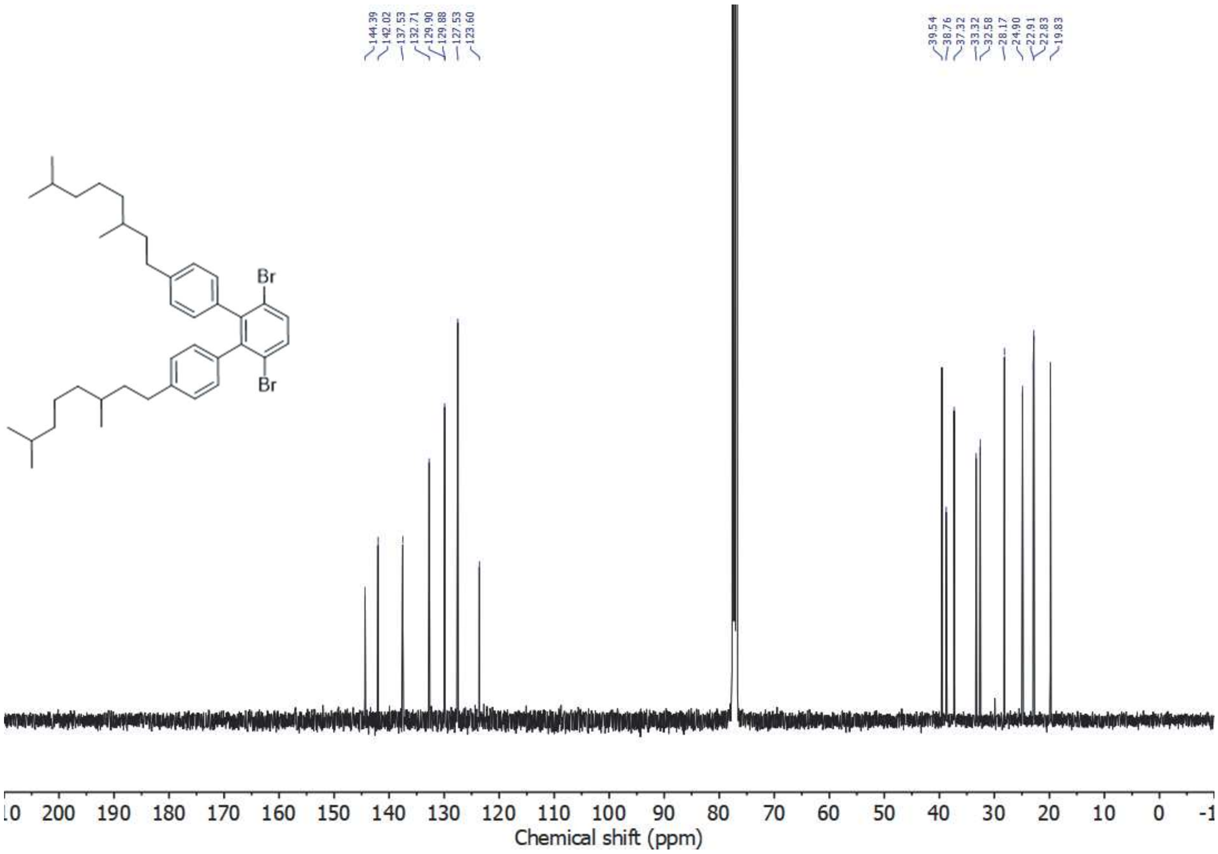

^{13}C NMR spectrum of **5** (CDCl$_3$, 100 MHz, 25°C)

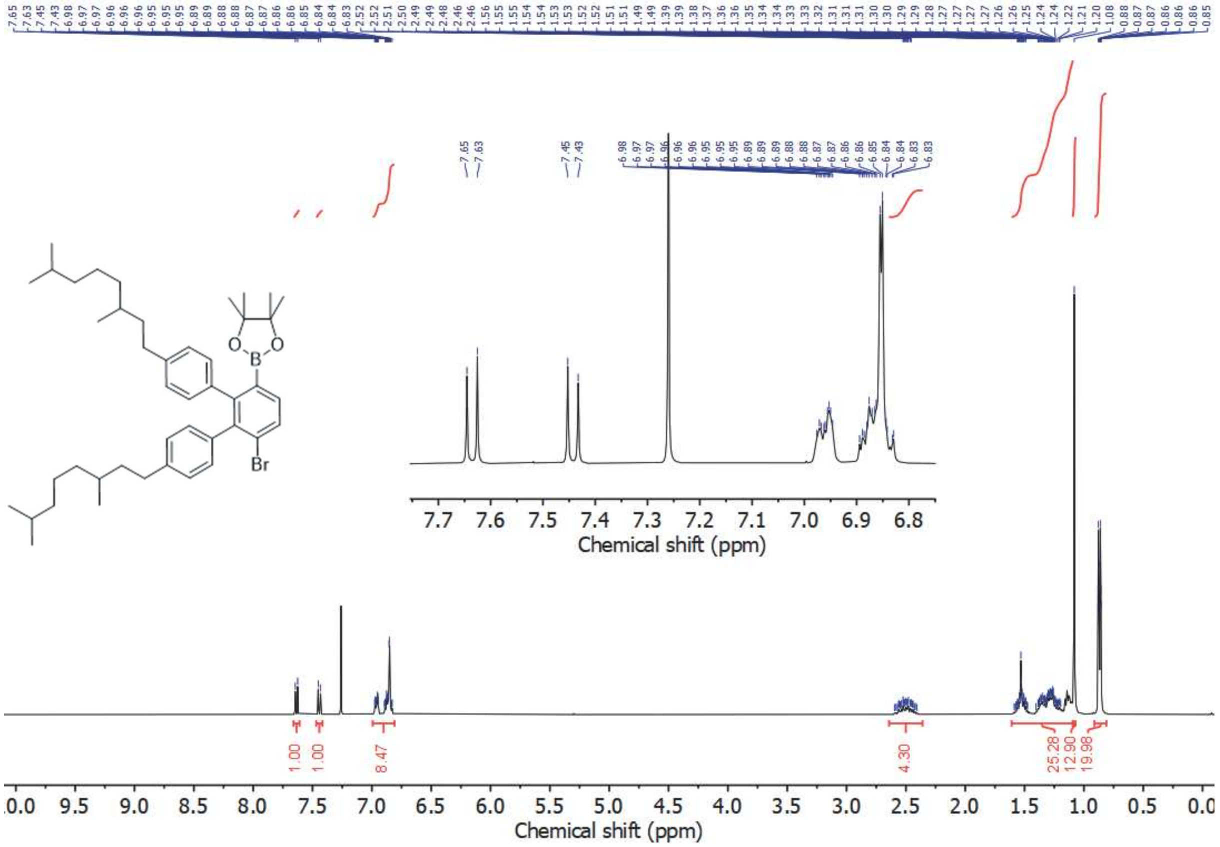

^{1}H NMR spectrum of **6** (CDCl$_3$, 400 MHz, 25°C)

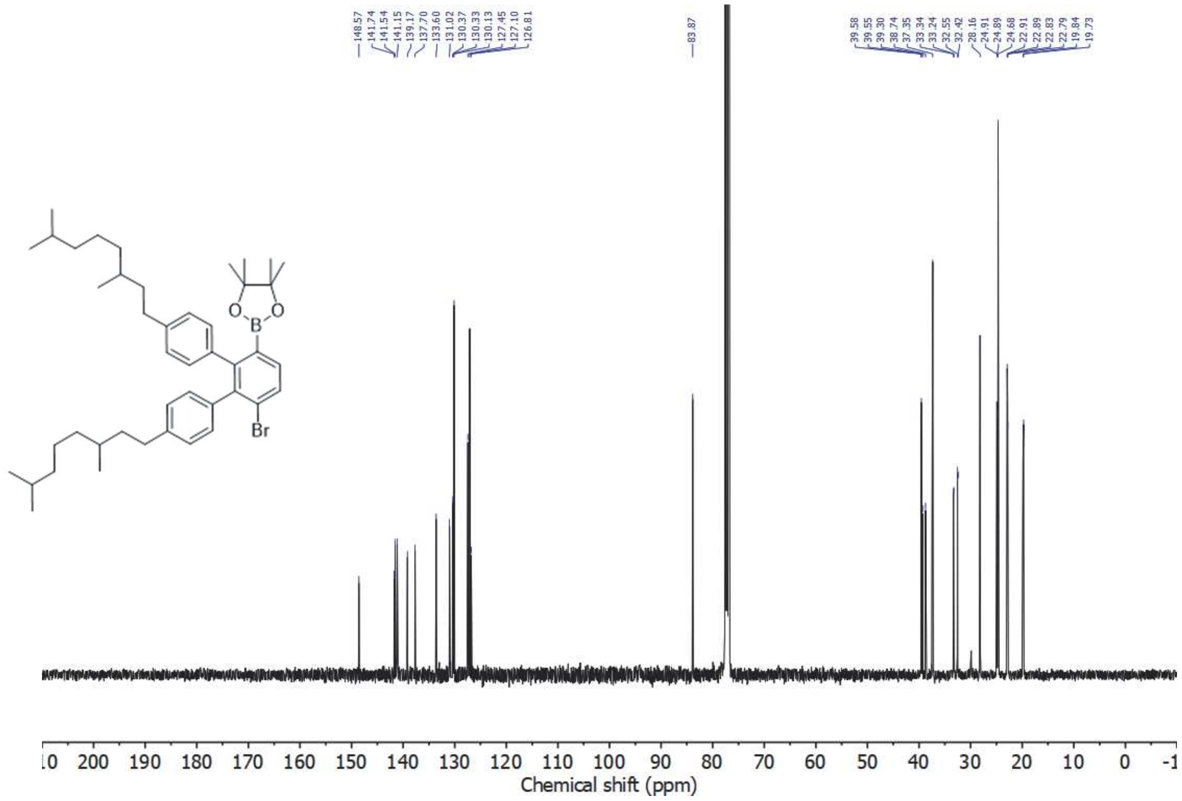

^{13}C NMR spectrum of **6** (CDCl$_3$, 100 MHz, 25°C)

Supporting Figures – Spectroscopic Characterization 9-aGNRs

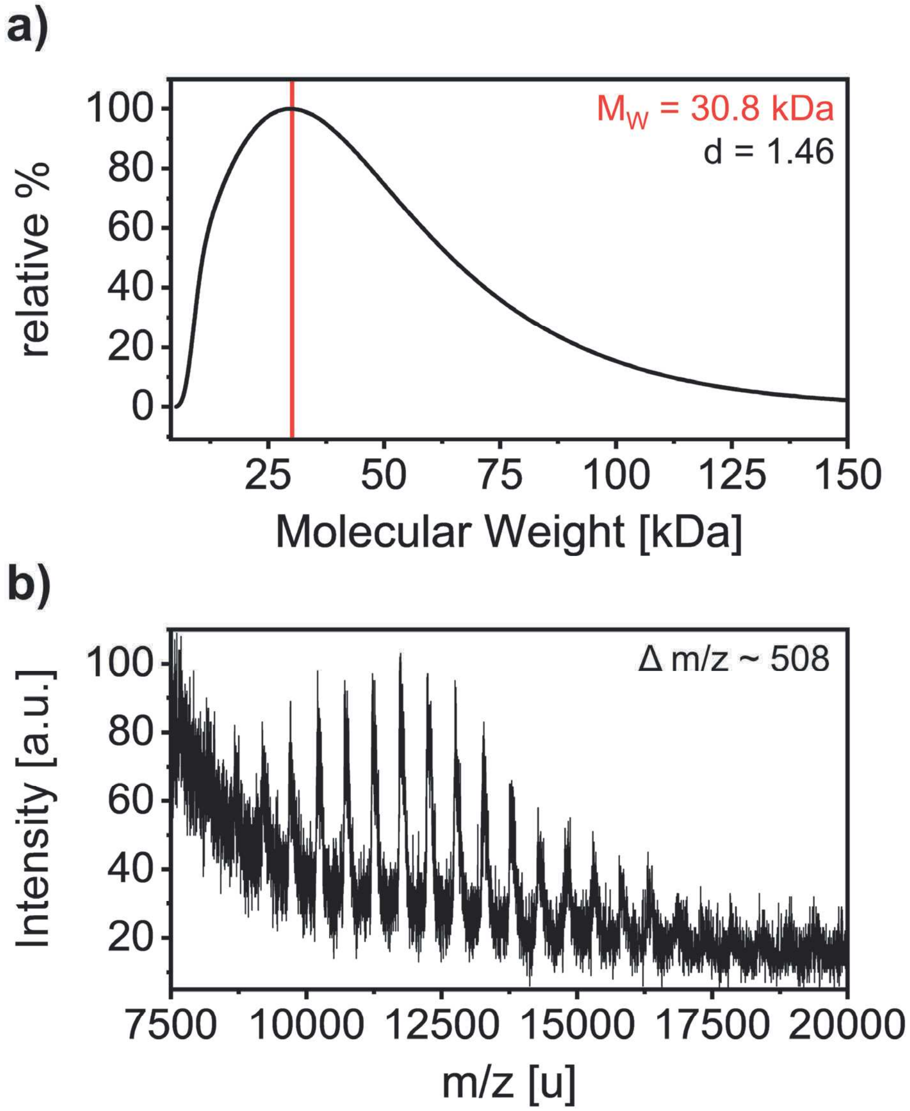

Figure S1. Length Characterization of 9-aGNR precursor polymer. a) Size exclusion chromatogram of a solution of precursor polymer in THF against a polystyrene standard. The determined M_W is marked by a red line in the chromatogram. The depicted M_W corresponds to 60 coupled terphenyl units and a length of ~25 nm. **b)** MALDI-TOF mass spectrum of precursor polymer. Peaks are spaced by ~508 u which corresponds to the molecular weight of a monomer unit. Peaks can be clearly observed up to a m/z ratio of 17500, indicating a length of ~35 terphenyl units, corresponding to ~15 nm.

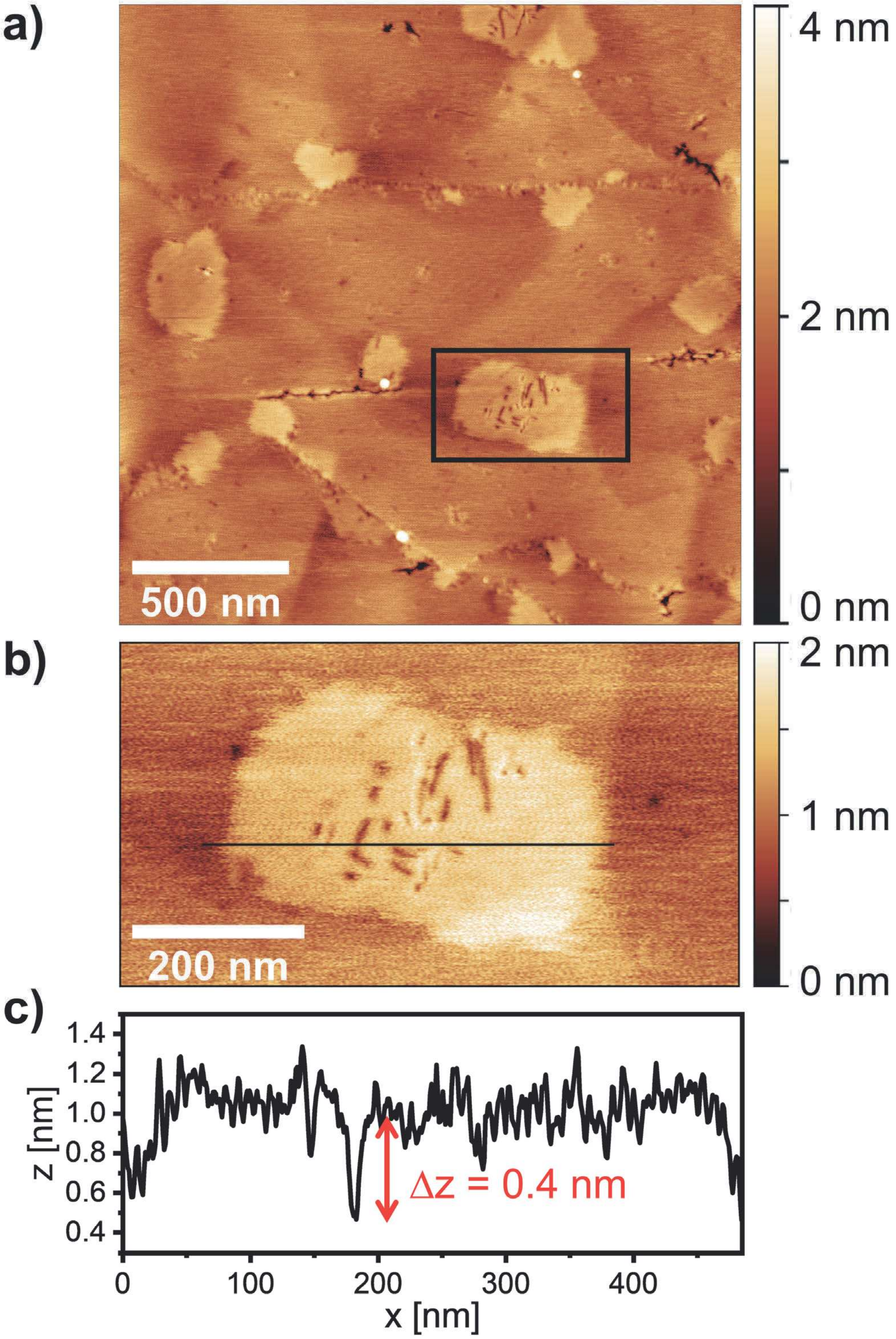

Figure S2. a) Tapping-mode AFM image (Bruker Dimension Icon equipped with OLTESPA-V3 tips) of self-assembled 9-aGNRs on freshly cleaved HOPG. 15 µL of a diluted dispersion (optical density of 0.04 at 820 nm) of the 0.2-1 k*g* fraction 9-aGNR in toluene were drop-cast onto a freshly cleaved HOPG substrate. The substrate temperature was held at 50 °C for 5 minutes and then increased to 80 °C for another 10 min to facilitate slow evaporation of solvent. The image shows several small irregular islands that originate from GNR self-assembly

b) Zoom-in on the highlighted area in (a) showing an island of self-assembled GNRs. While individual GNRs cannot be resolved, ribbon-shaped vacancies in the island indicate the presence of GNRs with different lengths in the dispersion. **c)** Height profile along the line in (b) confirming the height of a nanoribbon island as 0.4 nm as previously reported by Li *et al.* [1]

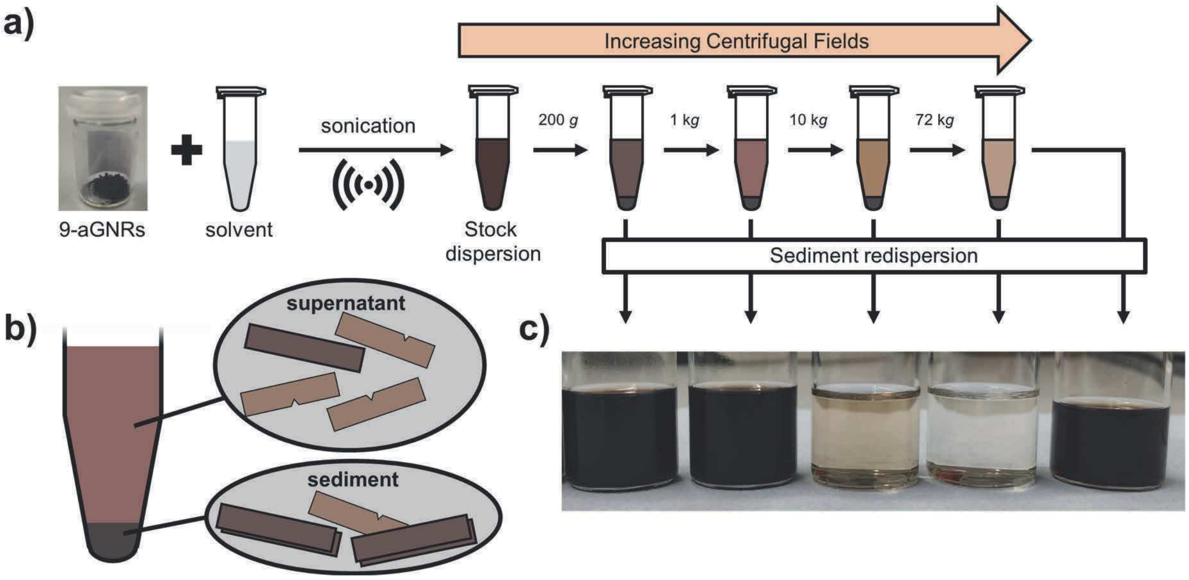

Figure S3. a) Schematic depiction of dispersion and liquid cascade centrifugation (LCC) process. 9-aGNRs are exfoliated in THF or toluene *via* sonication. The resulting stock dispersion is then centrifuged at 200 *g*. The supernatant is carefully removed and subjected to another centrifugation step at higher RCF, while the sediment is redispersed in fresh solvent. This process is repeated at RCF values of 1 k*g*, 10 k*g* and 72 k*g*. **b)** The sediment is expected to contain aggregated and mostly defect-free GNRS, while the supernatant should contain mostly defective GNRs. With each centrifugation step, more defect-free GNRs are removed from the dispersion. **c)** Photograph of the resulting dispersions.

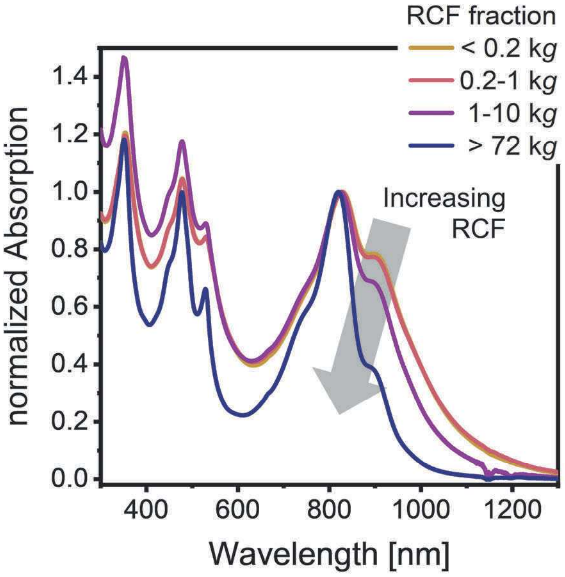

Figure S4. Absorption spectra for resulting 9-aGNR dispersions in toluene after LCC. A slight redshift of ~2 nm of the peak maxima compared to dispersions in THF can be explained with the different dielectric environment of the two solvents.

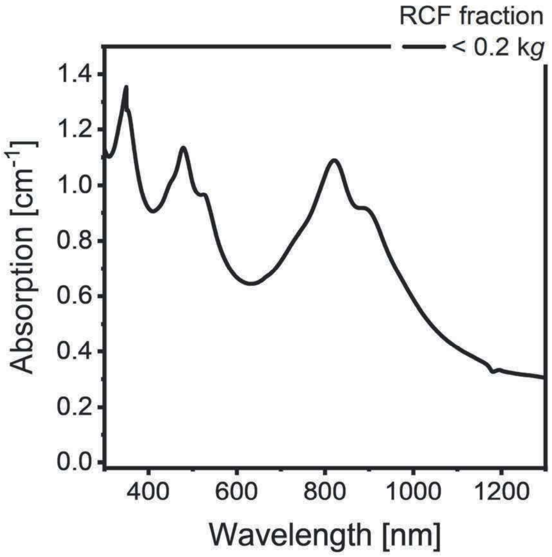

Figure S5. Uncorrected absorption spectrum for <0.2 k*g* fraction in THF. The spectrum shows a scattering background with an onset of ~0.3 at 1300 nm.

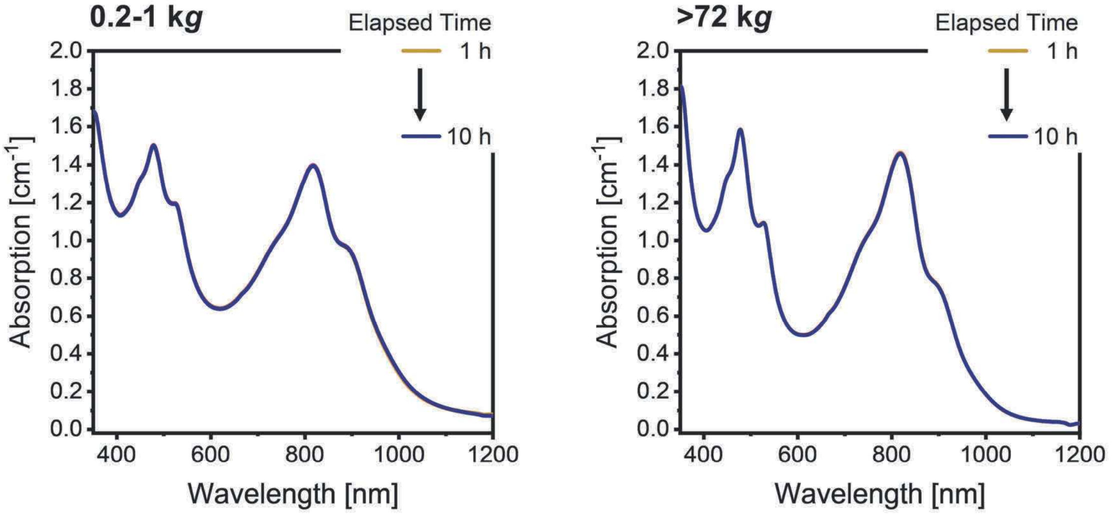

Figure S6. Absorption spectra of exfoliated 9-aGNRs in THF over 10 h. Spectra were measured once per hour for 10 h without moving the cuvette. As absorption spectra do not change, the first spectrum is barely visible. This indicates a high dispersion stability.

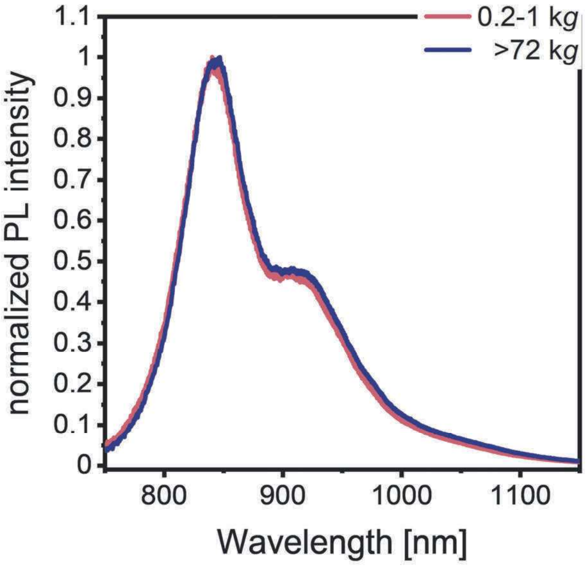

Figure S7. PL spectra of a 0.2-1 k*g* >72 k*g* 9-aGNR fraction in toluene.

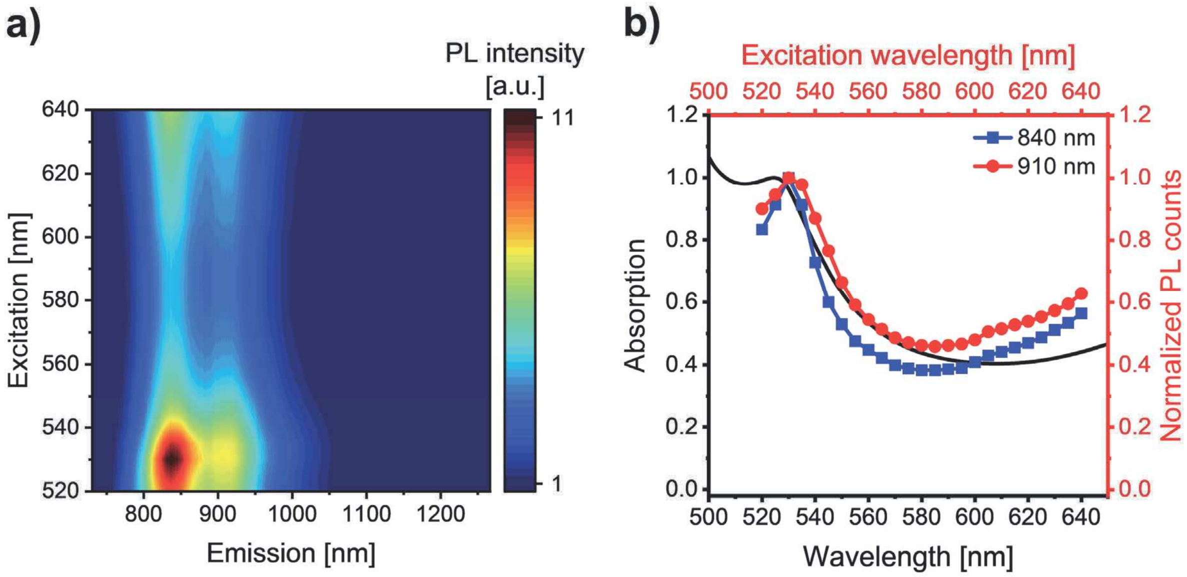

Figure S8. a) PL excitation-emission map of a >72 k*g* 9-aGNR fraction. **b)** Excitation spectrum obtained for emission at 840 nm (blue) and 920 nm (red). An absorption spectrum of the corresponding >72 k*g* fraction normalized to the absorption at 525 nm is shown as a black line for comparison.

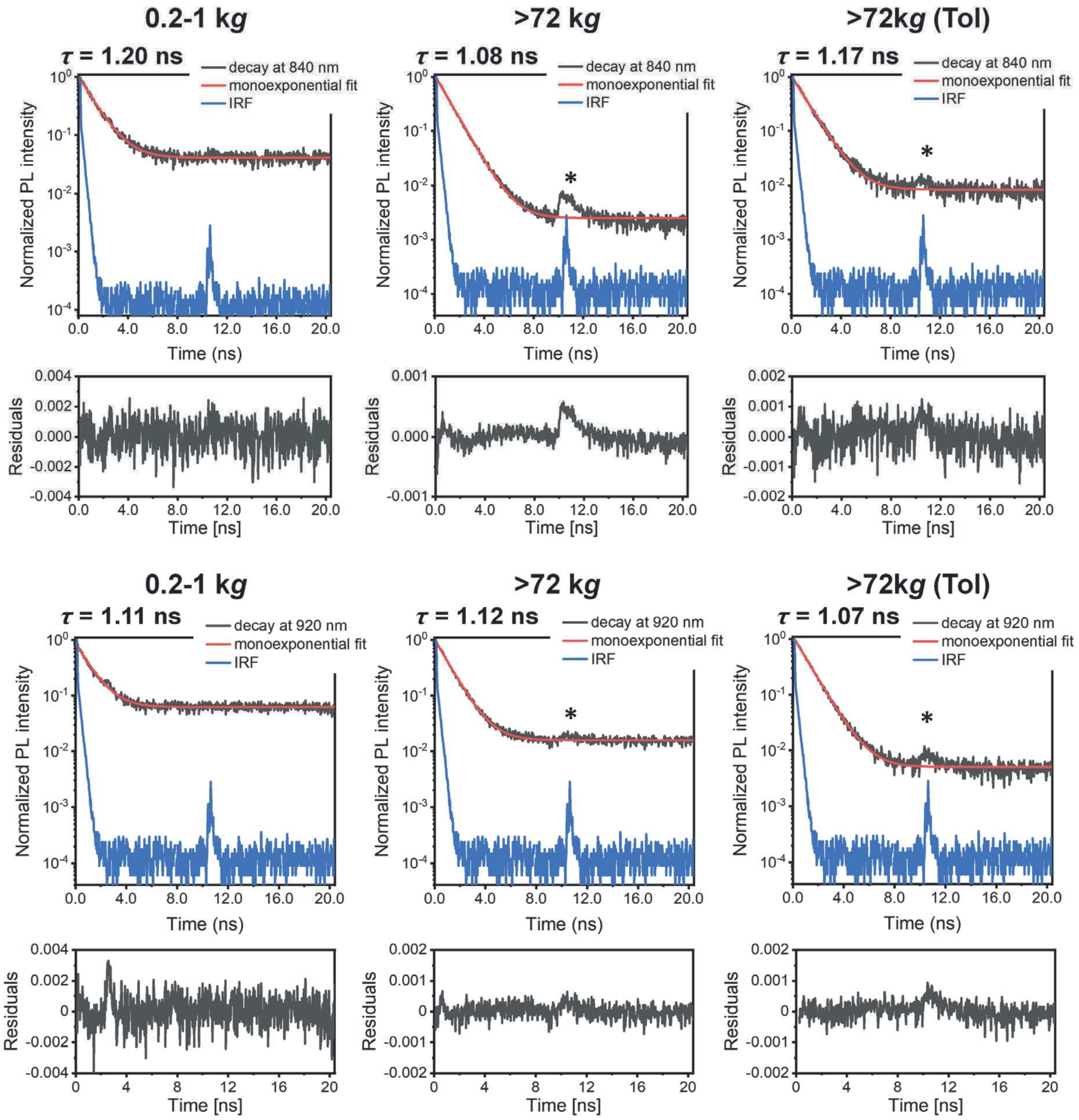

Figure S9. TCSPC histograms for PL decay at the emission features at 840 nm (upper panel) and 920 nm (lower panel) under excitation at 535 nm. The measured instrument response function (IRF) is shown in blue. Histograms were measured for 0.2-1 k*g* and >72 k*g* 9-aGNR fractions in THF and a >72 k*g* 9-aGNR fraction in toluene. The peak at 10 ns (marked with an asterisk) also appears in the IRF and is an artefact of the TCSPC setup. All histograms were fitted with a mono-exponential tail-fit procedure (fit function $f(t) = A \cdot e^{\frac{t-t_o}{\tau}} + c$, where τ is the extracted PL lifetime). Residuals of the fitting procedures are shown below. The extracted lifetimes vary between 1.0 and 1.2 ns with those at 920 nm being insignificantly shorter than those at 840 nm. Although fitting two exponential decays with different amplitudes should be possible for the expected two different GNR species, such multi-parameter fits would not be reliable for the available data.

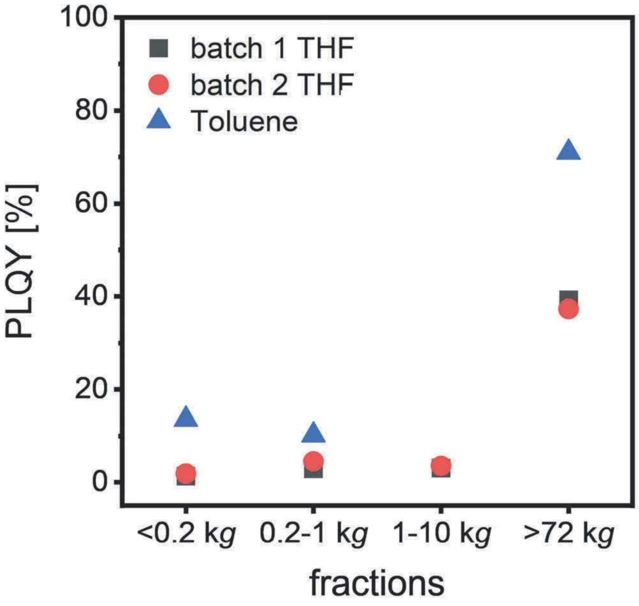

Figure S10. PL quantum yields (PLQY) of 9-aGNR dispersions in THF and toluene. PLQYs increase with increasing RCF.

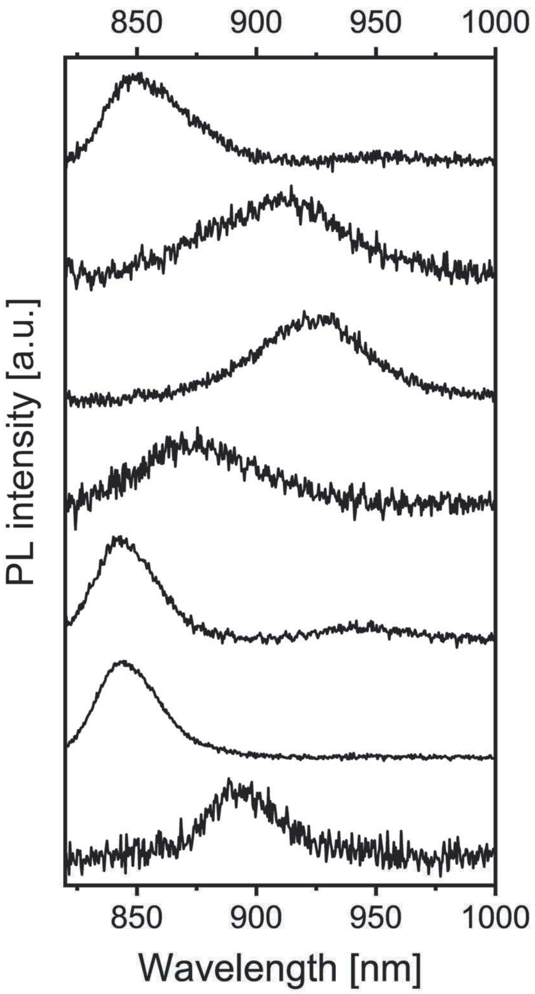

Figure S11. Room temperature PL spectra of 0.2-1 k*g* 9-aGNRs embedded in a polystyrene matrix.

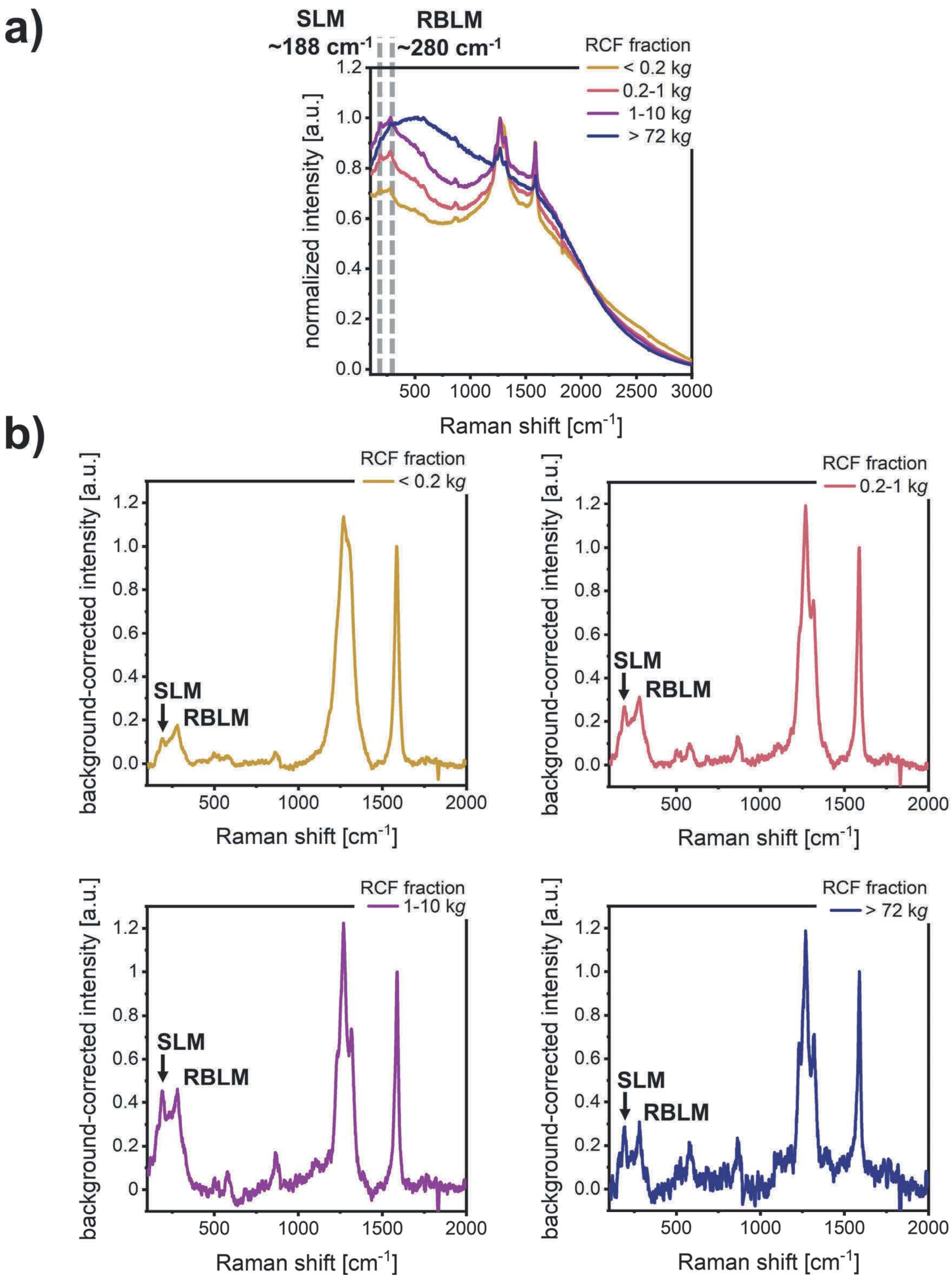

Figure S12. Raman spectra of exfoliated 9-aGNRs excited with a 785 nm laser. **a)** Uncorrected Raman spectra showing a high PL background. The RBLM at 280 cm^{-1} and SLM at 188 cm^{-1} (dashed lines) are clearly visible in all LCC fractions. **b)** Background-corrected Raman spectra for all fractions.

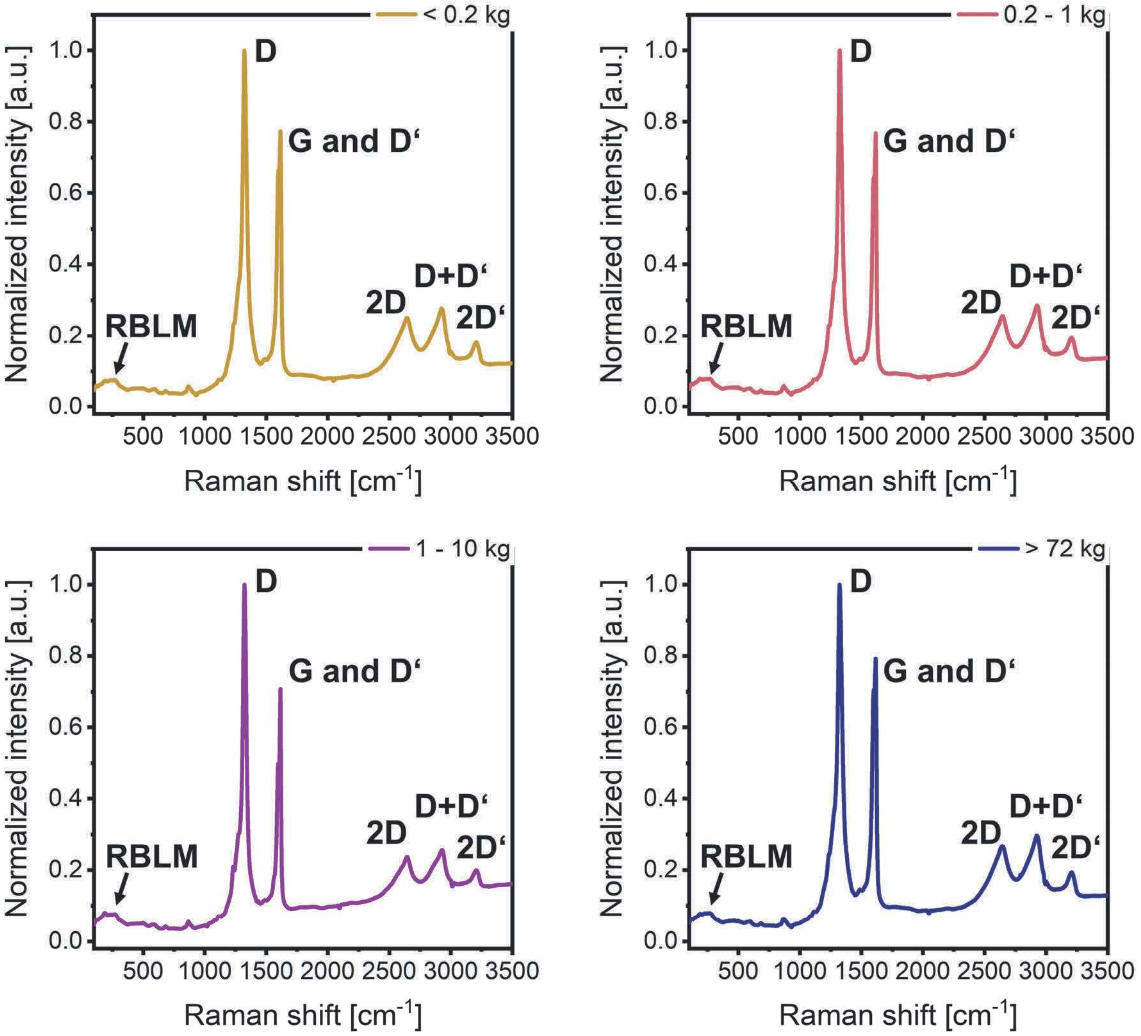

Figure S13. Full range Raman spectra of all LCC fraction of exfoliated 9-aGNRs in THF (as shown in Figure 4 of the main text) excited with a 532 nm laser.

Quantum chemical calculations of neutral 9-aGNRs

All optimized geometries are available at the following data repository:
https://doi.org/10.11588/data/JAV0ZK

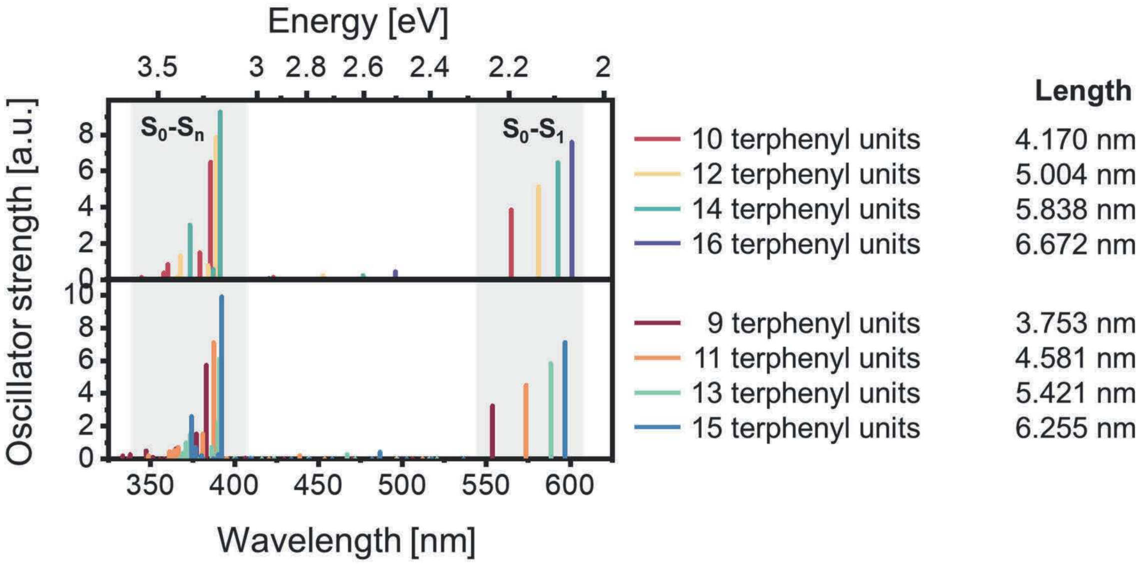

Figure S14: Comparison between the excited state vertical transition energies as computed at the TD-DFT (ωB97X-D/6-31G*) level for different oligomers with parallel (top) and trapezoidal (bottom) shapes.

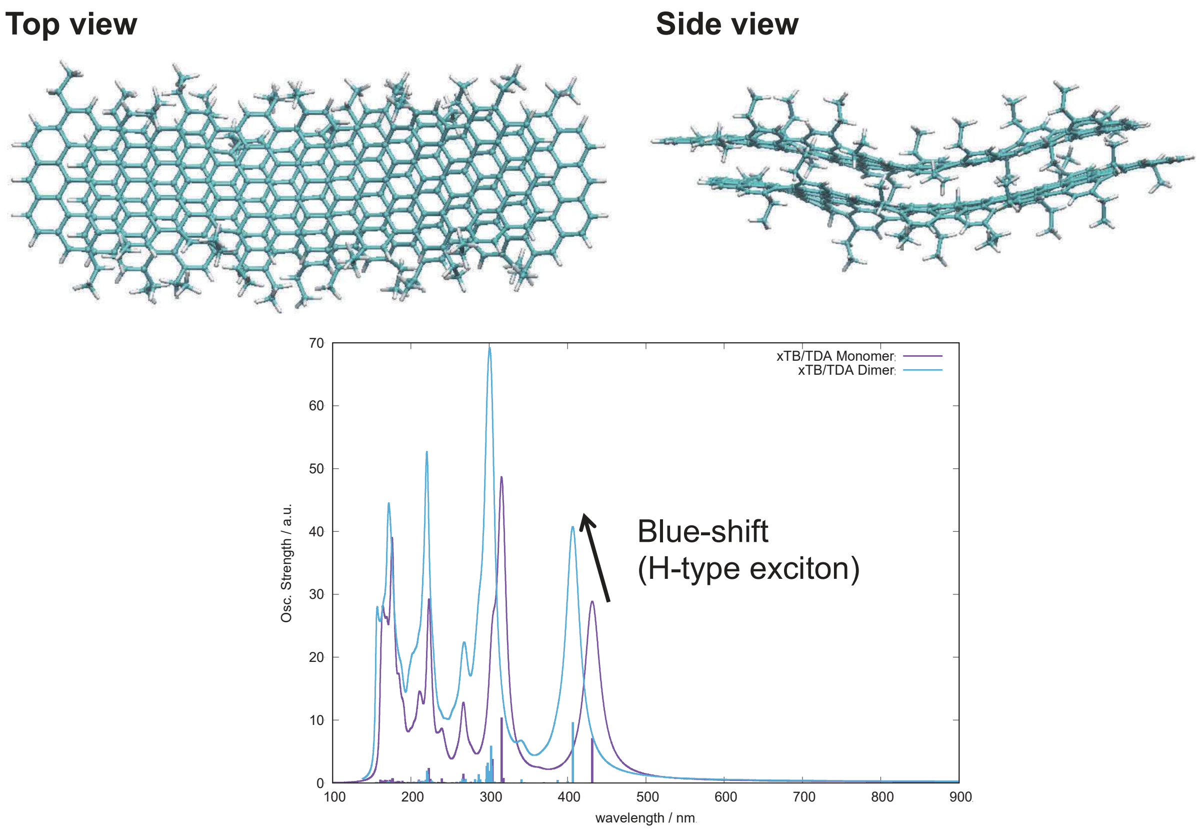

Figure S15. GFN2-xTB optimized geometry for the 9-aGNR dimer (top and side views). Comparison between the sTD-DFT transition energies (unscaled values) computed for the monomer (purple line) and dimer (light blue line).

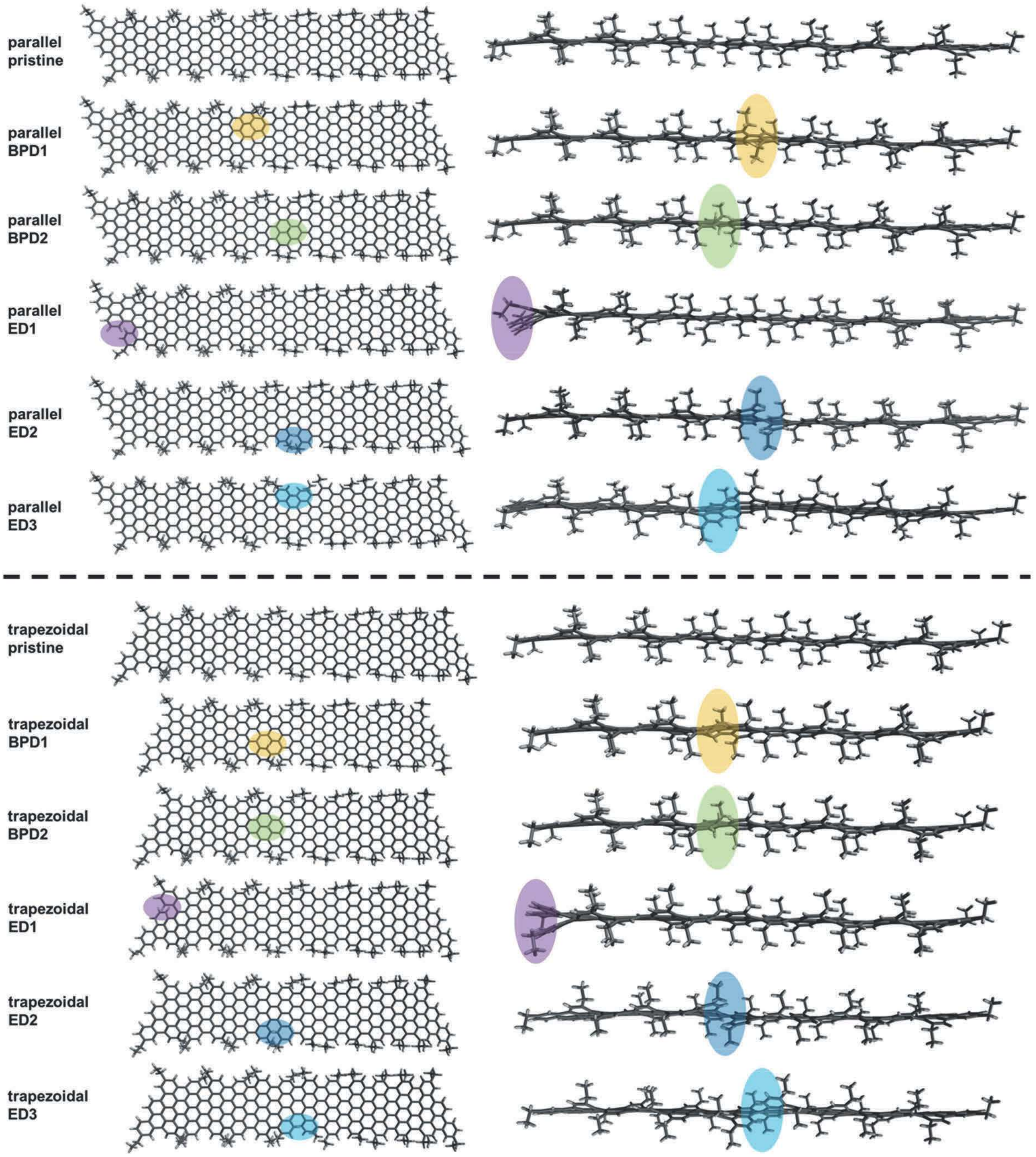

Figure S16. Optimized (GFN2-xTB) structures for parallel 9-aGNRs (top panel) and trapezoidal 9-aGNRs (bottom panel). The coloured regions highlight the positions of the respective defect.

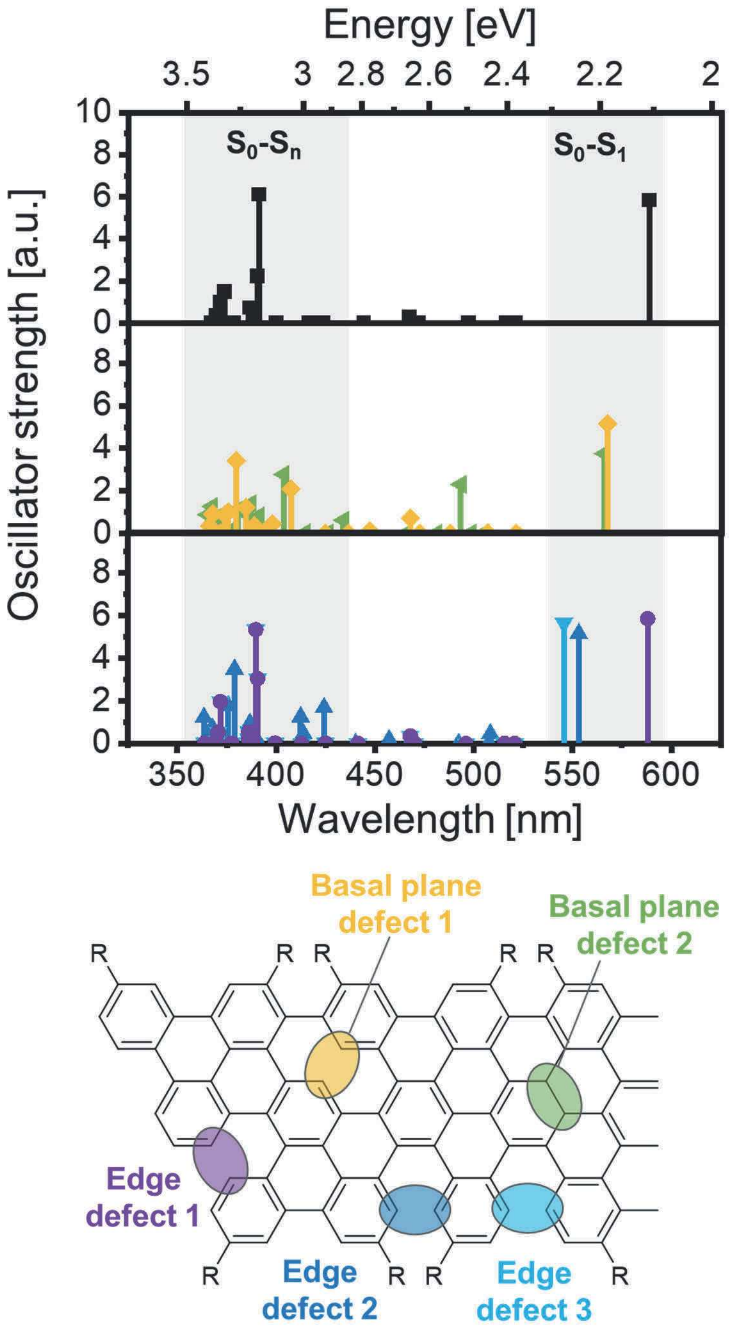

Figure S17: TD-DFT transition energies computed for the **trapezoidal 9-aGNR**: comparison between pristine and defected nanoribbons. Pristine (top panel, black line), BP1 (middle panel, yellow line), BP2 (middle panel, green line), ED1 (bottom panel, purple line), ED2 (bottom panel, dark blue line), ED1 (bottom panel, light blue line).

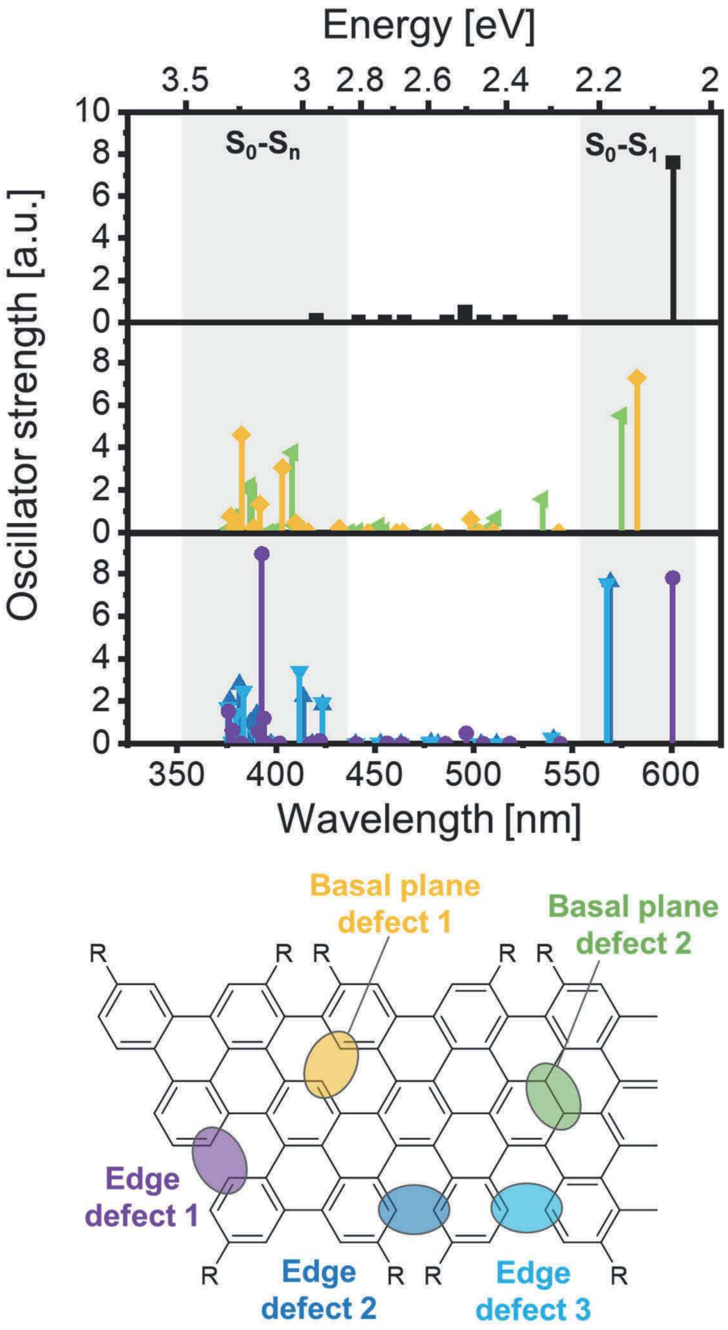

Figure S18: TD-DFT transition energies computed for the **parallel 9-aGNR**: comparison between pristine and defected nanoribbons. Pristine (top panel, black line), BP1 (middle panel, yellow line), BP2 (middle panel, green line), ED1 (bottom panel, purple line), ED2 (bottom panel, dark blue line), ED1 (bottom panel, light blue line).

Supporting Figures – Doped 9-aGNRs

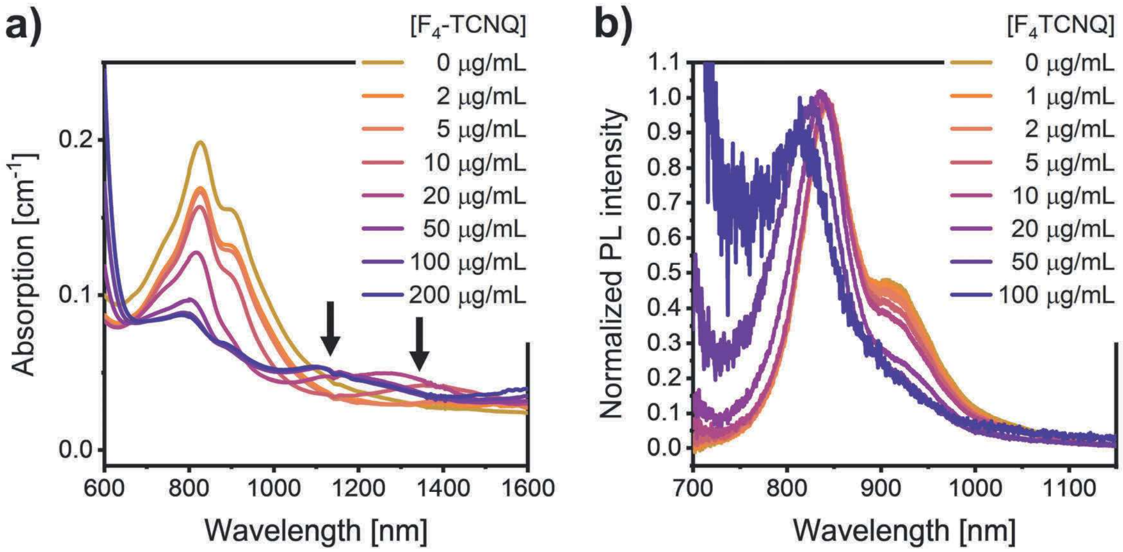

Figure S19. a) Absorption spectra of a >0.2-1 kg 9-aGNR dispersion doped with F4TCNQ. Charge-induced absorption peaks are marked by arrows. **b)** Normalized PL spectra of a > 0.2-1 kg 9-aGNR dispersion doped with F4TCNQ showing blue-shift and concentration-dependent quenching of the main emission peaks.

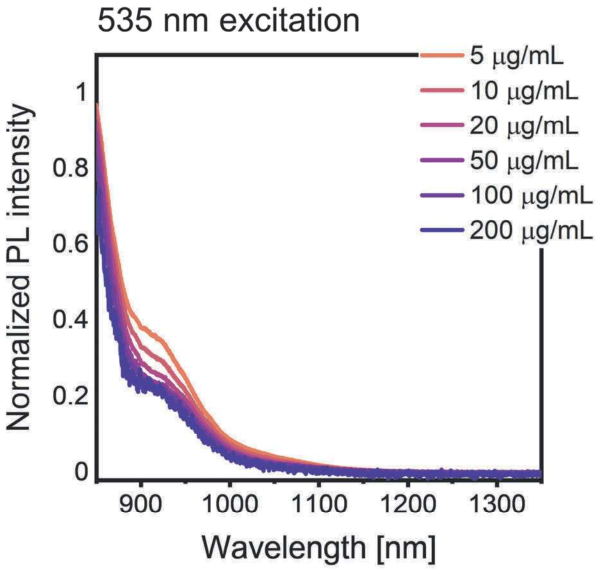

Figure S20. PL spectra of F4TCNQ-doped >72 kg 9-aGNR dispersions recorded at longer wavelengths. No new red-shifted emission features are visible.

Quantum chemical calculations of charged 9-aGNRs

The structure of doped (i.e., positively charged species, +1) 9-aGNRs was optimized at the GFN2-xTB level. The electronic transitions were computed at the TD-UDFT level (UωB97X-D/6-31G*).

The calculated electronic transitions of undoped - neutral (yellow bars) vs. doped - charged (purple bars) 9-aGNR of trapezoid (upper panel) and parallel (bottom panel) shapes are compared in **Figure S21.** For each species (in their neutral and charged state) we considered the pristine case (without defects) and the presence of an edge defect type 2 (ED2). Charged species show dipole allowed electronic transitions lower in energy than the neutral species (see 700-1000 nm region). The shapes (trapezoid or parallel) and the structural defects, slightly affect the transition energies of charged species.

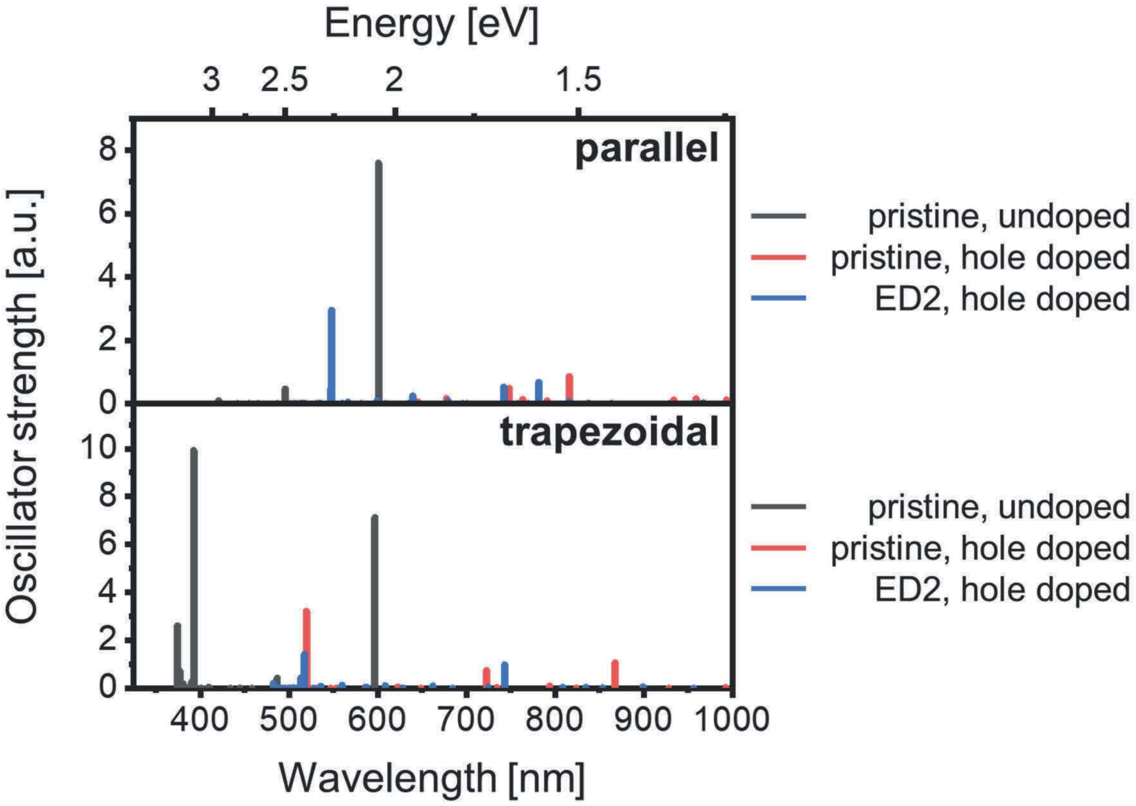

Figure S21: Comparison between the TD-UDFT (UωB97X-D/6-31G*) transition energies (unscaled data) computed for the parallel (top) and trapezoidal (bottom) 9-aGNRs for their pristine undoped (neutral, black line), pristine doped (charged, +1, red line) and defective ED2 doped species (charged, +1, blue line). The structural models considered refer to 16 terphenyl units for the parallel shape, and 15 units for the trapezoidal shape.

REFERENCES

1. Li, G.; Yoon, K. Y.; Zhong, X.; Zhu, X.; Dong, G., Efficient Bottom-Up Preparation of Graphene Nanoribbons by Mild Suzuki-Miyaura Polymerization of Simple Triaryl Monomers. *Chemistry* **2016,** *22* (27), 9116-20.

CHAPTER 6

PUBLICATION P4

Healing Defects in Armchair Graphene Nanoribbons for Improved Charge Transport

Lindenthal, S.; Sebastian, F. L.; Herrmann, N. J.; Zorn, N. F.; Zaumseil J.

.*ACS Applied Nano Materials* **2025,** *XX,* XXXXX-XXXXX
https://doi.org/10.1021/acsanm.5c01848

For this publication we investigate the effect of thermal annealing on films of solution-synthesized 9-aGNRs and find that heating films to 300 ℃ in an inert atmosphere leads to healing of defects as shown by Raman and absorption spectroscopy. The GNRs are then integrated into electrolyte-gated transistors and the effect of defects on charge transport is investigated. We find significant improvement of charge transport upon healing of defects.

Formblatt Kumulative Dissertation

1. **Publikation:** Vollständige bibliographische Referenz/*Complete bibliographic reference*:

Lindenthal, S.; Sebastian, F. L..; Herrmann, N. J.; Zorn, N. F.; Zaumseil, J., Healing Defects in Armchair Graphene Nanoribbons for Enhanced Charge Transport. *ACS Applied Nano Materials* **2025,** *XX*, XXXXX-XXXXX, https://doi.org/10.1021/acsanm.5c01848.

2. **Erst- oder gleichberechtigte Autorenschaft/*First or equal authorship*:**

☒ Ja/*yes* ☐ Nein/*no*

3. **Status der Veröffentlichung/*Status of publication*:**

☐ Veröffentlicht/*Published*
☒ Zur Veröffentlichung angenommen/*Accepted*
☐ Eingereicht/*Submitted*
☐ Noch nicht eingereicht/*Not yet submitted*

4. **Beteiligungen/*Contributions***:**

	Doktorand/in/*Doctoral student*
Name, first name	**Lindenthal, Sebastian**
Methodology	**X**
Software	
Validation	**X**
Formal Analysis	**X**
Investigation	**X**
Resources	
Data Curation	**X**
Writing – Original Draft	**X**
Writing – Review & Editing	**X**
Visualization	**X**
Supervision	
Project Administration	
Funding Acquisition	

****Kategorien des CRediT (*Contributor Roles Taxonomy*, https://credit.niso.org/)**

Hiermit bestätige ich, dass alle obigen Angaben korrekt sind/*I confirm that all declarations made above are correct.*

Unterschrift/*Signature* ____________________
Doktorand/in/*Doctoral student*

Betreuungsperson/*Supervisor*:
Hiermit bestätige ich, dass alle obigen Angaben korrekt sind und dass die selbstständigen Arbeitsanteile des Doktoranden an der aufgeführten Publikation hinreichend und signifikant sind/*I confirm that all declarations made above are correct and that the doctoral student's independent contribution to this publication is significant and sufficient to be considered for the cumulative dissertation.*

Prof. Dr. Jana Zaumseil
Name/*Name*

Unterschrift/*Signature*

27.5.2025
Datum/*Date*

ACS APPLIED
NANO MATERIALS

www.acsanm.org
Article

Healing Defects in Armchair Graphene Nanoribbons for Enhanced Charge Transport

Sebastian Lindenthal, Finn L. Sebastian, Niklas J. Herrmann, Nicolas F. Zorn, and Jana Zaumseil*

Cite This: https://doi.org/10.1021/acsanm.5c01848
Read Online

ACCESS | Metrics & More | Article Recommendations | Supporting Information

ABSTRACT: Graphene nanoribbons (GNRs) are promising carbon-based nanomaterials for next-generation nanoelectronic devices. However, their synthesis (in-solution or on-surface) is not perfect and the impact of defects in the sp^2 carbon lattice of GNRs on their charge transport properties is not yet fully understood. Here, we investigate the influence of lattice defects on the macroscopic charge transport in thin films of solution-synthesized 9-armchair GNRs (9-aGNRs) with intrinsic edge defects. The density of these edge defects could be reduced by thermal annealing at 260−300 °C in inert atmosphere, which is proposed to induce postsynthetic cyclization. The decreasing number of defects with annealing time and temperature was corroborated by absorption spectroscopy and a decreasing D/G Raman mode ratio while the film morphologies remained unaltered. Annealed 9-aGNR films showed ambipolar charge transport characteristics in electrolyte-gated transistors with significantly higher on-currents, transconductances and on/off-ratios for both hole and electron transport compared to films that were annealed below the temperature required for defect healing. Consequently, defect healing by annealing in inert atmosphere should be a key step in GNR device processing to achieve optimal charge transport.

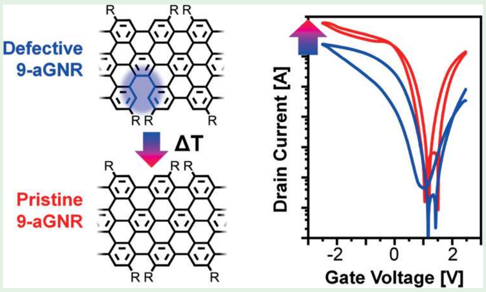

KEYWORDS: *graphene nanoribbons, lattice defects, charge transport, electrolyte-gated transistors, Raman spectroscopy*

■ INTRODUCTION

Graphene nanoribbons (GNRs) are nanoscale, quasi-one-dimensional stripes of graphene with electronic properties that strongly depend on their width and edge structure.[1−3] Armchair-edged GNRs (n-aGNRs) are semiconductors with a bandgap that is inversely proportional to their width.[3] The index n of n-aGNRs represents the number of carbon dimer lines perpendicular to the aGNRs long axis, and hence is a measure for their width. Top-down fabrication approaches such as lithography or catalytic etching of graphene typically produce GNRs with poor control over edge type and ribbon width.[4,5] As a result, bottom-up synthesis or growth of narrow GNRs with atomically precise edges has been pursued over the past decade. Nowadays, a multitude of bottom-up synthesis methods gives access to many different n-aGNRs, for example, via metal-catalyzed on-surface reactions[6,7] or solution-mediated organic synthesis.[8,9]

The growing availability of atomically precise GNRs with tunable bandgaps and properties such as ballistic electron transport[10] or the possibility to realize sophisticated lattice geometries (e.g., multiterminal junctions),[11,12] make them promising candidates for applications in (nano)electronic devices. Consequently, identifying and eliminating factors that may limit charge transport in and thus performance of GNRs in real devices is crucial.[13,14] While the impact of nanoribbon length and contact resistance have been investigated thoroughly,[14−21] the influence of structural defects within the GNR lattice on charge transport remains poorly understood.

Lattice defects have been shown to disrupt charge transport in other carbon nanomaterials, such as single-walled carbon nanotubes (SWCNTs), graphene or reduced graphene oxide. For example, the introduction of sp^3-defects in the sp^2-lattice of SWCNTs leads to a reduction of conductance within individual nanotubes, which is attributed to charge scattering at defect sites.[22−24] However, macroscopic charge carrier mobilities in networks of SWCNT also decrease upon introduction of defects as determined from field-effect transistor measurement.[25] Similar effects have been observed for charge transport across defects in graphene. Theoretical and experimental studies showed reduced carrier mobilities in devices with defective single layer graphene.[26−28] Notably, defect healing, such as the reduction of graphene oxide in the presence of a carbon source, has been shown to partially restore these properties.[29,30]

Unintentional structural irregularities and defects are also present in the lattices of bottom-up-synthesized GNRs. The

Received: March 30, 2025
Revised: May 17, 2025
Accepted: May 20, 2025

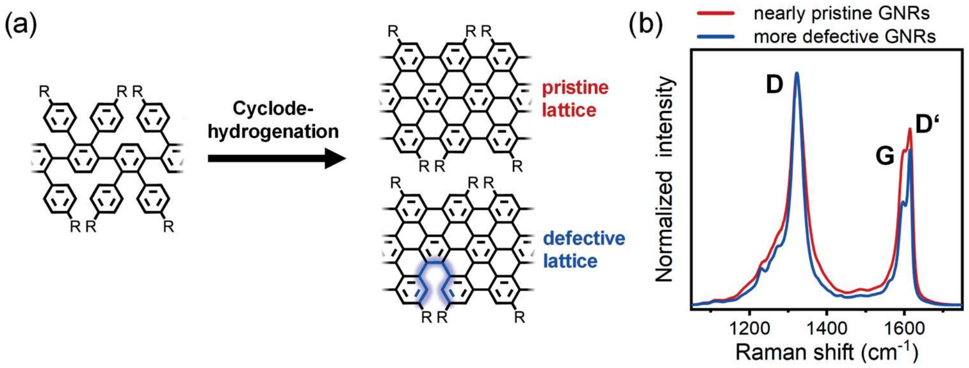

Figure 1. (a) Schematic depiction of the synthesis of 9-aGNRs (pristine and defective) by cyclodehydrogenation of a polymer precursor. Lattice defects (blue) result from incomplete cyclodehydrogenation. (b) Averaged Raman spectra of drop-cast films of two different fractions (high and low RCF) of GNR dispersions after liquid cascade centrifugation, normalized to the D-peak (excitation wavelength 532 nm).

cyclodehydrogenation reactions to convert the precursor polymers into graphene nanoribbons − thermally for on-surface synthesis and oxidative for solution-mediated synthesis − typically do not proceed to completion and leave behind structural defects. They manifest in the form of either "bite" defects (i.e., missing phenyl rings) for on-surface-synthesized GNRs[18,31,32] or edge defects (i.e., unclosed carbon−carbon bonds) for solution-synthesized GNRs[33] as shown schematically in Figure 1a. For 9-aGNRs, edge defects introduced during cyclodehydrogenation substantially alter their aggregation behavior, their absorption bands and their Raman spectra (D/G ratio, see Figure 1b), which enable the distinction between nearly pristine and defective GNRs.[33]

The influence of these defects on charge transport in GNRs has been studied mainly theoretically. First-principles calculations of charge transport across "bite" defects in a single aGNR predict a substantial decrease in conductivity depending on width and defect density.[32] A single "bite" defect in 9-aGNRs is predicted to reduce the conductance by 74%. A subsequent study that used scanning tunneling microscopy to determine defect densities in on-surface-synthesized 9-aGNRs found a reduction of on-currents by 2 orders of magnitude in short-channel (channel length $L = 20$ nm) 9-aGNR field-effect transistors.[18] To the best of our knowledge, similar studies for edge defects in solution synthesized GNRs have not been performed yet. Given their potential to severely affect charge transport and the growing interest in GNRs for nanoscale devices, it is necessary to experimentally investigate charge transport in defective and pristine graphene nanoribbons.

Here, we use dispersions of solution-synthesized 9-aGNRs from which fractions of defective and nearly pristine GNRs are obtained by liquid cascade centrifugation (LCC). Thin films prepared from these dispersions are characterized by absorption and Raman spectroscopy to quantify their defect densities. We find that thermal annealing in inert atmosphere is a suitable method to 'heal' defects in GNR films postsynthetically. Annealing time and temperature have a direct impact on the final defect densities without affecting the film morphology. Ambipolar electrolyte-gated field-effect transistors based on thin films of 9-aGNRs demonstrate the effect of annealing and defect density on hole and electron transport.

■ EXPERIMENTAL METHODS

9-aGNR Synthesis. 9-aGNRs were synthesized via a solution-based approach using an adapted protocol by Li et al.[34] The detailed description of the synthesis was reported by Lindenthal et al.[33]

Dispersion and Liquid Cascade Centrifugation of 9-aGNRs. 9-aGNR powder was sonicated in toluene (1 mg mL^{-1}) for 4 h at 20 °C using a Branson 2510 sonication bath. The sample was then centrifuged at 200 and 1000*g* using a Hettich Mikro 220R centrifuge, equipped with a 11.95A fixed-angle rotor to sediment the pristine GNRs. The sedimented GNRs were redispersed in fresh toluene. This procedure led to three 9-aGNR fractions (<0.2, 0.2−1 and >1 kg) of which only the <0.2 and >1 kg fractions were used.

Film Deposition by Mixed Cellulose Ester Transfer. The desired volume of 9-aGNR dispersion with an absorbance of $A_{820\text{ nm}} = 1\text{ cm}^{-1}$ was diluted in 50 mL of toluene and sonicated for 30 min prior to filtration. The diluted dispersion was then vacuum filtered (88 kPa pressure difference) through a mixed cellulose ester (MCE) membrane filter (Merck MF-Millipore, VSWP, pore size 0.025 μm, diameter 25 mm). Membranes were cut to size and placed upside-down on the desired substrates that were previously rinsed with acetone. The membranes were wetted with 2-propanol, pressed onto the respective substrate. Subsequently they were submerged in acetone (five times for 15 min each) to dissolve the MCE membrane, resulting in a clean film of GNRs on the substrate.

Spectroscopic Characterization. Baseline-corrected UV−vis−nIR absorption spectra of GNR dispersions (cuvette path length: 1 cm) and transferred films were measured on an Agilent 6000i (Varian, Inc.). Raman spectra of GNR films were recorded with a Renishaw inVia confocal Raman microscope equipped with an Olympus 50× long-working distance objective (N.A. 0.5). Samples were excited at either 532 or 785 nm. To minimize the spot-to-spot variation, more than 1000 individual spectra were collected and averaged for each sample. For spatially resolved measurements, characteristic spots on the substrate (i.e., edges of electrode structures) were identified and used to measure the same area before and after annealing. The peak areas of D, G and D′ bands were extracted using the fitting function (Lorentzian line shapes, linear baseline) of the Wire 3.4 software.

Characterization of Film Morphology. A Bruker DektakXT Stylus profilometer was employed to determine film thicknesses of at least 8 spots for each sample before and after annealing. AFM images ($5 \times 5\ \mu\text{m}^2$) were recorded with a Bruker Dimension Icon microscope in ScanAsyst mode, using a ScanAsyst Tip. The root-mean-square (rms) roughness was determined using Gwyddion 2.5.7. Bright field optical microscopy images were recorded with an Olympus BX51 microscope.

Device Fabrication. Interdigitated bottom-contact electrodes ($L = 2\ \mu$m, $W = 10$ mm) were patterned by photolithography (LOR5B/S1813 resist, microresist technology GmbH) and electron beam evaporation of chromium (3 nm) and gold (30 nm) on low-sodium glass substrates (Schott AG, AF32eco, 500 μm thickness). 9-aGNR films were transferred onto the electrodes by MCE transfer and annealed in a dry nitrogen glovebox for 6 h at either 200 or 300 °C. After annealing, an ion gel layer was deposited by spin-coating (8000 rpm, 60 s) a mixture of the ionic liquid [EMIM][FAP] (for synthesis, Merck KGaA), the polymer P(VDF-HFP) ($M_W \sim 400$ kDa, Sigma-

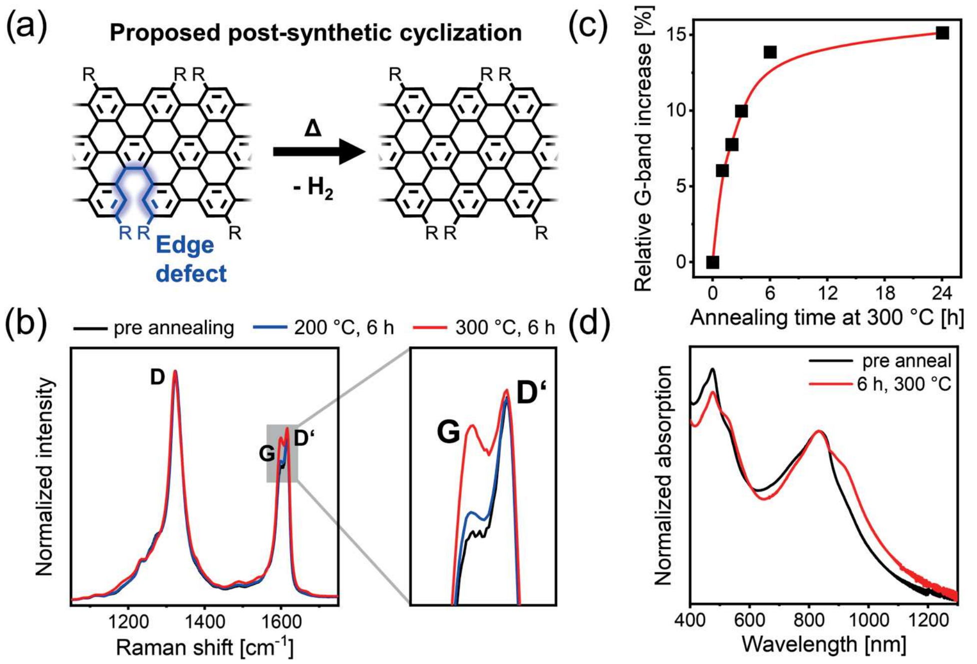

Figure 2. (a) Schematic depiction of proposed cyclization reaction of edge defects upon thermal annealing. The blue highlighted bonds show the edge defects in solution-synthesized GNRs. (b) Normalized Raman spectra of 9-aGNR films (>1 kg fraction) before and after annealing at 200 and 300 °C (excitation wavelength 532 nm). (c) The relative G-band increase as a measure of defect removal versus annealing time at 300 °C. The red line is a guide to the eye. (d) Absorption spectra of a 9-aGNR film before and after annealing (6 h, 300 °C), normalized to the band at 820 nm corresponding to defect absorption (S_{1d}).

Aldrich) and acetone (mass ratio 1:4:14). Excess ion gel was carefully wiped away before annealing the substrates overnight at 80 °C.

Device Characterization. Transfer characteristics of 9-aGNR EGTs were measured in inert atmosphere with an Agilent 4156C semiconductor parameter analyzer at low gate sweep rates (~3 mV/s) to minimize device hysteresis. To enable ion migration into the channel, the starting gate voltage was applied for 60 s prior to the voltage sweep.

■ RESULTS AND DISCUSSION

Thin Films of Defective and Pristine GNRs. Solution-synthesized 9-aGNRs were obtained by adapting a protocol by Li et al.[33,34] The resulting GNR raw material was dispersed in toluene and subjected to liquid cascade centrifugation (LCC) (see Experimental Methods). LCC utilizes the different sedimentation coefficients of nanomaterials to sequentially sediment them at increasing rotational centrifugal fields (RCF).[35,36] Nearly pristine graphene nanoribbons have a stronger aggregation tendency due to their higher planarity. The resulting aggregates exhibit a larger sedimentation coefficient and thus sediment at lower RCF values (fraction <0.2 kg), which enables their separation from more defective but unaggregated GNRs (fraction >1 kg).[33]

The amount of defective and pristine GNRs in different LCC fractions is reflected in their Raman and absorption spectra. Raman spectra of drop-cast 9-aGNR films (see Figure 1b) exhibit pronounced D, G and D′ peaks at 1320, 1596, and 1615 cm^{-1}, respectively, for both fractions. While the G-mode is intrinsic to any sp^2-hybridized carbon lattice, the D and D′ modes are disorder-related and induced by armchair edges and (edge) defects in GNRs.[37] As LCC does not affect the length distribution of the dispersed GNRs and thus neither the ratio of edges to sp^2-hybridized carbon lattice, the D/G ratio can be used as a metric to assess the amount of defective GNRs in a GNR dispersion. Note that the density of edge defects in a single nanoribbon is expected to be low (~1 edge defect per GNR), as the oxidative cyclodehydrogenation is still rather efficient and ribbons with very high defect densities are removed during purification of the GNR raw material.[33] Consequently, the high D/G-ratio in the >1 kg fraction is indicative of a high ratio of defective to pristine GNRs and not for a large number of defects per individual GNR.

The higher ratio of defective to pristine GNRs is also evident from the absorption spectra of the GNR dispersions. Pristine 9-aGNRs show an absorption band at 900 nm (Figure S1a, S_{1p}), whereas defective 9-aGNRs exhibit a blue-shifted absorption band at 820 nm (S_{1d}) as shown previously.[33] The relative intensities reflect the ratio of pristine to defective GNRs within the LCC fractions. A high defective-to-pristine ratio is apparent for the >1 kg fraction, while the <0.2 kg fraction contains a large share of pristine GNRs. The presence of the S_{1d} and S_{1p} bands in the absorption spectra of both LCC fractions, however, indicates that the LCC process does not entirely separate pristine from defective GNRs.

After preparing films from both the <0.2 and >1 kg fractions via filtration and mixed cellulose ester (MCE) membrane filter (MCE) transfer (see Experimental Methods and Figure S2), optical microscopy revealed drastic variations of the film morphologies for the two fractions (see Figure S3). Films prepared from the <0.2 kg fraction showed tearing, as well as a significant number of large aggregates of a few tens of micrometers. In contrast to that, the films of the >1 kg fraction were very uniform and did not show any signs of tearing. While there were still some large aggregates present, they did not dominate the film morphology. This observation is consistent with our previous findings of strong GNR aggregation within the low-RCF fractions (more pristine GNRs), while the fractions with mostly defective GNRs were shelf-stable for months.[33] A high scattering background, observed in

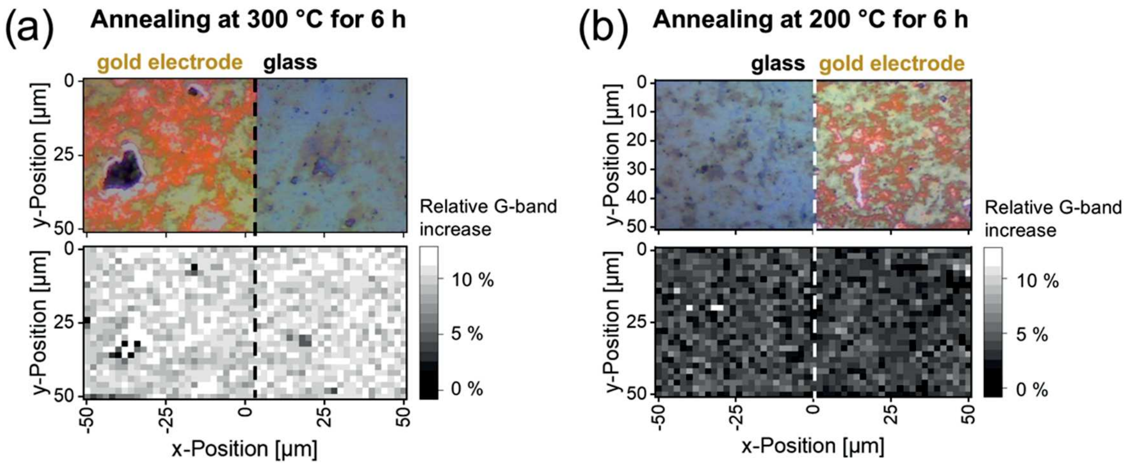

Figure 3. Optical microscope image (top, 50× magnification) of film area sampled by Raman mapping and corresponding map of the relative G-band increase (bottom) for 9-aGNR films (>1 kg fraction) annealed at (a) 300 °C for 6 h and (b) 200 °C for 6 h. The dashed line marks the interface between gold electrode (left) and glass (right).

absorption spectra of the <0.2 kg fraction (Figure S1b) further corroborates the notion of a large amount of aggregated or nonexfoliated nanoribbons within the <0.2 kg fraction. Consequently, only thin films of the >1 kg fraction could be used for charge transport measurements and their properties are studied in the following.

Healing Defects by Thermal Annealing. On-surface synthesis methods typically use catalytic metal surfaces to facilitate planarization and hydrogen abstraction during cyclodehydrogenation.[21,38−40] Ab initio studies have shown that polymer planarization is one of the drivers of this cyclization reaction and that further cyclodehydrogenation occurs preferentially near already planar, cyclized GNR segments.[41] This reaction can also occur on nonmetal surfaces like metal oxides.[42,43] For example, Ma *et. al* utilized molecular strain to achieve cyclodehydrogenation of polymer precursors that were not in contact with any surface but only with other GNRs.[44] Edge defects in solution-synthesized 9-aGNR are structurally very similar to reaction intermediates in on-surface cyclo-dehydrogenation reactions. They also distort the GNR edge and induce strain in the lattice near the defect site.[33] Hence, thermal annealing might enable postsynthetic cyclization of edge defects in the GNR films, as schematically shown in Figure 2a. Due to the preorientation of the reaction sites in defective but still mostly planar GNRs, a significantly lower annealing temperature compared to rapid thermal annealing methods[45] should be sufficient to facilitate cyclodehydrogenation.

To test this hypothesis, several 9-aGNR films (thickness approximately 130 nm) were prepared from the >1 kg fraction via MCE transfer onto glass substrates. Photolithographically patterned markers (chromium/gold) aided the identification of the same area of film before and after annealing. Since the D/G-ratio is a metric for the number of defective GNRs in the film, Raman spectra were recorded before and after annealing at temperatures of 200 and 300 °C for 6 h in dry nitrogen atmosphere (for details see Experimental Methods). To minimize the influence of spot-to-spot variations, over 1000 individual spectra were recorded at different locations of the films and averaged. Averaged Raman spectra before and after annealing are shown in Figure 2b.

While the Raman spectrum of the sample annealed at 200 °C does not exhibit any significant changes of the D/G-ratio, a substantial decrease of the D/G-ratio occurs for the sample annealed at 300 °C (see Figure 2b). This decrease is only observed for annealing temperatures above 260 °C (see Figure S4). The decrease in D/G-ratio also correlates with annealing time (see Figure S5). The relative G-band increase (calculated as $(D/G)_{\mathrm{preanneal}}/(D/G)_{\mathrm{postanneal}}$ with the D- and G-band areas fitted with Lorentzians) reaches up to 14% for an annealing time of 6 h and then starts to saturate for longer annealing times (see Figure 2c). Note that the exact ratio of pristine to defective GNRs cannot be calculated as the D/G-ratio of a film of only pristine or only defective 9-aGNRs is unknown. However, the D/G-ratios achieved by annealing films prepared from the >1 kg fraction are lower than those for the <0.2 kg fraction (Figure S6), indicating a higher fraction of pristine GNRs in the annealed films.

The Raman spectra of GNR films annealed at 300 °C (Figures 2b and S5) also exhibit small changes in the spectral region between 1150 and 1275 cm^{-1}, which are absent for annealing at 200 °C. This region is typically associated with CH-bending modes at the GNR edges[46,47] and changes are indicative of alterations of the edge structure. UV−vis-nIR absorption spectra of a 9-aGNR film (>1 kg fraction) before and after annealing at 300 °C for 6 h (Figure 2d) further point toward healing of defects, as the S_{1p} band (associated with pristine GNRs) increases for the annealed film compared to the defect-related S_{1d} band.

In contrast to annealing under dry nitrogen atmosphere, heating GNR films to 300 °C for 6 h under ambient conditions resulted in severe film degradation as evidenced by overall Raman signal reduction and frequency shifts of the GNR related Raman bands, as well as merging of the G- and D′-bands (see Figure S7). This behavior is typically associated with very high defect densities and degradation of graphene-based materials.[37] Thus, thermal annealing of GNR films must be performed in an inert atmosphere.

To corroborate that thermal annealing heals defects without altering the general structure of the 9-aGNRs (e.g., by cleaving off the alkyl side-chains), Raman spectra at wavenumbers below 1000 cm^{-1} were recorded before and after annealing (see Figure S8). Shear-like (SLM) and radial breathing-like modes (RBLM and RBLM3) as well as vibrations originating from CH-side chains are represented in this spectral region.[48−50] Since alkyl side chains move in phase with the

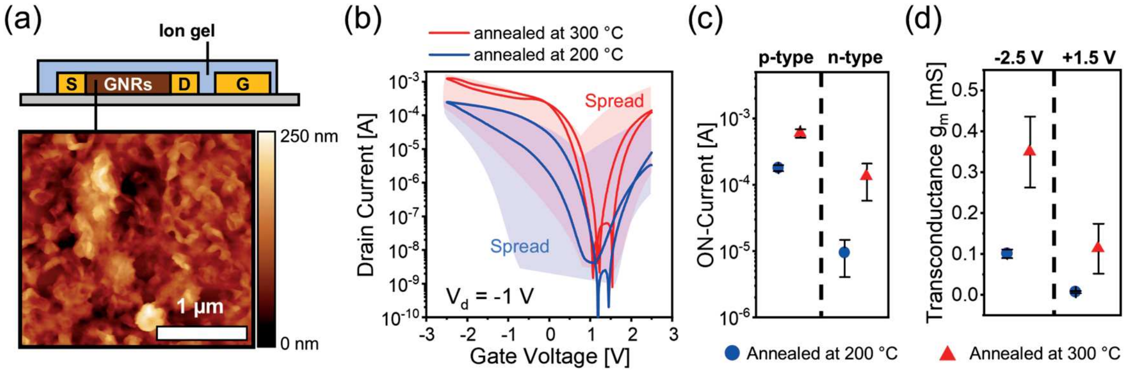

Figure 4. (a) Schematic device layout of 9-aGNR EGTs with ion gel and side-gate including representative AFM image of a transferred 9-aGNR film. (b) Transfer characteristics of representative EGTs with 9-aGNR films annealed at 200 and 300 °C. The spread of transfer curves over all devices is indicated by light blue and red shaded areas. (c) Average ON-currents for hole (p-type) and electron (n-type) transport for films annealed at 200 °C (blue) and 300 °C (red). Error bars represent standard deviation of the mean. (d) Average transconductance g_m at $V_g = -2.5$ V and $V_g = +1.5$ V for devices annealed at 200 and 300 °C. Error bars represent standard deviation of the mean.

GNR lattice carbon atoms, they effectively increase the GNR width and thus influence the RBLM frequency. As shown in Figure S8, the RBLM and RBLM3 frequencies remain unchanged after annealing up to 300 °C and the CH-related Raman bands are still present, indicating that annealing temperatures of up to 300 °C do not remove alkyl side chains.

The averaged Raman spectra suggest that defect curing in 9-aGNR films occurs upon thermal annealing at temperatures above 260 °C as depicted in Figure 2a. To control the defect density of GNR films in devices by postsynthesis annealing, the defect healing must be homogeneous throughout the film and should not alter the film morphology (i.e., thickness or roughness). To quantify the spatial uniformity of defect curing, Raman spectra were collected from the same 50 × 100 μm^2 area of MCE-transferred >1 kg 9-aGNR films before and after annealing at either 200 or 300 °C for 6 h. At each measurement spot, the peak areas of the D, G and D′ modes were fitted (see Experimental Methods) and the corresponding D/G-ratios were determined before and after annealing. The relative G-band increase for each spot was calculated using the ratio $(D/G)_{\text{preannealing}}/(D/G)_{\text{postannealing}}$. Maps of the relative G-band increases for films annealed at 200 and 300 °C together with an optical microscope image of the sampled area are presented in Figure 3.

Figure 3a shows a uniform relative G-band increase of more than 10% across the entire measured area for the 9-aGNR film annealed at 300 °C. Deviations are only observed at film irregularities such as aggregates (e.g., at $x = -40$ μm, $y = -30$ μm or $x = -15$ μm, $y = -5$ μm). As expected for 130 nm thick films, the substrate material (*i.e.*, gold or glass) does not have any effect on the annealing process. At an annealing temperature of 200 °C, the relative G-band intensity remains unchanged (see Figure 3b). This absence of any variation is also uniform throughout the film.

In addition to the spectroscopic properties, the influence of annealing temperature on film morphology was investigated by atomic force microscopy (AFM) and profilometry. Representative AFM images of 9-aGNR films before and after annealing are shown in Figure S9a,c. Upon MCE-transfer, the GNRs formed large flakes or aggregates with a lateral size of at least a few 100 nm. The films were quite rough on a microscopic scale with root-mean-square (rms) roughness values between 20 and 25 nm. This roughness, however, did not seem to change upon annealing, as AFM images of annealed films are very similar to untreated samples (Figure S9b,d).

To quantify this, the rms roughnesses and film thicknesses were measured at eight different spots of each sample (before and after annealing) and averaged. Neither film thickness nor roughness were significantly altered (see Figure S10), further indicating that defective GNRs in thin films do not decompose at elevated temperatures but transform into pristine GNRs. GNR decomposition would lead to dramatic changes in film thickness and morphology. The very similar morphology of the different annealed and as-deposited samples on a microscopic level and the homogeneity of defect healing throughout the entire films for both annealing temperatures enables comparison of charge transport in 9-aGNR films annealed at 200 and 300 °C and thus of GNR films with different defect densities.

Defect Density-Dependent Charge Transport. To quantify charge transport in dense films of 9-aGNRs, they were integrated in electrolyte-gated transistors with interdigitated source/drain electrodes (channel length $L = 2$ μm, channel width $W = 10$ mm) and a side-gate. The schematic device layout of the electrolyte-gated transistors (EGTs) is shown in Figure 4a and an optical image is presented in Figure S11. Electrolyte-gating uses liquid or solid (ion gel) electrolytes with mobile cations and anions instead of a conventional insulating dielectric for electrostatic gating. It relies on the movement of the ions toward the semiconducting channel and the gate electrode upon application of a gate field to form electric double layers at the interfaces with very high capacitances (on the order of few $\mu F/cm^2$). Hence, very high carrier densities can be accumulated even at very low applied gate voltages (V_g, 1−3 V) and the gate electrode can even be located on the side rather than on top of the channel.[51,52] Electrolyte-gating is very effective for porous semiconducting layers as the ions can penetrate and efficiently gate the entire film leading to higher source-drain currents (I_d) compared to conventional electrostatic gating. GNR transistors showed notably increased on-currents upon electrolyte gating.[53] Here, a commonly used ion gel[54] consisting of the ionic liquid 1-ethyl-3-methylimidazolium tris(pentafluoroethyl)trifluorophosphate ([EMIM][FAP]) and the matrix polymer poly(vinylidene fluoride-*co*-hexafluoropropylene) (P-(VDF-HFP)) was applied to gate the 9-aGNR films.

To ensure comparability between different EGTs, all 9-aGNR films were prepared from the same filter membrane, at the same time and under the same environmental conditions. Despite inherent device-to-device variations, substantial differences in performance might be attributed to different defect densities of the GNR films. As shown in Figure S2 the GNR films were cut to size and transferred such that they only covered the immediate channel area. Substrates were then annealed for 6 h at either 200 or 300 °C in dry nitrogen atmosphere to remove residual oxygen and water and to cure defects when annealed at 300 °C. Note that annealing at 200 °C is already sufficient for nearly complete removal of water and oxygen. Overall, 12 GNR EGTs were fabricated and annealed at 300 °C and another 10 devices were annealed at 200 °C.

Transfer characteristics at drain voltages (V_d) of −1 V were recorded at a slow gate voltage sweep rate (~ 3 mV/s) to ensure ion migration in and out of the channel and thus minimize current hysteresis. In addition, the starting gate voltage was held for 60 s to allow for equilibration prior to measurement. Figure 4b shows representative transfer curves of EGTs with 9-aGNR films annealed at 200 or 300 °C, as well as the spread of transfer curves for all measured EGTs as a shaded area (for complete transfer curves of all devices see Figures S12 and S13).

All EGTs show ambipolar charge transport with higher hole than electron currents for the applied gate voltage range. Measurements at more positive gate voltages were not feasible due to the limited electrochemical window of [EMIM]-[FAP].[55] Gate leakage currents (due to capacitive charging and ionic conductivity) were generally low (~10 nA) and did not affect the measurements. Interestingly, all transfer curves were shifted toward positive gate voltages. This shift indicates p-doping of the GNRs, which is common for many small-bandgap semiconductors when exposed to air. To check if 9-aGNR films were still p-doped after annealing, we performed gated absorption measurements on encapsulated EGTs (for details see Supporting Information). Figure S14 shows the absorption spectra of a 9-aGNR film at gate voltages of 0 and −1 V compared to the absorption spectrum at a gate voltage of +1 V. An absorption bleach is observed for a gate voltage of 0 V, which is a clear indicator for intrinsic doping.

To compare charge transport between devices annealed at 200 and 300 °C, ON-currents (maximum I_d within voltage range) and ON/OFF-ratios ($I_d(\max)/I_d(\min)$ within voltage range) for hole and electron transport were extracted from the forward sweeps of transfer curves and averaged over all devices (Figures 4c and S15). ON-currents for EGTs with GNR films annealed at 300 °C (i.e., with a higher fraction of defect-free GNRs) are higher than those for devices annealed at 200 °C by a factor of about three for hole transport and ten for electron transport (see Figure 4c). Similarly, the calculated ON/OFF-ratios improved 4-fold for films annealed at 300 °C (see Figure S15).

The effective charge carrier mobilities of the 9-aGNR films are proportional to the transconductances (g_m) of the EGTs ($g_m = dI_d/dV_g$). Since channel geometries (i.e., length and width) and processing conditions (which affect the device capacitance) were identical, the transconductance can be used to compare the EGTs without determining the capacitance of the devices. To correct for device-dependent shifts of the transfer curves, all transfer curves were shifted such that the minimum of the forward sweep was set to 0 V (i.e., plotted I_d vs. $V_g - V_g$ (minimum I_d)). The transconductances were extracted at $V_g - V_g$(minimum I_d) = −2.5 V (for holes) and +1.5 V (for electrons) to compare the g_m for EGTs annealed at different temperatures. Again, 9-aGNR films annealed at 300 °C showed consistently higher transconductances and hence higher carrier mobilities than films annealed at 200 °C (see Figure 4d).

The lower ON-currents, ON/OFF-ratios and transconductances/mobilities of devices with a higher fraction of defective 9-aGNRs confirm that edge defects in GNRs indeed impair both hole and electron transport. The impact of these defects in the lattice of the 9-aGNRs is substantial enough to be reflected even in the macroscopic transport through films that requires hopping from nanoribbon to nanoribbon. As nanoribbons with defects have more negative ionization potentials compared to pristine GNRs,[33] they should not be able to act as traps (for holes), however, an increase in energetic disorder within the film due to the presence of GNRs with defects might lower carrier mobilities similar to organic semiconductors.[56,57]

For comparison to previous studies, effective charge carrier mobilities in the GNR network were estimated from the transconductances. Assuming an ion gel capacitance of approximately 10 μFcm^{-2},[54] yielded hole mobilities on the order of 10^{-3} cm^2 V^{-1} s^{-1} and electron mobilities of 10^{-4}–10^{-3} cm^2 V^{-1} s^{-1}. These values are similar to carrier mobilities reported for other GNR network-based FETs (10^{-4}–10^{-2} cm^2 V^{-1} s^{-1}).[15,58] However, intrinsic carrier mobilities measured by optical techniques are typically on the order of 10–10^3 cm^2 V^{-1} s^{-1}.[59,60] This large difference is caused by the necessary carrier hopping between disordered GNRs and GNR domains and highlights the need for longer GNRs and better film morphology (e.g., alignment) to improve the performance of GNR-network FETs. To fully understand the impact of lattice defects on charge transport in GNRs, microscopic transport within individual nanoribbons should be investigated, for example, with ultrafast optical-pump terahertz probe (OPTP) spectroscopy[61] or dark microwave conductivity measurements.[62]

■ CONCLUSIONS

We investigated the impact of intrinsic structural defects on charge transport in thin films of solution-synthesized armchair graphene nanoribbons (9-aGNRs) and established thermal annealing as an effective postsynthetic method for defect healing. Defective 9-aGNRs sorted by liquid cascade centrifugation form high-quality thin films by filtration, whereas nearly defect-free GNRs tend to aggregate in dispersion leading to poor film morphologies. Annealing films of defective GNRs in inert atmosphere at temperatures above 260 °C effectively reduces the number of lattice defects as corroborated by Raman and UV–vis-nIR absorption spectroscopy. Electrolyte-gated transistors with thin films of 9-aGNRs annealed at 300 °C showed significantly higher ON-currents, transconductances, and ON/OFF ratios compared to devices with films annealed at only 200 °C. These results are consistent with theoretical predictions for GNRs with defects as well as experimental observations of other carbon-based nanomaterials. They highlight the detrimental role of edge defects even for macroscopic charge transport in GNR thin films. Consequently, future studies of devices with solution-synthesized GNRs should include high-temperature annealing as a key processing step to optimize their performance. As this study specifically addresses edge defects arising from incomplete graphitization in solution-synthesized GNRs, annealing may not heal bite defects, which are commonly found in on-surface-synthesized GNRs. Alternative synthesis routes and defect-healing strategies (e.g., thermal annealing in the presence of a carbon source as demonstrated for reduced graphene oxide[30]) may further enhance charge transport in GNR thin films.

■ ASSOCIATED CONTENT

Supporting Information

The Supporting Information is available free of charge at https://pubs.acs.org/doi/10.1021/acsanm.5c01848.

> UV−vis-nIR absorption spectra of GNR dispersions after LCC; detailed description of MCE transfer process; optical microscope images of GNR films prepared via MCE transfer; Raman spectra of annealed GNR films in dependence of annealing time, temperature, and annealing atmosphere; Raman spectra of RBLM-region of GNRs for different annealing temperatures; AFM images of GNR films; film morphology data before and after annealing of films; optical microscope images of electrode structure; transfer curves of all measured devices; UV−vis-nIR absorption spectrum of electrochemically doped GNRs; ON/OFF ratios of devices for different annealing temperatures (PDF)

■ AUTHOR INFORMATION

Corresponding Author

Jana Zaumseil − *Institute for Physical Chemistry, Heidelberg University, 69120 Heidelberg, Germany;* orcid.org/0000-0002-2048-217X; Email: zaumseil@uni-heidelberg.de

Authors

Sebastian Lindenthal − *Institute for Physical Chemistry, Heidelberg University, 69120 Heidelberg, Germany*

Finn L. Sebastian − *Institute for Physical Chemistry, Heidelberg University, 69120 Heidelberg, Germany;* orcid.org/0000-0003-1161-633X

Niklas J. Herrmann − *Institute for Physical Chemistry, Heidelberg University, 69120 Heidelberg, Germany;* orcid.org/0000-0002-2218-2517

Nicolas F. Zorn − *Institute for Physical Chemistry, Heidelberg University, 69120 Heidelberg, Germany;* orcid.org/0000-0001-9651-5612

Complete contact information is available at: https://pubs.acs.org/10.1021/acsanm.5c01848

Author Contributions

S.L. performed all of the measurements and analyzed the data. F.L.S. prepared electrode structures for device fabrication. N.J.H. helped with device measurements and data analysis. N.F.Z. assisted with measurement of electrochemically doped GNRs. J.Z. conceived and supervised the project. S.L. and J.Z. wrote the manuscript with input from all the authors. All authors have given approval to the final version of the manuscript

Notes

The authors declare no competing financial interest.

■ ACKNOWLEDGMENTS

This project received funding from the European Research Council (ERC) under the European Union's Horizon 2020 research and innovation program (Grant Agreement No. 817494 "TRIFECTs").

■ REFERENCES

(1) Barone, V.; Hod, O.; Scuseria, G. E. Electronic Structure and Stability of Semiconducting Graphene Nanoribbons. *Nano Lett.* **2006**, *6*, 2748−2754.

(2) Ezawa, M. Peculiar Width Dependence of the Electronic Properties of Carbon Nanoribbons. *Phys. Rev. B* **2006**, *73*, No. 045432.

(3) Son, Y.-W.; Cohen, M. L.; Louie, S. G. Energy Gaps in Graphene Nanoribbons. *Phys. Rev. Lett.* **2006**, *97*, No. 216803.

(4) Datta, S. S.; Strachan, D. R.; Khamis, S. M.; Johnson, A. T. C. Crystallographic Etching of Few-Layer Graphene. *Nano Lett.* **2008**, *8*, 1912−1915.

(5) Tapasztó, L.; Dobrik, G.; Lambin, P.; Biró, L. P. Tailoring the Atomic Structure of Graphene Nanoribbons by Scanning Tunnelling Microscope Lithography. *Nat. Nanotechnol.* **2008**, *3*, 397−401.

(6) Chen, Z.; Narita, A.; Müllen, K. Graphene Nanoribbons: On-Surface Synthesis and Integration into Electronic Devices. *Adv. Mater.* **2020**, *32*, No. 2001893.

(7) Hao, Z.; Zhang, H.; Ruan, Z.; Yan, C.; Lu, J.; Cai, J. Tuning the Electronic Properties of Atomically Precise Graphene Nanoribbons by Bottom-Up Fabrication. *ChemNanoMat* **2020**, *6*, 493−515.

(8) Jolly, A.; Miao, D.; Daigle, M.; Morin, J.-F. Emerging Bottom-Up Strategies for the Synthesis of Graphene Nanoribbons and Related Structures. *Angew. Chem., Int. Ed.* **2020**, *59*, 4624−4633.

(9) Yoon, K.-Y.; Dong, G. Liquid-Phase Bottom-Up Synthesis of Graphene Nanoribbons. *Mater. Chem. Front.* **2020**, *4*, 29−45.

(10) Baringhaus, J.; Ruan, M.; Edler, F.; Tejeda, A.; Sicot, M.; Taleb-Ibrahimi, A.; Li, A.-P.; Jiang, Z.; Conrad, E. H.; Berger, C.; Tegenkamp, C.; de Heer, W. A. Exceptional Ballistic Transport in Epitaxial Graphene Nanoribbons. *Nature* **2014**, *506*, 349−354.

(11) Cai, J.; Pignedoli, C. A.; Talirz, L.; Ruffieux, P.; Söde, H.; Liang, L.; Meunier, V.; Berger, R.; Li, R.; Feng, X.; Müllen, K.; Fasel, R. Graphene Nanoribbon Heterojunctions. *Nat. Nanotechnol.* **2014**, *9*, 896−900.

(12) Dienel, T.; Kawai, S.; Söde, H.; Feng, X.; Müllen, K.; Ruffieux, P.; Fasel, R.; Gröning, O. Resolving Atomic Connectivity in Graphene Nanostructure Junctions. *Nano Lett.* **2015**, *15*, 5185−5190.

(13) Gao, J.; Uribe-Romo, F. J.; Saathoff, J. D.; Arslan, H.; Crick, C. R.; Hein, S. J.; Itin, B.; Clancy, P.; Dichtel, W. R.; Loo, Y.-L. Ambipolar Transport in Solution-Synthesized Graphene Nanoribbons. *ACS Nano* **2016**, *10*, 4847−4856.

(14) Saraswat, V.; Jacobberger, R. M.; Arnold, M. S. Materials Science Challenges to Graphene Nanoribbon Electronics. *ACS Nano* **2021**, *15*, 3674−3708.

(15) Richter, N.; Chen, Z.; Tries, A.; Prechtl, T.; Narita, A.; Müllen, K.; Asadi, K.; Bonn, M.; Kläui, M. Charge Transport Mechanism in Networks of Armchair Graphene Nanoribbons. *Sci. Rep.* **2020**, *10*, No. 1988.

(16) Huang, W.; Braun, O.; Indolese, D. I.; Barin, G. B.; Gandus, G.; Stiefel, M.; Olziersky, A.; Müllen, K.; Luisier, M.; Passerone, D.; Ruffieux, P.; Schönenberger, C.; Watanabe, K.; Taniguchi, T.; Fasel, R.; Zhang, J.; Calame, M.; Perrin, M. L. Edge Contacts to Atomically Precise Graphene Nanoribbons. *ACS Nano* **2023**, *17*, 18706−18715.

(17) Lin, Y. C.; Mutlu, Z.; Borin Barin, G.; Hong, Y.; Llinas, J. P.; Narita, A.; Singh, H.; Müllen, K.; Ruffieux, P.; Fasel, R.; Bokor, J. Scaling and Statistics of Bottom-Up Synthesized Armchair Graphene Nanoribbon Transistors. *Carbon* **2023**, *205*, 519−526.

(18) Mutlu, Z.; Dinh, C.; Barin, G. B.; Jacobse, P. H.; Kumar, A.; Polley, D.; Singh, H.; Wang, Z.; Lin, Y. C.; Schwartzberg, A.; Crommie, M. F.; Mullen, K.; Ruffieux, P.; Fasel, R.; Bokor, J. Contact Engineering for Graphene Nanoribbon Devices. *Appl. Phys. Rev.* **2023**, *10*, No. 041412, DOI: 10.1063/5.0172432.

(19) Tian, C.; Miao, W.; Zhao, L.; Wang, J. Graphene Nanoribbons: Current Status and Challenges as Quasi-one-dimensional Nanomaterials. *Phys. Rev.* **2023**, *10*, No. 100082.

(20) Zhang, J.; Qian, L.; Barin, G. B.; Daaoub, A. H. S.; Chen, P.; Müllen, K.; Sangtarash, S.; Ruffieux, P.; Fasel, R.; Sadeghi, H.; Zhang, J.; Calame, M.; Perrin, M. L. Contacting Individual Graphene Nanoribbons Using Carbon Nanotube Electrodes. *Nat. Electron.* **2023**, *6*, 572−581.

(21) Yin, J.; Wang, H.; Pyle, D.; Choi, S.; Liu, Y.; Wen, J.; Guest, J. R.; Lyding, J. W.; Dong, G. Synthesis and Self-Assembly of Monodisperse Graphene Nanoribbons: Access to Submicron Architectures with Long-Range Order and Uniform Orientation. *ACS Nano* **2025**, *19*, 4366−4376.

(22) Bouilly, D.; Hon, J.; Daly, N. S.; Trocchia, S.; Vernick, S.; Yu, J.; Warren, S.; Wu, Y.; Gonzalez, R. L., Jr.; Shepard, K. L.; Nuckolls, C. Single-Molecule Reaction Chemistry in Patterned Nanowells. *Nano Lett.* **2016**, *16*, 4679−4685.

(23) Wilson, H.; Ripp, S.; Prisbrey, L.; Brown, M. A.; Sharf, T.; Myles, D. J. T.; Blank, K. G.; Minot, E. D. Electrical Monitoring of sp^3 Defect Formation in Individual Carbon Nanotubes. *J. Phys. Chem. C* **2016**, *120*, 1971−1976.

(24) Zheng, W.; Zorn, N. F.; Bonn, M.; Zaumseil, J.; Wang, H. I. Probing Carrier Dynamics in sp^3-Functionalized Single-Walled Carbon Nanotubes with Time-Resolved Terahertz Spectroscopy. *ACS Nano* **2022**, *16*, 9401−9409.

(25) Zorn, N. F.; Berger, F. J.; Zaumseil, J. Charge Transport in and Electroluminescence from sp^3-Functionalized Carbon Nanotube Networks. *ACS Nano* **2021**, *15*, 10451−10463.

(26) Haskins, J.; Kınacı, A.; Sevik, C.; Sevinçli, H.; Cuniberti, G.; Çağın, T. Control of Thermal and Electronic Transport in Defect-Engineered Graphene Nanoribbons. *ACS Nano* **2011**, *5*, 3779−3787.

(27) Dong, X.; Long, Q.; Wei, A.; Zhang, W.; Li, L.-J.; Chen, P.; Huang, W. The Electrical Properties of Graphene Modified by Bromophenyl Groups Derived from a Diazonium Compound. *Carbon* **2012**, *50*, 1517−1522.

(28) Lherbier, A.; Dubois, S. M. M.; Declerck, X.; Niquet, Y.-M.; Roche, S.; Charlier, J.-C. Transport Properties of Graphene Containing Structural Defects. *Phys. Rev. B* **2012**, *86*, No. 075402.

(29) Su, C.-Y.; Xu, Y.; Zhang, W.; Zhao, J.; Liu, A.; Tang, X.; Tsai, C.-H.; Huang, Y.; Li, L.-J. Highly Efficient Restoration of Graphitic Structure in Graphene Oxide Using Alcohol Vapors. *ACS Nano* **2010**, *4*, 5285−5292.

(30) Grimm, S.; Schweiger, M.; Eigler, S.; Zaumseil, J. High-Quality Reduced Graphene Oxide by CVD-Assisted Annealing. *J. Phys. Chem. C* **2016**, *120*, 3036−3041.

(31) Talirz, L.; Söde, H.; Dumslaff, T.; Wang, S.; Sanchez-Valencia, J. R.; Liu, J.; Shinde, P.; Pignedoli, C. A.; Liang, L.; Meunier, V.; Plumb, N. C.; Shi, M.; Feng, X.; Narita, A.; Müllen, K.; Fasel, R.; Ruffieux, P. On-Surface Synthesis and Characterization of 9-Atom Wide Armchair Graphene Nanoribbons. *ACS Nano* **2017**, *11*, 1380−1388.

(32) Pizzochero, M.; Čerņevičs, K.; Borin Barin, G.; Wang, S.; Ruffieux, P.; Fasel, R.; Yazyev, O. V. Quantum Electronic Transport Across "Bite" Defects in Graphene Nanoribbons. *2D Mater.* **2021**, *8*, No. 035025.

(33) Lindenthal, S.; Fazzi, D.; Zorn, N. F.; El Yumin, A. A.; Settele, S.; Weidinger, B.; Blasco, E.; Zaumseil, J. Understanding the Optical Properties of Doped and Undoped 9-Armchair Graphene Nanoribbons in Dispersion. *ACS Nano* **2023**, *17*, 18240−18252.

(34) Li, G.; Yoon, K.-Y.; Zhong, X.; Zhu, X.; Dong, G. Efficient Bottom-Up Preparation of Graphene Nanoribbons by Mild Suzuki−Miyaura Polymerization of Simple Triaryl Monomers. *Chem. - Eur. J.* **2016**, *22*, 9116−9120.

(35) Backes, C.; Szydłowska, B. M.; Harvey, A.; Yuan, S.; Vega-Mayoral, V.; Davies, B. R.; Zhao, P.-l.; Hanlon, D.; Santos, E. J. G.; Katsnelson, M. I.; Blau, W. J.; Gadermaier, C.; Coleman, J. N. Production of Highly Monolayer Enriched Dispersions of Liquid-Exfoliated Nanosheets by Liquid Cascade Centrifugation. *ACS Nano* **2016**, *10*, 1589−1601.

(36) Backes, C.; Higgins, T. M.; Kelly, A.; Boland, C.; Harvey, A.; Hanlon, D.; Coleman, J. N. Guidelines for Exfoliation, Characterization and Processing of Layered Materials Produced by Liquid Exfoliation. *Chem. Mater.* **2017**, *29*, 243−255.

(37) Ferrari, A. C.; Basko, D. M. Raman Spectroscopy as a Versatile Tool for Studying the Properties of Graphene. *Nat. Nanotechnol.* **2013**, *8*, 235−246.

(38) Cai, J.; Ruffieux, P.; Jaafar, R.; Bieri, M.; Braun, T.; Blankenburg, S.; Muoth, M.; Seitsonen, A. P.; Saleh, M.; Feng, X.; Müllen, K.; Fasel, R. Atomically Precise Bottom-Up Fabrication of Graphene Nanoribbons. *Nature* **2010**, *466*, 470−473.

(39) Talirz, L.; Ruffieux, P.; Fasel, R. On-Surface Synthesis of Atomically Precise Graphene Nanoribbons. *Adv. Mater.* **2016**, *28*, 6222−6231.

(40) Yano, Y.; Mitoma, N.; Ito, H.; Itami, K. A Quest for Structurally Uniform Graphene Nanoribbons: Synthesis, Properties, and Applications. *J. Org. Chem.* **2020**, *85*, 4−33.

(41) Blankenburg, S.; Cai, J.; Ruffieux, P.; Jaafar, R.; Passerone, D.; Feng, X.; Müllen, K.; Fasel, R.; Pignedoli, C. A. Intraribbon Heterojunction Formation in Ultranarrow Graphene Nanoribbons. *ACS Nano* **2012**, *6*, 2020−2025.

(42) Kolmer, M.; Steiner, A.-K.; Izydorczyk, I.; Ko, W.; Engelund, M.; Szymonski, M.; Li, A.-P.; Amsharov, K. Rational Synthesis of Atomically Precise Graphene Nanoribbons Directly on Metal Oxide Surfaces. *Science* **2020**, *369*, 571−575.

(43) Zuzak, R.; Castro-Esteban, J.; Engelund, M.; Pérez, D.; Peña, D.; Godlewski, S. On-Surface Synthesis of Nanographenes and Graphene Nanoribbons on Titanium Dioxide. *ACS Nano* **2023**, *17*, 2580−2587.

(44) Ma, C.; Wang, J.; Ma, H.; Yin, R.; Zhao, X.-J.; Du, H.; Meng, X.; Ke, Y.; Hu, W.; Li, B.; Tan, S.; Tan, Y.-Z.; Yang, J.; Wang, B. Remote-Triggered Domino-like Cyclodehydrogenation in Second-Layer Topological Graphene Nanoribbons. *J. Am. Chem. Soc.* **2023**, *145*, 10126−10135.

(45) Tosic, D.; Markovic, Z.; Jovanovic, S.; Prekodravac, J.; Budimir, M.; Kepic, D.; Holclajtner-Antunovic, I.; Dramicanin, M.; Todorovic-Markovic, B. Rapid thermal annealing of nickel-carbon nanowires for graphene nanoribbons formation. *Synth. Met.* **2016**, *218*, 43−49.

(46) Zhao, S.; Borin Barin, G.; Rondin, L.; Raynaud, C.; Fairbrother, A.; Dumslaff, T.; Campidelli, S.; Müllen, K.; Narita, A.; Voisin, C.; Ruffieux, P.; Fasel, R.; Lauret, J.-S. Optical Investigation of On-Surface Synthesized Armchair Graphene Nanoribbons. *Phys. Status Solidi B* **2017**, *254*, No. 1700223.

(47) Borin Barin, G.; Fairbrother, A.; Rotach, L.; Bayle, M.; Paillet, M.; Liang, L.; Meunier, V.; Hauert, R.; Dumslaff, T.; Narita, A.; Müllen, K.; Sahabudeen, H.; Berger, R.; Feng, X.; Fasel, R.; Ruffieux, P. Surface-Synthesized Graphene Nanoribbons for Room Temperature Switching Devices: Substrate Transfer and ex Situ Characterization. *ACS Appl. Nano Mater.* **2019**, *2*, 2184−2192.

(48) Verzhbitskiy, I. A.; Corato, M. D.; Ruini, A.; Molinari, E.; Narita, A.; Hu, Y.; Schwab, M. G.; Bruna, M.; Yoon, D.; Milana, S.; Feng, X.; Müllen, K.; Ferrari, A. C.; Casiraghi, C.; Prezzi, D. Raman Fingerprints of Atomically Precise Graphene Nanoribbons. *Nano Lett.* **2016**, *16*, 3442−3447.

(49) Overbeck, J.; Borin Barin, G.; Daniels, C.; Perrin, M. L.; Liang, L.; Braun, O.; Darawish, R.; Burkhardt, B.; Dumslaff, T.; Wang, X.-Y.; Narita, A.; Müllen, K.; Meunier, V.; Fasel, R.; Calame, M.; Ruffieux, P. Optimized Substrates and Measurement Approaches for Raman Spectroscopy of Graphene Nanoribbons. *Phys. Status Solidi B* **2019**, *256*, No. 1900343.

(50) Rizzo, D.; Prezzi, D.; Ruini, A.; Nagyte, V.; Keerthi, A.; Narita, A.; Beser, U.; Xu, F.; Mai, Y.; Feng, X.; Müllen, K.; Molinari, E.; Casiraghi, C. Multiwavelength Raman Spectroscopy of Ultranarrow Nanoribbons Made by Solution-Mediated Bottom-up Approach. *Phys. Rev. B* **2019**, *100*, No. 045406.

(51) Kim, S. H.; Hong, K.; Xie, W.; Lee, K. H.; Zhang, S.; Lodge, T. P.; Frisbie, C. D. Electrolyte-Gated Transistors for Organic and Printed Electronics. *Adv. Mater.* **2013**, *25*, 1822−1846.

(52) Zaumseil, J.; Jakubka, F.; Wang, M.; Gannott, F. In Situ Raman Mapping of Charge Carrier Distribution in Electrolyte-Gated Carbon Nanotube Network Field-Effect Transistors. *J. Phys. Chem. C* **2013**, *117*, 26361−26370.

(53) Llinas, J. P.; Fairbrother, A.; Borin Barin, G.; Shi, W.; Lee, K.; Wu, S.; Yong Choi, B.; Braganza, R.; Lear, J.; Kau, N.; Choi, W.; Chen, C.; Pedramrazi, Z.; Dumslaff, T.; Narita, A.; Feng, X.; Müllen, K.; Fischer, F.; Zettl, A.; Ruffieux, P.; Yablonovitch, E.; Crommie, M.; Fasel, R.; Bokor, J. Short-Channel Field-Effect Transistors with 9-Atom and 13-Atom Wide Graphene Nanoribbons. *Nat. Commun.* **2017**, *8*, No. 633.

(54) Lee, K. H.; Kang, M. S.; Zhang, S.; Gu, Y.; Lodge, T. P.; Frisbie, C. D. "Cut and Stick" Rubbery Ion Gels as High Capacitance Gate Dielectrics. *Adv. Mater.* **2012**, *24*, 4457−4462.

(55) Thiemann, S.; Sachnov, S.; Porscha, S.; Wasserscheid, P.; Zaumseil, J. Ionic Liquids for Electrolyte-Gating of ZnO Field-Effect Transistors. *J. Phys. Chem. C* **2012**, *116*, 13536−13544.

(56) Noriega, R.; Rivnay, J.; Vandewal, K.; Koch, F. P. V.; Stingelin, N.; Smith, P.; Toney, M. F.; Salleo, A. A General Relationship between Disorder, Aggregation and Charge Transport in Conjugated Polymers. *Nat. Mater.* **2013**, *12*, 1038−1044.

(57) Venkateshvaran, D.; Nikolka, M.; Sadhanala, A.; Lemaur, V.; Zelazny, M.; Kepa, M.; Hurhangee, M.; Kronemeijer, A. J.; Pecunia, V.; Nasrallah, I.; Romanov, I.; Broch, K.; McCulloch, I.; Emin, D.; Olivier, Y.; Cornil, J.; Beljonne, D.; Sirringhaus, H. Approaching Disorder-free Transport in High-mobility Conjugated Polymers. *Nature* **2014**, *515*, 384−388.

(58) Passi, V.; Gahoi, A.; Senkovskiy, B. V.; Haberer, D.; Fischer, F. R.; Grüneis, A.; Lemme, M. C. Field-Effect Transistors Based on Networks of Highly Aligned, Chemically Synthesized N = 7 Armchair Graphene Nanoribbons. *ACS Appl. Mater. Interfaces* **2018**, *10*, 9900−9903.

(59) Jänsch, D.; Ivanov, I.; Zagranyarski, Y.; Duznovic, I.; Baumgarten, M.; Turchinovich, D.; Li, C.; Bonn, M.; Müllen, K. Ultra-Narrow Low-Bandgap Graphene Nanoribbons from Bromoperylenes—Synthesis and Terahertz-Spectroscopy. *Chem. - Eur. J.* **2017**, *23*, 4870−4875.

(60) Varghese, S.; Mehew, J. D.; Wang, H. I.; Wuttke, M.; Zhou, Y.; Müllen, K.; Narita, A.; Cummings, A. W.; Tielrooij, K.-J. Ultrafast Charge and Exciton Diffusion in Monolayer Films of 9-Armchair Graphene Nanoribbons. *Adv. Mater.* **2024**, *36*, No. 2407796.

(61) Tries, A.; Osella, S.; Zhang, P.; Xu, F.; Ramanan, C.; Kläui, M.; Mai, Y.; Beljonne, D.; Wang, H. I. Experimental Observation of Strong Exciton Effects in Graphene Nanoribbons. *Nano Lett.* **2020**, *20*, 2993−3002.

(62) Ferguson, A. J.; Reid, O. G.; Nanayakkara, S. U.; Ihly, R.; Blackburn, J. L. Efficiency of Charge-Transfer Doping in Organic Semiconductors Probed with Quantitative Microwave and Direct-Current Conductance. *J. Phys. Chem. Lett.* **2018**, *9*, 6864−6870.

SUPPORTING INFORMATION

Healing Defects in Armchair Graphene Nanoribbons for Enhanced Charge Transport

Sebastian Lindenthal[1], *Finn L. Sebastian*[1], *Niklas J. Herrmann*[1], *Nicolas F. Zorn*[1], *Jana Zaumseil**[,1]

[1] Institute for Physical Chemistry, Heidelberg University 69120 Heidelberg, Germany

*E-mail: *zaumseil@uni-heidelberg.de*

General Characterization of GNR dispersions and MCE films

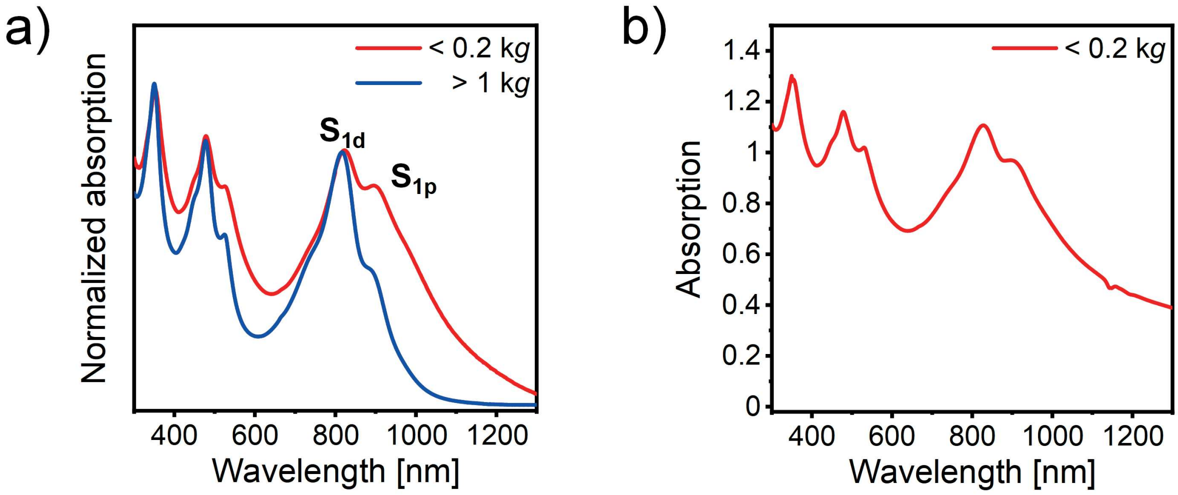

Figure S1. a) UV-Vis-nIR absorption spectra of GNR dispersions after liquid cascade centrifugation (LCC) normalized to the absorption band at 820 nm. The absorption spectrum of the < 0.2 kg fraction is baseline-corrected to account for a large scattering background. The lowest energy absorption bands of defective and pristine GNRs are labelled as S_{1d} and S_{1p}, respectively. **b)** Uncorrected UV-Vis-nIR absorption spectrum of < 0.2 k*g* 9-aGNR fraction obtained from LCC exhibiting a strong scattering background, indicative of unexfoliated material in the < 0.2 k*g* fraction.

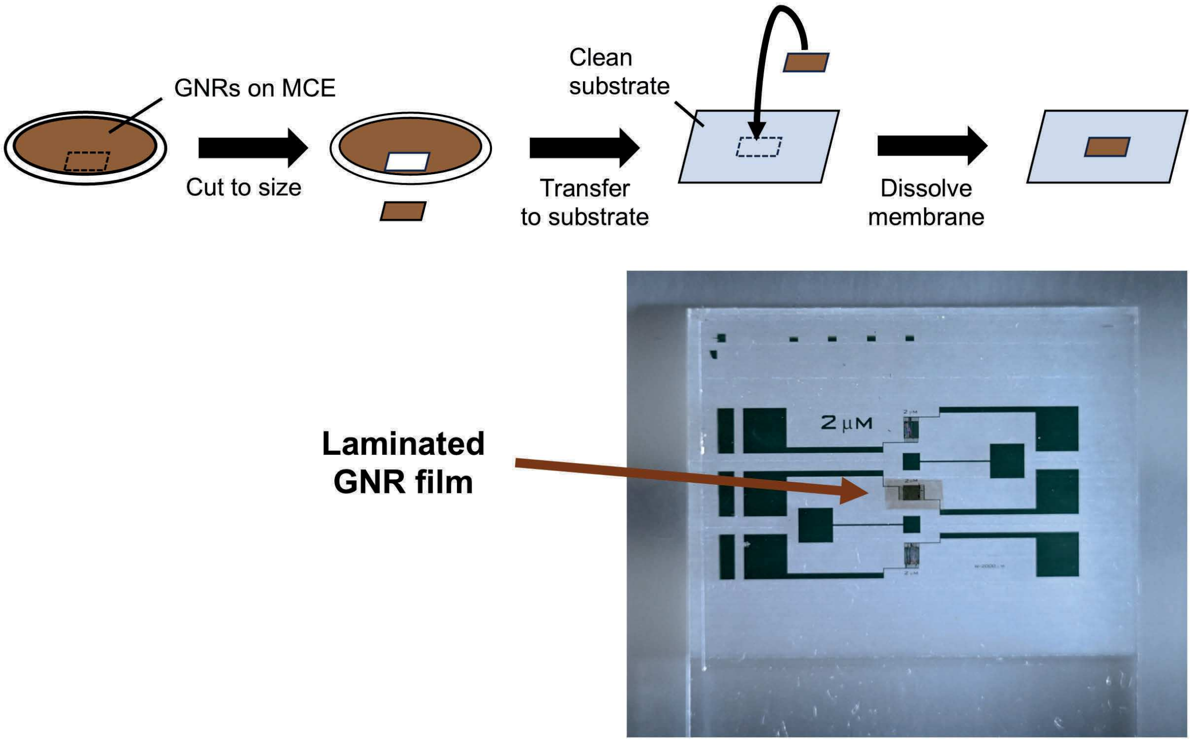

Figure S2. Preparation of 9-aGNR films *via* mixed cellulose ester (MCE) transfer. A diluted dispersion of 9-aGNRs, previously subjected to LCC, was vacuum filtered onto a MCE membrane (Merck MF-Millipore, VSWP, pore size 0.025 μm, diameter 25 mm) to create a GNR film on top of the MCE membrane. The thickness of the film was determined by the volume and concentration (*i.e.*, the optical density) of the filtered GNR dispersion (AmL - absorbance times volume of filtered dispersion). The absorption at the S_{1d} transition (820 nm) of a dispersion was used as a metric for the GNR concentration. The MCE filter was cut to size and placed on a freshly cleaned substrate with the GNR-side down. The filter was wetted with isopropanol and pressure was applied to the back of the MCE filter, such that it thoroughly adhered to the substrate. Subsequently, the substrate was slowly immersed in a large volume of acetone for at least 15 min to dissolve the MCE membrane. The last step was repeated 4 times to remove any residues of MCE membrane and obtain a continuous GNR film on the substrate. The bottom panel shows a photograph of a > 1 kg 9-aGNR film MCE-transferred on top of interdigitated gold electrodes.

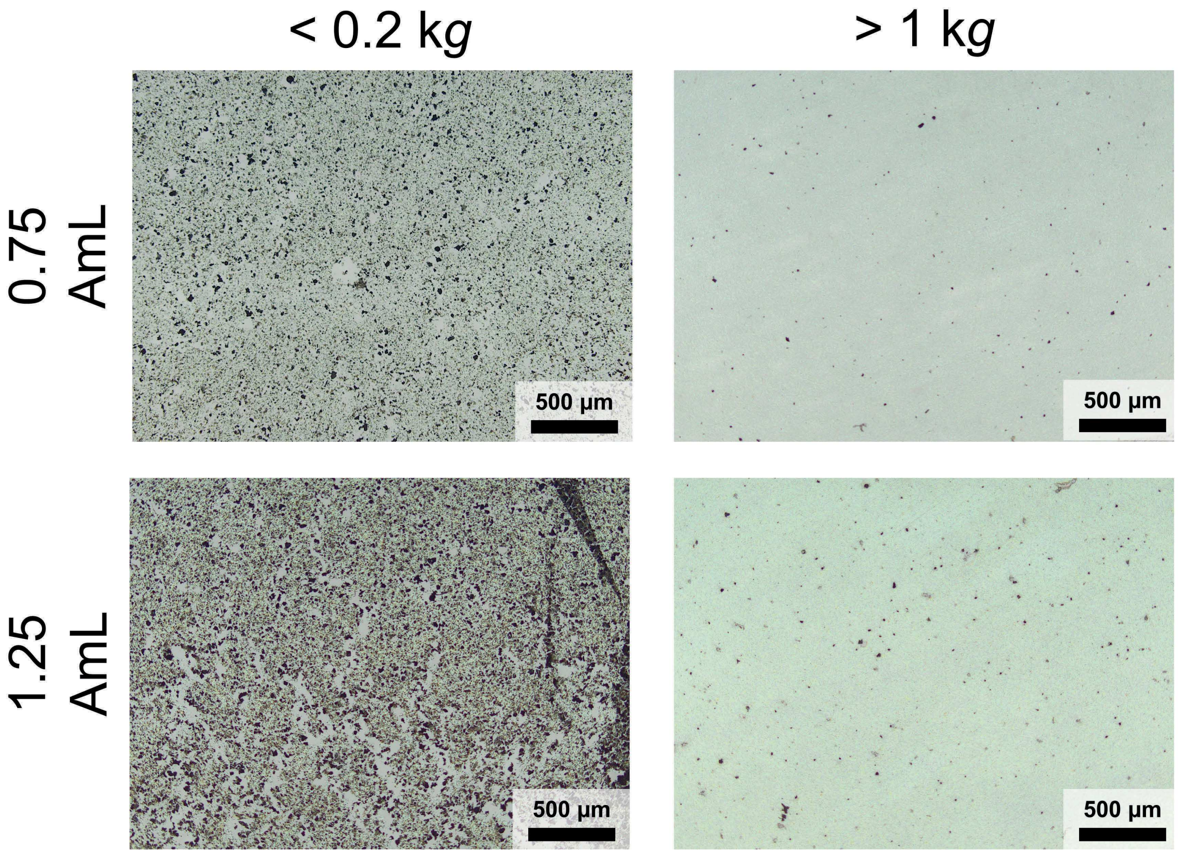

Figure S3. Optical microscope images of MCE-transferred films prepared from < 0.2 k*g* fractions (left) and > 1 k*g* fractions (right). Films on the top (bottom) row were prepared by filtering 0.75 mL (1.25 mL) dispersion with an absorbance of 1 cm^{-1} at the S_{1d} transition (0.75 AmL or 1.25 AmL as a measure of expected film thickness). Films prepared from the < 0.2 k*g* fraction display a large number of aggregates, fissures and folds, while films prepared from the > 1 k*g* fraction are homogeneous and only show few large aggregates.

Curing Defects by Thermal Annealing

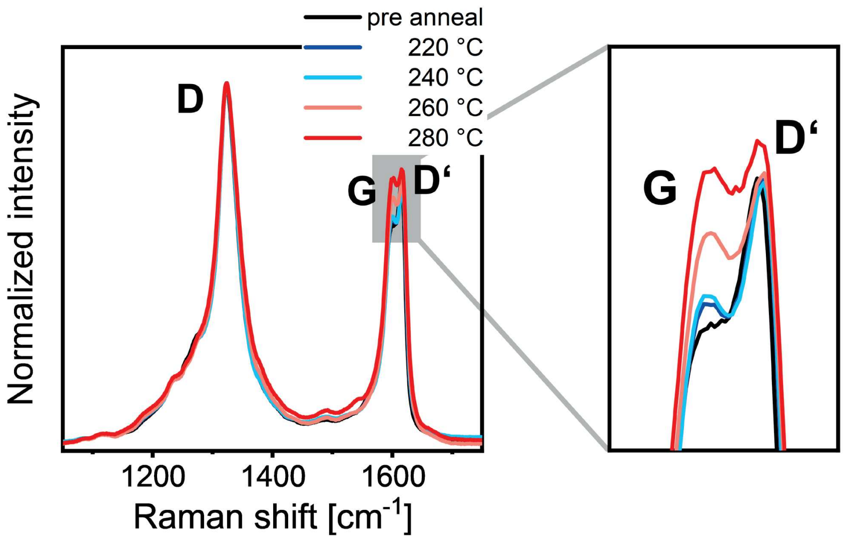

Figure S4. Averaged Raman spectra (excitation wavelength 532 nm) normalized to the D-band of MCE-transferred > 1 k*g* GNR films annealed for 3 h at different temperatures. The D/G-ratio decrease, which is indicative of defect curing, is only observed for annealing temperatures equal to or higher than 260 °C. As films were prepared from the same MCE membrane, Raman spectra of pre annealed samples were all very similar. For simplicity, only the Raman spectrum of the 220 °C sample prior to annealing (black line) is shown for comparison.

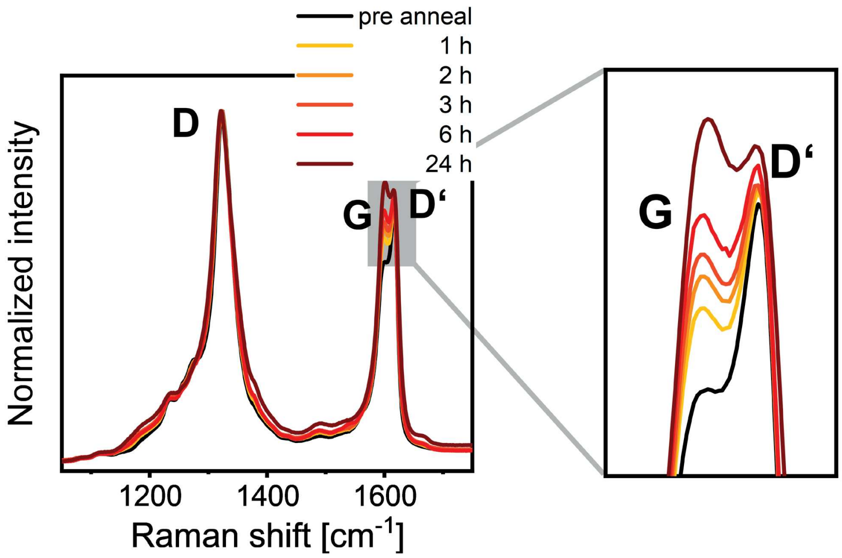

Figure S5. Raman spectra (excitation wavelength 532 nm) normalized to the D-band of MCE-transferred > 1 k*g* GNR films annealed at 300 °C for different amounts of time. As films for each annealing experiment were prepared from the same MCE membrane, Raman spectra of pre-annealed samples were all very similar. Thus, Raman spectra of untreated samples except for one spectrum have been omitted for clarity. The right panel shows a zoom-in on the grey highlighted region, clearly showing the decrease of D/G-ratios for increased annealing times.

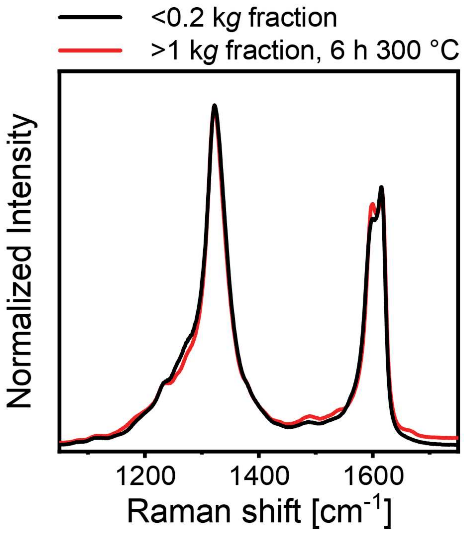

Figure S6. Comparison of Raman spectra of an untreated <0.2 k*g* GNR film and an annealed GNR film (6 h, 300 °C) of the >1 k*g* fraction.

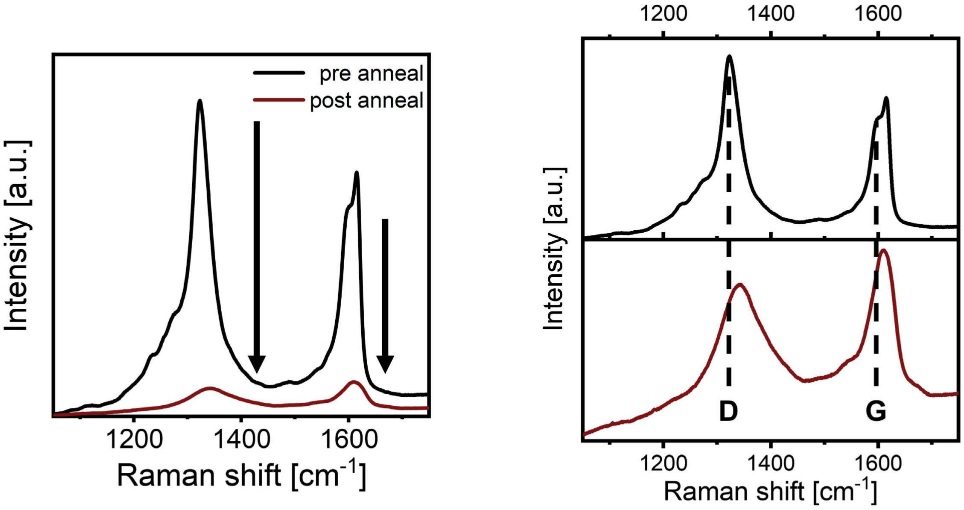

Figure S7. Raman spectra (excitation wavelength 532 nm) of MCE-transferred > 1 kg GNR films annealed at 300 °C under ambient conditions for 6 h. The left panel shows the spectra on the same scale and reveals a significant drop in Raman band intensity upon heating the sample to 300 °C in air, indicating severe degradation. The right panel shows normalized spectra for comparison of Raman shift and line shape before and after annealing.

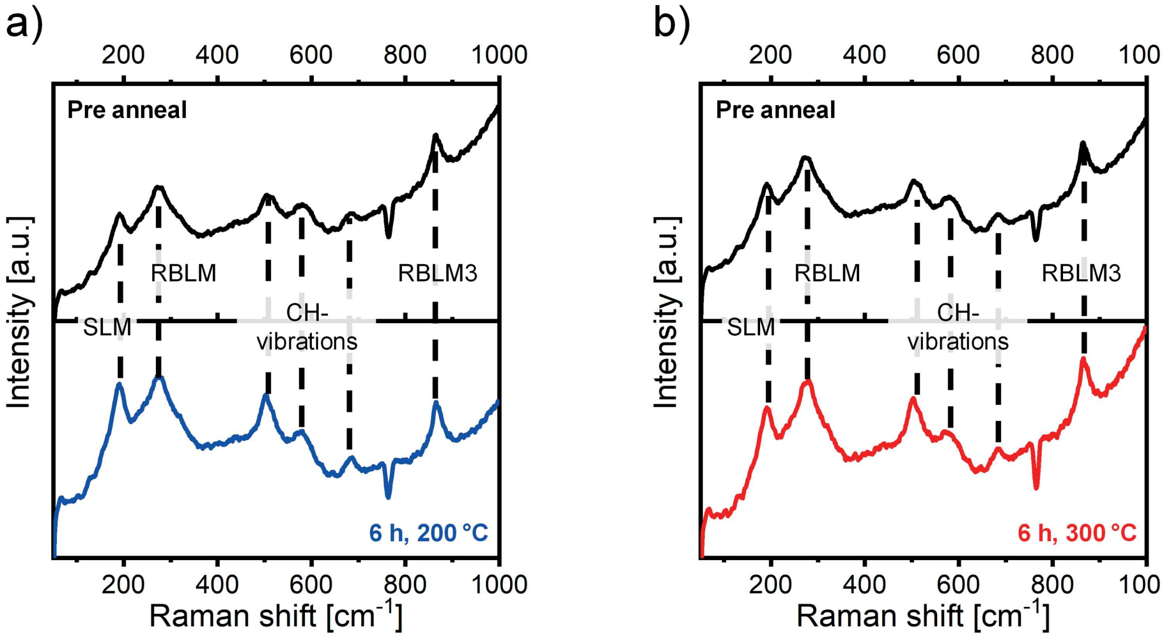

Figure S8. RBLM region of Raman spectra recorded on > 1 kg 9-aGNR films before and after annealing at **a)** 200 °C and **b)** 300 °C. Raman bands that are expected to shift upon major structural damage are labelled. The dashed lines indicate invariable Raman shifts for all labelled bands independent of annealing temperature.

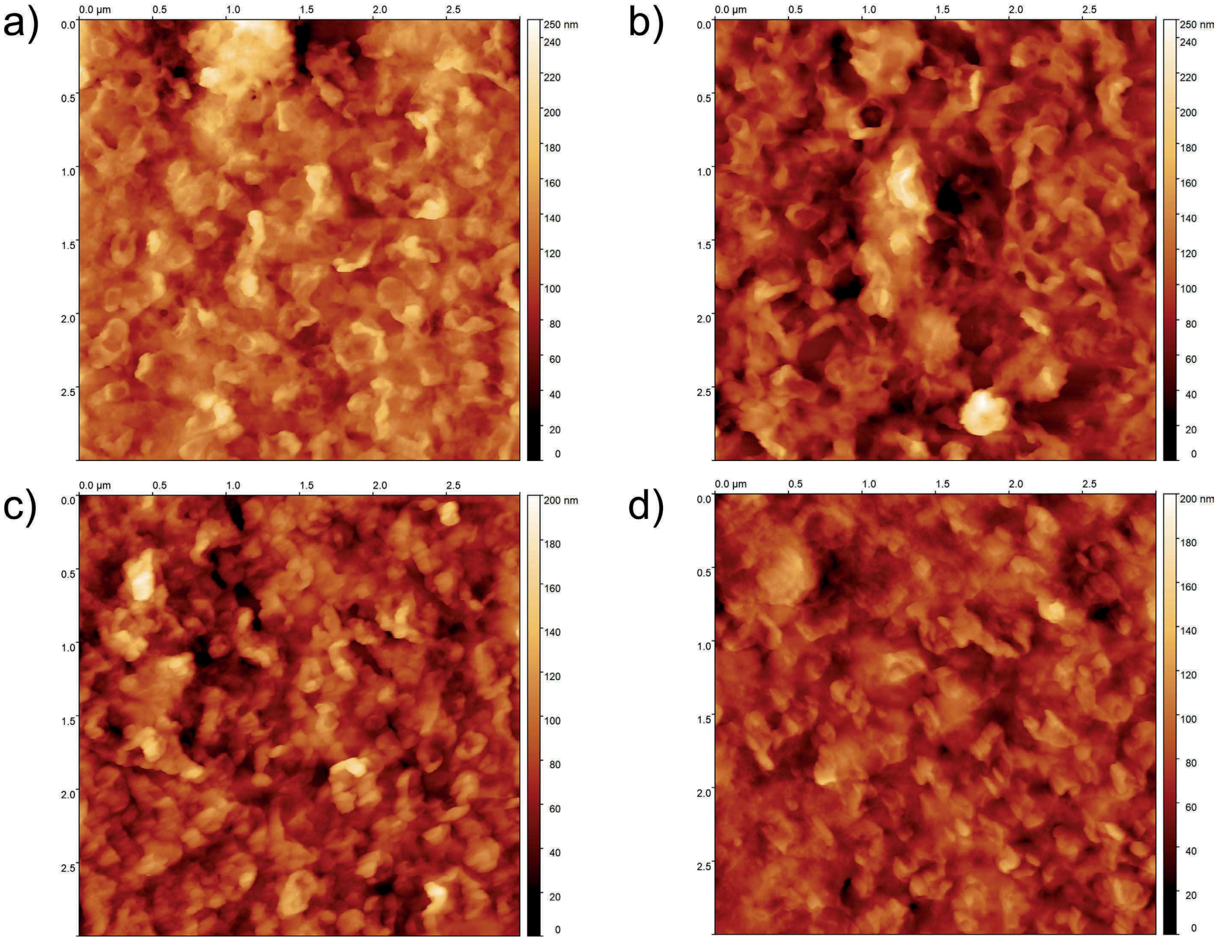

Figure S9. AFM images (3 x 3 µm Bruker Dimension Icon, ScanAsyst mode, ScanAsyst tips) of MCE-transferred 9-aGNR films (>1 kg films) obtained from **a)** a sample before and **b)** after annealing at 300 °C, **c)** a sample before and **d)** after annealing at 200 °C.

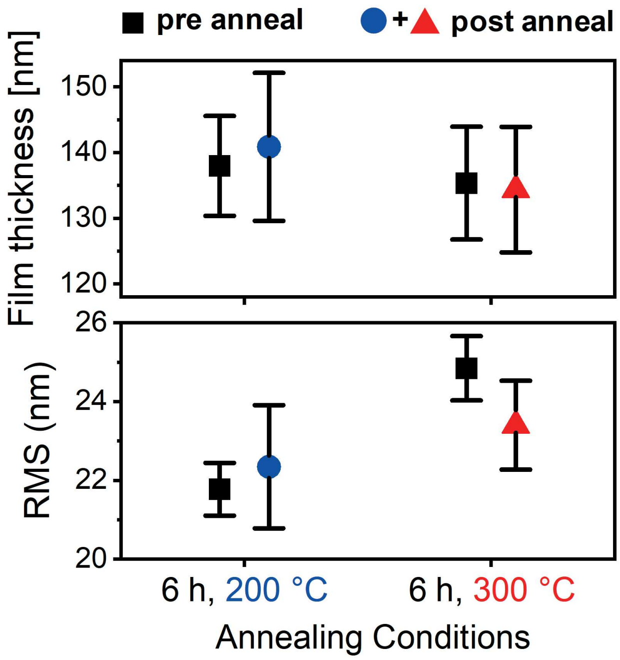

Figure S10. Film thickness (top panel) and rms roughness (bottom panel) of 9-aGNR films before and after annealing at 200 and 300 °C. The error bars depict the standard deviation of the mean.

Electrical Characterization of EGTs

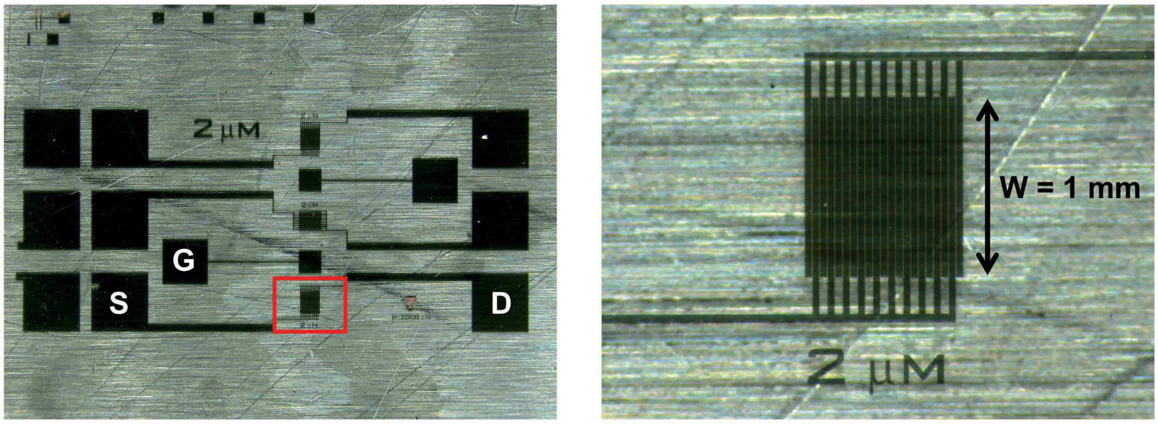

Figure S11. Electrode layout of electrolyte-gate transistor (EGT) on glass substrate. Each substrate has 3 sets of source (S) and drain (D) electrodes (interdigitated channel length L = 2 µm, total channel width W = 10 mm) and two side-gate (G) electrodes.

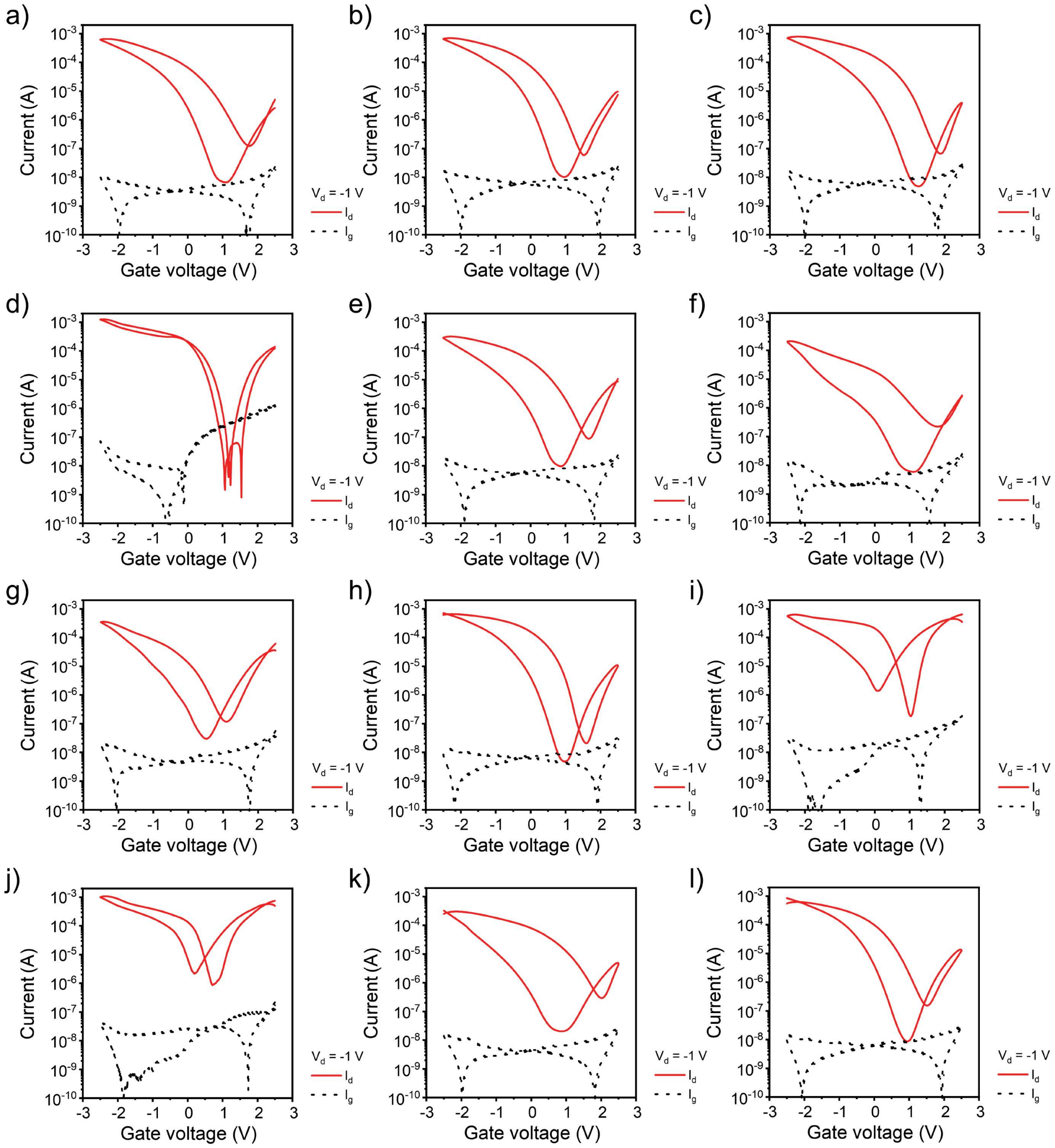

Figure S12. Transfer characteristics (I_d *vs*. V_g including gate leakage currents I_g) of all EGTs annealed at 300 °C.

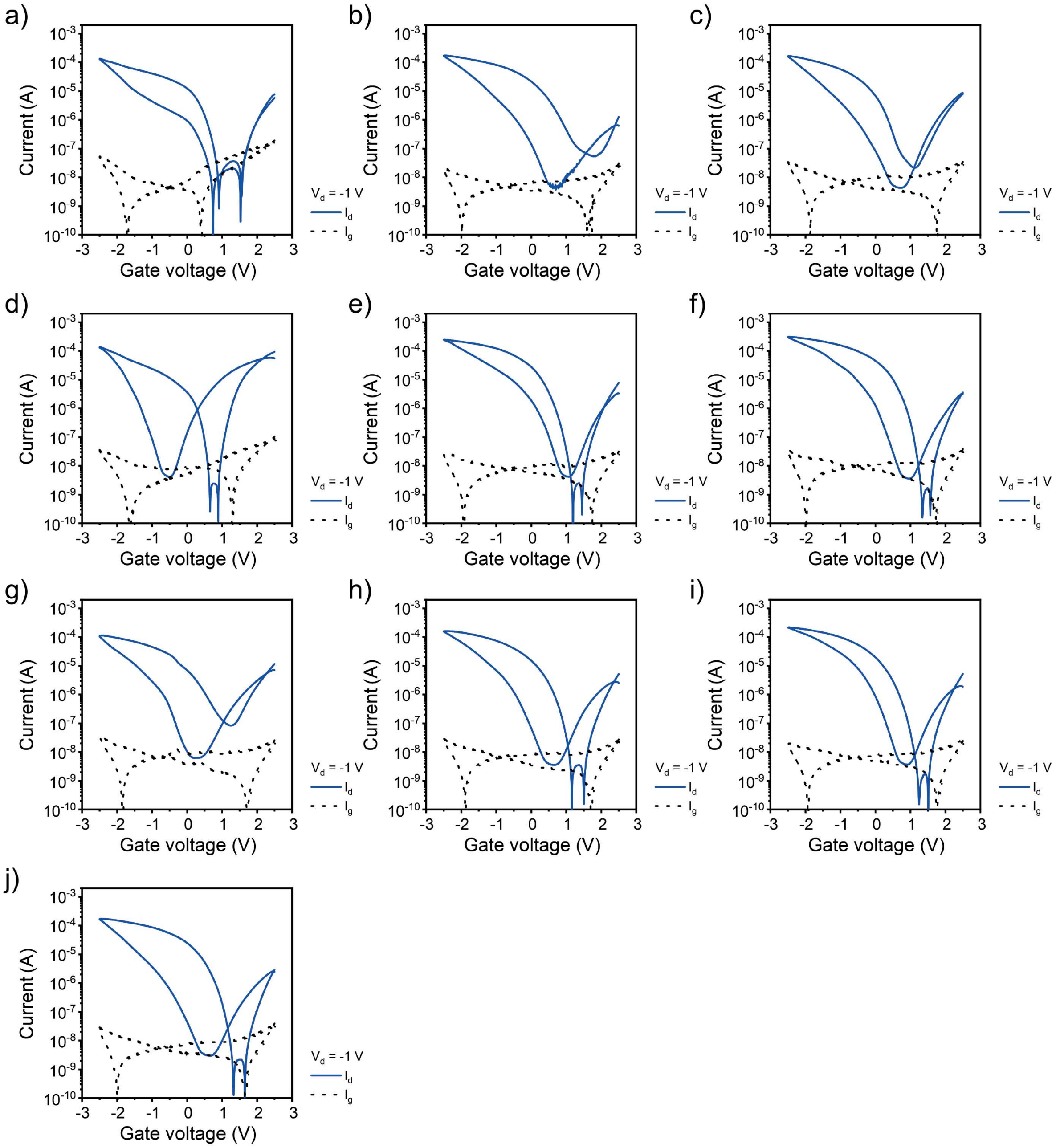

Figure S13. Transfer characteristics (I_d *vs*. V_g including gate leakage currents I_g) of all EGTs annealed at 200 °C.

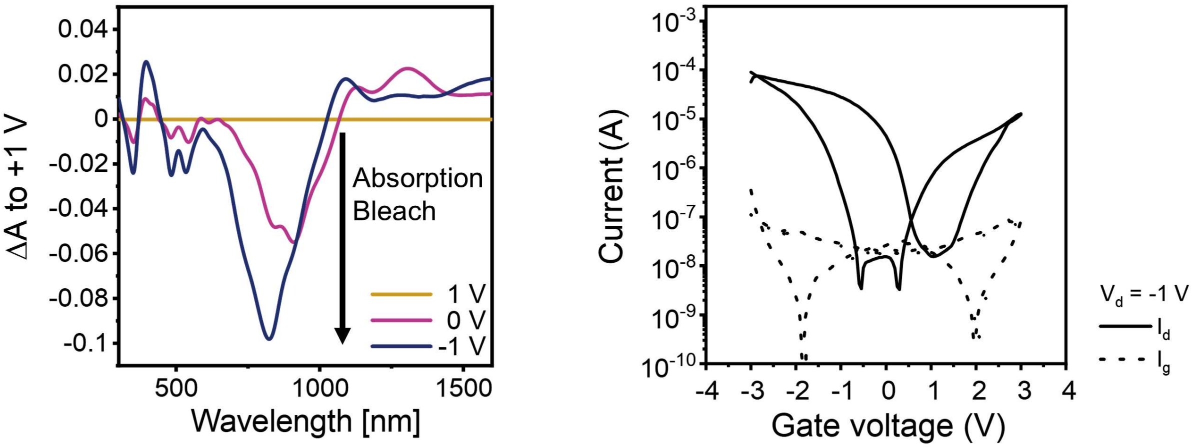

Figure S14. Differential absorption spectra of electrochemically doped 9-aGNRs at gate voltages +1, 0 and -1 V (left, source and drain electrodes were shorted for the measurement). The spectrum at V_g = +1 V was chosen as the reference spectrum to visualize the absorption bleach of the S_{1d} and S_{1p} transitions at V_g = 0 and -1 V. To exclude contact with air and humidity during absorption measurements, devices were encapsulated with a cover glass slide and UV-hardening epoxy (DELO KATIOBOND LP655) after addition of the ion gel. UV-exposure (400 nm) during hardening of the epoxy does not affect ambipolar device performance as shown by the transfer curve measured after device encapsulation (right).

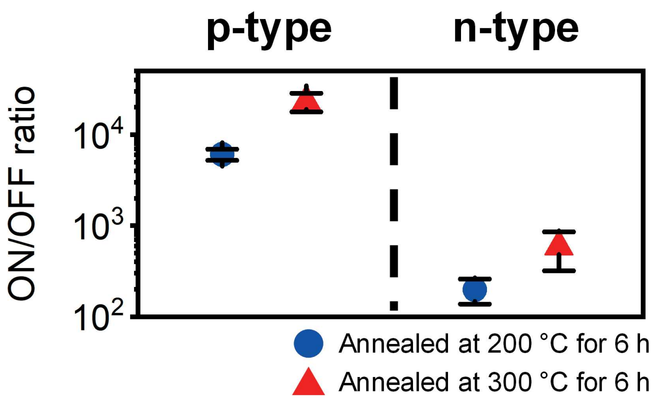

Figure S15. Average ON/OFF ratios of p- and n-type transport for devices annealed at 200 °C and 300 °C. The error bars represent the standard deviation of the mean.

CHAPTER 7

SUMMARY AND CONCLUSION

This work investigated the optoelectronic properties of two related yet distinctly different carbon-based, low-dimensional semiconductors: graphene nanoribbons and single-walled carbon nanotubes. SWCNTs have already been investigated for three decades and are consequently more mature in terms of fundamental understanding and processing techniques. Their physical properties (*e.g.*, charge transport, exciton formation and dynamics, environmental interaction) have been widely explored. In contrast, atomically-precise GNRs – first studied almost a decade later – are still in an earlier stage of research, where many aspects from synthesis and fundamental physical properties to processing are still under active investigation. While **Chapter 3** and **4**, associated with SWCNTs, present solutions to practical problems associated with the progression of SWCNTs from fundamental research to applications, the presented work on GNRs (**Chapter 5** and **6**) answers fundamental questions about their physical properties. In the following the main findings of this thesis will be summarized briefly and potential implications for future research in these fields are discussed.

One of the persistent problems associated with the application of SWCNT in electronic devices is their purification from commercially available raw materials. Previous studies relied on sonication-based exfoliation methods, which introduce defects into the SWCNTs and lack scalability, hence limiting their suitability in industrial-scale application. A major step forward was made by Graf *et al.* in 2016, who introduced shear force mixing in combination with polymer-wrapping as a mild and scalable exfoliation method to selectively disperse (6,5) SWCNTs while simultaneously limiting the unintentional creation of defects.[20] However, larger diameter semiconducting SWCNTs offer superior charge transport properties. As the dispersion process is highly sensitive to any changes in process conditions, the protocol originally developed for (6,5) SWCNTs could not simply be transferred to selectively disperse other nanotube chiralities. Instead, a thorough screening of dispersion parameters was necessary to successfully disperse (7,5) and semiconducting Plasma Torch SWCNTs by shear force mixing. The adapted dispersion procedures, as well as the fundamental insights on the dispersion process are summarized in **Chapter 3** and provide important processing details to the research community as a type of white book. The detailed description of the established processes already facilitated successful adaptation of shear force mixing by other research groups. This work provides a solid foundation for further expansion of the shear force mixing process towards other nanotube chiralities by employing different polymer/raw material combinations or even different solvent systems. Applying shear force mixing in aqueous systems would be especially interesting, as sorting techniques like aqueous two-phase extraction already provide access to almost any SWCNT chirality. Furthermore, scaling up the process by using larger shear force mixers will be an important step toward industrial deployment of high-quality semiconducting SWCNTs in optoelectronic applications.

The general interaction of SWCNTs with dopants has been studied thoroughly for more than a decade.[21] Previous studies already developed models to explain the changes in electronic and optical properties upon introduction of charge carriers[128,247,248,257,261] and established a broad a variety of chemical dopants, as well as doping methods to modulate the electron density in carbon nanotubes.[21,222,245] However, most of these dopants have drawbacks, such as poor solubility, high reactivity, or limited commercial availability. **Chapter 4** of this thesis added tris(pentafluorophenyl)borane (BCF) to the library of p-dopants suitable for doping small-diameter SWCNTs. BCF as a low-cost, readily available, and highly soluble Lewis acid showed strong p-doping of PFO-BPy-wrapped SWCNTs, despite a comparatively low electron affinity. The doping mechanism, investigated by absorption, photoluminescence and ^{11}B and ^{19}F NMR spectroscopy, relies on a unique interaction between BCF/water complexes, BCF molecules complexed to pyridinic nitrogen in the wrapping polymer PFO-BPy and the SWCNTs. Since the resulting counter-ion (a BCF-OH$^-$ anion) is expected to be spaced quite far away from the induced charge, the doped SWCNTs should exhibit high conductivities due to a weaker Coulomb screening.[226] Hence, future studies could investigate BCF as a dopant to achieve highly conductive SWCNT networks in electronic devices. Additionally, this study demonstrates that polymer-wrapping not only enables selective dispersion of distinct SWCNT chiralities but also actively enhances the functionality of the wrapped SWCNTs. While the basic principle has already been used to build SWCNT-based copper and glyphosate sensors[294], chemical engineering of wrapping polymers to include more (or more specific) functionalities might facilitate interactions between small molecules, wrapping polymers and SWCNTs for sensing applications.

In contrast to SWCNTs, the chemical doping of atomically precise GNRs remained largely unexplored until recently. Deilmann *et al.* predicted large trion binding energies for armchair

GNRs and Fedotov *et al.* observed charge-induced, red-shifted photoluminescence in on-surface synthesized 7-aGNRs upon p-type doping with F_4TCNQ, which they assigned to trionic emission. However, direct experimental evidence confirming the formation of trions in GNRs was not presented. In **Chapter 5**, a method to disperse solution-synthesized 9-aGNRs in common organic solvents was established. Liquid cascade centrifugation revealed the presence of two distinct GNR populations with different optical properties. While previous studies often assigned such spectral features to excimer formation or aggregation, various spectroscopic techniques (Raman, cryogenic single-GNR photoluminescence and absorption) combined with theoretical modelling showed that the observed spectral features arise from GNRs with and without edge defects. These structural irregularities in GNRs are expected to be present in virtually any solution-synthesized GNR raw material, due to the limitations of the Scholl reaction and hampered purification possibilities (*e.g.*, no column chromatography). Consequently, future studies on the optical properties of GNRs have to consider defective GNRs as a possible source of unexpected spectral features.

Chemical doping of defective and pristine 9-aGNRs with F_4TCNQ led to charge-induced absorption but no charge-induced emission features, which hints at the formation of polarons instead of trions. Supporting theoretical studies corroborate polaron formation upon doping. This study is the first to experimentally show polaron formation in GNRs upon introduction of excess charge carriers. The strong carrier-phonon coupling, which is also observed for polymers, appears to drive polaron formation and might also generally influence charge transport in GNRs. The difference between solution- and on-surface synthesized GNRs (which are more rigid due to the lack of sterically demanding side-chains) should be investigated in future research.

A follow-up study which investigated the optical signatures in the mid-IR region, as well as microscopic and macroscopic conductivities of 9-aGNR films doped with p-dopants of varying sizes and compared the results to those obtained for polymers and SWCNTs. It found a direct connection between polaronic optical signatures and increased conductivities, suggesting a polaron-assisted charge transport mechanism (similar to polymers) which is also predicted by several theoretical studies.[308-312] Hence, the formation of polarons in presence of excess charge carriers has direct implications for the integration of solution-synthesized GNRs into electronic devices, and strategies which improve polymer-based electronics might be applicable to GNR-based devices. Both studies show that (solution-synthesized) GNRs are distinctively different from SWCNTs and should rather be seen as rigid polymers.

In the final results chapter, a method to heal defects in films of solution-synthesized, defective 9-aGNRs based on thermal annealing in an inert atmosphere was established. The extent of defect healing was examined by absorption and spatially resolved Raman spectroscopy. Additionally, it was shown that the annealing process does not cleave any side chains or negatively affects the film morphology. Electrolyte-gated transistors with GNR films that were subjected to the defect healing process showed a significantly improved device performance, compared to those that still contained the original fraction of defective GNRs. Moreover, high on/off ratios of up to 10^5 were measured in these long-channel electrolyte-gated transistors.

Chapter 6 presents the first experimental evidence for a direct correlation between edge disorder in atomically-precise GNRs and impaired charge transport – an effect that was so far only predicted theoretically.[303-305] With the omnipresence of defects in solution-synthesized GNRs, the development of methods to heal these defects is crucial for the integration of GNRs into electronic devices. Thermal annealing at elevated temperatures is expected to become a standard procedure for device fabrication with solution-synthesized GNRs as a channel material. Moreover, these findings also raise the question about an adapted procedure for defect healing in on-surface synthesized GNRs. In particular, 'bite defects' which are characterized by the absence of a phenyl ring, are unlikely to be repaired by thermal treatment alone. A process in the presence of a carbon source – as has been performed for defect healing in graphene[313] – might be necessary to produce defect-free on-surface synthesized GNRs. Based on the detrimental effect of edge irregularities on charge transport, finding an equivalent process (or significantly improving the synthesis to avoid defects in the first place) is necessary to produce on-surface synthesized GNRs suitable for device integration.

In summary, this thesis provides new insights and practical advancements for doping and device integration of two low-dimensional carbon-based semiconductors. With the optimization of the shear force mixing process and the establishment of BCF as an attractive p-dopant for polymer-wrapped nanotubes, the toolbox for successful device integration of SWCNTs is expanded. For GNRs, a direct correlation between defect density and changes in optical and electrical properties is established and a method to improve charge transport in GNRs by healing of defects is presented. These results contribute to future research aimed towards integration of low-dimensional carbon-based semiconductors into optoelectronic devices and contribute toward a better understanding of their fundamental properties.

REFERENCES

Note that the bibliography below only contains the references for **Chapters 1**, **2** and **7**. References used within the publications in this work (**Chapter 3 - 6**) can be found in the bibliography of the respective paper or supporting information.

1. Havemann, R. H.; Hutchby, J. A., High-Performance Interconnects: an Integration Overview. *Proceedings of the IEEE* **2001,** *89*, 586-601, https://doi.org/10.1109/5.929646.

2. Facchetti, A.; Yoon, M.-H.; Marks, T. J., Gate Dielectrics for Organic Field-Effect Transistors: New Opportunities for Organic Electronics. *Advanced Materials* **2005,** *17*, 1705-1725, https://doi.org/10.1002/adma.200500517.

3. Mack, C. A., Fifty Years of Moore's Law. *IEEE Transactions on Semiconductor Manufacturing* **2011,** *24*, 202-207, https://doi.org/10.1109/TSM.2010.2096437.

4. Ito, T.; Okazaki, S., Pushing the Limits of Lithography. *Nature* **2000,** *406*, 1027-1031, https://doi.org/10.1038/35023233.

5. Thompson, S. E.; Chau, R. S.; Ghani, T.; Mistry, K.; Tyagi, S.; Bohr, M. T., In Search of "Forever," Continued Transistor Scaling One New Material at a Time. *IEEE Transactions on Semiconductor Manufacturing* **2005,** *18*, 26-36, https://doi.org/10.1109/TSM.2004.841816.

6. Allard, S.; Forster, M.; Souharce, B.; Thiem, H.; Scherf, U., Organic Semiconductors for Solution-Processable Field-Effect Transistors (OFETs). *Angewandte Chemie International Edition* **2008,** *47*, 4070-4098, https://doi.org/10.1002/anie.200701920.

7. Ward, J. W.; Lamport, Z. A.; Jurchescu, O. D., Versatile Organic Transistors by Solution Processing. *ChemPhysChem* **2015,** *16*, 1118-1132, https://doi.org/10.1002/cphc.201402757.

8. Avouris, P.; Chen, Z.; Perebeinos, V., Carbon-Based Electronics. *Nature Nanotechnology* **2007,** *2*, 605-615, https://doi.org/10.1038/nnano.2007.300.

9. Rao, R.; Pint, C. L.; Islam, A. E.; Weatherup, R. S.; Hofmann, S.; Meshot, E. R.; Wu, F.; Zhou, C.; Dee, N.; Amama, P. B.; Carpena-Nuñez, J.; Shi, W.; Plata, D. L.; Penev, E. S.; Yakobson, B. I.; Balbuena, P. B.; Bichara, C.; Futaba, D. N.; Noda, S.; Shin, H.; Kim, K. S.; Simard, B.; Mirri, F.; Pasquali, M.; Fornasiero, F.; Kauppinen, E. I.; Arnold, M.; Cola, B. A.; Nikolaev, P.; Arepalli, S.; Cheng, H.-M.; Zakharov, D. N.; Stach, E. A.; Zhang, J.; Wei, F.; Terrones, M.; Geohegan, D. B.; Maruyama, B.; Maruyama, S.; Li, Y.; Adams, W. W.; Hart, A. J., Carbon Nanotubes and Related Nanomaterials: Critical Advances and

Challenges for Synthesis toward Mainstream Commercial Applications. *ACS Nano* **2018,** *12*, 11756-11784, https://doi.org/10.1021/acsnano.8b06511.

10. Wang, H.; Wang, H. S.; Ma, C.; Chen, L.; Jiang, C.; Chen, C.; Xie, X.; Li, A.-P.; Wang, X., Graphene Nanoribbons for Quantum Electronics. *Nature Reviews Physics* **2021,** *3*, 791-802, https://doi.org/10.1038/s42254-021-00370-x.

11. Blackburn, J. L.; Ferguson, A. J.; Cho, C.; Grunlan, J. C., Carbon-Nanotube-Based Thermoelectric Materials and Devices. *Advanced Materials* **2018,** *30*, 1704386, https://doi.org/10.1002/adma.201704386.

12. Prakash, P.; Mohana Sundaram, K.; Anto Bennet, M., A Review on Carbon Nanotube Field Effect Transistors (CNTFETs) for Ultra-Low Power Applications. *Renewable and Sustainable Energy Reviews* **2018,** *89*, 194-203, https://doi.org/10.1016/j.rser.2018.03.021.

13. Gaviria Rojas, W. A.; Hersam, M. C., Chirality-Enriched Carbon Nanotubes for Next-Generation Computing. *Advanced Materials* **2020,** *32*, 1905654, https://doi.org/10.1002/adma.201905654.

14. Du, C.; Ren, Y.; Qu, Z.; Gao, L.; Zhai, Y.; Han, S.-T.; Zhou, Y., Synaptic Transistors and Neuromorphic Systems Based on Carbon Nano-Materials. *Nanoscale* **2021,** *13*, 7498-7522, https://doi.org/10.1039/D1NR00148E.

15. Yao, X.; Zhang, Y.; Jin, W.; Hu, Y.; Cui, Y., Carbon Nanotube Field-Effect Transistor-Based Chemical and Biological Sensors. *Sensors* **2021,** *21*, 995, https://doi.org/10.3390/s21030995.

16. Zahoor, F.; Hanif, M.; Isyaku Bature, U.; Bodapati, S.; Chattopadhyay, A.; Azmadi Hussin, F.; Abbas, H.; Merchant, F.; Bashir, F., Carbon Nanotube Field Effect Transistors: An Overview of Device Structure, Modeling, Fabrication and Applications. *Physica Scripta* **2023,** *98*, 082003, https://doi.org/10.1088/1402-4896/ace855.

17. Yahyazadeh, A.; Nanda, S.; Dalai, A. K., Carbon Nanotubes: A Review of Synthesis Methods and Applications. *Reactions* **2024,** *5*, 429-451, https://doi.org/10.3390/reactions5030022.

18. Fujigaya, T.; Nakashima, N., Non-Covalent Polymer Wrapping of Carbon Nanotubes and the Role of Wrapped Polymers as Functional Dispersants. *Science and Technology of Advanced Materials* **2015,** *16*, 024802, https://doi.org/10.1088/1468-6996/16/2/024802.

19. Wang, J.; Lei, T., Separation of Semiconducting Carbon Nanotubes Using Conjugated Polymer Wrapping. *Polymers* **2020,** *12*, 1548, https://doi.org/10.3390/polym12071548.

20. Graf, A.; Zakharko, Y.; Schießl, S. P.; Backes, C.; Pfohl, M.; Flavel, B. S.; Zaumseil, J., Large Scale, Selective Dispersion of Long Single-Walled Carbon Nanotubes with High Photoluminescence Quantum Yield by Shear Force Mixing. *Carbon* **2016,** *105*, 593-599, https://doi.org/10.1016/j.carbon.2016.05.002.

21. Liu, Y.; Zhao, Z.; Kang, L.; Qiu, S.; Li, Q., Molecular Doping Modulation and Applications of Structure-Sorted Single-Walled Carbon Nanotubes: A Review. *Small* **2024,** *20*, 2304075, https://doi.org/10.1002/smll.202304075.

22. Yoon, K.-Y.; Dong, G., Liquid-Phase Bottom-Up Synthesis of Graphene Nanoribbons. *Materials Chemistry Frontiers* **2020,** *4*, 29-45, https://doi.org/10.1039/C9QM00519F.

23. Houtsma, R. S. K.; de la Rie, J.; Stöhr, M., Atomically Precise Graphene Nanoribbons: Interplay of Structural and Electronic Properties. *Chemical Society Reviews* **2021,** *50*, 6541-6568, https://doi.org/10.1039/D0CS01541E.

24. Saraswat, V.; Jacobberger, R. M.; Arnold, M. S., Materials Science Challenges to Graphene Nanoribbon Electronics. *ACS Nano* **2021,** *15*, 3674-3708, https://doi.org/10.1021/acsnano.0c07835.

25. Novoselov, K. S.; Geim, A. K.; Morozov, S. V.; Jiang, D.; Zhang, Y.; Dubonos, S. V.; Grigorieva, I. V.; Firsov, A. A., Electric Field Effect in Atomically Thin Carbon Films. *Science* **2004,** *306*, 666-669, https://doi.org/10.1126/science.1102896.

26. Geim, A. K.; Novoselov, K. S., The Rise of Graphene. *Nature Materials* **2007,** *6*, 183-191, https://doi.org/10.1038/nmat1849.

27. Castro Neto, A. H.; Guinea, F.; Peres, N. M. R.; Novoselov, K. S.; Geim, A. K., The Electronic Properties of Graphene. *Reviews of Modern Physics* **2009,** *81*, 109-162, https://doi.org/10.1103/RevModPhys.81.109.

28. Papageorgiou, D. G.; Kinloch, I. A.; Young, R. J., Mechanical Properties of Graphene and Graphene-Based Nanocomposites. *Progress in Materials Science* **2017,** *90*, 75-127, https://doi.org/10.1016/j.pmatsci.2017.07.004.

29. Iijima, S., Helical Microtubules of Graphitic Carbon. *Nature* **1991,** *354*, 56-58, https://doi.org/10.1038/354056a0.

30. Dresselhaus, M. S.; Dresselhaus, G.; Saito, R., Physics of Carbon Nanotubes. *Carbon* **1995,** *33*, 883-891, https://doi.org/10.1016/0008-6223(95)00017-8.

31. Odom, T. W.; Huang, J.-L.; Kim, P.; Lieber, C. M., Structure and Electronic Properties of Carbon Nanotubes. *The Journal of Physical Chemistry B* **2000,** *104*, 2794-2809, https://doi.org/10.1021/jp993592k.

32. Charlier, J. C.; Blase, X.; Roche, S., Electronic and Transport Properties of Nanotubes. *Reviews of Modern Physics* **2007,** *79*, 677-732, https://doi.org/10.1103/RevModPhys.79.677.

33. Hayashi, T.; Kim, Y. A.; Matoba, T.; Esaka, M.; Nishimura, K.; Tsukada, T.; Endo, M.; Dresselhaus, M. S., Smallest Freestanding Single-Walled Carbon Nanotube. *Nano Letters* **2003,** *3*, 887-889, https://doi.org/10.1021/nl034080r.

34. Ma, J.; Wang, J. N.; Wang, X. X., Large-Diameter and Water-Dispersible Single-Walled Carbon Nanotubes: Synthesis, Characterization and Applications. *Journal of Materials Chemistry* **2009,** *19*, 3033-3041, https://doi.org/10.1039/B820088B.

35. Zhang, C.; Bets, K.; Lee, S. S.; Sun, Z.; Mirri, F.; Colvin, V. L.; Yakobson, B. I.; Tour, J. M.; Hauge, R. H., Closed-Edged Graphene Nanoribbons from Large-Diameter Collapsed Nanotubes. *ACS Nano* **2012,** *6*, 6023-6032, https://doi.org/10.1021/nn301039v.

36. Li, Y., Edge-Closed Graphene Nanoribbons Fabricated by Spontaneous Collapse of Few-Walled Carbon Nanotubes. *Physical Chemistry Chemical Physics* **2014,** *16*, 1921-1929, https://doi.org/10.1039/C3CP53785D.

37. Picheau, E.; Impellizzeri, A.; Rybkovskiy, D.; Bayle, M.; Mevellec, J.-Y.; Hof, F.; Saadaoui, H.; Noé, L.; Torres Dias, A. C.; Duvail, J.-L.; Monthioux, M.; Humbert, B.; Puech, P.; Ewels, C. P.; Pénicaud, A., Intense Raman D Band without Disorder in Flattened Carbon Nanotubes. *ACS Nano* **2021,** *15*, 596-603, https://.doi.org/10.1021/acsnano.0c06048.

38. Wei, X.; Tanaka, T.; Yomogida, Y.; Sato, N.; Saito, R.; Kataura, H., Experimental Determination of Excitonic Band Structures of Single-Walled Carbon Nanotubes Using Circular Dichroism Spectra. *Nature Communications* **2016,** *7*, 12899, https://doi.org/10.1038/ncomms12899.

39. Sato, N.; Tatsumi, Y.; Saito, R., Circular Dichroism of Single-Wall Carbon Nanotubes. *Physical Review B* **2017,** *95*, 155436, https://doi.org/10.1103/PhysRevB.95.155436.

40. Liu, B.; Wu, F.; Gui, H.; Zheng, M.; Zhou, C., Chirality-Controlled Synthesis and Applications of Single-Wall Carbon Nanotubes. *ACS Nano* **2017,** *11*, 31-53, https://doi.org/10.1021/acsnano.6b06900.

41. Guo, T.; Nikolaev, P.; Thess, A.; Colbert, D. T.; Smalley, R. E., Catalytic Growth of Single-Walled Nanotubes by Laser Vaporization. *Chemical Physics Letters* **1995,** *243*, 49-54, https://doi.org/10.1016/0009-2614(95)00825-O.

42. Ando, Y.; Zhao, X.; Hirahara, K.; Suenaga, K.; Bandow, S.; Iijima, S., Mass Production of Single-Wall Carbon Nanotubes by the Arc Plasma Jet Method. *Chemical Physics Letters* **2000,** *323*, 580-585, https://doi.org/10.1016/S0009-2614(00)00556-X.

43. Su Kim, K.; Cota-Sanchez, G.; Kingston, C. T.; Imris, M.; Simard, B.; Soucy, G., Large-Scale Production of Single-Walled Carbon Nanotubes by Induction Thermal Plasma. *Journal of Physics D: Applied Physics* **2007,** *40*, 2375, https://doi.org/10.1088/0022-3727/40/8/S17.

44. Prasek, J.; Drbohlavova, J.; Chomoucka, J.; Hubalek, J.; Jasek, O.; Adam, V.; Kizek, R., Methods for Carbon Nanotubes Synthesis—Review. *Journal of Materials Chemistry* **2011,** *21*, 15872-15884, https://doi.org/10.1039/C1JM12254A.

45. Nikolaev, P.; Bronikowski, M. J.; Bradley, R. K.; Rohmund, F.; Colbert, D. T.; Smith, K. A.; Smalley, R. E., Gas-Phase Catalytic Growth of Single-Walled Carbon Nanotubes from Carbon Monoxide. *Chemical Physics Letters* **1999,** *313*, 91-97, https://doi.org/10.1016/S0009-2614(99)01029-5.

46. Bronikowski, M. J.; Willis, P. A.; Colbert, D. T.; Smith, K. A.; Smalley, R. E., Gas-Phase Production of Carbon Single-Walled Nanotubes from Carbon Monoxide via the HiPco Process: A Parametric Study. *Journal of Vacuum Science & Technology A* **2001,** *19*, 1800-1805, https://doi.org/10.1116/1.1380721.

47. Kitiyanan, B.; Alvarez, W. E.; Harwell, J. H.; Resasco, D. E., Controlled Production of Single-Wall Carbon Nanotubes by Catalytic Decomposition of CO on Bimetallic Co–Mo

Catalysts. *Chemical Physics Letters* **2000,** *317*, 497-503, https://doi.org/10.1016/S0009-2614(99)01379-2.

48. Resasco, D. E.; Alvarez, W. E.; Pompeo, F.; Balzano, L.; Herrera, J. E.; Kitiyanan, B.; Borgna, A., A Scalable Process for Production of Single-walled Carbon Nanotubes (SWNTs) by Catalytic Disproportionation of CO on a Solid Catalyst. *Journal of Nanoparticle Research* **2002,** *4*, 131-136, https://doi.org/10.1023/A:1020174126542.

49. Bachilo, S. M.; Balzano, L.; Herrera, J. E.; Pompeo, F.; Resasco, D. E.; Weisman, R. B., Narrow (n,m)-Distribution of Single-Walled Carbon Nanotubes Grown Using a Solid Supported Catalyst. *Journal of the American Chemical Society* **2003,** *125*, 11186-11187, https://doi.org/10.1021/ja036622c.

50. Lolli, G.; Zhang, L.; Balzano, L.; Sakulchaicharoen, N.; Tan, Y.; Resasco, D. E., Tailoring (n,m) Structure of Single-Walled Carbon Nanotubes by Modifying Reaction Conditions and the Nature of the Support of CoMo Catalysts. *The Journal of Physical Chemistry B* **2006,** *110*, 2108-2115, https://doi.org/10.1021/jp056095e.

51. Thess, A.; Lee, R.; Nikolaev, P.; Dai, H.; Petit, P.; Robert, J.; Xu, C.; Lee, Y. H.; Kim, S. G.; Rinzler, A. G.; Colbert, D. T.; Scuseria, G. E.; Tománek, D.; Fischer, J. E.; Smalley, R. E., Crystalline Ropes of Metallic Carbon Nanotubes. *Science* **1996,** *273*, 483-487, https://doi.org/10.1126/science.273.5274.483.

52. Girifalco, L. A.; Hodak, M.; Lee, R. S., Carbon Nanotubes, Buckyballs, Ropes, and a Universal Graphitic Potential. *Physical Review B* **2000,** *62*, 13104-13110, https://doi.org/10.1103/PhysRevB.62.13104.

53. Vaisman, L.; Wagner, H. D.; Marom, G., The Role of Surfactants in Dispersion of Carbon Nanotubes. *Advances in Colloid and Interface Science* **2006,** *128-130*, 37-46, https://doi.org/10.1016/j.cis.2006.11.007.

54. Yu, H.; Hermann, S.; Schulz, S. E.; Gessner, T.; Dong, Z.; Li, W. J., Optimizing sonication parameters for dispersion of single-walled carbon nanotubes. *Chemical Physics* **2012,** *408*, 11-16, https://doi.org/10.1016/j.chemphys.2012.08.020.

55. Sesis, A.; Hodnett, M.; Memoli, G.; Wain, A. J.; Jurewicz, I.; Dalton, A. B.; Carey, J. D.; Hinds, G., Influence of Acoustic Cavitation on the Controlled Ultrasonic Dispersion of Carbon Nanotubes. *The Journal of Physical Chemistry B* **2013,** *117*, 15141-15150, https://doi.org/10.1021/jp410041y.

56. Wenseleers, W.; Vlasov, I. I.; Goovaerts, E.; Obraztsova, E. D.; Lobach, A. S.; Bouwen, A., Efficient Isolation and Solubilization of Pristine Single-Walled Nanotubes in Bile Salt Micelles. *Advanced Functional Materials* **2004,** *14*, 1105-1112, https://doi.org/10.1002/adfm.200400130.

57. Fitó-Parera, A.; López Carrillo, M. Á.; Tonye, M. E.; Erkens, M.; Cool, P.; Wenseleers, W.; Forel, S.; Cambré, S., Mild Opening Procedure to Obtain Open-Ended yet Long Single-Wall Carbon Nanotubes for Subsequent Filling. *Carbon Trends* **2025,** *18*, 100439, https://doi.org/10.1016/j.cartre.2024.100439.

58. Ham, H. T.; Choi, Y. S.; Chung, I. J., An Explanation of Dispersion States of Single-Walled Carbon Nanotubes in Solvents and Aqueous Surfactant Solutions Using Solubility Parameters. *Journal of Colloid and Interface Science* **2005,** *286*, 216-223, https://doi.org/10.1016/j.jcis.2005.01.002.

59. Bergin, S. D.; Sun, Z.; Rickard, D.; Streich, P. V.; Hamilton, J. P.; Coleman, J. N., Multicomponent Solubility Parameters for Single-Walled Carbon Nanotube−Solvent Mixtures. *ACS Nano* **2009,** *3*, 2340-2350, https://doi.org/10.1021/nn900493u.

60. Coleman, J. N., Liquid-Phase Exfoliation of Nanotubes and Graphene. *Advanced Functional Materials* **2009,** *19*, 3680-3695, https://doi.org/10.1002/adfm.200901640.

61. Lee, K. P.; Chromey, N. C.; Culik, R.; Barnes, J. R.; Schneider, P. W., Toxicity of N-methyl-2-pyrrolidone (NMP): Teratogenic, subchronic, and two-year inhalation studies. *Fundamental and Applied Toxicology* **1987,** *9*, 222-235, https://doi.org/10.1016/0272-0590(87)90045-5.

62. Kim, T. H.; Kim, S. G., Clinical Outcomes of Occupational Exposure to N,N-Dimethylformamide: Perspectives from Experimental Toxicology. *Safety and Health at Work* **2011,** *2*, 97-104, https://doi.org/10.5491/SHAW.2011.2.2.97.

63. Wang, J.; Lei, T., Enrichment of High-Purity Large-Diameter Semiconducting Single-Walled Carbon Nanotubes. *Nanoscale* **2022,** *14*, 1096-1106, https://doi.org/10.1039/D1NR06635H.

64. Pramanik, D.; Maiti, P. K., DNA-Assisted Dispersion of Carbon Nanotubes and Comparison with Other Dispersing Agents. *ACS Applied Materials & Interfaces* **2017,** *9*, 35287-35296, https://doi.org/10.1021/acsami.7b06751.

65. Yang, H.; Neal, L.; Flores, E. E.; Adronov, A.; Kim, N. Y., Role and Impact of Surfactants in Carbon Nanotube Dispersions and Sorting. *Journal of Surfactants and Detergents* **2023,** *26*, 607-622, https://doi.org/10.1002/jsde.12702.

66. Arnold, M. S.; Green, A. A.; Hulvat, J. F.; Stupp, S. I.; Hersam, M. C., Sorting Carbon Nanotubes by Electronic Structure Using Density Differentiation. *Nature Nanotechnology* **2006,** *1*, 60-65, https://doi.org/10.1038/nnano.2006.52.

67. Ghosh, S.; Bachilo, S. M.; Weisman, R. B., Advanced Sorting of Single-Walled Carbon Nanotubes by Nonlinear Density-Gradient Ultracentrifugation. *Nature Nanotechnology* **2010,** *5*, 443-450, https://doi.org/10.1038/nnano.2010.68.

68. Ihara, K.; Endoh, H.; Saito, T.; Nihey, F., Separation of Metallic and Semiconducting Single-Wall Carbon Nanotube Solution by Vertical Electric Field. *The Journal of Physical Chemistry C* **2011,** *115*, 22827-22832, https://doi.org/10.1021/jp2071474.

69. Tu, X.; Manohar, S.; Jagota, A.; Zheng, M., DNA Sequence Motifs for Structure-Specific Recognition and Separation of Carbon Nanotubes. *Nature* **2009,** *460*, 250-253, https://doi.org/10.1038/nature08116.

70. Liu, H.; Nishide, D.; Tanaka, T.; Kataura, H., Large-Scale Single-Chirality Separation of Single-Wall Carbon Nanotubes by Simple Gel Chromatography. *Nature Communications* **2011,** *2*, 309, https://doi.org/10.1038/ncomms1313.

71. Khripin, C. Y.; Fagan, J. A.; Zheng, M., Spontaneous Partition of Carbon Nanotubes in Polymer-Modified Aqueous Phases. *Journal of the American Chemical Society* **2013,** *135*, 6822-6825, https://doi.org/10.1021/ja402762e.

72. Fagan, J. A., Aqueous Two-Polymer Phase Extraction of Single-Wall Carbon Nanotubes Using Surfactants. *Nanoscale Advances* **2019,** *1*, 3307-3324, https://doi.org/10.1039/C9NA00280D.

73. Rice, N. A.; Adronov, A., Selective Interactions of a High-Molecular-Weight Polycarbazole with Different Commercial Nanotube Samples. *Journal of Polymer Science Part A: Polymer Chemistry* **2014,** *52*, 2738-2747, https://doi.org/10.1002/pola.27292.

74. Fong, D.; Adronov, A., Recent Developments in the Selective Dispersion of Single-Walled Carbon Nanotubes Using Conjugated Polymers. *Chemical Science* **2017,** *8*, 7292-7305, https://doi.org/10.1039/C7SC02942J.

75. Gao, W.; Xu, W.; Ye, J.; Liu, T.; Wang, J.; Tan, H.; Lin, Y.; Tange, M.; Sun, D.; Wu, L.; Okazaki, T.; Yang, Y.; Zhang, Z.; Zhao, J.; Cui, Z.; Ma, C.-Q., Selective Dispersion of Large-Diameter Semiconducting Carbon Nanotubes by Functionalized Conjugated Dendritic Oligothiophenes for Use in Printed Thin Film Transistors. *Advanced Functional Materials* **2017,** *27*, 1703938, https://doi.org/10.1002/adfm.201703938.

76. Gao, J.; Loi, M. A.; de Carvalho, E. J. F.; dos Santos, M. C., Selective Wrapping and Supramolecular Structures of Polyfluorene–Carbon Nanotube Hybrids. *ACS Nano* **2011,** *5*, 3993-3999, https://doi.org/10.1021/nn200564n.

77. Nish, A.; Hwang, J.-Y.; Doig, J.; Nicholas, R. J., Highly Selective Dispersion of Single-Walled Carbon Nanotubes Using Aromatic Polymers. *Nature Nanotechnology* **2007,** *2*, 640-646, https://doi.org/10.1038/nnano.2007.290.

78. Ozawa, H.; Ide, N.; Fujigaya, T.; Niidome, Y.; Nakashima, N., One-pot Separation of Highly Enriched (6,5)-Single-walled Carbon Nanotubes Using a Fluorene-based Copolymer. *Chemistry Letters* **2011,** *40*, 239-241, https://doi.org/10.1246/cl.2011.239.

79. Hwang, J.-Y.; Nish, A.; Doig, J.; Douven, S.; Chen, C.-W.; Chen, L.-C.; Nicholas, R. J., Polymer Structure and Solvent Effects on the Selective Dispersion of Single-Walled Carbon Nanotubes. *Journal of the American Chemical Society* **2008,** *130*, 3543-3553, https://doi.org/10.1021/ja0777640.

80. Wang, H.; Koleilat, G. I.; Liu, P.; Jiménez-Osés, G.; Lai, Y.-C.; Vosgueritchian, M.; Fang, Y.; Park, S.; Houk, K. N.; Bao, Z., High-Yield Sorting of Small-Diameter Carbon Nanotubes for Solar Cells and Transistors. *ACS Nano* **2014,** *8*, 2609-2617, https://doi.org/10.1021/nn406256y.

81. Stürzl, N.; Hennrich, F.; Lebedkin, S.; Kappes, M. M., Near Monochiral Single-Walled Carbon Nanotube Dispersions in Organic Solvents. *The Journal of Physical Chemistry C* **2009,** *113*, 14628-14632, https://doi.org/10.1021/jp902788y.

82. Tange, M.; Okazaki, T.; Iijima, S., Selective Extraction of Large-Diameter Single-Wall Carbon Nanotubes with Specific Chiral Indices by Poly(9,9-dioctylfluorene-alt-

benzothiadiazole). *Journal of the American Chemical Society* **2011,** *133*, 11908-11911, https://doi.org/10.1021/ja204698d.

83. Jakubka, F.; Schießl, S. P.; Martin, S.; Englert, J. M.; Hauke, F.; Hirsch, A.; Zaumseil, J., Effect of Polymer Molecular Weight and Solution Parameters on Selective Dispersion of Single-Walled Carbon Nanotubes. *ACS Macro Letters* **2012,** *1*, 815-819, https://doi.org/10.1021/mz300147g.

84. Mistry, K. S.; Larsen, B. A.; Blackburn, J. L., High-Yield Dispersions of Large-Diameter Semiconducting Single-Walled Carbon Nanotubes with Tunable Narrow Chirality Distributions. *ACS Nano* **2013,** *7*, 2231-2239, https://doi.org/10.1021/nn305336x.

85. Just, D.; Wasiak, T.; Dzienia, A.; Milowska, K. Z.; Mielańczyk, A.; Janas, D., Explicating Conjugated Polymer Extraction Used for the Differentiation of Single-Walled Carbon Nanotubes. *Nanoscale Horizons* **2024,** *9*, 2349-2359, https://doi.org/10.1039/D4NH00427B.

86. Wang, H.; Hsieh, B.; Jiménez-Osés, G.; Liu, P.; Tassone, C. J.; Diao, Y.; Lei, T.; Houk, K. N.; Bao, Z., Solvent Effects on Polymer Sorting of Carbon Nanotubes with Applications in Printed Electronics. *Small* **2015,** *11*, 126-133, https://doi.org/10.1002/smll.201401890.

87. Wang, H.; Bao, Z., Conjugated Polymer Sorting of Semiconducting Carbon Nanotubes and their Electronic Applications. *Nano Today* **2015,** *10*, 737-758, https://doi.org/10.1016/j.nantod.2015.11.008.

88. Lei, T.; Pochorovski, I.; Bao, Z., Separation of Semiconducting Carbon Nanotubes for Flexible and Stretchable Electronics Using Polymer Removable Method. *Accounts of Chemical Research* **2017,** *50*, 1096-1104, https://doi.org/10.1021/acs.accounts.7b00062.

89. Ding, J.; Li, Z.; Lefebvre, J.; Du, X.; Malenfant, P. R. L., Mechanistic Consideration of pH Effect on the Enrichment of Semiconducting SWCNTs by Conjugated Polymer Extraction. *The Journal of Physical Chemistry C* **2016,** *120*, 21946-21954, https://doi.org/10.1021/acs.jpcc.6b05965.

90. Brohmann, M.; Berger, F. J.; Matthiesen, M.; Schießl, S. P.; Schneider, S.; Zaumseil, J., Charge Transport in Mixed Semiconducting Carbon Nanotube Networks with Tailored Mixing Ratios. *ACS Nano* **2019,** *13*, 7323-7332, https://doi.org/10.1021/acsnano.9b03699.

91. Gomulya, W.; Costanzo, G. D.; de Carvalho, E. J. F.; Bisri, S. Z.; Derenskyi, V.; Fritsch, M.; Fröhlich, N.; Allard, S.; Gordiichuk, P.; Herrmann, A.; Marrink, S. J.; dos Santos, M. C.; Scherf, U.; Loi, M. A., Semiconducting Single-Walled Carbon Nanotubes on Demand by Polymer Wrapping. *Advanced Materials* **2013,** *25*, 2948-2956, https://doi.org/10.1002/adma.201300267.

92. Ding, J.; Li, Z.; Lefebvre, J.; Cheng, F.; Dubey, G.; Zou, S.; Finnie, P.; Hrdina, A.; Scoles, L.; Lopinski, G. P.; Kingston, C. T.; Simard, B.; Malenfant, P. R. L., Enrichment of Large-Diameter Semiconducting SWCNTs by Polyfluorene Extraction for High Network Density Thin Film Transistors. *Nanoscale* **2014,** *6*, 2328-2339, https://doi.org/10.1039/C3NR05511F.

93. Lee, H. W.; Yoon, Y.; Park, S.; Oh, J. H.; Hong, S.; Liyanage, L. S.; Wang, H.; Morishita, S.; Patil, N.; Park, Y. J.; Park, J. J.; Spakowitz, A.; Galli, G.; Gygi, F.; Wong, P. H. S.; Tok, J. B. H.; Kim, J. M.; Bao, Z., Selective Dispersion of High Purity Semiconducting Single-Walled Carbon Nanotubes with Regioregular Poly(3-alkylthiophene)s. *Nature Communications* **2011,** *2*, 541, https://doi.org/10.1038/ncomms1545.

94. Ozawa, H.; Fujigaya, T.; Niidome, Y.; Hotta, N.; Fujiki, M.; Nakashima, N., Rational Concept To Recognize/Extract Single-Walled Carbon Nanotubes with a Specific Chirality. *Journal of the American Chemical Society* **2011,** *133*, 2651-2657, https://doi.org/10.1021/ja109399f.

95. Lei, T.; Lai, Y.-C.; Hong, G.; Wang, H.; Hayoz, P.; Weitz, R. T.; Chen, C.; Dai, H.; Bao, Z., Diketopyrrolopyrrole (DPP)-Based Donor–Acceptor Polymers for Selective Dispersion of Large-Diameter Semiconducting Carbon Nanotubes. *Small* **2015,** *11*, 2946-2954, https://doi.org/10.1002/smll.201403761.

96. Rice, N. A.; Adronov, A., Supramolecular Interactions of High Molecular Weight Poly(2,7-carbazole)s with Single-Walled Carbon Nanotubes. *Macromolecules* **2013,** *46*, 3850-3860, https://doi.org/10.1021/ma400081d.

97. Berton, N.; Lemasson, F.; Hennrich, F.; Kappes, M. M.; Mayor, M., Influence of Molecular Weight on Selective Oligomer-Assisted Dispersion of Single-Walled Carbon Nanotubes and Subsequent Polymer Exchange. *Chemical Communications* **2012,** *48*, 2516-2518, https://doi.org/10.1039/C2CC17508H.

98. Rice, N. A.; Subrahmanyam, A. V.; Laengert, S. E.; Adronov, A., The Effect of Molecular Weight on the Separation of Semiconducting Single-Walled Carbon Nanotubes Using Poly(2,7-carbazole)s. *Journal of Polymer Science Part A: Polymer Chemistry* **2015,** *53*, 2510-2516, https://doi.org/10.1002/pola.27715.

99. Shea, M. J.; Mehlenbacher, R. D.; Zanni, M. T.; Arnold, M. S., Experimental Measurement of the Binding Configuration and Coverage of Chirality-Sorting Polyfluorenes on Carbon Nanotubes. *The Journal of Physical Chemistry Letters* **2014,** *5*, 3742-3749, https://doi.org/10.1021/jz5017813.

100. Ji, D.; Kim, S.; Han, M.; Jeon, S.; Lim, B.; Noh, Y.-Y., One-Step Sorting of Nearly Single-Chiral Carbon Nanotubes with (10,9) Chirality of 1.3 nm Diameter by Backbone Planarization of Polydioctylfluorenes. *Carbon* **2024,** *219*, 118791, https://doi.org/10.1016/j.carbon.2024.118791.

101. Gomulya, W.; Salazar Rios, J. M.; Derenskyi, V.; Bisri, S. Z.; Jung, S.; Fritsch, M.; Allard, S.; Scherf, U.; dos Santos, M. C.; Loi, M. A., Effect of Temperature on the Selection of Semiconducting Single Walled Carbon Nanotubes Using Poly(3-dodecylthiophene-2,5-diyl). *Carbon* **2015,** *84*, 66-73, https://doi.org/10.1016/j.carbon.2014.11.037.

102. Barman, S. N.; LeMieux, M. C.; Baek, J.; Rivera, R.; Bao, Z., Effects of Dispersion Conditions of Single-Walled Carbon Nanotubes on the Electrical Characteristics of Thin Film Network Transistors. *ACS Applied Materials & Interfaces* **2010,** *2*, 2672-2678, https://doi.org/10.1021/am1005223.

103. Yang, K.; Yi, Z.; Jing, Q.; Yue, R.; Jiang, W.; Lin, D., Sonication-Assisted Dispersion of Carbon Nanotubes in Aqueous Solutions of the Anionic Surfactant SDBS: The Role of Sonication Energy. *Chinese Science Bulletin* **2013,** *58*, 2082-2090, https://doi.org/10.1007/s11434-013-5697-2.

104. Koh, B.; Cheng, W., The Impact of Sonication on the Surface Quality of Single-Walled Carbon Nanotubes. *Journal of Pharmaceutical Sciences* **2015,** *104*, 2594-2599, https://doi.org/10.1002/jps.24483.

105. Wong, H.-S. P.; Akinwande, D., *Carbon Nanotube and Graphene Device Physics*. Cambridge University Press: Cambridge, 2010, https://doi.org/10.1017/CBO9780511778124.

106. Wilder, J. W. G.; Venema, L. C.; Rinzler, A. G.; Smalley, R. E.; Dekker, C., Electronic Structure of Atomically Resolved Carbon Nanotubes. *Nature* **1998,** *391*, 59-62, https://doi.org/10.1038/34139.

107. Weisman, R. B.; Bachilo, S. M., Dependence of Optical Transition Energies on Structure for Single-Walled Carbon Nanotubes in Aqueous Suspension: An Empirical Kataura Plot. *Nano Letters* **2003,** *3*, 1235-1238, https://doi.org/10.1021/nl034428i.

108. Amori, A. R.; Hou, Z.; Krauss, T. D., Excitons in Single-Walled Carbon Nanotubes and Their Dynamics. *Annual Review of Physical Chemistry* **2018,** *69*, 81-99, https://doi.org/10.1146/annurev-physchem-050317-014241.

109. Blancon, J.-C.; Paillet, M.; Tran, H. N.; Than, X. T.; Guebrou, S. A.; Ayari, A.; Miguel, A. S.; Phan, N.-M.; Zahab, A.-A.; Sauvajol, J.-L.; Fatti, N. D.; Vallée, F., Direct Measurement of the Absolute Absorption Spectrum of Individual Semiconducting Single-Wall Carbon Nanotubes. *Nature Communications* **2013,** *4*, 2542, https://doi.org/10.1038/ncomms3542.

110. Kane, C. L.; Mele, E. J., Ratio Problem in Single Carbon Nanotube Fluorescence Spectroscopy. *Physical Review Letters* **2003,** *90*, 207401, https://doi.org/10.1103/PhysRevLett.90.207401.

111. Plentz, F.; Ribeiro, H. B.; Jorio, A.; Strano, M. S.; Pimenta, M. A., Direct Experimental Evidence of Exciton-Phonon Bound States in Carbon Nanotubes. *Physical Review Letters* **2005,** *95*, 247401, https://doi.org/10.1103/PhysRevLett.95.247401.

112. Spataru, C. D.; Ismail-Beigi, S.; Benedict, L. X.; Louie, S. G., Excitonic Effects and Optical Spectra of Single-Walled Carbon Nanotubes. *Physical Review Letters* **2004,** *92*, 077402, https://doi.org/10.1103/PhysRevLett.92.077402.

113. Maultzsch, J.; Pomraenke, R.; Reich, S.; Chang, E.; Prezzi, D.; Ruini, A.; Molinari, E.; Strano, M. S.; Thomsen, C.; Lienau, C., Exciton Binding Energies in Carbon Nanotubes from Two-Photon Photoluminescence. *Physical Review B* **2005,** *72*, 241402, https://doi.org/10.1103/PhysRevB.72.241402.

114. Wang, F.; Dukovic, G.; Brus, L. E.; Heinz, T. F., The Optical Resonances in Carbon Nanotubes Arise from Excitons. *Science* **2005,** *308*, 838-841, https://doi.org/10.1126/science.1110265.

115. Dresselhaus, M. S.; Dresselhaus, G.; Saito, R.; Jorio, A., Exciton Photophysics of Carbon Nanotubes. *Annual Review of Physical Chemistry* **2007,** *58*, 719-747, https://doi.org/10.1146/annurev.physchem.58.032806.104628.

116. Avouris, P.; Freitag, M.; Perebeinos, V., Carbon-Nanotube Photonics and Optoelectronics. *Nature Photonics* **2008,** *2*, 341-350, https://doi.org/10.1038/nphoton.2008.94.

117. Mortimer, I. B.; Nicholas, R. J., Role of Bright and Dark Excitons in the Temperature-Dependent Photoluminescence of Carbon Nanotubes. *Physical Review Letters* **2007,** *98*, 027404, https://doi.org/10.1103/PhysRevLett.98.027404.

118. Blackburn, J. L.; Holt, J. M.; Irurzun, V. M.; Resasco, D. E.; Rumbles, G., Confirmation of K-Momentum Dark Exciton Vibronic Sidebands Using 13C-labeled, Highly Enriched (6,5) Single-walled Carbon Nanotubes. *Nano Letters* **2012,** *12*, 1398-1403, https://doi.org/10.1021/nl204072x.

119. Vora, P. M.; Tu, X.; Mele, E. J.; Zheng, M.; Kikkawa, J. M., Chirality Dependence of the K-Momentum Dark Excitons in Carbon Nanotubes. *Physical Review B* **2010,** *81*, 155123, https://doi.org/10.1103/PhysRevB.81.155123.

120. Harrah, D. M.; Schneck, J. R.; Green, A. A.; Hersam, M. C.; Ziegler, L. D.; Swan, A. K., Intensity-Dependent Exciton Dynamics of (6,5) Single-Walled Carbon Nanotubes: Momentum Selection Rules, Diffusion, and Nonlinear Interactions. *ACS Nano* **2011,** *5*, 9898-9906, https://doi.org/10.1021/nn203604v.

121. Jones, M.; Engtrakul, C.; Metzger, W. K.; Ellingson, R. J.; Nozik, A. J.; Heben, M. J.; Rumbles, G., Analysis of photoluminescence from solubilized single-walled carbon nanotubes. *Physical Review B* **2005,** *71*, 115426, https://doi.org/10.1103/PhysRevB.71.115426.

122. Kadria-Vili, Y.; Bachilo, S. M.; Blackburn, J. L.; Weisman, R. B., Photoluminescence Side Band Spectroscopy of Individual Single-Walled Carbon Nanotubes. *The Journal of Physical Chemistry C* **2016,** *120*, 23898-23904, https://doi.org/10.1021/acs.jpcc.6b08768.

123. Zorn, N. F.; Settele, S.; Zhao, S.; Lindenthal, S.; El Yumin, A. A.; Wedl, T.; Li, H.; Flavel, B. S.; Högele, A.; Zaumseil, J., Near-Intrinsic Photo- and Electroluminescence from Single-Walled Carbon Nanotube Thin Films on BCB-Passivated Surfaces. *Advanced Optical Materials* **2023,** *11*, 2300236, https://doi.org/10.1002/adom.202300236.

124. Amori, A. R.; Rossi, J. E.; Landi, B. J.; Krauss, T. D., Defects Enable Dark Exciton Photoluminescence in Single-Walled Carbon Nanotubes. *The Journal of Physical Chemistry C* **2018,** *122*, 3599-3607, https://doi.org/10.1021/acs.jpcc.7b10565.

125. Tumiel, T. M.; Amin, M.; Krauss, T. D., Single-Walled Carbon Nanotube Dark Exciton Photoluminescence Dynamics. *The Journal of Physical Chemistry C* **2021,** *125*, 25022-25029, https://doi.org/10.1021/acs.jpcc.1c05818.

126. Englman, R.; Jortner, J., The energy gap law for radiationless transitions in large molecules. *Molecular Physics* **1970,** *18*, 145-164, https://doi.org/10.1080/00268977000100171.

127. Zhao, H.; Mazumdar, S., Electron-Electron Interaction Effects on the Optical Excitations of Semiconducting Single-Walled Carbon Nanotubes. *Physical Review Letters* **2004,** *93*, 157402, https://doi.org/10.1103/PhysRevLett.93.157402.

128. Eckstein, K. H.; Kunkel, P.; Voelckel, M.; Schöppler, F.; Hertel, T., Trions, Exciton Dynamics, and Spectral Modifications in Doped Carbon Nanotubes: A Singular Defect-Driven Mechanism. *The Journal of Physical Chemistry C* **2023,** *127*, 19659-19667, https://doi.org/10.1021/acs.jpcc.3c04889.

129. Nalige, S. S.; Galonska, P.; Kelich, P.; Sistemich, L.; Herrmann, C.; Vukovic, L.; Kruss, S.; Havenith, M., Fluorescence Changes in Carbon Nanotube Sensors Correlate with THz Absorption of Hydration. *Nature Communications* **2024,** *15*, 6770, https://doi.org/10.1038/s41467-024-50968-9.

130. Hertel, T.; Himmelein, S.; Ackermann, T.; Stich, D.; Crochet, J., Diffusion Limited Photoluminescence Quantum Yields in 1-D Semiconductors: Single-Wall Carbon Nanotubes. *ACS Nano* **2010,** *4*, 7161-7168, https://doi.org/10.1021/nn101612b.

131. Birkmeier, K.; Hertel, T.; Hartschuh, A., Probing the Ultrafast Dynamics of Excitons in Single Semiconducting Carbon Nanotubes. *Nature Communications* **2022,** *13*, 6290, https://doi.org/10.1038/s41467-022-33941-2.

132. Cognet, L.; Tsyboulski, D. A.; Rocha, J.-D. R.; Doyle, C. D.; Tour, J. M.; Weisman, R. B., Stepwise Quenching of Exciton Fluorescence in Carbon Nanotubes by Single-Molecule Reactions. *Science* **2007,** *316*, 1465-1468, https://doi.org/10.1126/science.1141316.

133. Naumov, A. V.; Tsyboulski, D. A.; Bachilo, S. M.; Weisman, R. B., Length-dependent optical properties of single-walled carbon nanotube samples. *Chemical Physics* **2013,** *422*, 255-263, https://doi.org/10.1016/j.chemphys.2012.12.033.

134. Nakada, K.; Fujita, M.; Dresselhaus, G.; Dresselhaus, M. S., Edge State in Graphene Ribbons: Nanometer Size Effect and Edge Shape Dependence. *Physical Review B* **1996,** *54*, 17954-17961, https://doi.org/10.1103/PhysRevB.54.17954.

135. Han, M. Y.; Ozyilmaz, B.; Zhang, Y.; Kim, P., Energy Band-Gap Engineering of Graphene Nanoribbons. *Physical Review Letters* **2007,** *98*, 206805, https://doi.org/10.1103/PhysRevLett.98.206805.

136. Ci, L.; Xu, Z.; Wang, L.; Gao, W.; Ding, F.; Kelly, K. F.; Yakobson, B. I.; Ajayan, P. M., Controlled Nanocutting of Graphene. *Nano Research* **2008,** *1*, 116-122, https://doi.org/10.1007/s12274-008-8020-9.

137. Tapasztó, L.; Dobrik, G.; Lambin, P.; Biró, L. P., Tailoring the Atomic Structure of Graphene Nanoribbons by Scanning Tunnelling Microscope Lithography. *Nature Nanotechnology* **2008,** *3*, 397-401, https://doi.org/10.1038/nnano.2008.149.

138. Bai, J.; Duan, X.; Huang, Y., Rational Fabrication of Graphene Nanoribbons Using a Nanowire Etch Mask. *Nano Letters* **2009,** *9*, 2083-2087, https://doi.org/10.1021/nl900531n.

139. Yang, X.; Dou, X.; Rouhanipour, A.; Zhi, L.; Räder, H. J.; Müllen, K., Two-Dimensional Graphene Nanoribbons. *Journal of the American Chemical Society* **2008,** *130*, 4216-4217, https://doi.org/10.1021/ja710234t.

140. Yano, Y.; Mitoma, N.; Ito, H.; Itami, K., A Quest for Structurally Uniform Graphene Nanoribbons: Synthesis, Properties, and Applications. *The Journal of Organic Chemistry* **2020,** *85*, 4-33, https://doi.org/10.1021/acs.joc.9b02814.

141. Daigle, M.; Miao, D.; Lucotti, A.; Tommasini, M.; Morin, J.-F., Helically Coiled Graphene Nanoribbons. *Angewandte Chemie International Edition* **2017,** *56*, 6213-6217, https://doi.org/10.1002/anie.201611834.

142. Niu, W.; Ma, J.; Soltani, P.; Zheng, W.; Liu, F.; Popov, A. A.; Weigand, J. J.; Komber, H.; Poliani, E.; Casiraghi, C.; Droste, J.; Hansen, M. R.; Osella, S.; Beljonne, D.; Bonn, M.; Wang, H. I.; Feng, X.; Liu, J.; Mai, Y., A Curved Graphene Nanoribbon with Multi-Edge Structure and High Intrinsic Charge Carrier Mobility. *Journal of the American Chemical Society* **2020,** *142*, 18293-18298, https://doi.org/10.1021/jacs.0c07013.

143. Song, S.; Teng, Y.; Tang, W.; Xu, Z.; He, Y.; Ruan, J.; Kojima, T.; Hu, W.; Giessibl, F. J.; Sakaguchi, H.; Louie, S. G.; Lu, J., Janus Graphene Nanoribbons with Localized States on a Single Zigzag Edge. *Nature* **2025,** *637*, 580-586, https://doi.org/10.1038/s41586-024-08296-x.

144. Li, G.; Yoon, K.-Y.; Zhong, X.; Zhu, X.; Dong, G., Efficient Bottom-Up Preparation of Graphene Nanoribbons by Mild Suzuki–Miyaura Polymerization of Simple Triaryl Monomers. *Chemistry – A European Journal* **2016,** *22*, 9116-9120, https://doi.org/10.1002/chem.201602007.

145. Pun, S. H.; Delgado, A.; Dadich, C.; Cronin, A.; Fischer, F. R., Controlled Catalyst-Transfer Polymerization in Graphene Nanoribbon Synthesis. *Chem* **2024,** *10*, 675-685, https://doi.org/10.1016/j.chempr.2023.11.002.

146. Stampfer, C.; Güttinger, J.; Hellmüller, S.; Molitor, F.; Ensslin, K.; Ihn, T., Energy Gaps in Etched Graphene Nanoribbons. *Physical Review Letters* **2009,** *102*, 056403, https://doi.org/10.1103/PhysRevLett.102.056403.

147. Li, X.; Wang, X.; Zhang, L.; Lee, S.; Dai, H., Chemically Derived, Ultrasmooth Graphene Nanoribbon Semiconductors. *Science* **2008,** *319*, 1229-1232, https://doi.org/10.1126/science.1150878.

148. Jiao, L.; Zhang, L.; Wang, X.; Diankov, G.; Dai, H., Narrow Graphene Nanoribbons from Carbon Nanotubes. *Nature* **2009,** *458*, 877-880, https://doi.org/10.1038/nature07919.

149. Kosynkin, D. V.; Higginbotham, A. L.; Sinitskii, A.; Lomeda, J. R.; Dimiev, A.; Price, B. K.; Tour, J. M., Longitudinal Unzipping of Carbon Nanotubes to Form Graphene Nanoribbons. *Nature* **2009,** *458*, 872-876, https://doi.org/10.1038/nature07872.

150. Cai, J.; Ruffieux, P.; Jaafar, R.; Bieri, M.; Braun, T.; Blankenburg, S.; Muoth, M.; Seitsonen, A. P.; Saleh, M.; Feng, X.; Müllen, K.; Fasel, R., Atomically Precise Bottom-Up Fabrication of Graphene Nanoribbons. *Nature* **2010,** *466*, 470-473, https://doi.org/10.1038/nature09211.

151. Sakaguchi, H.; Kawagoe, Y.; Hirano, Y.; Iruka, T.; Yano, M.; Nakae, T., Width-Controlled Sub-Nanometer Graphene Nanoribbon Films Synthesized by Radical-Polymerized Chemical Vapor Deposition. *Advanced Materials* **2014,** *26*, 4134-4138, https://doi.org/10.1002/adma.201305034.

152. Jordan, Robert S.; Wang, Y.; McCurdy, Ryan D.; Yeung, Michael T.; Marsh, Kristofer L.; Khan, Saeed I.; Kaner, Richard B.; Rubin, Y., Synthesis of Graphene Nanoribbons

via the Topochemical Polymerization and Subsequent Aromatization of a Diacetylene Precursor. *Chem* **2016,** *1*, 78-90, https://doi.org/10.1016/j.chempr.2016.06.010.

153. Jordan, R. S.; Li, Y. L.; Lin, C.-W.; McCurdy, R. D.; Lin, J. B.; Brosmer, J. L.; Marsh, K. L.; Khan, S. I.; Houk, K. N.; Kaner, R. B.; Rubin, Y., Synthesis of N = 8 Armchair Graphene Nanoribbons from Four Distinct Polydiacetylenes. *Journal of the American Chemical Society* **2017,** *139*, 15878-15890, https://doi.org/10.1021/jacs.7b08800.

154. Fedotov, P. V.; Rybkovskiy, D. V.; Chernov, A. I.; Obraztsova, E. A.; Obraztsova, E. D., Excitonic Photoluminescence of Ultra-Narrow 7-Armchair Graphene Nanoribbons Grown by a New “Bottom-Up” Approach on a Ni Substrate under Low Vacuum. *The Journal of Physical Chemistry C* **2020,** *124*, 25984-25991, https://doi.org/10.1021/acs.jpcc.0c07369.

155. de Oteyza, D. G.; García-Lekue, A.; Vilas-Varela, M.; Merino-Díez, N.; Carbonell-Sanromà, E.; Corso, M.; Vasseur, G.; Rogero, C.; Guitián, E.; Pascual, J. I.; Ortega, J. E.; Wakayama, Y.; Peña, D., Substrate-Independent Growth of Atomically Precise Chiral Graphene Nanoribbons. *ACS Nano* **2016,** *10*, 9000-9008, https://doi.org/10.1021/acsnano.6b05269.

156. Hao, Z.; Zhang, H.; Ruan, Z.; Yan, C.; Lu, J.; Cai, J., Tuning the Electronic Properties of Atomically Precise Graphene Nanoribbons by Bottom-Up Fabrication. *ChemNanoMat* **2020,** *6*, 493-515, https://doi.org/10.1002/cnma.201900706.

157. Kolmer, M.; Steiner, A.-K.; Izydorczyk, I.; Ko, W.; Engelund, M.; Szymonski, M.; Li, A.-P.; Amsharov, K., Rational Synthesis of Atomically Precise Graphene Nanoribbons Directly on Metal Oxide Surfaces. *Science* **2020,** *369*, 571-575, https://doi.org/10.1126/science.abb8880.

158. Mutlu, Z.; Llinas, J. P.; Jacobse, P. H.; Piskun, I.; Blackwell, R.; Crommie, M. F.; Fischer, F. R.; Bokor, J., Transfer-Free Synthesis of Atomically Precise Graphene Nanoribbons on Insulating Substrates. *ACS Nano* **2021,** *15*, 2635-2642, https://doi.org/10.1021/acsnano.0c07591.

159. Ruffieux, P.; Wang, S.; Yang, B.; Sánchez-Sánchez, C.; Liu, J.; Dienel, T.; Talirz, L.; Shinde, P.; Pignedoli, C. A.; Passerone, D.; Dumslaff, T.; Feng, X.; Müllen, K.; Fasel, R., On-Surface Synthesis of Graphene Nanoribbons with Zigzag Edge Topology. *Nature* **2016,** *531*, 489-492, https://doi.org/10.1038/nature17151.

160. Denk, R.; Hohage, M.; Zeppenfeld, P.; Cai, J.; Pignedoli, C. A.; Söde, H.; Fasel, R.; Feng, X.; Müllen, K.; Wang, S.; Prezzi, D.; Ferretti, A.; Ruini, A.; Molinari, E.; Ruffieux, P., Exciton-Dominated Optical Response of Ultra-Narrow Graphene Nanoribbons. *Nature Communications* **2014,** *5*, 4253, https://doi.org/10.1038/ncomms5253.

161. Merino-Díez, N.; Garcia-Lekue, A.; Carbonell-Sanromà, E.; Li, J.; Corso, M.; Colazzo, L.; Sedona, F.; Sánchez-Portal, D.; Pascual, J. I.; de Oteyza, D. G., Width-Dependent Band Gap in Armchair Graphene Nanoribbons Reveals Fermi Level Pinning on Au(111). *ACS Nano* **2017,** *11*, 11661-11668, https://doi.org/10.1021/acsnano.7b06765.

162. Pham, T. A.; Tran, B. V.; Nguyen, M.-T.; Stöhr, M., Chiral-Selective Formation of 1D Polymers Based on Ullmann-Type Coupling: The Role of the Metallic Substrate. *Small* **2017,** *13*, 1603675, https://doi.org/10.1002/smll.201603675.

163. Teeter, J. D.; Zahl, P.; Mehdi Pour, M.; Costa, P. S.; Enders, A.; Sinitskii, A., On-Surface Synthesis and Spectroscopic Characterization of Laterally Extended Chevron Graphene Nanoribbons. *ChemPhysChem* **2019,** *20*, 2281-2285, https://doi.org/10.1002/cphc.201900445.

164. Liu, J.; Li, B.-W.; Tan, Y.-Z.; Giannakopoulos, A.; Sanchez-Sanchez, C.; Beljonne, D.; Ruffieux, P.; Fasel, R.; Feng, X.; Müllen, K., Toward Cove-Edged Low Band Gap Graphene Nanoribbons. *Journal of the American Chemical Society* **2015,** *137*, 6097-6103, https://doi.org/10.1021/jacs.5b03017.

165. Fairbrother, A.; Sanchez-Valencia, J.-R.; Lauber, B.; Shorubalko, I.; Ruffieux, P.; Hintermann, T.; Fasel, R., High Vacuum Synthesis and Ambient Stability of Bottom-Up Graphene Nanoribbons. *Nanoscale* **2017,** *9*, 2785-2792, https://doi.org/10.1039/C6NR08975E.

166. Senkovskiy, B. V.; Pfeiffer, M.; Alavi, S. K.; Bliesener, A.; Zhu, J.; Michel, S.; Fedorov, A. V.; German, R.; Hertel, D.; Haberer, D.; Petaccia, L.; Fischer, F. R.; Meerholz, K.; van Loosdrecht, P. H. M.; Lindfors, K.; Grüneis, A., Making Graphene Nanoribbons Photoluminescent. *Nano Letters* **2017,** *17*, 4029-4037, https://doi.org/10.1021/acs.nanolett.7b00147.

167. Zhao, S.; Borin Barin, G.; Rondin, L.; Raynaud, C.; Fairbrother, A.; Dumslaff, T.; Campidelli, S.; Müllen, K.; Narita, A.; Voisin, C.; Ruffieux, P.; Fasel, R.; Lauret, J.-S., Optical Investigation of On-Surface Synthesized Armchair Graphene Nanoribbons. *physica status solidi (b)* **2017,** *254*, 1700223, https://doi.org/10.1002/pssb.201700223.

168. Passi, V.; Gahoi, A.; Senkovskiy, B. V.; Haberer, D.; Fischer, F. R.; Grüneis, A.; Lemme, M. C., Field-Effect Transistors Based on Networks of Highly Aligned, Chemically Synthesized N = 7 Armchair Graphene Nanoribbons. *ACS Applied Materials & Interfaces* **2018,** *10*, 9900-9903, https://doi.org/10.1021/acsami.8b01116.

169. Li, G.; Yoon, K.-Y.; Zhong, X.; Wang, J.; Zhang, R.; Guest, J. R.; Wen, J.; Zhu, X. Y.; Dong, G., A Modular Synthetic Approach for Band-Gap Engineering of Armchair Graphene Nanoribbons. *Nature Communications* **2018,** *9*, 1687, https://doi.org/10.1038/s41467-018-03747-2.

170. Narita, A.; Feng, X.; Hernandez, Y.; Jensen, S. A.; Bonn, M.; Yang, H.; Verzhbitskiy, I. A.; Casiraghi, C.; Hansen, M. R.; Koch, A. H. R.; Fytas, G.; Ivasenko, O.; Li, B.; Mali, K. S.; Balandina, T.; Mahesh, S.; De Feyter, S.; Müllen, K., Synthesis of Structurally Well-Defined and Liquid-Phase-Processable Graphene Nanoribbons. *Nature Chemistry* **2014,** *6*, 126-132, https://doi.org/10.1038/nchem.1819.

171. Huang, Y.; Mai, Y.; Beser, U.; Teyssandier, J.; Velpula, G.; van Gorp, H.; Straasø, L. A.; Hansen, M. R.; Rizzo, D.; Casiraghi, C.; Yang, R.; Zhang, G.; Wu, D.; Zhang, F.; Yan, D.; De Feyter, S.; Müllen, K.; Feng, X., Poly(ethylene oxide) Functionalized Graphene Nanoribbons with Excellent Solution Processability. *Journal of the American Chemical Society* **2016,** *138*, 10136-10139, https://doi.org/10.1021/jacs.6b07061.

172. Huang, Y.; Xu, F.; Ganzer, L.; Camargo, F. V. A.; Nagahara, T.; Teyssandier, J.; Van Gorp, H.; Basse, K.; Straasø, L. A.; Nagyte, V.; Casiraghi, C.; Hansen, M. R.; De Feyter, S.; Yan, D.; Müllen, K.; Feng, X.; Cerullo, G.; Mai, Y., Intrinsic Properties of Single Graphene Nanoribbons in Solution: Synthetic and Spectroscopic Studies. *Journal of the American Chemical Society* **2018,** *140*, 10416-10420, https://doi.org/10.1021/jacs.8b06028.

173. Niu, W.; Sopp, S.; Lodi, A.; Gee, A.; Kong, F.; Pei, T.; Gehring, P.; Nägele, J.; Lau, C. S.; Ma, J.; Liu, J.; Narita, A.; Mol, J.; Burghard, M.; Müllen, K.; Mai, Y.; Feng, X.; Bogani, L., Exceptionally Clean Single-Electron Transistors from Solutions of Molecular Graphene Nanoribbons. *Nature Materials* **2023,** *22*, 180-185, https://doi.org/10.1038/s41563-022-01460-6.

174. Hu, Y.; Xie, P.; De Corato, M.; Ruini, A.; Zhao, S.; Meggendorfer, F.; Straasø, L. A.; Rondin, L.; Simon, P.; Li, J.; Finley, J. J.; Hansen, M. R.; Lauret, J.-S.; Molinari, E.; Feng, X.; Barth, J. V.; Palma, C.-A.; Prezzi, D.; Müllen, K.; Narita, A., Bandgap Engineering of Graphene Nanoribbons by Control over Structural Distortion. *Journal of the American Chemical Society* **2018,** *140*, 7803-7809, https://doi.org/10.1021/jacs.8b02209.

175. Yao, X.; Zheng, W.; Osella, S.; Qiu, Z.; Fu, S.; Schollmeyer, D.; Müller, B.; Beljonne, D.; Bonn, M.; Wang, H. I.; Müllen, K.; Narita, A., Synthesis of Nonplanar Graphene Nanoribbon with Fjord Edges. *Journal of the American Chemical Society* **2021,** *143*, 5654-5658, https://doi.org/10.1021/jacs.1c01882.

176. Jassas, R. S.; Mughal, E. U.; Sadiq, A.; Alsantali, R. I.; Al-Rooqi, M. M.; Naeem, N.; Moussa, Z.; Ahmed, S. A., Scholl Reaction as a Powerful Tool for the Synthesis of Nanographenes: a Systematic Review. *RSC Advances* **2021,** *11*, 32158-32202, https://doi.org/10.1039/D1RA05910F.

177. McCurdy, R. D.; Jacobse, P. H.; Piskun, I.; Veber, G. C.; Rizzo, D. J.; Zuzak, R.; Mutlu, Z.; Bokor, J.; Crommie, M. F.; Fischer, F. R., Synergetic Bottom-Up Synthesis of Graphene Nanoribbons by Matrix-Assisted Direct Transfer. *Journal of the American Chemical Society* **2021,** *143*, 4174-4178, https://doi.org/10.1021/jacs.1c01355.

178. Wakabayashi, K.; Fujita, M.; Ajiki, H.; Sigrist, M., Electronic and Magnetic Properties of Nanographite Ribbons. *Physical Review B* **1999,** *59*, 8271-8282, https://doi.org/10.1103/PhysRevB.59.8271.

179. Kawai, T.; Miyamoto, Y.; Sugino, O.; Koga, Y., Graphitic Ribbons without Hydrogen-Termination: Electronic Structures and Stabilities. *Physical Review B* **2000,** *62*, R16349-R16352, https://doi.org/10.1103/PhysRevB.62.R16349.

180. Brey, L.; Fertig, H. A., Electronic States of Graphene Nanoribbons Studied with the Dirac Equation. *Physical Review B* **2006,** *73*, 235411, https://doi.org/10.1103/PhysRevB.73.235411.

181. Wakabayashi, K.; Sasaki, K.-i.; Nakanishi, T.; Enoki, T., Electronic States of Graphene Nanoribbons and Analytical Solutions. *Science and Technology of Advanced Materials* **2010,** *11*, 054504, https://doi.org/10.1088/1468-6996/11/5/054504.

182. Sasaki, K.-i.; Kato, K.; Tokura, Y.; Oguri, K.; Sogawa, T., Theory of Optical Transitions in Graphene Nanoribbons. *Physical Review B* **2011,** *84*, 085458, https://doi.org/10.1103/PhysRevB.84.085458.

183. Son, Y.-W.; Cohen, M. L.; Louie, S. G., Energy Gaps in Graphene Nanoribbons. *Physical Review Letters* **2006,** *97*, 216803, https://doi.org/10.1103/PhysRevLett.97.216803.

184. Merino-Díez, N.; Lobo-Checa, J.; Nita, P.; Garcia-Lekue, A.; Basagni, A.; Vasseur, G.; Tiso, F.; Sedona, F.; Das, P. K.; Fujii, J.; Vobornik, I.; Sambi, M.; Pascual, J. I.; Ortega, J. E.; de Oteyza, D. G., Switching from Reactant to Substrate Engineering in the Selective Synthesis of Graphene Nanoribbons. *The Journal of Physical Chemistry Letters* **2018,** *9*, 2510-2517, https://doi.org/10.1021/acs.jpclett.8b00796.

185. Lawrence, J.; Brandimarte, P.; Berdonces-Layunta, A.; Mohammed, M. S. G.; Grewal, A.; Leon, C. C.; Sánchez-Portal, D.; de Oteyza, D. G., Probing the Magnetism of Topological End States in 5-Armchair Graphene Nanoribbons. *ACS Nano* **2020,** *14*, 4499-4508, https://doi.org/10.1021/acsnano.9b10191.

186. Deniz, O.; Sánchez-Sánchez, C.; Dumslaff, T.; Feng, X.; Narita, A.; Müllen, K.; Kharche, N.; Meunier, V.; Fasel, R.; Ruffieux, P., Revealing the Electronic Structure of Silicon Intercalated Armchair Graphene Nanoribbons by Scanning Tunneling Spectroscopy. *Nano Letters* **2017,** *17*, 2197-2203, https://doi.org/10.1021/acs.nanolett.6b04727.

187. Talirz, L.; Söde, H.; Kawai, S.; Ruffieux, P.; Meyer, E.; Feng, X.; Müllen, K.; Fasel, R.; Pignedoli, C. A.; Passerone, D., Band Gap of Atomically Precise Graphene Nanoribbons as a Function of Ribbon Length and Termination. *ChemPhysChem* **2019,** *20*, 2348-2353, https://doi.org/10.1002/cphc.201900313.

188. Que, Y.; Liu, B.; Zhuang, Y.; Xu, C.; Wang, K.; Xiao, X., On-Surface Synthesis of Graphene Nanoribbons on Two-Dimensional Rare Earth–Gold Intermetallic Compounds. *The Journal of Physical Chemistry Letters* **2020,** *11*, 5044-5050, https://doi.org/10.1021/acs.jpclett.0c01398.

189. Sun, K.; Ji, P.; Zhang, J.; Wang, J.; Li, X.; Xu, X.; Zhang, H.; Chi, L., On-Surface Synthesis of 8- and 10-Armchair Graphene Nanoribbons. *Small* **2019,** *15*, 1804526, https://doi.org/10.1002/smll.201804526.

190. Talirz, L.; Söde, H.; Dumslaff, T.; Wang, S.; Sanchez-Valencia, J. R.; Liu, J.; Shinde, P.; Pignedoli, C. A.; Liang, L.; Meunier, V.; Plumb, N. C.; Shi, M.; Feng, X.; Narita, A.; Müllen, K.; Fasel, R.; Ruffieux, P., On-Surface Synthesis and Characterization of 9-Atom Wide Armchair Graphene Nanoribbons. *ACS Nano* **2017,** *11*, 1380-1388, https://doi.org/10.1021/acsnano.6b06405.

191. Chen, Y.-C.; de Oteyza, D. G.; Pedramrazi, Z.; Chen, C.; Fischer, F. R.; Crommie, M. F., Tuning the Band Gap of Graphene Nanoribbons Synthesized from Molecular Precursors. *ACS Nano* **2013,** *7*, 6123-6128, https://doi.org/10.1021/nn401948e.

192. Yamaguchi, J.; Hayashi, H.; Jippo, H.; Shiotari, A.; Ohtomo, M.; Sakakura, M.; Hieda, N.; Aratani, N.; Ohfuchi, M.; Sugimoto, Y.; Yamada, H.; Sato, S., Small Bandgap in Atomically Precise 17-Atom-Wide Armchair-Edged Graphene Nanoribbons. *Communications Materials* **2020,** *1*, 36, https://doi.org/10.1038/s43246-020-0039-9.

193. Zhang, H.; Lin, H.; Sun, K.; Chen, L.; Zagranyarski, Y.; Aghdassi, N.; Duhm, S.; Li, Q.; Zhong, D.; Li, Y.; Müllen, K.; Fuchs, H.; Chi, L., On-Surface Synthesis of Rylene-Type Graphene Nanoribbons. *Journal of the American Chemical Society* **2015,** *137*, 4022-4025, https://doi.org/10.1021/ja511995r.

194. Cervantes-Sodi, F.; Csányi, G.; Piscanec, S.; Ferrari, A. C., Edge-Functionalized and Substitutionally Doped Graphene Nanoribbons: Electronic and Spin Properties. *Physical Review B* **2008,** *77*, 165427, https://doi.org/10.1103/PhysRevB.77.165427.

195. Li, T. C.; Lu, S.-P., Quantum Conductance of Graphene Nanoribbons with Edge Defects. *Physical Review B* **2008,** *77*, 085408, https://doi.org/10.1103/PhysRevB.77.085408.

196. Gröning, O.; Wang, S.; Yao, X.; Pignedoli, C. A.; Borin Barin, G.; Daniels, C.; Cupo, A.; Meunier, V.; Feng, X.; Narita, A.; Müllen, K.; Ruffieux, P.; Fasel, R., Engineering of Robust Topological Quantum Phases in Graphene Nanoribbons. *Nature* **2018,** *560*, 209-213, https://doi.org/10.1038/s41586-018-0375-9.

197. Wang, S.; Talirz, L.; Pignedoli, C. A.; Feng, X.; Müllen, K.; Fasel, R.; Ruffieux, P., Giant Edge State Splitting at Atomically Precise Graphene Zigzag Edges. *Nature Communications* **2016,** *7*, 11507, https://doi.org/10.1038/ncomms11507.

198. Gundra, K.; Shukla, A., Theory of the Electro-Optical Properties of Graphene Nanoribbons. *Physical Review B* **2011,** *83*, 075413, https://doi.org/10.1103/PhysRevB.83.075413.

199. Yang, L.; Cohen, M. L.; Louie, S. G., Excitonic Effects in the Optical Spectra of Graphene Nanoribbons. *Nano Letters* **2007,** *7*, 3112-3115, https://doi.org/10.1021/nl0716404.

200. Yang, L.; Park, C.-H.; Son, Y.-W.; Cohen, M. L.; Louie, S. G., Quasiparticle Energies and Band Gaps in Graphene Nanoribbons. *Physical Review Letters* **2007,** *99*, 186801, https://doi.org/10.1103/PhysRevLett.99.186801.

201. Prezzi, D.; Varsano, D.; Ruini, A.; Marini, A.; Molinari, E., Optical Properties of Graphene Nanoribbons: The Role of Many-Body Effects. *Physical Review B* **2008,** *77*, 041404, https://doi.org/10.1103/PhysRevB.77.041404.

202. Soavi, G.; Dal Conte, S.; Manzoni, C.; Viola, D.; Narita, A.; Hu, Y.; Feng, X.; Hohenester, U.; Molinari, E.; Prezzi, D.; Müllen, K.; Cerullo, G., Exciton–Exciton Annihilation and Biexciton Stimulated Emission in Graphene Nanoribbons. *Nature Communications* **2016,** *7*, 11010, https://doi.org/10.1038/ncomms11010.

203. Pfeiffer, M.; Senkovskiy, B. V.; Haberer, D.; Fischer, F. R.; Yang, F.; Meerholz, K.; Ando, Y.; Grüneis, A.; Lindfors, K., Observation of Room-Temperature Photoluminescence Blinking in Armchair-Edge Graphene Nanoribbons. *Nano Letters* **2018,** *18*, 7038-7044, https://doi.org/10.1021/acs.nanolett.8b03006.

204. Tries, A.; Osella, S.; Zhang, P.; Xu, F.; Ramanan, C.; Kläui, M.; Mai, Y.; Beljonne, D.; Wang, H. I., Experimental Observation of Strong Exciton Effects in Graphene Nanoribbons. *Nano Letters* **2020,** *20*, 2993-3002, https://doi.org/10.1021/acs.nanolett.9b04816.

205. Chong, M. C.; Afshar-Imani, N.; Scheurer, F.; Cardoso, C.; Ferretti, A.; Prezzi, D.; Schull, G., Bright Electroluminescence from Single Graphene Nanoribbon Junctions. *Nano Letters* **2018,** *18*, 175-181, https://doi.org/10.1021/acs.nanolett.7b03797.

206. Ma, C.; Xiao, Z.; Puretzky, A. A.; Wang, H.; Mohsin, A.; Huang, J.; Liang, L.; Luo, Y.; Lawrie, B. J.; Gu, G.; Lu, W.; Hong, K.; Bernholc, J.; Li, A.-P., Engineering Edge States

of Graphene Nanoribbons for Narrow-Band Photoluminescence. *ACS Nano* **2020,** *14*, 5090-5098, https://doi.org/10.1021/acsnano.0c01737.

207. Jiang, S.; Neuman, T.; Boeglin, A.; Scheurer, F.; Schull, G., Topologically Localized Excitons in Single Graphene Nanoribbons. *Science* **2023,** *379*, 1049-1054, https://doi.org/10.1126/science.abq6948.

208. Zhu, X.; Su, H., Excitons of Edge and Surface Functionalized Graphene Nanoribbons. *The Journal of Physical Chemistry C* **2010,** *114*, 17257-17262, https://doi.org/10.1021/jp102341b.

209. Zhao, S.; Rondin, L.; Delport, G.; Voisin, C.; Beser, U.; Hu, Y.; Feng, X.; Müllen, K.; Narita, A.; Campidelli, S.; Lauret, J. S., Fluorescence from Graphene Nanoribbons of Well-Defined Structure. *Carbon* **2017,** *119*, 235-240, https://doi.org/10.1016/j.carbon.2017.04.043.

210. Lu, G.; Blakesley, J.; Himmelberger, S.; Pingel, P.; Frisch, J.; Lieberwirth, I.; Salzmann, I.; Oehzelt, M.; Di Pietro, R.; Salleo, A.; Koch, N.; Neher, D., Moderate Doping Leads to High Performance of Semiconductor/Insulator Polymer Blend Transistors. *Nature Communications* **2013,** *4*, 1588, https://doi.org/10.1038/ncomms2587.

211. Paterson, A. F.; Treat, N. D.; Zhang, W.; Fei, Z.; Wyatt-Moon, G.; Faber, H.; Vourlias, G.; Patsalas, P. A.; Solomeshch, O.; Tessler, N.; Heeney, M.; Anthopoulos, T. D., Small Molecule/Polymer Blend Organic Transistors with Hole Mobility Exceeding 13 cm2 V−1 s−1. *Advanced Materials* **2016,** *28*, 7791-7798, https://doi.org/10.1002/adma.201601075.

212. Walzer, K.; Maennig, B.; Pfeiffer, M.; Leo, K., Highly Efficient Organic Devices Based on Electrically Doped Transport Layers. *Chemical Reviews* **2007,** *107*, 1233-1271, https://doi.org/10.1021/cr050156n.

213. Yu, J.; Zheng, Y.; Huang, J., Towards High Performance Organic Photovoltaic Cells: A Review of Recent Development in Organic Photovoltaics. *Polymers* **2014,** *6*, 2473-2509, https://doi.org/10.3390/polym6092473.

214. Brus, V. V.; Lee, J.; Luginbuhl, B. R.; Ko, S.-J.; Bazan, G. C.; Nguyen, T.-Q., Solution-Processed Semitransparent Organic Photovoltaics: From Molecular Design to Device Performance. *Advanced Materials* **2019,** *31*, 1900904, https://doi.org/10.1002/adma.201900904.

215. Xiong, Q.; Han, G.; Wang, G.; Lu, X.; Zhou, X., The Doping Strategies for Modulation of Transport Properties in Thermoelectric Materials. *Advanced Functional Materials* **2024,** *34*, 2411304, https://doi.org/10.1002/adfm.202411304.

216. Lüssem, B.; Keum, C.-M.; Kasemann, D.; Naab, B.; Bao, Z.; Leo, K., Doped Organic Transistors. *Chemical Reviews* **2016,** *116*, 13714-13751, https://doi.org/10.1021/acs.chemrev.6b00329.

217. Jacobs, I. E.; Moulé, A. J., Controlling Molecular Doping in Organic Semiconductors. *Advanced Materials* **2017,** *29*, 1703063, https://doi.org/10.1002/adma.201703063.

218. Salzmann, I.; Heimel, G.; Oehzelt, M.; Winkler, S.; Koch, N., Molecular Electrical Doping of Organic Semiconductors: Fundamental Mechanisms and Emerging Dopant Design Rules. *Accounts of Chemical Research* **2016,** *49*, 370-378, https://doi.org/10.1021/acs.accounts.5b00438.

219. Arias, A. C.; MacKenzie, J. D.; McCulloch, I.; Rivnay, J.; Salleo, A., Materials and Applications for Large Area Electronics: Solution-Based Approaches. *Chemical Reviews* **2010,** *110*, 3-24, https://doi.org/10.1021/cr900150b.

220. Li, J.; Zhang, G.; Holm, D. M.; Jacobs, I. E.; Yin, B.; Stroeve, P.; Mascal, M.; Moulé, A. J., Introducing Solubility Control for Improved Organic P-Type Dopants. *Chemistry of Materials* **2015,** *27*, 5765-5774, https://doi.org/10.1021/acs.chemmater.5b02340.

221. Kumar, J.; Singh, R. K.; Singh, R.; Rastogi, R. C.; Kumar, V., Effect of $FeCl_3$ on the Stability of π-Conjugation of Electronic Polymer. *Corrosion Science* **2008,** *50*, 301-308, https://doi.org/10.1016/j.corsci.2007.11.014.

222. Hawkey, A.; Dash, A.; Rodríguez-Martínez, X.; Zhao, Z.; Champ, A.; Lindenthal, S.; Zharnikov, M.; Kemerink, M.; Zaumseil, J., Ion-Exchange Doping of Semiconducting Single-Walled Carbon Nanotubes. *Advanced Materials* **2024,** *36*, 2404554, https://doi.org/10.1002/adma.202404554.

223. Jha, M.; Mogollon Santiana, J.; Jacob, A. A.; Light, K.; Hong, M. L.; Lau, M. R.; Filardi, L. R.; Miao, H.; Gurses, S. M.; Kronawitter, C. X.; Mascal, M.; Moulé, A. J., Stability Study of Molecularly Doped Semiconducting Polymers. *The Journal of Physical Chemistry C* **2024,** *128*, 1258-1266, https://doi.org/10.1021/acs.jpcc.3c06044.

224. Matsunaga, R.; Matsuda, K.; Kanemitsu, Y., Observation of Charged Excitons in Hole-Doped Carbon Nanotubes Using Photoluminescence and Absorption Spectroscopy. *Physical Review Letters* **2011,** *106*, 037404, https://doi.org/10.1103/PhysRevLett.106.037404.

225. Lüssem, B.; Riede, M.; Leo, K., Doping of Organic Semiconductors. *physica status solidi (a)* **2013,** *210*, 9-43, https://doi.org/10.1002/pssa.201228310.

226. Murrey, T. L.; Aubry, T. J.; Ruiz, O. L.; Thurman, K. A.; Eckstein, K. H.; Doud, E. A.; Stauber, J. M.; Spokoyny, A. M.; Schwartz, B. J.; Hertel, T.; Blackburn, J. L.; Ferguson, A. J., Tuning Counterion Chemistry to Reduce Carrier Localization in Doped Semiconducting Carbon Nanotube Networks. *Cell Reports Physical Science* **2023,** *4*, 101407, https://doi.org/10.1016/j.xcrp.2023.101407.

227. Han, C. C.; Elsenbaumer, R. L., Protonic Acids: Generally Applicable Dopants for Conducting Polymers. *Synthetic Metals* **1989,** *30*, 123-131, https://doi.org/10.1016/0379-6779(89)90648-6.

228. Ausserlechner, S. J.; Gruber, M.; Hetzel, R.; Flesch, H.-G.; Ladinig, L.; Hauser, L.; Haase, A.; Buchner, M.; Resel, R.; Schürrer, F.; Stadlober, B.; Trimmel, G.; Zojer, K.; Zojer, E., Mechanism of Surface Proton Transfer Doping in Pentacene Based Organic Thin-Film Transistors. *physica status solidi (a)* **2012,** *209*, 181-192, https://doi.org/10.1002/pssa.201127595.

229. Ćirić-Marjanović, G., Recent Advances in Polyaniline Research: Polymerization Mechanisms, Structural Aspects, Properties and Applications. *Synthetic Metals* **2013,** *177*, 1-47, https://doi.org/10.1016/j.synthmet.2013.06.004.

230. Strano, M. S.; Huffman, C. B.; Moore, V. C.; O'Connell, M. J.; Haroz, E. H.; Hubbard, J.; Miller, M.; Rialon, K.; Kittrell, C.; Ramesh, S.; Hauge, R. H.; Smalley, R. E., Reversible,

Band-Gap-Selective Protonation of Single-Walled Carbon Nanotubes in Solution. *The Journal of Physical Chemistry B* **2003,** *107*, 6979-6985, https://doi.org/10.1021/jp027664a.

231. Welch, G. C.; Coffin, R.; Peet, J.; Bazan, G. C., Band Gap Control in Conjugated Oligomers via Lewis Acids. *Journal of the American Chemical Society* **2009,** *131*, 10802-10803, https://doi.org/10.1021/ja902789w.

232. Zalar, P.; Henson, Z. B.; Welch, G. C.; Bazan, G. C.; Nguyen, T.-Q., Color Tuning in Polymer Light-Emitting Diodes with Lewis Acids. *Angewandte Chemie International Edition* **2012,** *51*, 7495-7498, https://doi.org/10.1002/anie.201202570.

233. Zalar, P.; Kuik, M.; Henson, Z. B.; Woellner, C.; Zhang, Y.; Sharenko, A.; Bazan, G. C.; Nguyen, T.-Q., Increased Mobility Induced by Addition of a Lewis Acid to a Lewis Basic Conjugated Polymer. *Advanced Materials* **2014,** *26*, 724-727, https://doi.org/10.1002/adma.201303357.

234. Han, Y.; Barnes, G.; Lin, Y.-H.; Martin, J.; Al-Hashimi, M.; AlQaradawi, S. Y.; Anthopoulos, T. D.; Heeney, M., Doping of Large Ionization Potential Indenopyrazine Polymers via Lewis Acid Complexation with Tris(pentafluorophenyl)borane: A Simple Method for Improving the Performance of Organic Thin-Film Transistors. *Chemistry of Materials* **2016,** *28*, 8016-8024, https://doi.org/10.1021/acs.chemmater.6b03761.

235. Yan, H.; Chen, J.; Zhou, K.; Tang, Y.; Meng, X.; Xu, X.; Ma, W., Lewis Acid Doping Induced Synergistic Effects on Electronic and Morphological Structure for Donor and Acceptor in Polymer Solar Cells. *Advanced Energy Materials* **2018,** *8*, 1703672, https://doi.org/10.1002/aenm.201703672.

236. Yan, H.; Tang, Y.; Sui, X.; Liu, Y.; Gao, B.; Liu, X.; Liu, S. F.; Hou, J.; Ma, W., Increasing Quantum Efficiency of Polymer Solar Cells with Efficient Exciton Splitting and Long Carrier Lifetime by Molecular Doping at Heterojunctions. *ACS Energy Letters* **2019,** *4*, 1356-1363, https://doi.org/10.1021/acsenergylett.9b00843.

237. Suh, E. H.; Oh, J. G.; Jung, J.; Noh, S. H.; Lee, T. S.; Jang, J., Brønsted Acid Doping of P3HT with Largely Soluble Tris(pentafluorophenyl)borane for Highly Conductive and Stable Organic Thermoelectrics Via One-Step Solution Mixing. *Advanced Energy Materials* **2020,** *10*, 2002521, https://doi.org/10.1002/aenm.202002521.

238. Zapata-Arteaga, O.; Perevedentsev, A.; Prete, M.; Busato, S.; Floris, P. S.; Asatryan, J.; Rurali, R.; Martín, J.; Campoy-Quiles, M., A Universal, Highly Stable Dopant System for Organic Semiconductors Based on Lewis-Paired Dopant Complexes. *ACS Energy Letters* **2024,** *9*, 3567-3577, https://doi.org/10.1021/acsenergylett.4c01278.

239. Shirakawa, H.; Louis, E. J.; MacDiarmid, A. G.; Chiang, C. K.; Heeger, A. J., Synthesis of electrically conducting organic polymers: halogen derivatives of polyacetylene, $(CH)_x$. *Journal of the Chemical Society, Chemical Communications* **1977**, 578-580, https://doi.org/10.1039/C39770000578.

240. Lee, R. S.; Kim, H. J.; Fischer, J. E.; Thess, A.; Smalley, R. E., Conductivity Enhancement in Single-Walled Carbon Nanotube Bundles Doped with K and Br. *Nature* **1997,** *388*, 255-257, https://doi.org/10.1038/40822.

241. Zhou, C.; Kong, J.; Yenilmez, E.; Dai, H., Modulated Chemical Doping of Individual Carbon Nanotubes. *Science* **2000,** *290*, 1552-1555, https://doi.org/10.1126/science.290.5496.1552.

242. Fischer, J. E., Chemical Doping of Single-Wall Carbon Nanotubes. *Accounts of Chemical Research* **2002,** *35*, 1079-1086, https://doi.org/10.1021/ar0101638.

243. Tietze, M. L.; Pahner, P.; Schmidt, K.; Leo, K.; Lüssem, B., Doped Organic Semiconductors: Trap-Filling, Impurity Saturation, and Reserve Regimes. *Advanced Functional Materials* **2015,** *25*, 2701-2707, https://doi.org/10.1002/adfm.201404549.

244. Gotthardt, J. M.; Schneider, S.; Brohmann, M.; Leingang, S.; Sauter, E.; Zharnikov, M.; Himmel, H.-J.; Zaumseil, J., Molecular n-Doping of Large- and Small-Diameter Carbon Nanotube Field-Effect Transistors with Tetrakis(tetramethylguanidino)benzene. *ACS Applied Electronic Materials* **2021,** *3*, 804-812, https://doi.org/10.1021/acsaelm.0c00957.

245. Hawkey, A.; Rodríguez‐Martínez, X.; Lindenthal, S.; Jansen, M. C. F.; Crispin, R.; Zaumseil, J., Bandgap‐Dependent Doping of Semiconducting Carbon Nanotube Networks by Proton‐Coupled Electron Transfer for Stable Thermoelectrics. *Advanced Electronic Materials* **2025,** *n/a*, 2400817, https://doi.org/10.1002/aelm.202400817.

246. Schneider, S.; Gotthardt, J. M.; Steuer, L.; Leingang, S.; Himmel, H.-J.; Zaumseil, J., Improving Electron Injection and Transport in Polymer Field-Effect Transistors with Guanidino-Functionalized Aromatic n-Dopants. *Journal of Materials Chemistry C* **2021,** *9*, 7485-7493, https://doi.org/10.1039/D1TC00968K.

247. Eckstein, K. H.; Oberndorfer, F.; Achsnich, M. M.; Schöppler, F.; Hertel, T., Quantifying Doping Levels in Carbon Nanotubes by Optical Spectroscopy. *The Journal of Physical Chemistry C* **2019,** *123*, 30001-30006, https://doi.org/10.1021/acs.jpcc.9b08663.

248. Eckstein, K. H.; Hartleb, H.; Achsnich, M. M.; Schöppler, F.; Hertel, T., Localized Charges Control Exciton Energetics and Energy Dissipation in Doped Carbon Nanotubes. *ACS Nano* **2017,** *11*, 10401-10408, https://doi.org/10.1021/acsnano.7b05543.

249. Rønnow, T. F.; Pedersen, T. G.; Cornean, H. D., Stability of Singlet and Triplet Trions in Carbon Nanotubes. *Physics Letters A* **2009,** *373*, 1478-1481, https://doi.org/10.1016/j.physleta.2009.02.049.

250. Stanton, N. J.; Ihly, R.; Norton-Baker, B.; Ferguson, A. J.; Blackburn, J. L., Solution-Phase p-Type Doping of Highly Enriched Semiconducting Single-Walled Carbon Nanotubes for Thermoelectric Thin Films. *Applied Physics Letters* **2021,** *119*, 023302, https://doi.org/10.1063/5.0055837.

251. Park, J. S.; Hirana, Y.; Mouri, S.; Miyauchi, Y.; Nakashima, N.; Matsuda, K., Observation of Negative and Positive Trions in the Electrochemically Carrier-Doped Single-Walled Carbon Nanotubes. *Journal of the American Chemical Society* **2012,** *134*, 14461-14466, https://doi.org/10.1021/ja304282j.

252. Jakubka, F.; Grimm, S. B.; Zakharko, Y.; Gannott, F.; Zaumseil, J., Trion Electroluminescence from Semiconducting Carbon Nanotubes. *ACS Nano* **2014,** *8*, 8477-8486, https://doi.org/10.1021/nn503046y.

253. Hartleb, H.; Späth, F.; Hertel, T., Evidence for Strong Electronic Correlations in the Spectra of Gate-Doped Single-Wall Carbon Nanotubes. *ACS Nano* **2015,** *9*, 10461-10470, https://doi.org/10.1021/acsnano.5b04707.

254. Yoshida, M.; Popert, A.; Kato, Y. K., Gate-Voltage Induced Trions in Suspended Carbon Nanotubes. *Physical Review B* **2016,** *93*, 041402, https://doi.org/10.1103/PhysRevB.93.041402.

255. Graf, A.; Murawski, C.; Zakharko, Y.; Zaumseil, J.; Gather, M. C., Infrared Organic Light-Emitting Diodes with Carbon Nanotube Emitters. *Advanced Materials* **2018,** *30*, 1706711, https://doi.org/10.1002/adma.201706711.

256. Zorn, N. F.; Settele, S.; Sebastian, F. L.; Lindenthal, S.; Zaumseil, J., Tuning Electroluminescence from Functionalized SWCNT Networks Further into the Near-Infrared. *ACS Applied Optical Materials* **2023,** *1*, 1706-1714, https://doi.org/10.1021/acsaom.3c00261.

257. Nishihara, T.; Yamada, Y.; Okano, M.; Kanemitsu, Y., Trion Formation and Recombination Dynamics in Hole-Doped Single-Walled Carbon Nanotubes. *Applied Physics Letters* **2013,** *103*, 023101, https://doi.org/10.1063/1.4813014.

258. Watanabe, K.; Asano, K., Trions in Semiconducting Single-Walled Carbon Nanotubes. *Physical Review B* **2012,** *85*, 035416, https://doi.org/10.1103/PhysRevB.85.035416.

259. Nishihara, T.; Yamada, Y.; Okano, M.; Kanemitsu, Y., Dynamics of the Lowest-Energy Excitons in Single-Walled Carbon Nanotubes under Resonant and Nonresonant Optical Excitation. *The Journal of Physical Chemistry C* **2015,** *119*, 28654-28659, https://doi.org/10.1021/acs.jpcc.5b09485.

260. El Yumin, A. A.; Zorn, N. F.; Berger, F. J.; Heimfarth, D.; Zaumseil, J., Trion Emission from Frozen p-n Junctions in Networks of Electrolyte-Gated (6,5) Single-Walled Carbon Nanotubes. *Carbon* **2023,** *202*, 547-553, https://doi.org/10.1016/j.carbon.2022.11.025.

261. Koyama, T.; Shimizu, S.; Miyata, Y.; Shinohara, H.; Nakamura, A., Ultrafast Formation and Decay Dynamics of Trions in p-Doped Single-Walled Carbon Nanotubes. *Physical Review B* **2013,** *87*, 165430, https://doi.org/10.1103/PhysRevB.87.165430.

262. Mouri, S.; Miyauchi, Y.; Iwamura, M.; Matsuda, K., Temperature Dependence of Photoluminescence Spectra in Hole-Doped Single-Walled Carbon Nanotubes: Implications of Trion Localization. *Physical Review B* **2013,** *87*, 045408, https://doi.org/10.1103/PhysRevB.87.045408.

263. Akizuki, N.; Iwamura, M.; Mouri, S.; Miyauchi, Y.; Kawasaki, T.; Watanabe, H.; Suemoto, T.; Watanabe, K.; Asano, K.; Matsuda, K., Nonlinear Photoluminescence Properties of Trions in Hole-Doped Single-Walled Carbon Nanotubes. *Physical Review B* **2014,** *89*, 195432, https://doi.org/10.1103/PhysRevB.89.195432.

264. Bai, Y.; Olivier, J.-H.; Bullard, G.; Liu, C.; Therien, M. J., Dynamics of Charged Excitons in Electronically and Morphologically Homogeneous Single-Walled Carbon Nanotubes. *Proceedings of the National Academy of Sciences* **2018,** *115*, 674-679, https://doi.org/10.1073/pnas.1712971115.

265. Eremin, T. V.; Obraztsov, P. A.; Velikanov, V. A.; Shubina, T. V.; Obraztsova, E. D., Many-Particle Excitations in Non-Covalently Doped Single-Walled Carbon Nanotubes. *Scientific Reports* **2019,** *9*, 14985, https://doi.org/10.1038/s41598-019-50333-7.

266. Zorn, N. F.; Zaumseil, J., Charge Transport in Semiconducting Carbon Nanotube Networks. *Applied Physics Reviews* **2021,** *8*, 041318, https://doi.org/10.1063/5.0065730.

267. Matsunaga, R.; Matsuda, K.; Kanemitsu, Y., Origin of Low-Energy Photoluminescence Peaks in Single Carbon Nanotubes: K-Momentum Dark Excitons and Triplet Dark Excitons. *Physical Review B* **2010,** *81*, 033401, https://doi.org/10.1103/PhysRevB.81.033401.

268. Santos, S. M.; Yuma, B.; Berciaud, S.; Shaver, J.; Gallart, M.; Gilliot, P.; Cognet, L.; Lounis, B., All-Optical Trion Generation in Single-Walled Carbon Nanotubes. *Physical Review Letters* **2011,** *107*, 187401, https://doi.org/10.1103/PhysRevLett.107.187401.

269. Gaulke, M.; Janissek, A.; Peyyety, N. A.; Alamgir, I.; Riaz, A.; Dehm, S.; Li, H.; Lemmer, U.; Flavel, B. S.; Kappes, M. M.; Hennrich, F.; Wei, L.; Chen, Y.; Pyatkov, F.; Krupke, R., Low-Temperature Electroluminescence Excitation Mapping of Excitons and Trions in Short-Channel Monochiral Carbon Nanotube Devices. *ACS Nano* **2020,** *14*, 2709-2717, https://doi.org/10.1021/acsnano.9b07207.

270. Furukawa, Y.; Shimokawa, D., Polarons, Bipolarons, and Electrical Properties of Crystalline Conducting Polymers. *Bulletin of the Chemical Society of Japan* **2023,** *96*, 1243-1251, https://doi.org/10.1246/bcsj.20230175.

271. Ghosh, R.; Spano, F. C., Excitons and Polarons in Organic Materials. *Accounts of Chemical Research* **2020,** *53*, 2201-2211, https://doi.org/10.1021/acs.accounts.0c00349.

272. Deilmann, T.; Rohlfing, M., Huge Trionic Effects in Graphene Nanoribbons. *Nano Letters* **2017,** *17*, 6833-6837, https://doi.org/10.1021/acs.nanolett.7b03111.

273. Fedotov, P. V.; Obraztsova, E. D., Near Infrared Photoluminescence of the Bottom-Up Produced 7-Armchair Graphene Nanoribbons. *Applied Physics Letters* **2023,** *122*, 013101, https://doi.org/10.1063/5.0131405.

274. Zhou, G.; Cen, C.; Wang, S.; Deng, M.; Prezhdo, O. V., Electron–Phonon Scattering Is Much Weaker in Carbon Nanotubes than in Graphene Nanoribbons. *The Journal of Physical Chemistry Letters* **2019,** *10*, 7179-7187, https://doi.org/10.1021/acs.jpclett.9b02874.

275. Bennett, P. B.; Pedramrazi, Z.; Madani, A.; Chen, Y.-C.; de Oteyza, D. G.; Chen, C.; Fischer, F. R.; Crommie, M. F.; Bokor, J., Bottom-Up Graphene Nanoribbon Field-Effect Transistors. *Applied Physics Letters* **2013,** *103*, https://doi.org/10.1063/1.4855116.

276. Klauk, H., Organic Thin-Film Transistors. *Chemical Society Reviews* **2010,** *39*, 2643-2666, https://doi.org/10.1039/B909902F.

277. Zaumseil, J.; Sirringhaus, H., Electron and Ambipolar Transport in Organic Field-Effect Transistors. *Chemical Reviews* **2007,** *107*, 1296-1323, https://doi.org/10.1021/cr0501543.

278. Wilk, G. D.; Wallace, R. M.; Anthony, J. M., High-κ Gate Dielectrics: Current Status and Materials Properties Considerations. *Journal of Applied Physics* **2001,** *89*, 5243-5275, https://doi.org/10.1063/1.1361065.

279. Held, M.; Schießl, S. P.; Miehler, D.; Gannott, F.; Zaumseil, J., Polymer/Metal Oxide Hybrid Dielectrics for Low Voltage Field-Effect Transistors with Solution-Processed, High-Mobility Semiconductors. *Applied Physics Letters* **2015,** *107*, https://doi.org/10.1063/1.4929461.

280. Kim, K. T.; Jung, J. W.; Jo, W. H., Synthesis of Graphene Nanoribbons with Various Widths and its Application to Thin-Film Transistor. *Carbon* **2013,** *63*, 202-209, https://doi.org/10.1016/j.carbon.2013.06.074.

281. Gao, J.; Uribe-Romo, F. J.; Saathoff, J. D.; Arslan, H.; Crick, C. R.; Hein, S. J.; Itin, B.; Clancy, P.; Dichtel, W. R.; Loo, Y.-L., Ambipolar Transport in Solution-Synthesized Graphene Nanoribbons. *ACS Nano* **2016,** *10*, 4847-4856, https://doi.org/10.1021/acsnano.6b00643.

282. Salleo, A., Charge Transport in Polymeric Transistors. *Materials Today* **2007,** *10*, 38-45, https://doi.org/10.1016/S1369-7021(07)70018-4.

283. Schießl, S. P.; de Vries, X.; Rother, M.; Massé, A.; Brohmann, M.; Bobbert, P. A.; Zaumseil, J., Modeling Carrier Density Dependent Charge Transport in Semiconducting Carbon Nanotube Networks. *Physical Review Materials* **2017,** *1*, 046003, https://doi.org/10.1103/PhysRevMaterials.1.046003.

284. Kim, S. H.; Hong, K.; Xie, W.; Lee, K. H.; Zhang, S.; Lodge, T. P.; Frisbie, C. D., Electrolyte-Gated Transistors for Organic and Printed Electronics. *Advanced Materials* **2013,** *25*, 1822-1846, https://doi.org/10.1002/adma.201202790.

285. Kang, M. S.; Frisbie, C. D., A Pedagogical Perspective on Ambipolar FETs. *ChemPhysChem* **2013,** *14*, 1547-1552, https://doi.org/10.1002/cphc.201300014.

286. Friedlein, J. T.; McLeod, R. R.; Rivnay, J., Device physics of organic electrochemical transistors. *Organic Electronics* **2018,** *63*, 398-414, https://doi.org/10.1016/j.orgel.2018.09.010.

287. Bernards, D. A.; Malliaras, G. G., Steady-State and Transient Behavior of Organic Electrochemical Transistors. *Advanced Functional Materials* **2007,** *17*, 3538-3544, https://doi.org/10.1002/adfm.200601239.

288. Thiemann, S.; Sachnov, S.; Porscha, S.; Wasserscheid, P.; Zaumseil, J., Ionic Liquids for Electrolyte-Gating of ZnO Field-Effect Transistors. *The Journal of Physical Chemistry C* **2012,** *116*, 13536-13544, https://doi.org/10.1021/jp3024233.

289. Yao, Y.; Huang, W.; Chen, J.; Liu, X.; Bai, L.; Chen, W.; Cheng, Y.; Ping, J.; Marks, T. J.; Facchetti, A., Flexible and Stretchable Organic Electrochemical Transistors for Physiological Sensing Devices. *Advanced Materials* **2023,** *35*, 2209906, https://doi.org/10.1002/adma.202209906.

290. Takemoto, A.; Araki, T.; Nishimura, K.; Akiyama, M.; Uemura, T.; Kiriyama, K.; Koot, J. M.; Kasai, Y.; Kurihira, N.; Osaki, S.; Wakida, S.-i.; den Toonder, J. M. J.; Sekitani, T., Fully Transparent, Ultrathin Flexible Organic Electrochemical Transistors with Additive Integration for Bioelectronic Applications. *Advanced Science* **2023,** *10*, 2204746, https://doi.org/10.1002/advs.202204746.

291. Song, G.; Wang, Y.; Tan, D. Q., A review of surface roughness impact on dielectric film properties. *IET Nanodielectrics* **2022,** *5*, 1-23, https://doi.org/10.1049/nde2.12026.

292. Siemons, N.; Pearce, D.; Yu, H.; Tuladhar, S. M.; LeCroy, G. S.; Sheelamanthula, R.; Hallani, R. K.; Salleo, A.; McCulloch, I.; Giovannitti, A.; Frost, J. M.; Nelson, J., Controlling swelling in mixed transport polymers through alkyl side-chain physical cross-linking. *Proceedings of the National Academy of Sciences* **2023,** *120*, e2306272120, https://doi.org/10.1073/pnas.2306272120.

293. Huang, Y.; Zhou, Y.; Wieland, S.; Li, Y.; Zhao, N.; Zaumseil, J., Tunable Tactile Synapses Enabled by Erasable Doping in Iongel-Gated Nanotube Network Transistors. *Advanced Functional Materials* **2025,** *n/a*, 2423030, https://doi.org/10.1002/adfm.202423030.

294. Balcı Leinen, M.; Lindenthal, S.; Heimfarth, D.; Zaumseil, J., Networks of As-Dispersed, Polymer-Wrapped (6,5) Single-Walled Carbon Nanotubes for Selective Cu^{2+} and Glyphosate Sensing. *Nanoscale* **2022,** *14*, 13542-13550, https://doi.org/10.1039/D2NR02517E.

295. Llinas, J. P.; Fairbrother, A.; Borin Barin, G.; Shi, W.; Lee, K.; Wu, S.; Yong Choi, B.; Braganza, R.; Lear, J.; Kau, N.; Choi, W.; Chen, C.; Pedramrazi, Z.; Dumslaff, T.; Narita, A.; Feng, X.; Müllen, K.; Fischer, F.; Zettl, A.; Ruffieux, P.; Yablonovitch, E.; Crommie, M.; Fasel, R.; Bokor, J., Short-Channel Field-Effect Transistors with 9-Atom and 13-Atom Wide Graphene Nanoribbons. *Nature Communications* **2017,** *8*, 633, https://doi.org/10.1038/s41467-017-00734-x.

296. Martini, L.; Chen, Z.; Mishra, N.; Barin, G. B.; Fantuzzi, P.; Ruffieux, P.; Fasel, R.; Feng, X.; Narita, A.; Coletti, C.; Müllen, K.; Candini, A., Structure-Dependent Electrical Properties of Graphene Nanoribbon Devices with Graphene Electrodes. *Carbon* **2019,** *146*, 36-43, https://doi.org/10.1016/j.carbon.2019.01.071.

297. Huang, W.; Braun, O.; Indolese, D. I.; Barin, G. B.; Gandus, G.; Stiefel, M.; Olziersky, A.; Müllen, K.; Luisier, M.; Passerone, D.; Ruffieux, P.; Schönenberger, C.; Watanabe, K.; Taniguchi, T.; Fasel, R.; Zhang, J.; Calame, M.; Perrin, M. L., Edge Contacts to Atomically Precise Graphene Nanoribbons. *ACS Nano* **2023**, 18706–18715, https://doi.org/10.1021/acsnano.3c00782.

298. Lin, Y. C.; Mutlu, Z.; Borin Barin, G.; Hong, Y.; Llinas, J. P.; Narita, A.; Singh, H.; Müllen, K.; Ruffieux, P.; Fasel, R.; Bokor, J., Scaling and Statistics of Bottom-Up Synthesized Armchair Graphene Nanoribbon Transistors. *Carbon* **2023,** *205*, 519-526, https://doi.org/10.1016/j.carbon.2023.01.054.

299. Derycke, V.; Martel, R.; Appenzeller, J.; Avouris, P., Controlling Doping and Carrier Injection in Carbon Nanotube Transistors. *Applied Physics Letters* **2002,** *80*, 2773-2775, https://doi.org/10.1063/1.1467702.

300. Sakaguchi, H.; Song, S.; Kojima, T.; Nakae, T., Homochiral Polymerization-Driven Selective Growth of Graphene Nanoribbons. *Nature Chemistry* **2017,** *9*, 57-63, https://doi.org/10.1038/nchem.2614.

301. Richter, N.; Chen, Z.; Tries, A.; Prechtl, T.; Narita, A.; Müllen, K.; Asadi, K.; Bonn, M.; Kläui, M., Charge Transport Mechanism in Networks of Armchair Graphene Nanoribbons. *Scientific Reports* **2020,** *10*, 1988, https://doi.org/10.1038/s41598-020-58660-w.

302. Jänsch, D.; Ivanov, I.; Zagranyarski, Y.; Duznovic, I.; Baumgarten, M.; Turchinovich, D.; Li, C.; Bonn, M.; Müllen, K., Ultra-Narrow Low-Bandgap Graphene Nanoribbons from Bromoperylenes—Synthesis and Terahertz-Spectroscopy. *Chemistry – A European Journal* **2017,** *23*, 4870-4875, https://doi.org/10.1002/chem.201605859.

303. Pizzochero, M.; Borin Barin, G.; Čerņevičs, K. n.; Wang, S.; Ruffieux, P.; Fasel, R.; Yazyev, O. V., Edge Disorder in Bottom-Up Zigzag Graphene Nanoribbons: Implications for Magnetism and Quantum Electronic Transport. *The Journal of Physical Chemistry Letters* **2021,** *12*, 4692-4696, https://doi.org/10.1021/acs.jpclett.1c00921.

304. Pizzochero, M.; Čerņevičs, K.; Borin Barin, G.; Wang, S.; Ruffieux, P.; Fasel, R.; Yazyev, O. V., Quantum Electronic Transport Across 'Bite' Defects in Graphene Nanoribbons. *2D Materials* **2021,** *8*, 035025, https://doi.org/10.1088/2053-1583/abf716.

305. Mutlu, Z.; Dinh, C.; Barin, G. B.; Jacobse, P. H.; Kumar, A.; Polley, D.; Singh, H.; Wang, Z.; Lin, Y. C.; Schwartzberg, A.; Crommie, M. F.; Mullen, K.; Ruffieux, P.; Fasel, R.; Bokor, J., Contact Engineering for Graphene Nanoribbon Devices. *Applied Physics Reviews* **2023,** *10*, 041412, https://doi.org/10.1063/5.0172432.

306. Chen, Z.; Zhang, W.; Palma, C.-A.; Lodi Rizzini, A.; Liu, B.; Abbas, A.; Richter, N.; Martini, L.; Wang, X.-Y.; Cavani, N.; Lu, H.; Mishra, N.; Coletti, C.; Berger, R.; Klappenberger, F.; Kläui, M.; Candini, A.; Affronte, M.; Zhou, C.; De Renzi, V.; del Pennino, U.; Barth, J. V.; Räder, H. J.; Narita, A.; Feng, X.; Müllen, K., Synthesis of Graphene Nanoribbons by Ambient-Pressure Chemical Vapor Deposition and Device Integration. *Journal of the American Chemical Society* **2016,** *138*, 15488-15496, https://doi.org/10.1021/jacs.6b10374.

307. Zhang, J.; Qian, L.; Barin, G. B.; Daaoub, A. H. S.; Chen, P.; Müllen, K.; Sangtarash, S.; Ruffieux, P.; Fasel, R.; Sadeghi, H.; Zhang, J.; Calame, M.; Perrin, M. L., Contacting Individual Graphene Nanoribbons Using Carbon Nanotube Electrodes. *Nature Electronics* **2023,** *6*, 572-581, https://doi.org/10.1038/s41928-023-00991-3.

308. Ribeiro, L. A., Jr.; da Cunha, W. F.; Fonseca, A. L. d. A.; e Silva, G. M.; Stafström, S., Transport of Polarons in Graphene Nanoribbons. *The Journal of Physical Chemistry Letters* **2015,** *6*, 510-514, https://doi.org/10.1021/jz502460g.

309. Abreu, A. V. P.; Teixeira, J. F.; Fonseca, A. L. d. A.; Gargano, R.; e Silva, G. M.; Ribeiro, L. A. J., Impact of the Electron–Phonon Interactions on the Polaron Dynamics in Graphene Nanoribbons. *The Journal of Physical Chemistry A* **2016,** *120*, 4901-4906, https://doi.org/10.1021/acs.jpca.5b12482.

310. da Cunha, W. F.; Acioli, P. H.; de Oliveira Neto, P. H.; Gargano, R.; e Silva, G. M., Polaron Properties in Armchair Graphene Nanoribbons. *The Journal of Physical Chemistry A* **2016,** *120*, 4893-4900, https://doi.org/10.1021/acs.jpca.5b12491.

311. Silva, G. G.; da Cunha, W. F.; de Sousa Junior, R. T.; Almeida Fonseca, A. L.; Ribeiro Júnior, L. A.; e Silva, G. M., Influence of Quasi-Particle Density over Polaron Mobility in Armchair Graphene Nanoribbons. *Physical Chemistry Chemical Physics* **2018,** *20*, 16712-16718, https://doi.org/10.1039/C8CP02373E.

312. Pereira Júnior, M. L.; da Cunha, W. F.; de Sousa Junior, R. T.; Giozza, W. F.; e Silva, G. M.; Ribeiro Junior, L. A., Charge Transport Mechanism in Chevron-Graphene Nanoribbons. *The Journal of Physical Chemistry C* **2020,** *124*, 22392-22398, https://doi.org/10.1021/acs.jpcc.0c06625.

313. Grimm, S.; Schweiger, M.; Eigler, S.; Zaumseil, J., High-Quality Reduced Graphene Oxide by CVD-Assisted Annealing. *The Journal of Physical Chemistry C* **2016,** *120*, 3036-3041, https://doi.org/10.1021/acs.jpcc.5b11598.

EIDESSTATTLICHE VERSICHERUNG

Gemäß §8 der Promotionsordnung für die Gesamtfakultät für Mathematik, Ingenieur- und Naturwissenschaften der Universität Heidelberg.

1. Bei der eingereichten Dissertation zu dem Thema “*Synthesis, Purification, Doping of and Charge Transport in Low-Dimensional Carbon-Based Semiconductors”* handelt es sich um meine eigenständig erbrachte Leistung.

2. Ich habe nur die angegebenen Quellen und Hilfsmittel (inkl. KI-basierter Hilfsmittel) benutzt und mich keiner unzulässigen Hilfe Dritter bedient. Insbesondere habe ich wörtlich oder sinngemäß aus anderen Werken übernommene Inhalte als solche kenntlich gemacht.

3. Die Arbeit oder Teile davon habe ich bislang nicht an einer Hochschule des In- oder Auslands als Bestandteil einer Prüfungs- oder Qualifikationsleistung vorgelegt.

4. Die Richtigkeit der vorstehenden Erklärungen bestätige ich.

5. Die Bedeutung der eidesstattlichen Versicherung und die strafrechtlichen Folgen einer unrichtigen oder unvollständigen eidesstattlichen Versicherung sind mir bekannt.

Ich versichere hiermit an Eides statt, dass ich nach bestem Wissen die reine Wahrheit erklärt und nichts verschwiegen habe.

Speyer, 30. Mai 2025

Sebastian Lindenthal